

UNIVERSITÄT ZÜRICH

DER MATHEMATISCH-NATURWISSENSCHAFTLICHEN FAKULTÄT
ZUR ERLANGUNG DER
VENIA LEGENDI
EINGEREICHTEN HABILITATIONSSCHRIFT

Advanced Analytical Technologies
enabled by
Soft X-ray Plasma-Lasing

vorgelegt von
Dr Davide Bleiner aus Rom, Italien

Projekt durch den SNF als Förderungsprofessur 2011 finanziert

*The task is not so much to see
what no one has yet seen;
but to think what nobody has yet thought,
about that which everybody sees.*
Erwin Schrödinger (1887-1961)

CURRICULUM VITAE

Davide Bleiner, *born in* Rome (Italy), on February, 11th 1973

Career

2014–now Head of Laboratory for Advanced Analytical Technologies at the Empa

2011–2015 SNSF Professorship

2007–2010 Oberassistent at the Institute for Energy Technologies, ETH Zurich

2005–2007 FWO Postdoc Fellow at the University of Antwerp

2002–2005 Scientific collaborator at the Empa

1999–2002 Ph.D. at the Institute of Inorganic Chemistry, ETH Zurich

1993–1998 Laurea *summa cum Laude* in Geological Sciences at University of Rome "La Sapienza".

Own Publications Related to this Habilitation Thesis

1. Masoudnia, L., Bleiner, D. Table-top Two-color Soft X-ray Laser by means of Ni-like Plasmas, Phys. of Plasmas, in press
2. Masoudnia, L., Bleiner, D. Optimum Pump Pulse Duration for X-Ray Ar-Plasma Lasing (2015) Photonics 2(1), 164-183
3. Masoudnia, L., Bleiner, D. Optimum Electron Temperature And Density For Short-Wavelength Plasma-Lasing From Nickel-Like Ions (2014) Nuclear Instruments and Methods in Physics Research, Section B: Beam Interactions with Materials and Atoms, 323, pp. 59-70
4. Ruiz-Lopez, M., Bleiner, D. Implementing The Plasma-Lasing Potential For Tabletop Nano-Imaging (2014) Applied Physics B: Lasers and Optics, 115 (3), pp. 311-324.
5. Masoudnia, L., Bleiner, D. Plasma Homogenization For Overcoming Refractive Losses In X-Ray Lasers (2014) Springer Proceedings in Physics, 147, pp. 171-174
6. Staub, F., Bleiner, D., Jia, F., Balmer, J.E. Line-Focus Generation For X-Ray Laser Pumping (2014) Springer Proceedings in Physics, 147, pp. 235-238
7. Bleiner, D. Coherent Short-Wavelength Plasma Radiation For Lab-Scale Nano-Inspection Tools (2014) Springer Proceedings in Physics, 147, pp. 39-44
8. Bleiner, D., Yulin, S., Martynczuk, J., Ruiz-Lopez, M., Arbelo, Y., Balmer, J.E., Günther, D. Actinic Damage Of Y/Mo Multilayer Optics In A Table-Top Plasma-Driven X-Ray Laser (2014) Applied Optics, (22), pp. 4894-4902
9. Bleiner, D., Arbelo-Pena, Y., Masoudnia, L., Ruiz-Lopez, M. Table-Top X-Ray Lasers Using A Plasma Gain-Medium: Limits And Potentials (2014) Physica Scripta, T162, art. no. 014050
10. Bleiner, D., Feurer, T. Fourier Optics Study Of Traveling-Wave Excitation At Short-Wavelength Plasma-Lasing (2014) Springer Proceedings in Physics, 147, pp. 35-38
11. Ruiz-Lopez, M., Staub, F., Bleiner, D. Optical Correction Of X-Ray Laser Illumination For Short-Wavelength Microscopy (2014) Springer Proceedings in Physics, 147, pp. 227-230
12. Masoudnia, L., Bleiner, D. Hohlraum Target For Overcoming Refractive Losses In Plasma X-Ray Lasers (2013) Laser Physics, 23 (5), art. no. 056003
13. Bleiner, D., Feurer, T. Pulse-Front Tilt For Short-Wavelength Lasing By Means Of Traveling-Wave Plasma-Excitation (2012) Applied Optics, 51 (36), pp. 8848-8853.
14. Lienemann, P., Bleiner, D. Elemental Analysis With X-Ray Fluorescence Spectrometry (2012) Proceedings of SPIE - The International Society for Optical Engineering, 8678, art. no. 86780D
15. Bleiner, D. Comparison Of Laboratory-Scale XUV Laser With XFELs (2012) Proceedings of SPIE - The International Society for Optical Engineering, 8678, art. no. 867806

16. Bleiner, D. Saturation Gain-Length Product During Short-Wavelength Plasma Lasing (2012) Applied Physics Letters, 101 (8), art. no. 081105
17. Staub, F., Imesch, C., Bleiner, D., Balmer, J.E. Soft-X-Ray Lasing In Nickel-Like Barium At 9.2nm Using The Grazing-Incidence Scheme (2012) Optics Communications, 285 (8), pp. 2118-2121
18. Balmer, J.E., Bleiner, D., Staub, F. Extreme Ultraviolet Lasers: Principles And Potential For Next-Generation Lithography (2012) Journal of Micro/Nanolithography, MEMS, and MOEMS, 11 (2), art. no. 021119
19. Bleiner, D., Balmer, J.E., Staub, F. Line Focusing For Soft X-Ray Laser-Plasma Lasing (2011) Applied Optics, 50 (36), pp. 6689-6696.
20. Aquila, A., Bleiner, D., Balmer, J., Bajt, S. Polarization Measurements Of Plasma Excited X-Ray Lasers (2011) Proceedings of SPIE - The International Society for Optical Engineering, 8140, art. no. 81400Z
21. Balmer, J.E., Staub, F., Imesch, C., Bleiner, D. Sub-10-nm Wavelength Ni-Like-Ion Collisional X-Ray Lasers (2011) Proceedings of SPIE - The International Society for Optical Engineering, 8140, art. no. 81400X
22. Bleiner, D., Staub, F., Balmer, J.E. EUV Microscopy Using A Lab-Scale X-Ray Laser Source (2011) Proceedings of SPIE - The International Society for Optical Engineering, 8140, art. no. 814014
23. Bleiner, D., Staub, F., Guzenko, V., Ekinici, Y., Balmer, J.E. Evaluation Of Lab-Scale EUV Microscopy Using A Table-Top Laser Source (2011) Optics Communications, 284 (19), pp. 4577-4583.

Abstract

Short-wavelength light sources (VUV, DUV, EUV, and X-rays) have dramatically impacted on material- and bio-analytics, enabling the possibility of retrieving the structure of molecules and proteins, the valence state of elements, the kinetics of electronic transitions, and intermediate states of reactive pathways. Further, the $< 150\text{nm}$ wavelength has offered access to nano-scale imaging and also visualization of the internal structure of samples by means of tomography.

Besides such remarkable impact in science, industry has also benefited too. The semiconductor industry is striving for extending the growth leveraged on deep UV lasers, and move on towards Extreme UV at $\lambda = 13.5\text{nm}$ for advanced nano-patterning. The latter resides on hopes for technology readiness of powerful 150–300W EUV sources for high volume manufacturing of nano-chips. Besides *patterning* sources, also technology readiness of compact EUV lasers for mask *defect metrology*, is not fulfilled. Mask defectivity degrades the production yield and has thus huge economic relevance.

Advanced X-ray sources, e.g. synchrotron, have the advantage of high brightness and spectral tunability. Unfortunately, the construction and running costs of third and fourth generation synchrotrons are prohibitive for a single research group or industrial enterprise, i.e. 0.5–1.5 billion Swiss francs. Furthermore, it is impossible obtaining frequent measurement shifts at any of the few worldwide installations.

Fortunately, the perspective to engineer table-top EUV laser setups is at hand. Indeed, micro-plasmas are bright sources of radiation. In brief, a powerful *pump pulse* (approx. 1 TW) directed on a *target* material generates a rapidly expanding brilliant *micro-plasma*. The plasma emissivity is largely in the X-ray domain, and shaping the plasma as a 50-by-100 μm by 15mm "column" leads to laser action. In fact, if the focal spot is a line, the elongated geometry of the plasma medium is favorable to support amplified spontaneous emission across its length, up to output brightness as high as 6 orders of magnitudes larger than the synchrotron's!

Plasma-based laser action is thus attractive as a platform for advanced analytical technologies, such as X-ray nano-scale imaging and spectroscopy on a table-top. Tremendous progress has been made, such that nowadays wavelengths as low as $\lambda = 6\text{ nm}$ (ca. 200eV photon) are possible on a table-top setup. The *technology readiness* of plasma XUV lasers is, however, still at research level. Fundamental and applied aspects on plasma-lasing are presented in this habilitation thesis, showing that some intrinsic trade-offs were overcome in my research.

A computational study was performed here to understand the effect of parameters such as the pump-pulse shape, duration and delay, and the plasma temperature and density controlling the laser action, until the obtainment of a saturated XUV laser output. The line focus generation was also simulated and compared to experimental data. A scaling-law was obtained, function of the plasma column geometry, to predict the saturation limit in short-wavelength plasma-lasing.

It emerged that for *scaling-down the wavelength*, large angles of target-incidence are essential to penetrate the pump deep into the plasma. On the other hand, to maximize the interaction length between the pump and the plasma medium, and *have better efficiency*, a small target-incidence irradiation is preferred. The fundamental conclusion was a trade-off between *wavelength scalability vs. efficiency* of the plasma laser. However, by adopting a "*traveling-wave excitation*" scheme such trade-off was overcome in this work.

An applied part on the plasma-laser imaging, combined with design-adapted objectives, concludes the present study. The ultimate nano-scale resolution was dictated by both the diffraction-limited and the wavefront-limited resolution, which imposed a combined study of both the source and the optics. A demonstrator is shown as well as experimental imaging results on a Siemens star reference sample. Besides imaging applications, spectroscopy with X-ray pulses with bimodal spectra ("two-color") is also shown as an additional benefit from plasma lasing.

CONTENTS

1. <i>INTRODUCTION</i>	13
1.1 X-ray Lasing Technologies	18
1.2 X-ray Plasma Lasing	18
1.2.1 Plasma as a Gain-medium	18
1.2.2 Processes in the Plasma & Interaction with Laser	22
1.2.3 The Transient Collisional Excitation Scheme	27
1.3 Research gap	31
1.4 Aims of the Thesis	32
1.5 Structure of the Thesis	32
2. <i>METHODS</i>	34
2.1 Plasma Lasing Modeling Codes	34
2.1.1 Hydrodynamic Codes	34
2.1.2 Atomic Spectroscopy Codes	36
2.1.3 Boundary Conditions for Ar Target	38
2.2 Optical Codes	38
2.2.1 Ray-tracing in Optics Design	38
2.2.2 Ray-tracing across Plasmas	39
2.2.3 Boundary Conditions	40
2.3 Experimental Equipment	41
2.3.1 Terawatt Pump Laser & Soft X-ray Plasma Laser	41
2.3.2 Near and Far-field XUV Characterization	42
2.3.3 Spatial Coherence Characterization	43
2.3.4 Target Chamber & Microscopy	44
2.3.5 Conditions for the Two-color Laser	46
3. <i>OPTIMIZATION OF PLASMA X-RAY LASING</i>	47
3.1 Line Focusing & Plasma Column	48
3.1.1 Parametric Study	49
3.1.2 Amplification Length	53
3.1.3 GRIP Technique by Tilting the Target	55
3.1.4 Summary on Line Focusing	56
3.2 Pump-Pulse Shaping	58
3.2.1 Calculation with Gaussian vs. Flat-top Pulse	59
3.2.2 Calculation of Effect of Pump-pulse Clipping on XUV Lasing	59
3.2.3 Calculation of Effect of Pump-pulse Rise-time on XUV lasing	59
3.2.4 Summary on Pulse Shaping	62
3.3 Pump Pulse Timing	63
3.3.1 Theory	64
3.3.1.1 Ionization Time	64
3.3.1.2 Plasma Energy Dissipation Time	64
3.3.1.3 Atomic Level Transition Times	65
3.3.1.4 Pumping & Relaxation Time	65
3.3.2 Calculation of Time-scale(s) for Plasma Lasing	67
3.3.2.1 Ionization Time of Neutral Ar ⁰	67
3.3.2.2 Ionization Time up to Ne-Like Lasing Stage	68
3.3.2.3 Transition Time among Ne-Like Levels	70
3.3.2.4 Pumping Time vs. Relaxation Time among Ne-Like Levels	71

3.3.3	Calculation of the Effect of Pulse Duration on Hydrodynamic Parameters	72
3.3.3.1	Optimum pump-Laser Intensity for Achieving Ne-like Ar^{+8}	73
3.3.4	Summary on Pulse Duration & Timing	74
3.4	Laser-produced Plasma Conditions	76
3.4.1	Theory	79
3.4.2	Experimental Affinity Ne-Like to Ni-Like Ions	82
3.4.3	Scaling-laws for Neon-like Plasma Lasers	82
3.4.4	Scaling-laws for Nickel-like Plasma Lasers	82
3.4.5	Nickel-like Ion Population	83
3.4.5.1	LTE Numerical Description	83
3.4.5.2	Non-LTE Numerical Description	84
3.4.5.3	LTE vs. Non-LTE frameworks	85
3.4.6	Gain Across the Laser-produced Plasma	86
3.4.6.1	Collisional Pumping	86
3.4.6.2	Population Inversion	87
3.4.6.3	Amplified Spontaneous Emission	88
3.4.7	Comparison Analytical vs. Numerical Models	90
3.4.7.1	Optimum Electron Temperature and Density	91
3.4.8	Plasma Gain-Medium Pumping	92
3.4.9	Summary on Laser-produced Plasma Conditions	93
3.5	Saturation of Gain for Plasma-lasing	95
3.5.1	Gain-length Product for Saturation	96
3.5.2	Experimental Validation	98
3.6	Traveling-wave Plasma-Excitation	100
3.6.1	Fourier Optics Theory & Model	102
3.6.2	Calculation of Tilted Pulse-front Characteristics	104
3.6.3	Summary on Travelling-Wave Excitation	108
4.	ADVANCED ANALYTICS	109
4.1	Implementing Plasma-lasers in Nano-imaging	110
4.1.0.1	Pointing Stability	111
4.1.0.2	Condenser	111
4.1.0.3	Repetition rate	112
4.1.0.4	Coherence Degree	112
4.1.0.5	Objective	112
4.1.1	Optical Theory & Model	113
4.1.2	Characterization of the XUV Plasma-laser	117
4.1.2.1	Spatial coherence measurement	117
4.1.2.2	Fluence for EUV imaging	117
4.1.2.3	Pointing Stability and Divergence at TGRIP vs. TCE Pumping	117
4.1.2.4	Micro-collimator for beam matching	119
4.1.2.5	Optimum fluence for quality nano-imaging	120
4.1.3	Performance of the Four Objective Designs for Nano-scale Imaging	122
4.1.4	XUV Microscopy Demonstrator	123
4.1.5	Summary on XUV Imaging Optics	126
4.2	Table-top Nano-imaging by Plasma-Lasers	128
4.2.1	Imaging Optimization	129
4.2.2	XUV Imaging Experiments	132
4.2.3	Summary on Plasma Laser XUV Imaging	133
4.3	Two-color XUV Laser for Nano-spectroscopy	136
4.3.1	Two-color Laser Theory & Model	138
4.3.2	Two-color Atomic model of the Gain Medium	138
4.3.2.1	Gain with Electron Collisional Pumping (Monopole Mode)	138
4.3.2.2	Gain with Photo-pumping (Dipole Mode)	138
4.3.3	Two-color Lasing Process & Saturation	140
4.3.4	Two-color Light Propagation across the Gain Medium	140
4.3.4.1	XUV Ray-tracing	140
4.3.4.2	Divergence and Pointing-stability	141

4.3.5	Experimental Two-color Laser Characterization	141
4.3.5.1	Molybdenum Two-color Laser	141
4.3.5.2	Palladium Two-color Laser	143
4.3.6	Computational Modeling	143
4.3.6.1	Calculation of the Two-color XUV Lasing Process	143
4.3.6.2	Calculation of Time and Space Distribution of Two-color Gain .	144
4.3.7	Discrete Tunability of Two-color XUV Laser	147
4.3.8	Summary on Plasma Laser Spectroscopy	148
5.	<i>GENERAL DISCUSSION & CONCLUSIONS</i>	150

1. INTRODUCTION

Unpublished. Main themes here:

- *Fundamentals on X-ray Lasing*
- *Fundamentals on Plasmas*
- *Research Gap and Aims of this Research Program*

Laser is slightly more than half a century technology, which developed from a niche breakthrough in atomic spectroscopy to an enabling technology for the industry and society. *Enabling technologies* are key platforms that have epochal impact, linking academia to industry and society. The ability to probe and manipulate the spatial and temporal distribution of a pulse of photons found immediate application in material science, spectroscopy, microscopy, medicine, measurement, sensing and ranging, entertainment, to quote but a few. *Enabling technologies* are the technology transfer of a long scientific and engineering process, initiated with a ground-breaking *proof-of-concept*.

A discussion on light sources must begin with a major distinction between laser sources (coherent) and lamps ones (incoherent): the former rely on stimulated emission while the latter on spontaneous fluorescence. Laser sources have, besides a well-defined phase relation, a collimated emission, a narrow bandwidth (a color!), and with that an enhanced brightness. Commercially available laser systems offer the shortest wavelength in the DUV/VUV with the excimer lasers, e.g. the ArF's 193nm in wavelength (6.4eV in photon energy) or F_2 at 157nm (7.9eV). For higher photon energies, i.e. shorter wavelength, there is no laser option at-hand. On the other hand, incoherent sources are already well represented in the short-wavelength domain, such as extreme ultraviolet or X-rays lamps.

X-rays have dramatically modified material and bio- chemistry, by enabling the possibility of studying the structure of molecules and proteins, the valence state of elements, the kinetics of electronic transitions, and intermediate states of reactive pathways. Further, the reduced wavelength has offered access to nano-scale imaging and the internal structure of samples by tomography. The use of laser-like radiations, such as the synchrotron, has added the advantage of high brightness (Fig. 1.2) and spectral selectivity thanks to a tunable narrow-line beam. It is therefore of major advantage the perspective to demonstrate laser action in compact "table-top" setups.

Besides the scientific impact, industry would benefit too. The semiconductor industry is striving for moving on towards next generation lithography in due time to sustain growth trends. This is not only a matter of high volume manufacturing sources, but implies access to lab-scale bright EUV sources for mask defect inspection. The production yield is indeed a function of lithographic throughput and yield. With many workers having demonstrated the feasibility of lithography in the EUV, the remaining challenge is that of scaling-down the short-wavelength sources.

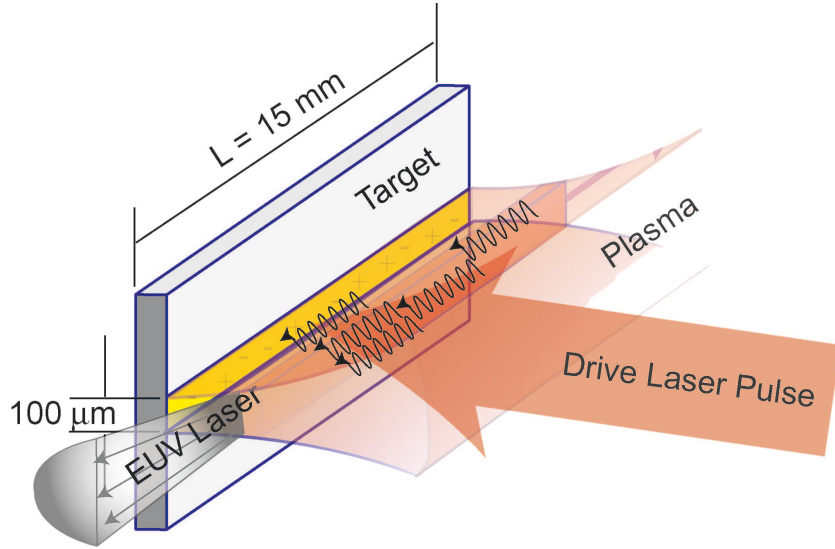


Fig. 1.1: Principle of the plasma lasing process. A pump laser irradiates a target with a line-focus. A hot and dense plasma column is formed and sustain high-gain single-pass amplified spontaneous emission.

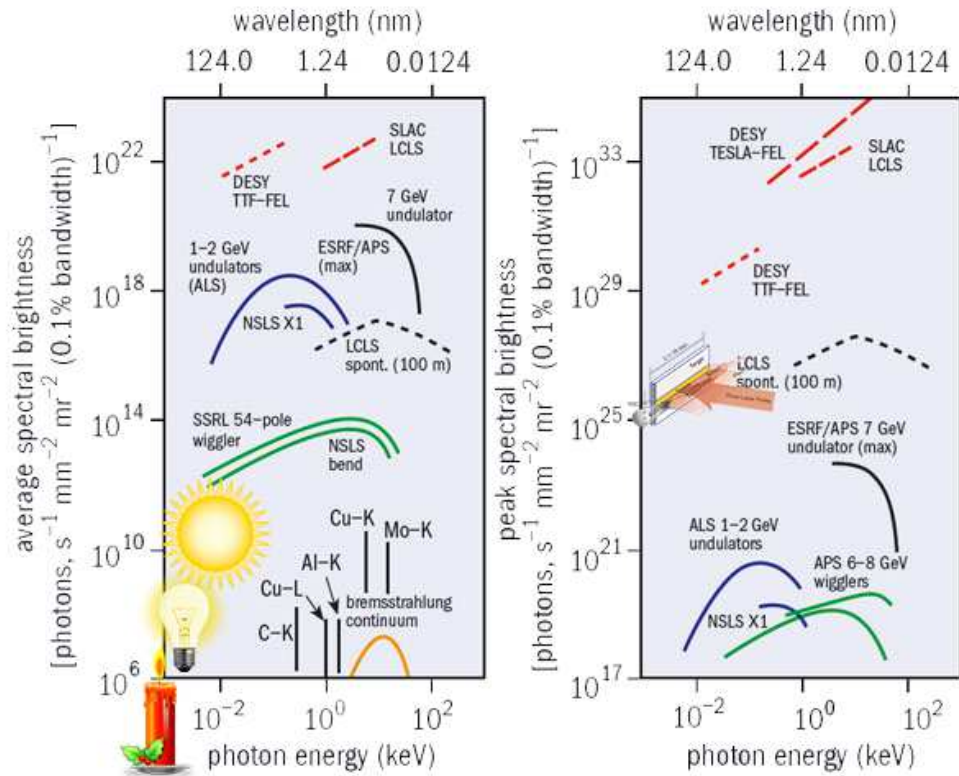


Fig. 1.2: Comparison of the brightness of a number of coherent light sources, and for reference lamps such as a candle, a bulb, a the sun. The plasma laser is also depicted in the RHS panel.

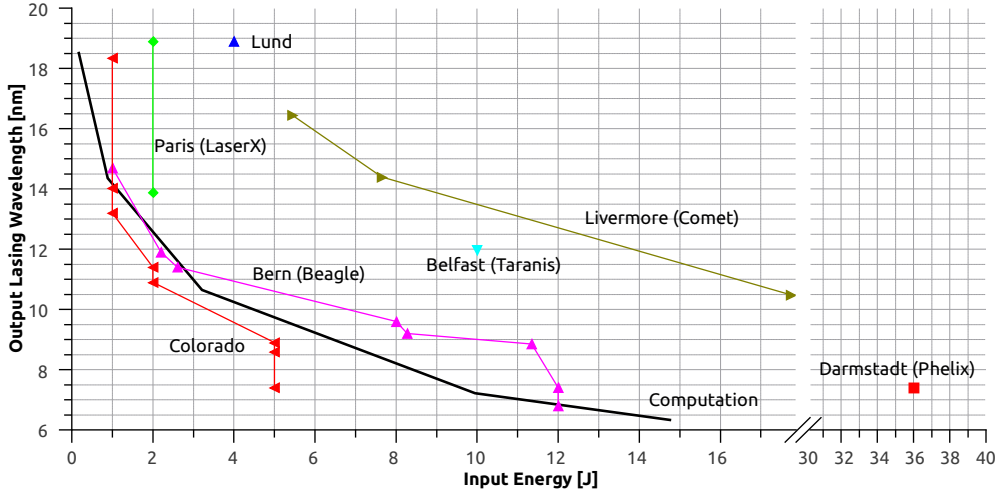


Fig. 1.3: Worldwide plasma-based X-ray laser facilities based on compact architecture (Multi-TW and PW systems are excluded), with output wavelengths as a function input pump energy. The results refer to the stand-of-technology in 2010. Experimental results are compared with the computational prediction.

The imbalance between stimulated and spontaneous emission at short-wavelength is however a fundamental fact well explained via Einstein's theory. Indeed, the ratio between spontaneous rate (A_{ul}) and stimulated emission (B_{ul}) for a transition from upper (u) to lower (l) atomic level, as expressed using Einstein's coefficients, scales with the wavelength (λ) as follows:

$$\frac{A_{ul}}{B_{ul}} = \frac{8\pi h}{\lambda^3} \quad (1.0.0.1)$$

The ratio in Eq. 1.0.0.1, which defines the equilibrium radiation energy-density per unit volume per unit frequency as from Planck's theory, scales with a cubic dependence on wavelength, such that short-wavelength stimulated emission is cubically harder to achieve in favor of the spontaneous emission rate. The generation of short-wavelength *coherent* photons is thus a formidable challenge because demands *fast* and *intensive* pumping. The experimental rule of thumb is such that for a factor of 2 reduction of wavelength in the XUV, approx. a factor of 10 higher pumping energy is required as shown in Fig. 1.3.

Scaling-down the current lasing barrier on a commodity setup seemed originally impossible because no solid, liquid, or gaseous materials can be used as gain medium for lasing in such short-wavelength range. To further complicate the task, also reflective optics potentially used for the laser cavity, are not more than 50% efficient in the XUV and soft X-ray range. Eventually, the solution for short-wavelength lasing has been that of utilizing "transient ensembles" such as laser-produced or discharge-produced plasmas as high-gain single-pass (no cavity) amplification media (Fig. 1.1). A powerful *pump pulse* (approx. 1 TW) directed on a *target* material generates a rapidly expanding brilliant *micro-plasma*. The plasma emissivity is largely in the X-ray domain, and shaping the plasma as a 50-by-100 μm by 15mm "column" leads to laser action. In fact, if the focal spot is a line, the elongated geometry of the plasma medium is favorable to support amplified spontaneous emission across its length, up to output brightness as high as 6 orders of magnitudes larger than the synchrotron's!

Coherent X-ray radiation generated from amplified spontaneous emission (ASE) across a plasma-medium, as discussed throughout this monograph, has the advantage to be integrated within compact table-top tools. Proof-of-principle of *lab-scale* and even table-top systems is so far provided for extreme ultraviolet radiation [67, 258]. Soft X-rays have been indeed produced too, though with very high intensity pump lasers, of very low repetition rates.

Coherent radiation generated using free-electron undulators attached to particle accelerators is also a popular option but demands large and costly facilities. A few countries have afforded

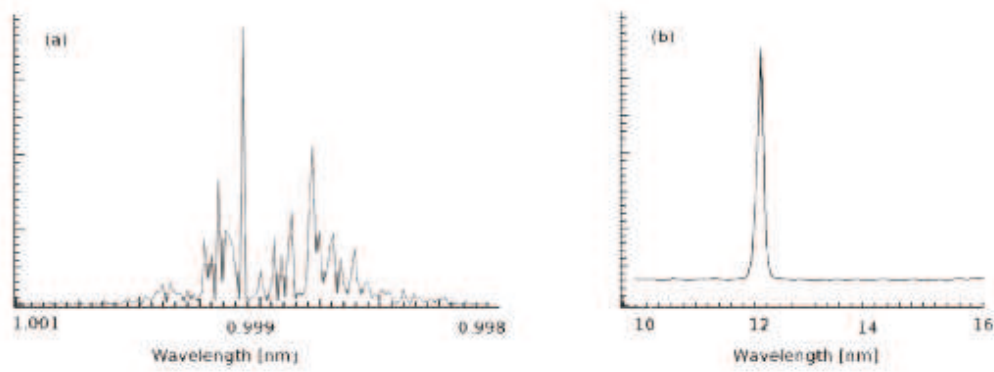


Fig. 1.4: (a) Calculated spectrum from a xFEL spectrum indicative of performance at any of the various facilities when unseeded. (b) Experimental spectrum obtained from a plasma-based XUV laser.

hundreds of a million up to a billion for the realization and operation of fourth-generation accelerator sources, producing tunable coherent soft and hard X-ray radiation from the free-electron laser. Such large facilities are run on “*beamtime*” terms, which implies proof-of-principle research but no industrial perspective due to cost issues.

Fig. 1.4 compares the **spectrum** from (a) a xFEL pulse and one from (b) a plasma-based XUV laser. Besides the difference in emission wavelength, i.e. X-ray range for the accelerator architecture and EUV for the plasma-driven one, the most evident distinction is given by the spectral structure. The former shows a multi-spike structure with chaotic noise-induced modes. Strategies for xFEL seeding have shown to clean-up such “raw spectrum” [94], but are alignment-challenging and expensive. Regarding the spectral bandwidth, the xFEL pulses show 0.1–1% as relative to the central wavelength, whereas the plasma-based XUV laser is unsurpassed with spectral width of 0.001–0.01%, due to gain-narrowing [318]. The downside of an ultranarrow bandwidth is the limited time resolution, which is the inverse of the former (so-called “*time-bandwidth product*”). Therefore, sources recommended for ultrafast spectroscopy (e.g. high-harmonic generation) may suffer a lack of spectral selectivity, and viceversa sources with excellent selectivity may not have a time resolution better than a few ps.

The **time resolution** is thus a clear strength for xFEL sources. The pulse duration is in the order of 10–100 fs, which allows insights in many ultrafast processes in physics and chemistry. For even faster spectroscopy, i.e. so-called “*atto-second science*”, broader bandwidth sources are needed. Such a tremendous potential of the xFEL is unfortunately partly limited by the jitter of the pulses. In pump–probe experiments the exact synchronisation of signals at such ultrafast time-scale can be hard, when dealing with a jitter in the range of hundreds of fs [316]. However, a number interesting processes in physics and chemistry are probed already with ps time resolution [280], such that the author is convinced that plasma-driven lasers can impact as enabling technology, because plasma-based X-ray laser has pulse durations of a few ps, when generated across laser-produced, or a few ns, when generated across discharge-produced plasmas.

The most appealing feature of an accelerator-based source is the possibility to **tune continuously** the wavelength. This can be accomplished either by changing the energy of the accelerated electron bunch or by adjusting the magnetic field changing the undulator gap. For small wavelength changes the latter option is preferred. The use of monochromators on a broadband beam (“pink beam”) is customary to reduce the bandwidth below 1%. This is particularly important for spectral scans, especially when probing near edge response (NEXAFS). The plasma-based X-ray laser instead generates a discrete set of wavelengths, each associated to a specific target material. Although limiting in terms of continuous selection of wavelength, the “*discrete tunability*” offers the possibility to generate coherently two (or more) lines, simply using multi-elemental targets.

The pulses of light emitted by either the plasma-based or the xFEL systems may suffer from spatial as well as temporal **fluctuations** along the beampath. The spatial fluctuations are expressed as pointing stability of the optical axis and as collimation stability of the propagation divergence. The former refers to the horizontal and vertical drift of the beam centroid. The latter indicates the solid angle fluctuation, which determines the beam width in horizontal and

	FLASH	LCLS	SACLA	EuroXFEL	SwissFEL
	Hamburg, Germany	Stanford, USA	Hyogo, Japan	Hamburg, Germany	Villigen, Switzerland
Length [m]	300	3000	750	3400	800
Max energy [GeV]	1	4.54–14.3	4–8	17.5	5.8
Stations	5	3–5	4	6–10	2
Divergence [μrad]	90 ± 10	Xray 3 ± 0.3 , XUV 30 ± 7.2	< 4	1	2
Pulse energy [mJ]	0.01–0.1	2.1	0.1–0.5	10	0.15
Tunability [nm]	6.8–47	0.15–1.5	0.1–60	0.05–6	0.1–7
Rel. Bandwidth [%]	1	0.1–0.5	0.06	0.1	N/A
Repetition rate [Hz]	5	120	10–60	10	100
Pulse duration [fs]	10–70	230	500	107	24
Peak Brightness [$\text{phs}^{-1}\text{mrad}^{-2}\text{mm}^{-2}$ 0.1% BW]	$6 \cdot 10^{29}$	$8.5 \cdot 10^{32}$	$5 \cdot 10^{33}$	$5 \cdot 10^{33}$	$< 10^{33}$
Start of operation	2005	2009	2011	2017	2017
Cost of realization [M\$]	160	380	370	1,300	350

Tab. 1.1: Comparison of performance of the a selection of short-wavelength free-electron lasers. Data from refs. [85, 107, 174, 270, 310].

vertical components at the sample location. Akre et al. [4] have studied the beam stability specifications for the LCLS Free-Electron Laser. The RMS vibration of 48 LCLS quadrupole sectors was characterized as 14.2% (horizontal) and 9.5% (vertical) of the beam width, with peak values of $2 \mu\text{m}$ (H) and $0.5 \mu\text{m}$ (V). In this work we have characterized the illumination of a plasma-based XUV laser and come to figures of 31% (horizontal) and 27% (vertical). We could however develop optical correction setups, using telecentric collimation and relay-imaging projection, such that they improved pointing stability and divergence of the source by one order of magnitude, i.e. below half a mrad. Further details are in sect. 4.1.

The number of pulses per unit time (**repetition rate**) is important to achieve a good measurement statistics within a given time. Generally, there is a tradeoff between pulse energy (E_p) and repetition rate (f), given that the product is a constant, i.e. the source average power ($P = E_p \cdot f$). The free-electron laser operating at short-wavelength have repetition rates in the range of 10–120 Hz. The pulse energy is in the range of multi mJ, typically leading to the sample destruction, which demands rapid detection. The repetition rate of the plasma XUV-laser is critically influenced by the wavelength, with practically single-shot operation in the sub-10-nm range. Several groups have however presented platforms for 10 and even 100 Hz operation [170, 322, 332]. The pulse stability is affected by the heat incubation on the target material, such that automated target-shifting devices, e.g. tape, are mandatory. For some soft materials, e.g. Sn, this is however a major difficulty because just a few shots can be delivered on the same spot, prior to massive pitting. The use of gas-target dramatically reduces the radiator density and affects the efficiency.

The **financial effort** to realize a short-wavelength FEL is such that only national budgets of a few countries can afford such facility construction and operation. Often, it is even the contribution of multiple such countries that results necessary. In this respect the plasma-based

<i>Range: 2007-12</i>	FLASH	LCLS	xFEL Total	XPL Total	xFEL/XPL
Publications	178	52	230	85	2.7x
Publication rate [p.a.]	35.6	10.4	46	17	2.7x
Days to paper	10.3	35.1	7.9	21.5	0.4x
Citations	1344	613	1957	443	4.4x
Citation/Publications	7.6	11.8	8.5	5.2	1.6x
Facility Cost [M USD]	160	380	539	-	-
Cost of unit paper [M USD]	0.9	7.3	2.3	0.1	23x
Cost of unit citation [k USD]	119	618	275	14	19.6x

Tab. 1.2: Bibliometric analysis for xFEL and X-ray Plasma-Laser (XPL) communities, on five years 2007-12, realized on May 9th, 2012, using the *Web of Knowledge* interface accessing all data bases. The “XPL community funding” is calculated scaling the xFEL cost by the publication rates of the two communities.

X-ray laser is a more widely-accessible platform. A own bibliometric analysis from 2012 (Tab. 1), done for the two operating short-wavelength facilities, e.g. LCLS and FLASH, and for the plasma-based short-wavelength laser community, compared such "*paper productivity metrics*" with the costs. If thus one computes the cost for each individual publication or citation, for simplicity based on the facility realization cost only, interesting observations can be made. Firstly, the plasma-based XUV laser community, although by factor of 2.7 lower in publication rate in the considered 5 years, completes its papers at less than a few percent unit cost versus the xFEL. Secondly, the xFELs have a much larger personnel "load" and thus prolong their cost ballast over the entire facility lifetime, being salaries one remarkable cost driver. The cost for plasma X-ray laser are basically driven by the construction investment in first place. Finally, the user-facility approach had a significant impact on duty cycle, with about 1 paper per week at xFELs, whereas lab-scale facilities may be run in a more discontinuous mode.

It is also noteworthy to say the xFEL papers were mostly on advanced science cases whereas the XPL one were essentially contributions on research-level instrumentation development. It is therefore essential to begin testing advanced science cases also on compact plasma-based facilities, to fully exploit their potential, and close the current gap.

1.1 X-ray Lasing Technologies

Synchrotron radiation (SR), free electron lasers (FEL), and high harmonic generation (HHG) are typical types of coherent (laser-like) X-ray sources not requiring the use of plasmas as gain medium. SR and FEL are large facilities, meanwhile HHG is a table-top source. Here some salient characteristics are reviewed.

Synchrotrons as the 3rd generation X-ray light sources are based on relativistic electrons moving in a large circle bending undulator or/and wiggler magnetic configuration. Thus, electrons emit dipole radiations due to the radial accelerations and radiation is emitted tangentially to the curvature of the electrons. **Free electron lasers (FELs)** as the 4th generation X-ray light sources are based on a relativistic bunch of electrons guided through an undulator or/and the wiggler magnetic configuration. This arrangement of periodic, transverse magnetic fields, generated by alternating magnetic poles, leads to the acceleration of the electrons and resulting generation of the coherent X-ray radiations [204]. In a FEL, a coherent beam is created through self-amplified spontaneous emission (SASE).

High harmonic generation (HHG) sources are generated by nonlinear effects in the interaction of intense laser fields with gas or solid targets. In this way, odd multiples of the laser frequency (harmonics) are produced. High harmonic generation yields an X-ray source with a high beam quality and spatial coherence [327].

1.2 X-ray Plasma Lasing

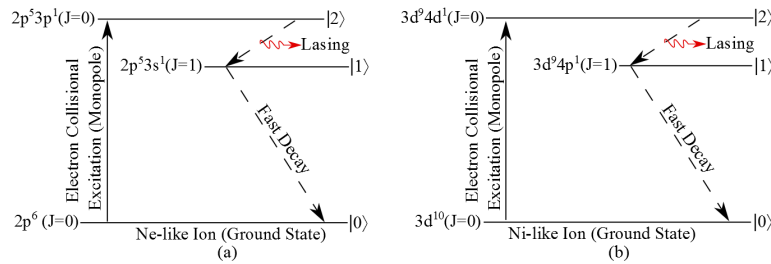


Fig. 1.5: Simplified energy level diagram showing the process of collision excitation X-ray lasers for (a) Ne-like and (b) Ni-like schemes. The upper level is shown by $|2\rangle$, the lower level is shown by $|1\rangle$, and the ground state is shown by $|0\rangle$.

1.2.1 Plasma as a Gain-medium

A plasma is known as the fourth state of matter beyond solid, liquid, and gas (Fig. 1.6). In a plasma state, a substantial fraction of its atoms is ionized, but the electrons lost remain in the proximity to fulfill a quasi-neutrality condition. One can characterize a plasma in terms

of the electron density and temperature. The plasma medium can be described by two main categories of ionization models (i) local thermodynamic equilibrium (LTE) and (ii) non-local thermodynamic equilibrium (NLTE). In LTE, all three types of particles- the ions, the electrons, and the radiation- are in equilibrium ($T_e = T_{\text{ion}} = T_{\text{rad}}$). With the dominance of collisional processes in LTE plasmas, the populations of the various energy levels of LTE plasmas are determined by the Boltzmann and Saha equations [169]. In fact, in LTE collisional processes are far more important than radiative processes and radiative processes do not affect population distributions.

When the LTE model breaks, a non-local thermodynamic equilibrium (NLTE) situation is considered, where $T_e \neq T_{\text{ion}} \neq T_{\text{rad}}$. In the NLTE plasma, the population distribution does not depend only upon plasma parameters, unlike in the LTE model. In NLTE plasmas, the populations of the various energy levels can be obtained by detailed collisional and radiative processes in the plasmas.

Fig. 1.6 summarizes a variety of phenomena made from plasma as a function of their density and temperature [39–42, 165, 203, 233].

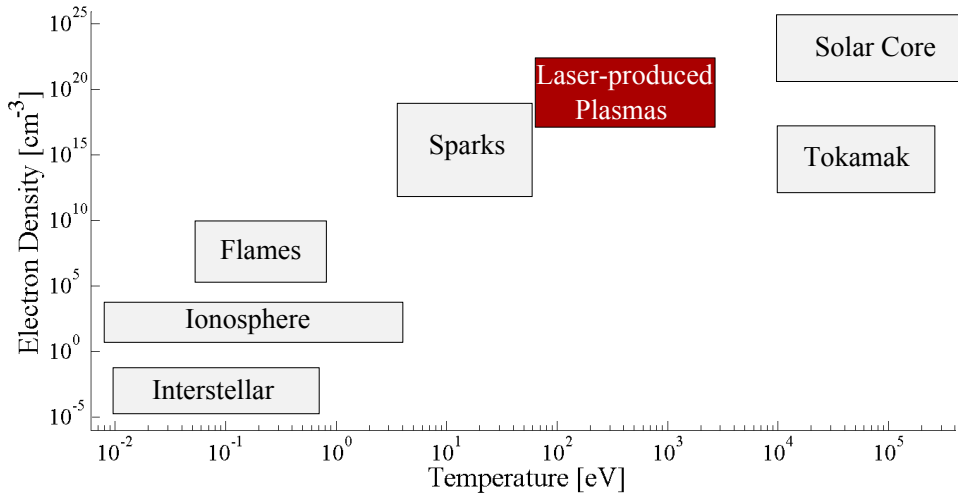


Fig. 1.6: Ranges of plasmas [39–42, 165, 203, 233]. Horizontal axis is temperature of the plasma, note that $1 \text{ eV} \equiv 11604.5 \text{ K}$.

In X-ray plasma lasers (XPL), the lasing medium is indeed the ions in the plasma. The plasma which serves as an active medium requires highly charged ions and free electrons with an electron density of $\geq 10^{17} \text{ cm}^{-3}$ and an electron temperature of $\simeq 100 - 1000 \text{ eV}$, as shown in Fig. 1.6. The Debye length gives a scale to the short and long range interactions in a plasma. In terms of the electron density and temperature of the plasma, the Debye length can be calculated as follows [56]:

$$\lambda_D = \sqrt{\frac{\varepsilon_0 k_B T_e}{n_e e^2}} \approx 69 \sqrt{\frac{T_K}{n_m^{-3}}} \quad (1.2.1.1)$$

where n_e is the electron density (in m^{-3} in the approximation) and T_e is the electron temperature (in K in the approximation), while the constants are the Boltzmann constant (k_B), the permittivity in vacuum (ε_0), and the electron charge (e). For a 300 eV plasma at $5 \cdot 10^{20} \text{ cm}^{-3}$, the Debye length is about $5.8 \mu\text{m}$.

The fact that plasma particles behave collectively means that a plasma can support a wide variety of wave motions and oscillations. Oscillation arises if a group of electrons is slightly displaced from their equilibrium positions. The displaced electrons experience an electrostatic force seeking to restore them to their equilibrium positions. Namely, the kinetic energy of electrons converts to a potential energy and an electron oscillation is set up. Since the oscillation is fast, the massive ions do not respond to the oscillating field and can be considered fix. Thus,

the oscillation frequency known as the plasma frequency depends on the electron density [56]:

$$\omega_p = \left(\frac{n_e e^2}{m_e \varepsilon_0} \right)^{1/2} \approx 56.4 \sqrt{n_m^{-3}} \quad (1.2.1.2)$$

where n_e is the number density of electrons, e is the electric charge, m_e is the effective mass of the electron, and ε_0 is the permittivity of free space. The plasma frequency ω_p depends only on n_e , and for a plasma at $5 \cdot 10^{20} \text{ cm}^{-3}$, it is approx. $1.3 \cdot 10^{15}$.

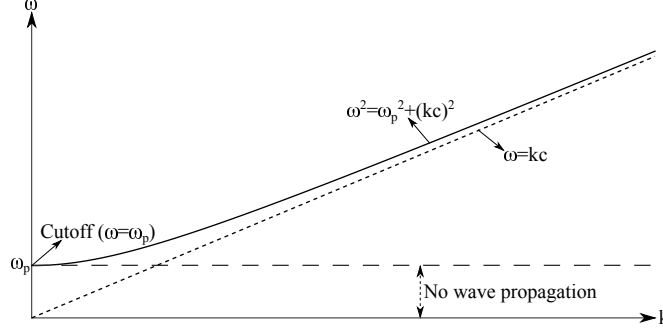


Fig. 1.7: ω versus k of the dispersion relation for a plane wave propagating in a plasma.

For a plane wave of the form $E(r, t) = E_0 e^{-i(\omega t - k \cdot r)}$ the dispersion relation in plasma with a uniform density is as follows:

$$\omega^2 = \omega_p^2 + (kc)^2. \quad (1.2.1.3)$$

Based on Eq. 1.2.1.3, the plasma frequency ω_p can be transparent or opaque to light transmission in any of the following three cases:

- (i) $\omega > \omega_p \rightarrow k > 0$, light propagates in the plasma, known as an under-dense plasma.
- (ii) $\omega = \omega_p \rightarrow k = 0$, light cannot propagate in the plasma. Then $\omega = \omega_p$ is called the cutoff frequency of the optical EM wave in plasmas.
- (iii) $\omega < \omega_p \rightarrow k$ is imaginary, light is reflected by the plasma, named as over-dense plasma.

The density where $\omega = \omega_p$ is known as the critical density n_c for the angular frequency ω of that wave.

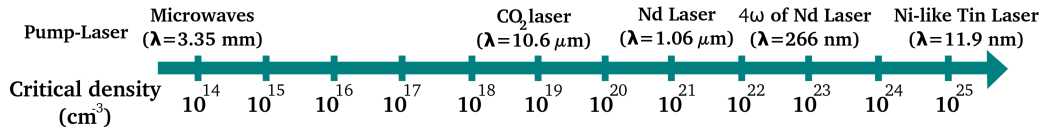


Fig. 1.8: Critical electron density for some lasers.

Namely, a laser pulse with wavelength λ can only penetrate through the under-dense plasma up to the critical electron density n_c [144, 315]:

$$n_c [\text{cm}^{-3}] = \frac{\varepsilon_0 m_e}{e^2} \omega^2 = \frac{1.11 \cdot 10^{21}}{\lambda^2 [\mu\text{m}]} \quad (1.2.1.4)$$

Fig. 1.8 shows the critical electron density for some lasers where laser frequency is equal to plasma frequency ($\omega = \omega_p$). Fig. 1.8 shows that plasmas with high electron densities of $n_e > 10^{23} \text{ cm}^{-3}$ can be probed by XUV and soft X-ray lasers only. When $\omega > \omega_p$ (Eq. 1.2.1.3), the laser light propagates in the plasma with phase velocity $v_\phi = \omega/k$. From Eq. 1.2.1.3 the phase velocity of the wave is [144]:

$$v_\phi = \frac{\omega}{k} = \frac{c}{\sqrt{1 - \frac{\omega_p^2}{\omega^2}}} = \frac{c}{\sqrt{1 - \frac{n_e^2}{n_c^2}}} \quad (1.2.1.5)$$

Here, the refractive index of the plasma, $\tilde{n} = c/v_\phi$, is given:

$$\tilde{n} = \sqrt{1 - \frac{n_e^2}{n_c^2}}. \quad (1.2.1.6)$$

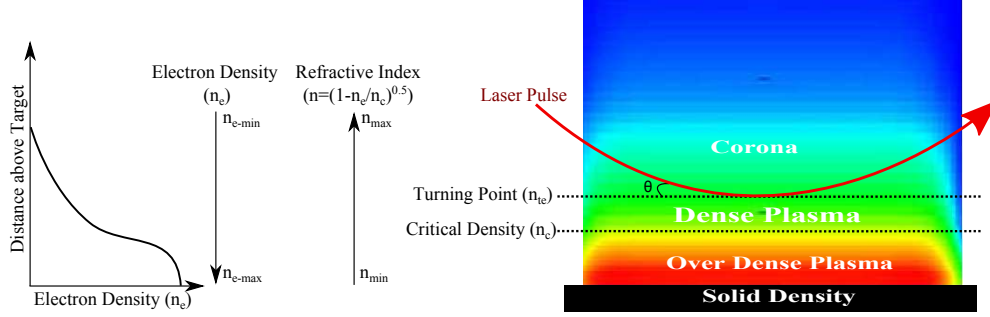


Fig. 1.9: A schematic of the turning point in the XUV or soft X-ray laser-produced plasma. The refraction of the laser in a plasma is caused by the density gradient normal to the propagation direction. The closer to the surface of the target, the higher electron density, and the smaller refractive index.

Based on Eq. 1.2.1.6, the refractive index of the plasma is always smaller than one ($n < 1$). According to Snell's law, if light enters the plasma with an incident angle (θ) as described in Fig. 1.9, it will be then reflected from plasma at the turning point. Indeed, the turning point is the maximum penetration depth of the laser light in the plasma. The electron density at the turning point is [166]:

$$n_{te} = n_c \sin^2 \theta \quad (1.2.1.7)$$

where n_c is critical density, and θ is called the grazing incidence angle of the laser light (Fig. 1.9). The scheme in Fig. 1.9 shows the turning point in the XUV or soft X-ray laser-produced plasma where the refraction of the laser is caused by the density gradient normal to the propagation direction.

Table 1.3 summarizes the main differences between amplified spontaneous emission (ASE) plasma lasers and commodity optical lasers [10, 62, 271, 289, 293, 336].

Tab. 1.3: Comparison of characteristics of plasma laser versus optical lasers.

Types of laser	Wavelength	Spatial coherence	Line width ($\frac{\Delta\lambda}{\lambda}$)	Coherence length	Amplification mode	Gain medium
Optical laser	157 nm-360 μ m [336]	Full	$\ll 10^{-6}$ [291]	1 μ m-100 km [62, 271, 289]	High finesse cavity [336]	Solid state, atoms, and ions [336]
Plasma laser	7 - 47 nm [10]	20-50% of beam diameter	$\approx 10^{-4}$	≤ 1 mm [293]	Single-Pass (no cavity) [10, 289]	Highly ionized ions [10]

In the optical laser, the gain medium is a stable substance and one needs flashlamps or diodes to pump it, as shown in Fig. 1.10a. Meanwhile, the gain medium in the plasma laser is a highly ionized plasma. Indeed, it has to be prepared and optimized right before pumping it, Fig. 1.10b. An infrared or near-infrared laser with the pulse-duration of, e.g., ps/ns is used for pumping the plasma [95, 196, 207, 282, 288, 296, 353]. In such kind of plasma-based laser, the ion energy levels will allow transitions within the XUV to the soft X-ray wavelength (3-100 nm), as summarized in Tab. 1.3.

In the plasma laser (Fig. 1.10b), there is no resonator and the amplified XUV or soft X-ray signal is initiated by noise from spontaneous emission. Due to the short plasma life-time, the cavity and mirrors in the plasma laser cannot be used for multi-pass amplification. Namely, light in the vacuum propagates at a speed of $c \approx 300 \mu\text{m/ps}$, which considering a gain medium with lifetime of $\lesssim 10$ ps suggests the use of a mirror pair at $\lesssim 3$ mm for round-trip. In such a close distance, mirrors will be also damaged by plasma debris.

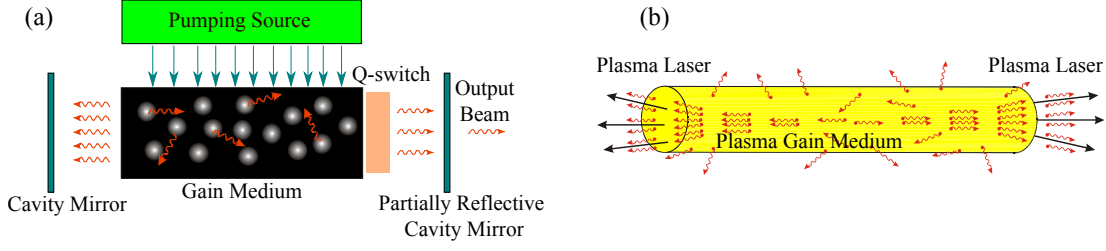


Fig. 1.10: Comparison between optical laser and plasma laser. a) Photons are reflected back and forth across the gain medium, within a Q-switched cavity, pumped by a flashlamp or diode. b) Amplified spontaneous emission (ASE) across a hot and dense laser-produced plasma column, with stimulated emission at both endings.

1.2.2 Processes in the Plasma & Interaction with Laser

There are different atomic processes in a hot plasma, which are listed in Table. 1.4. Depending on the mechanism of energy transfer involved in the process, each process is either collisional or radiative.

Tab. 1.4: Atomic processes in a plasma.

Direct process	Reverse process	Scheme
Spontaneous decay	Resonant photo-absorption	$\text{Atom}^{+i*} \leftrightarrow \text{Atom}^{+i} + h\nu$
Electron impact ionization	Three-body recombination	$\text{Atom}^{+i} + e \leftrightarrow \text{Atom}^{+i+1} + 2e$
Electron impact excitation	Electron impact deexcitation	$\text{Atom}^{+i} + e \leftrightarrow \text{Atom}^{+i*} + e$
Photoionization	Radiative recombination	$\text{Atom}^{+i} + h\nu \leftrightarrow \text{Atom}^{(+i+1)} + e$
Autoionization	Dielectronic recombination	$\text{Atom}^{+i*} \leftrightarrow \text{Atom}^{(+i+1)} + e$
Bremsstrahlung (B)	Inverse Bremsstrahlung (IB)	$\text{Atom}^{+i} + e^* \leftrightarrow \text{Atom}^{+i} + h\nu + e$

When the laser light propagates across the plasma, several mechanisms can account for transfer of energy from the electromagnetic wave to the plasma. The dominant linear absorption mechanism at the intensity of interest is collisional absorption, known as inverse Bremsstrahlung (80 – 90% of the laser energy is absorbed so). In this process free-electron oscillations are excited by the laser and converted into thermal motion by electron-ion collisions. These collisions either ionize or excite atoms or ions in the plasma. The inverse Bremsstrahlung absorption (IB) coefficient k_{ib} away from the critical surface (singularity at $n_e = n_c$) is estimated by the following equation [144]:

$$k_{ib}(x) [cm^{-1}] \simeq 3.4 \frac{(n_e/n_c)^2 \bar{z} \overbrace{\ln \Lambda_{e-i}}^{\text{Coulomb logarithm}}}{\underbrace{\sqrt{1 - n_e/n_c}}_{\text{Refractive index}} \lambda_L^2 [\mu m] (kT_e [keV])^{3/2}} \quad (1.2.2.1)$$

where n_c is the critical density previously defined in Eq. 1.2.1.4, λ_L is the wavelength of the laser in μm , \bar{z} is the mean ion charge, and kT_e is electron temperature in keV. $\ln \Lambda$ is the Coulomb logarithm for inverse Bremsstrahlung. Hughes [139] calculated the Coulomb logarithm, where $\ln \Lambda \simeq 31 - \ln \left(n_e^{1/2} [cm^{-3}] T_e^{-1} [keV] \right)$. The inverse Bremsstrahlung optical depth of the plasma from $x = x_0$ to $x = \infty$ is given by the expression [116]:

$$\tau(x) = \int_{x_0}^{\infty} k_{ib}(x) dx \quad (1.2.2.2)$$

where the laser intensity at point x_0 is $I(x_0) = I_0 e^{-\tau(x_0)}$. I_0 is the incident laser intensity. The fraction of laser energy absorbed through inverse Bremsstrahlung mechanism during the propagation up to the critical density can be written as follows [338]:

$$f_{abs} = 1 - e^{(-k_{ib}L)} \quad (1.2.2.3)$$

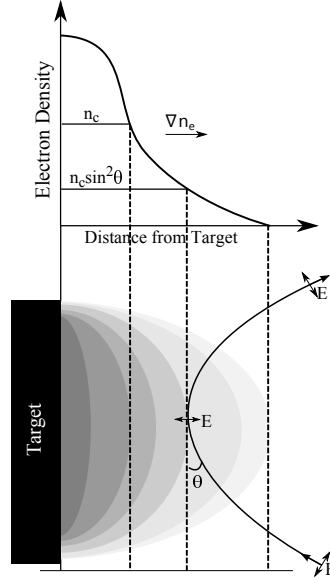


Fig. 1.11: The requirement for P-polarization for resonant absorption beyond the critical surface.

where L is the density scale-length defined as [305]:

$$L = \frac{n_e}{|\vec{\nabla} n_e|} \quad (1.2.2.4)$$

where, L is related to the on-axis electron density as $n_e(z) = n_{e0}e^{-z/L}$, z is vertical expansion axis of plasma and n_{e0} is the maximum electron density.

When the electron's quiver (oscillatory) velocity is larger than the electron's thermal velocity (high laser intensities), the electron-ion collision frequency is dominated by the oscillatory motion of the electrons in the laser electric field. Then, the effective inverse Bremsstrahlung coefficient reduces to the following [88]:

$$k_{ib}^{\text{eff}} = \frac{k_{ib}}{1 + \frac{3}{2} \left(\frac{v_q}{v_e} \right)^2} \quad (1.2.2.5)$$

where

$$v_q = \frac{eE_L}{m_e\omega} \propto \lambda I_L^{1/2}. \quad (1.2.2.6)$$

v_q is the electron's quiver velocity. E_L , I_L , and λ are the laser electric field, laser intensity, and laser wavelength, respectively. The electron's thermal velocity is:

$$v_e = (kT_e/m_e)^{1/2}. \quad (1.2.2.7)$$

When $\frac{v_q}{v_e}$ increases to more than unity, absorption changes from a linear dependence on the laser intensity I_L to a non-linear $I_L^{1/2}$ dependence. Therefore the absorption mechanism becomes less efficient when the laser intensity is increased. The laser-energy is absorbed near the critical density, either by inverse Bremsstrahlung or by resonance absorption [166]. In fact, the most prominent collision-less absorption in the laser-produced plasma is resonance absorption. When a grazing incident P-polarized laser-field (\vec{E}) arrives to the turning point, \vec{E} is parallel to $\vec{\nabla} n_e$, $\vec{E} \cdot \vec{\nabla} n_e \neq 0$. Thus, part of the field can resonantly excite electrons (Fig. 1.11). The grazing incidence angle of the laser light depends upon the density scale-length for which the resonance absorption is most efficient:

$$\cos \theta_{\text{max}} = \left| 0.8 \left(\frac{c}{\omega L} \right)^{1/3} \right|. \quad (1.2.2.8)$$

For a density scale-length of 100 μm and a laser wavelength 1.054 μm , this gives a grazing incidence angle of $\theta_{\text{max}} = 84.5^\circ$.

Table 1.5 summarizes the various lasing schemes for plasma-based short-wavelength lasers. The collisional pumping one is by far the most widely deployed. *Collisional excitation* is accomplished through a first step of plasma's free-electrons energization by inverse Bremsstrahlung absorption, and a second step of collisional ionization/excitation of bound electrons, until inversion in the Ne/Ni-like iso-electronic ion is accomplished. The high-ionization stage is functional to provide transitions in the XUV. When attempting to generate shorter wavelengths, it is found that the Ne-like scheme proves difficult to scale to wavelengths shorter than about $\lambda = 10$ nm because of the rapid increase of pump power required to achieve lasing-favorable conditions. Lasing in Ni-like ions is more favorable in this respect because of the higher *Stokes efficiency*, i.e. laser transition energy versus excitation energy. On the other hand, lasers in the Ni-like sequence have been shown to have more difficulties in providing a *saturated* output. In this monograph we have presented scaling-law expressions to predict the optimum plasma conditions for a given *Ni-like* ion in a lasing plasma, and highlighted the fundamental limitations in scaling down the wavelength with targets beyond $Z = 60$, unless using the 2ω pump.

Tab. 1.5: A summary of schemes for plasma-based short-wavelength lasers. Legend: $[h]$ hole.

Pumping by	Mechanism	Plasma Lasing Scheme
Excitation	Electron-collisional Photo-excitation	$X_o^{i+} + e \rightarrow X_u^{i+}$ $X_o^{i+} + h\nu \rightarrow X_u^{i+}$
Electron Capture	El.-coll. recombination Dielectr. recombination Charge transfer	$X_s^{(i+1)+} + 2e \rightarrow X_n^{i+} + e \rightarrow X_u^{i+} + e$ $X_s^{(i+1)+} + e \leftrightarrow (X_o^{i+})^{**} \rightarrow (X_u^{i+})^* + h\nu$ $Y + X_o^{(i+1)+} \rightarrow Y^+ + X_u^{i+}$
Ionization	Electron-collisional Photo-ionization Auger-decay	$X_o^{i+} + e \rightarrow X_o^{(i+1)+} [h]$ $X_o^{i+} + h\nu \rightarrow X_u^{(i+1)+} [h] + e$ $X + h\nu \rightarrow X^+ [K] \rightarrow X_u^{2+} [hh]$

Table-top X-ray lasers (plasma-driven X-ray lasers) are (i) recombination-pumped X-ray laser [38, 49, 236, 350], (ii) optical-field ionization [111, 283, 284], (iii) capillary discharge [19, 183, 193, 259], (iv) quasi-steady-state X-ray laser via laser-produced plasma [196, 207, 282], and (v) transient electron collisional excitation X-ray laser via laser-produced plasma [95, 288, 296, 353].

A recombination-pumped X-ray laser can produce an X-ray laser with a wavelength of 3.88 nm in H-like Al [38]. A recombination scheme was produced by irradiating on a foil target with a linear-polarized, ultrashort laser pulse with pulse duration of 100 fs – 2 ps, and with laser intensity of $\approx 10^{15} - 10^{16}$ W/cm² [49, 236, 350]. A recombination-pumped X-ray laser requires a very highly ionized plasma (H-like and Li-like ions). This implies very hot temperatures. In the recombination scheme, population inversion in H-like and Li-like ions happens through electron capture in highly excited states and subsequent decay to the upper lasing level [236]. The latter condition implies a rapidly cooling plasma, to favor coherent recombination. The two main requirement of hot (highly ionized) and cold (fast recombination) have limited the practical implementation of this scheme. Fig. 1.12 shows a schematic diagram of recombination-pumped X-ray laser

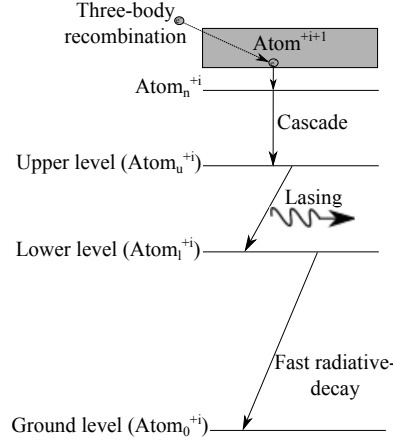


Fig. 1.12: The recombination laser consists of four fundamental stages. The population inversion happens by free electrons which recombine by the three-body recombination and then populate the upper laser level by the cascade. The three-body recombination and cascade processes are as follows $\text{Atom}^{++1} + 2e \xrightarrow{\text{Recombination}} \text{Atom}_n^{+i} + e \xrightarrow{\text{Cascade}} \text{Atom}_u^{+i} + e$.

Optical field ionization X-ray laser can generate an XUV or X-ray wavelengths less than 50 nm. In OFI X-ray lasers, saturation has been demonstrated at two wavelengths of 41.8 nm and 32.8 nm [111, 283, 284]. Here, amplifications have been achieved by using noble gases in glass cells or capillary tubes as targets. At low electron plasma densities in the range of $10^{17} - 10^{18} \text{ cm}^{-3}$ the ionization is initiated by optical field ionization (OFI) using high pump laser intensities in the range of $10^{15} - 10^{17} \text{ W/cm}^2$ [284]. Fig. 1.13 shows a schematic diagram of optical field ionization and explains the various ionization regimes. Since the ionization potential of the atom is greater than the photon energy ($h\nu$), the atom can absorb several photons to be ionized, so called multi-photon ionization (Fig. 1.13a). At strong laser intensities, the radiation field deforms the ionic potential that bound electrons can tunnel through the potential barrier in a process called tunneling ionization (Fig. 1.13b). For higher laser intensities, the electrons will be freed above the barrier as shown in Fig. 1.13b, so called over-barrier strong-field ionization. In OFI lasers, the population inversions (lasing) is induced by either collisional excitation (CE) or recombination processes.

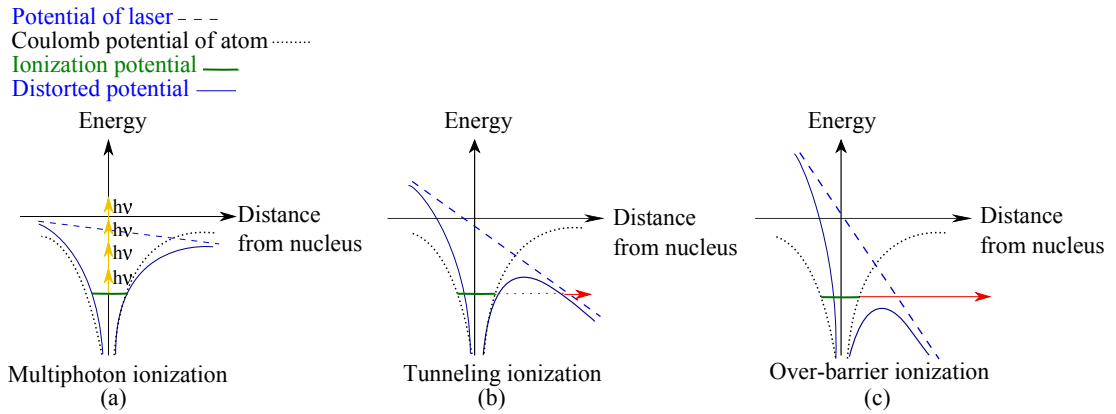


Fig. 1.13: Schematic diagram of optical field ionization of an atom. When the ionization potential of the neutral atom is larger than the energy of one photon $E_{ph} < E_I$, a high energy ultra-short pulses can lead to the possibility of (a) multi-photon ionization $E_I = n\hbar\omega$, (b) tunneling ionization, or (c) over-barrier strong-field ionization of an atom. Here, E_I is ionization energy of a neutral atom and $E_{ph} = \hbar\omega$ is energy of a photon.

Capillary discharge has been demonstrated at a wavelength of 46.9 nm in Ne-like Ar [183]. In this scheme, an electrical discharge creates a cylindrical plasma, which reaches the required temperature and density by compression on the cylindrical axis. In this way a high pumping

efficiency is obtained together with a high axial plasma-uniformity [183]. Fig. 1.14 shows the scheme of capillary discharge. Furthermore, this very compact high repetition rate source, with repetition rate (up to 10 Hz), opened the door to a wide variety of new applications [19, 193]. In particular, it constitutes an excellent source for X-ray interferometry. The excitation of plasma with an electric discharge is an efficient method to create quasi-steady state X-ray lasers [259], where pumping of the plasma (a population inversion) occurs by the exchanging of energy during collisions between free electrons and lasing ions, so called collisional excitation (CE) scheme.

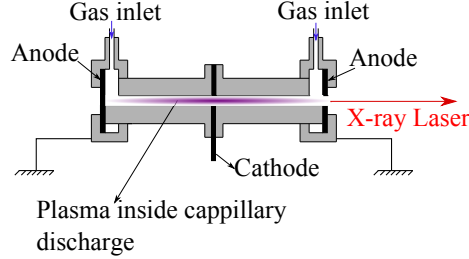


Fig. 1.14: A scheme of capillary discharge. The electrical discharge creates plasma in a cylindrical space, which called capillary.

Quasi-steady-state (QSS) X-ray laser via laser-produced plasma has been extended to wavelengths shorter than 50 nm [196, 207, 282]. In this scheme, the plasma is produced by irradiating the target with a long pulse-duration (sub-ns to ns) with 100 J – 1 kJ pulse-energy [277]. Since table top lasers cannot generate such high pulse energies, such experiments must be carried out at large scale laser facilities and thus the repetition rate of driving laser can be in the order of one shot per hour (low repetition rate). Under this scheme, the plasma parameters such as electron temperature changes slowly, so QSS approximation is valid. Here, population inversion happens by slow collisional pumping, so called "QSS collisional excitation laser" [90]. Fig. 1.15 shows a scheme of the QSS X-ray laser via laser-produced plasma.

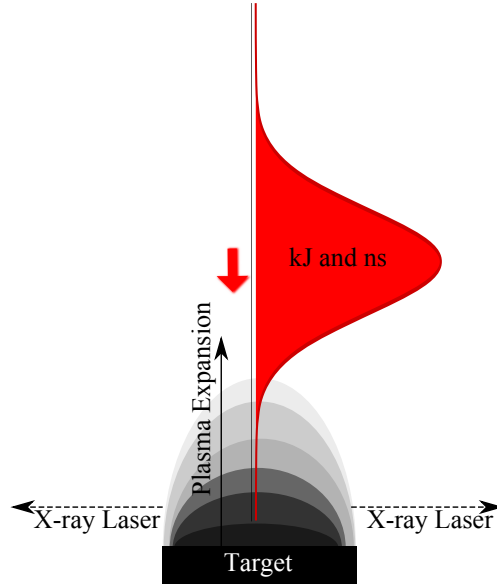


Fig. 1.15: In a quasi steady state (QSS) X-ray laser scheme, the plasma is produced by irradiating the target with a long duration pulse.

Transient collisional excitation (TCE) scheme via laser-produced plasma has been extended from "water window" to wavelengths shorter than 50 nm [95, 288, 296, 353]. In this scheme, a multi-pulse irradiating technique is used, see Fig. 1.16. The TCE technique reduces the total pumping energy to $\lesssim 1\%$ of energy required in the QSS scheme, thus reducing the total pumping energy raising the possibility for having a compact table-top setup. Furthermore, it increases the likely feasibility for a small scale laser facility with higher repetition rate [84].

In the classical TCE scheme, the target is irradiated orthogonally by a long pulse-duration ($\sim \text{ns}$) to ionize it to the lasing stage. After a delay time a short pulse-duration ($\sim \text{ps}$) with a grazing incidence angle as a main-pulse interacts with the plasma inducing the very strong pumping required for population inversion [190], see Fig. 1.16a.

In the multi-pulse TCE scheme, the target is irradiated by a number of short pulses ($\sim \text{ps}$) with specific time delays. In the past, the multi-pulse TCE scheme used transverse pumping in which all pulses are incident in the normal direction ($\theta = 90^\circ$). Later, for increasing conversion efficiency the multi-pulse TCE scheme under the grazing incidence pumping (GRIP) with a line-focus illuminating the target off normal ($0 < \theta \leq 50^\circ$) was suggested [190].

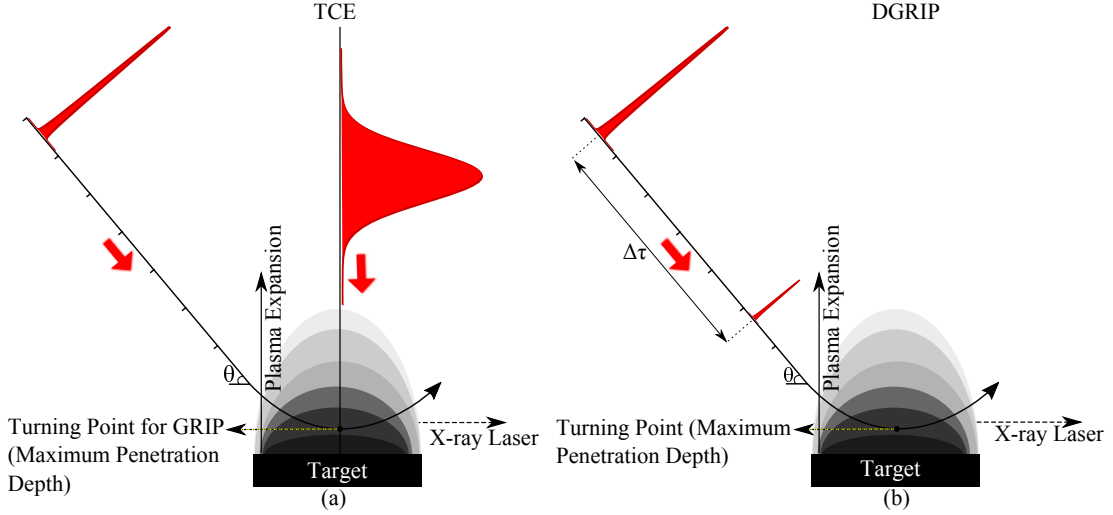


Fig. 1.16: In the transient collisional excitation (TCE) scheme, a multi-pulse irradiating technique is used. The incidence angle θ can be in the range of $0 < \theta \leq 90^\circ$. (a) Pre-plasma is produced by a long pre-pulse incident at the normal incidence. Then, the lasing is produced by a short main-pulse. (b) The pre-plasma is produced by a short pulse, and lasing is produced by another short main-pulse (double grazing incidence pumping: DGRIP). $\Delta\tau$ is the time delay between pulses, where it can be within picoseconds to nanoseconds range.

Fig. 1.16b shows double grazing incidence pumping, so called DGRIP. The first pre-pulses ionize target to the lasing stage. Afterwards, a population inversion created by transient collisional excitation (fast collisional heating) is produced by the main-pulse (the last pulse). The transient description explains pumping of the plasma (a population inversion) produced by a short pulse ($\sim \text{ps}$), where it does not have enough time to achieve stability on the plasma-hydrodynamic evolution time-scale. The main advantage of the multi-pulse TCE scheme over the classical TCE is the precision in adjusting the pre-pulses with the main pulse overlap on a same line-focus, see Fig. 1.16b.

In the plasma-driven X-ray lasers such as OFI, capillary discharge, TCE, and QSS, pumping of the plasma (the population inversion) occurs by electron collisional excitation (CE) pumping. Then, XUV or soft X-ray radiation is produced through amplified spontaneous emission (ASE). In addition, the seeding on ASE plasma amplifiers with high-harmonics is done where it has been demonstrated to generate XUV and soft X-ray laser pulses with full spatial coherence. Meanwhile, the laser-produced plasma XUV and soft X-ray lasers used in ASE regime (without-seeding) have limited spatial coherence.

Table. 1.6 summarizes plasma-driven XUV and soft X-ray lasers based on amplification mechanism with or without seeding [111, 128, 219, 261, 269, 284, 333].

1.2.3 The Transient Collisional Excitation Scheme

In the laser-produced plasma, amplified spontaneous emission (ASE) leads to the lasing process summarized as follows:

Tab. 1.6: Comparison of various plasma-based XUV and soft X-ray lasers pumped using the collisional excitation scheme, which are categorized in unseeded and seeded operation [111, 128, 219, 261, 269, 284, 333]. The duration of the generated X-ray pulse is given by τ_x , the wavelength is shown by λ_x , out-put power of X-ray laser is given by E_x , and repetition rate is displayed by RP .

Scheme	Amplification mechanism	λ_x [nm]	τ_x [ps]	P_x [μ W]	E_x [μ J]	RP [Hz]	Ref.
OFI	ASE	32.8	5	-	5	10	[284]
OFI	Seeding	32.8	1	-	0.3	10	[111]
Capillary discharge	ASE	46.9	~ 1000	150	-	12	[128]
TCE	ASE	13	-	2	-	10	[333]
TCE	Seeding	18.9	1.5	-	0.1	5	[219, 261]
QSS	ASE	21.2	100	-	4000	$5 \cdot 10^{-4}$	[269]

- (i) a drive laser with infrared or near-infrared pulses is fired to a polished metal target surface or a gas target,
- (ii) a hot dense plasma column induced. The plasma needs to be highly ionized and have a large fraction of ions in an ionization state, which is closed shell, i.e., Ne-like and Ni-like. Ne-like and Ni-like ions have a fully occupied outer shell and are hard to further ionize. So their advantage is that they remain stable against further ionization.
- (iii) short wavelength amplification started from amplified spontaneous emission (ASE).

The ionization energy of, e.g., Ar and Sn as a function of ionization stage is in Fig. 1.17. As can be seen from the Fig. 1.17, once a closed shell electron configuration is reached, the step up to the next ionization stage increases sharply and so the closed shell ion remains rather stable against further ionization leading to so-called "bottleneck ionization".

Fig. 1.18 shows that the abundance of Ne-like Ar and Ni-like Sn are more than the other ions due to being closed shell at these stages. In Fig. 1.18, ion fraction is calculated in the frame of a NLTE model. Indeed, an abrupt change in incidence pumping considering TCE scheme (looking at Fig. 1.16) leads to a steep electron density and temperature gradients indicating plasma in the non-local thermodynamic equilibrium (NLTE). Fig. 1.5 shows the atomic levels for the electron collisional excitation for Ne-like and Ni-like ion (as ground states). From Ne-like and Ni-like ion, the rapid electron collisional excitation creates the population inversion between upper $|2\rangle$ and

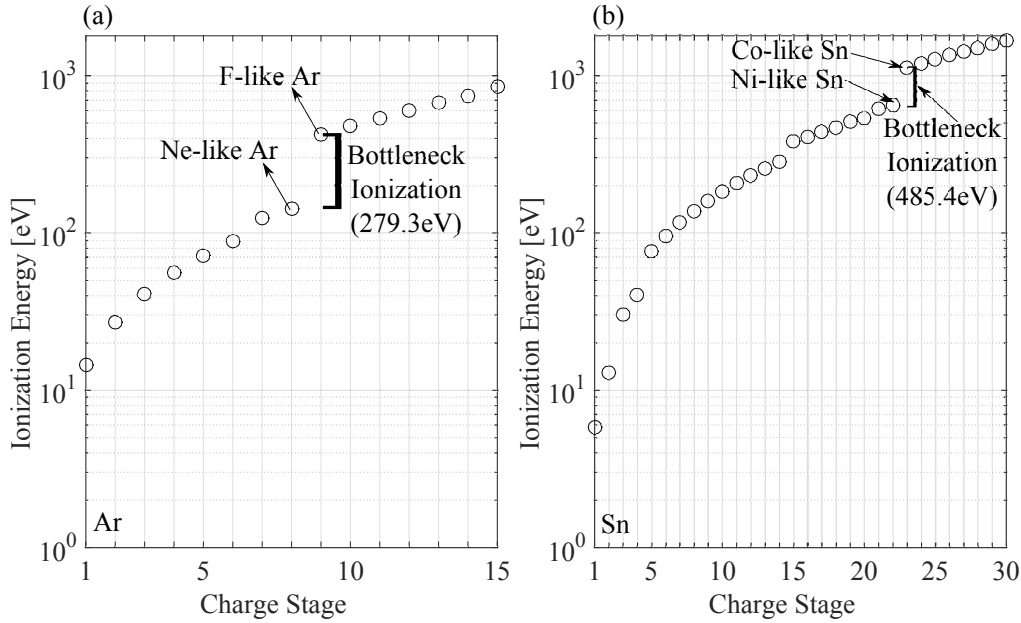


Fig. 1.17: Calculated ionization energy for (a) Ar and (b) Sn. Higher ionization from Ne-like Ar and Ni-like Sn are significantly large (bottleneck ionization).

lower $|1\rangle$ level. Ne-like and Ni-like ions contribute to the population inversion between $3p \rightarrow 3s$ and $4d \rightarrow 4p$, respectively (see Fig. 1.5). In lasing, the upper laser level $|2\rangle$ cannot decay to the ground state $|0\rangle$ due to the fact that radiative transition is forbidden under the selection rule and hence state $|2\rangle$ is metastable against decay to state $|0\rangle$. Meanwhile, the lower laser level $|1\rangle$ can decay rapidly and directly to the ground state $|0\rangle$ via a radiative dipole transition.

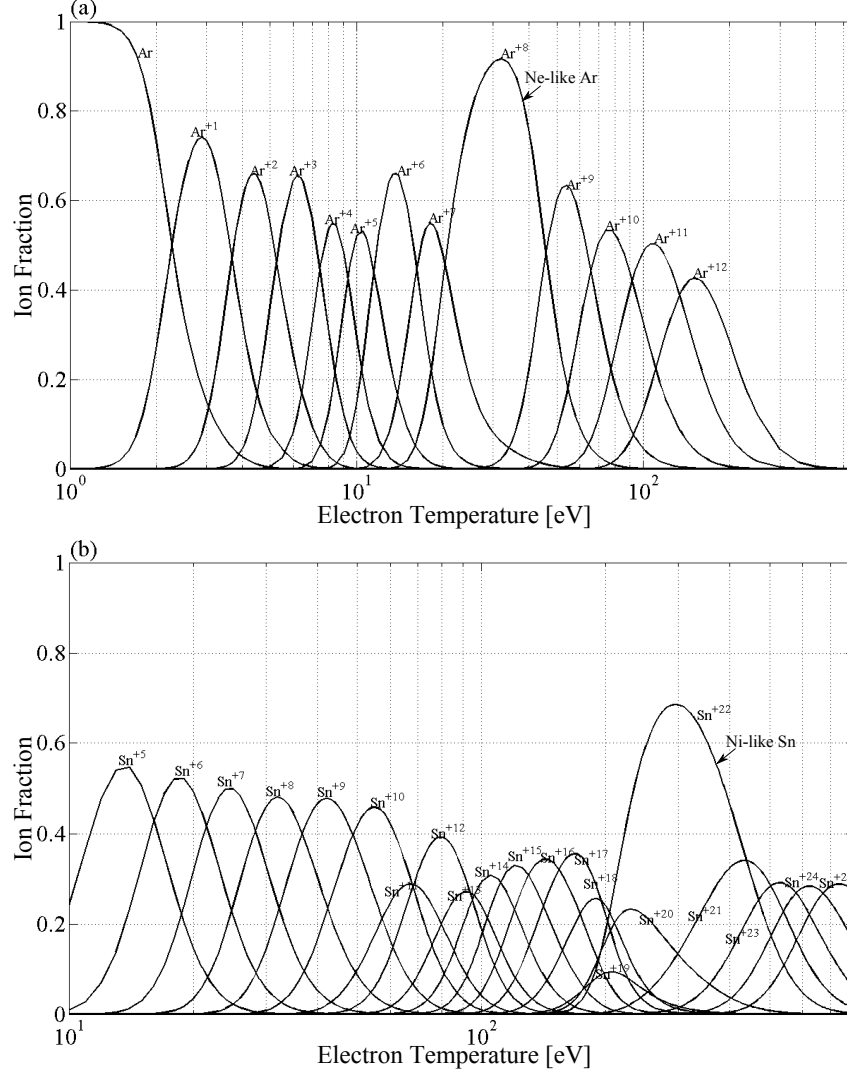
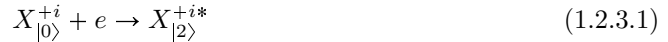


Fig. 1.18: Calculated ion fraction in the frame of a NLTE model for (a) Ar and for (b) Sn at their optimum electron densities. The optimum electron density for Ne-like Ar and Ni-like Sn are respectively $1.5 \cdot 10^{19} \text{ cm}^{-3}$ and $5 \cdot 10^{20} \text{ cm}^{-3}$ (Chapter. 3.4).

The electron collisional excitation (monopole) to the upper level (2) in Ne-like and Ni-like ions can be expressed as below:



where i is 10 and 28 for Ne-like and Ni-like ions, respectively.

Fig. 1.19 summarizes excitation energy from ground level to the upper level for Ne-like and Ni-like ions.

XUV and soft X-ray wavelengths for Ne-like and Ni-like ions in the laser-produced plasma through electron collisional scheme are shown in Fig. 1.20. It shows wavelengths for Ne-like and Ni-like ions contributing to the $3p(J=0) \rightarrow 3s(J=1)$ and $4d(J=0) \rightarrow 4p(J=1)$ transitions, respectively. These wavelengths have been demonstrated experimentally [22, 63, 68, 87, 151, 175, 179, 215, 216, 234, 235, 244, 259, 260, 292, 297–299, 340, 341, 349].

Fig. 1.17, Fig. 1.19, and Fig. 1.20 show that in order to achieve shorter wavelengths, one has to

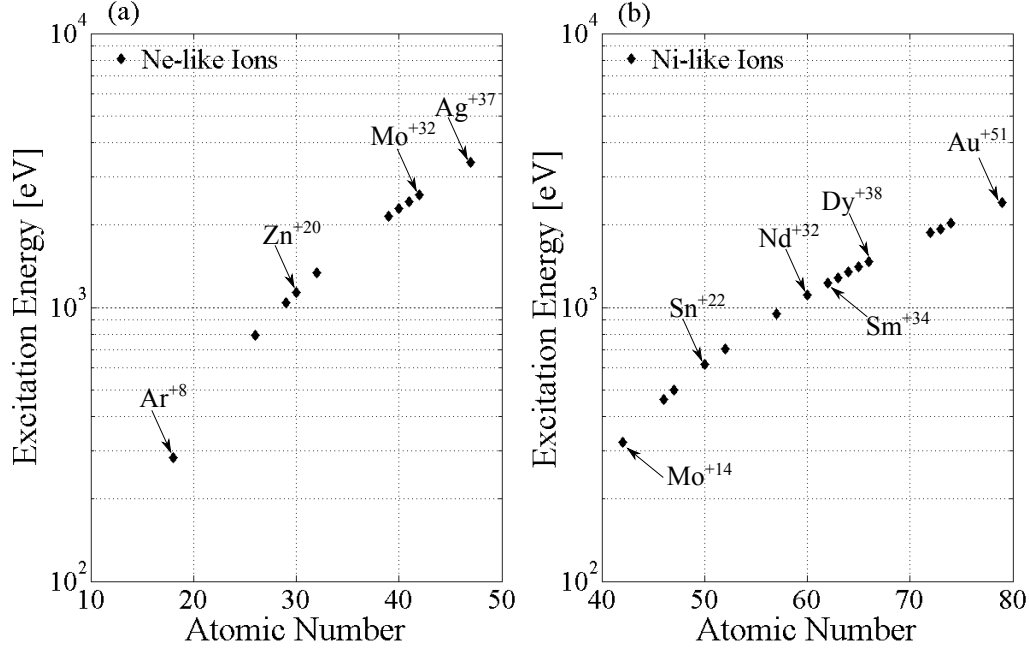


Fig. 1.19: Calculated excitation energy from ground level to the upper level for (a) Ne-like and (b) Ni-like ions.

work with higher atomic numbers requiring higher pump-laser-energy.

Fig. 1.19 and Fig. 1.20 show that the excitation energies of Ne-like Zn and Ni-like Nd are approximately equal, but the XUV wavelength produced by Ni-like Nd is ≈ 2.7 shorter than Ne-like Zn. Indeed, Ni-like ions can operate at wavelengths shorter than 10 nm making Ni-like ions more attractive (see Fig. 1.20).

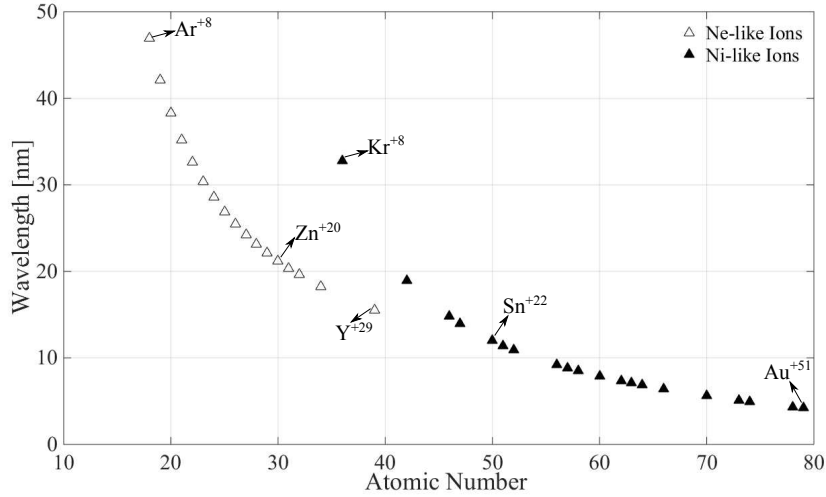


Fig. 1.20: Calculated XUV and soft X-ray wavelengths of the lasing lines as a function of atomic number Z for Ne-like and Ni-like ions. To achieve shorter wavelengths, high- Z elements are required as radiators.

Mapping the population of laser wavelengths, one observes that between approximately 10 eV (VUV, excimers) and 1 keV (X-ray, X-ray Free-Electron laser) there is essentially a "laser gap", i.e. no systems are available. Although such a gap can be filled as an extension of the accelerator-based architecture, e.g. FLASH, the latter is not for laboratory operation. The plasma-driven laser has thus a unique potential to fill such laser gap in the XUV.

Thanks to an extremely narrow linewidth ($\Delta\lambda/\lambda < 10^{-4}$), i.e. spectral purity, the brightness

of plasma-driven lasers is five to six orders of magnitude higher than that of third generation synchrotron sources. The high spectral purity is important not only for selective-excitation in XUV spectroscopy. The associated full time-coherence permits excellent implementation in interferometry.

Furthermore, the possibility of pumping a multi-elemental target material or multiple transition in the same atom offers a simple way to generate a two-color coherent pulse. This can be important either in two-photon imaging, differential cross-section spectroscopy, or in seeding experiments or self photopumping. Such a mode of operation is not at all simple in accelerator-based architectures, as it would require a bimodal electron energy distribution which conflicts with self-ASE.

1.3 Research gap

The use of a laser-produced plasmas as amplification media for XUV coherent emission has been demonstrated since the mid 1980s. In the last three decades, tremendous progress has been made in terms of efficiency, such that nowadays wavelengths as low as $\lambda = 6 - 48$ nm are possible on a table-top setup. The operation of such lasers is, however, still at research level. Turnkey systems are in principle possible and would complement the specifications of large-scale accelerator-based light sources (proof-of-principle use) and become implemented for technology-enabling applications. Fundamental physics has been discussed here, showing that some intrinsic trade-offs were overcome in my group, which is promising to enable turnkey soft X-ray lasers.

Indeed, researchers need a detailed understanding and parametric visualization of the laser-produced plasma aiming at an optimization of the plasma conditions for soft X-ray lasing. Most contributions regarding optimization in lasing conditions in XUV and soft X-ray come from experimental studies. Thus, there remains a lack of detailed theoretical analysis. In fact, the laser-produced plasma must satisfy some strict (transient) criteria for XUV lasing such as:

- (i) *What optimum pump pulse characteristics?* All of the optimization of pump pulse-duration and time-delay studies reported to date come from one-point parameter-fixed experimental studies [98, 102, 187] with a lack of analytical analysis.
- (ii) *What optimum pump pulse shape?* To our knowledge, there have not been a theoretical and experimental study for estimating pump pulse shape for XUV and soft X-ray lasing.
- (iii) *What optimum electron temperature and density in the plasma as an active medium?* Some references have presented theoretical studies of Ni-like plasmas for a selection of target materials [22, 68, 87, 151, 215, 234, 244, 260, 297–299, 340, 341, 349], obtaining optimum electron temperature and density that can be used as benchmark here. However, there is not a unique scaling law for predicting the optimum electron temperature and density for XUV and soft X-ray lasing of the *Ni-like ions* plasma.
- (iv) *What electron density gradient and plasma homogenization for mitigating soft X-ray or pump-pulse refraction is required?*
- (v) *What capability of "two-color" X-ray pulses?* The latter are very insightful probes to investigate the structure of matter, the dynamics of ultrafast physical processes, and chemical reactions [191]. Theoretically, the time scale of rotation, vibration, dissociation of molecules, atoms-excitation, atom-ionization, etc. are known [17, 69]. Ideally, one would measure experimentally such time-scales by time-resolved measurement using dual X-ray pulses with specific time delays and spectral separation. Besides, near-edge X-ray absorption spectroscopy to simultaneously probe the structure and surface chemistry is another application for two-color probes. Plasma-driven X-ray lasers offer the possibility of multiple transitions in a target material to generate a two-color XUV laser in a table-top setup. However, such a mode of operation is not simple at all in other huge facilities of X-ray laser sources such as Free electron lasers (FELs) [191].

1.4 Aims of the Thesis

This monograph summarizes main finding during the research done as SNSF Assistant Professor (2011-2015) guiding a team of three graduate students. The work is organized in three modules focused on fundamental aspects (called "LAPLAS"), on XUV imaging (called "ACTINIC"), and on XUV spectroscopy (called "XULPES"). The main goal of this research was in making plasma-driven lasers from a research-level platform to an enabling technology. This demands the following contributions:

1. Quantitative understanding of the parametric effect on the operation;
2. Assembling a compact "table-top" demonstrator;
3. Performing proof-of-principle experiments and validating the preliminary modeling.

A first part is dedicated to the optimization of the plasma X-ray lasing, analyzing mostly by means of computational tools, the functionals involved in the process. A second part shows a few results in nano-analytics.

1.5 Structure of the Thesis

The present habilitation thesis is organized as follows:

1. In Chapter "*Methods*" I present two sections. Section 2.1 summarizes the **computational methods** utilized to investigate the parameters and simulate the laser action across the plasma gain-medium; Section 2.3.1 summarizes the **experimental methods** self-developed and utilized to generate soft X-ray plasma lasing and to perform imaging and spectroscopy experiments;
2. In Chapter "*Optimization of Plasma X-Ray Lasing*" I investigate **fundamental aspects** on the generation of soft X-ray plasma lasing. I begin in Section 3.1 with the generation of a plasma column by means of line focusing; Then I move on analyzing the shape and timing of pump-pulses, in Sects. 3.2 and 3.3; further, the optimum plasma conditions,

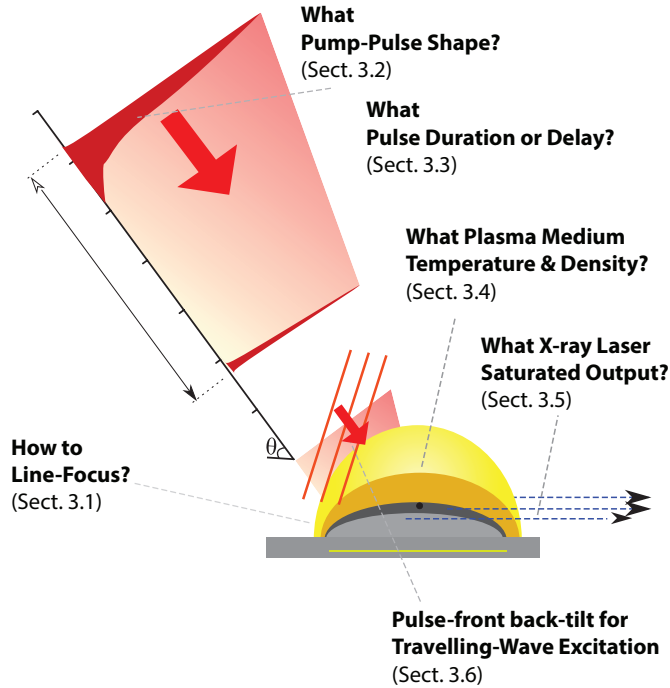


Fig. 1.21: Schematic of the fundamental methodological questions investigated in this work and related section in this monograph.

-
- i.e. temperature and density, are investigated and how these affect the laser gain (Sect. 3.4), such that the saturated laser output can be achieved (discussed in Sect. 3.5). Finally, travelling-wave excitation is investigated as an high-efficiency technique for plasma-lasing.
3. In Chapter "*Advanced Analytics*" I demonstrate **applied results** on imaging as well as related instrumentation self-developed within this research for collection and diagnostics (Sects. 4.1 and 4.2). Further, in Sect. 4.3 I investigate spectroscopic capabilities of the soft X-ray plasma laser as well as the generation of "two-color" pulses.

2. METHODS

Main themes here:

- *Theory and Codes for Plasma Modelling*
- *Theory and Codes for Laser Action Modelling*
- *Theory and Codes for Ray-tracing*

2.1 Plasma Lasing Modeling Codes

A suite of codes was used [71] (i) for modeling the hydro-dynamics of laser-produced plasmas gain media, (ii) the atomic and spectral characteristics and (iii) ray-tracing propagation through optical elements.

2.1.1 Hydrodynamic Codes

Electron and ion temperatures or densities can be modeled by hydrodynamic codes [9, 129, 141, 171, 172, 218], considering a plasma as a fluid of ions, electrons, and photons. The three fundamental conservation equations, related to mass (Eq. 2.1.1.1), momentum (Eq. 2.1.1.2), and energy (Eq. 2.1.1.3), create a complete set of coupled differential equations able to describe the fluids, as follows:

$$\begin{array}{c}
 \text{Mass density k-th species} \\
 \uparrow \\
 \frac{\partial (\rho_k)}{\partial t} \\
 \underbrace{\hspace{1.5cm}} \\
 \text{Rate of mass} \\
 \text{per unit volume}
 \end{array}
 +
 \begin{array}{c}
 \text{Velocity vector} \\
 \text{of the k-th species} \\
 \uparrow \\
 \nabla \cdot (\rho_k \vec{v}_k) \\
 \underbrace{\hspace{1.5cm}} \\
 \text{Rate of mass} \\
 \text{by convective transport} \\
 \text{per unit volume}
 \end{array}
 =
 \underbrace{S_k}_{\text{Source term}}
 \quad (2.1.1.1)$$

$$\begin{array}{c}
 \frac{\partial (\rho_k \vec{v}_k)}{\partial t} \\
 \underbrace{\hspace{1.5cm}} \\
 \text{Rate of} \\
 \text{momentum per} \\
 \text{unit volume}
 \end{array}
 +
 \begin{array}{c}
 \nabla \cdot (\rho_k \vec{v}_k \vec{v}_k) \\
 \underbrace{\hspace{1.5cm}} \\
 \text{Rate of momentum} \\
 \text{by convective transport} \\
 \text{per unit volume}
 \end{array}
 =
 -
 \underbrace{\nabla (P_f + P_r)}_{\substack{\text{Pressure gradient force} \\ \text{per unit volume}}}
 +
 \underbrace{F_b}_{\substack{\text{Body force} \\ \text{on fluid per} \\ \text{unit volume}}}
 \quad (2.1.1.2)$$

$$\begin{aligned}
& \text{Energy density of fluid} \\
& \underbrace{\frac{\partial(E_f)}{\partial t}}_{\text{Rate of energy per unit volume}} + \underbrace{\nabla \cdot (E_f \vec{v}_k)}_{\text{Rate of energy by convective transport per unit volume}} + \underbrace{\nabla \cdot ((P_f + P_r) \vec{v}_k)}_{\text{Rate of work done by pressure forces on the fluid per unit volume}} = \underbrace{S_E}_{\text{Laser energy source per unit volume}} + \underbrace{\nabla \cdot F_c}_{\text{Rate of heat per unit volume due to conduction}} + \underbrace{\nabla \cdot F_r}_{\text{Rate of heat per unit volume due to radiation}}
\end{aligned}
\tag{2.1.1.3}$$

For charged particles in the plasma, a source term (S_k) arises from ionization and recombination processes. Since the net production and loss of plasma particles are balanced (plasma is considered quasi-neutral), the source term is usually zero ($S_k = 0$). Body force density (F_b) comes from gravity or electromagnetic forces acting over the entire volume of the body. In the laser-produced plasma, F_b is negligible and considered zero ($F_b = 0$). The source term for energy (S_E) comes from the laser energy absorbed by the plasma.

Eulerian and Lagrangian methods are two approaches for solving Navier-Stokes equations such as Eq. 2.1.1.1-2.1.1.3. In both approaches, the plasma can be thought of as a box (computational grid) which is structured into computational cells. The **Eulerian method** keeps the volume of these cells fixed and assumes particles moving through the cells while the plasma is expanding. The change in number of particles in a cell results in a change in the density within the cell, as shown in Fig. 2.1a.

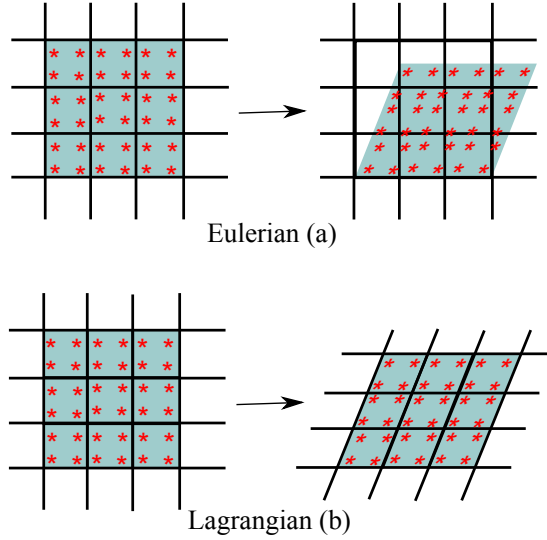


Fig. 2.1: The description of the moving fluid (plasma) can be done in the Eulerian or Lagrangian method. (a) In the Eulerian approach, fluid flows through fixed grids. (b) In Lagrangian approach, grids deform as the fluid flows.

Alternatively, in the **Lagrangian method**, the number of particles in a cell is fixed. This way, the cell gets larger or smaller to keep the number of the particles constant and in this approach grids move with particles (Fig. 2.1b), as shown in Fig. 2.1b, the number of particles in each cell remains constant.

In this study, a hydro-code based on the Lagrangian scheme is used for following reasons:

- (i) It is relatively easy to compare the Lagrangian models with experiments, as each particle in the simulation corresponds to one particle in the experiment. Meanwhile, the Eulerian schemes are advantageous for quasi-static situations where the fluid flow does not change much from one place to another and is pretty steady in time.
- (ii) In an expanding plasma, where the density changes by several orders of magnitude, it is computationally efficient to have the grid to move with the material. Indeed, the

Lagrangian description has the advantage of providing high-order accuracy at the least cost in computer time. In the Eulerian scheme one would have to have a great number of fine cells to accomplish the same resolution.

- (iii) The Lagrangian approach allows the interface between two different materials to be followed exactly. In the Eulerian scheme, numerical diffusion causes the interface to become fuzzy and ill-defined [141].
- (iv) The Lagrangian approach not only shows the ultimate pathway of an expanding plasma over a specified time period, but also reveals the expansion pathway. In an expanding plasma with complicated geometry, the ultimate expansion pathway is not always obvious and may not be well predicted by the Eulerian approach.
- (v) The tracking of a shock front is easily accomplished in the Lagrangian grid [141], whereas in the Eulerian prescription one has to resort to an artificial tracking scheme [46].

HYADES [141], MEDUSA [218], MULTI, HELIOS [129], and LASNEX [171, 172] are examples of one-dimensional Lagrangian hydrodynamic codes. MULTI 2D and ARWEN [9] are examples of two-dimensional hydrodynamic codes.

"HYADES" is used in this work. It is a one-dimensional, three-geometry (planar, cylindrical or spherical), three-fluid (electrons, ions and photons) hydrodynamics simulation code. The conservation equations for mass, momentum and energy are solved in a Lagrangian coordinate system. The three fluids are treated individually in a fluid approximation, each having its own temperature. Each fluid is assumed to be in LTE (local thermic equilibrium), which is to say that the electrons and the ions are described well in the classical limit by Maxwell-Boltzmann statistics, and the radiation field is Planckian.

Electron degeneracy effects, important in low-temperature, high-density plasmas, are taken into account. The equation of state (EOS) and related thermodynamic coefficients are obtained from external tables that have been compiled using experimental data and theoretical models. The energy transport by free-electrons and ions is modeled in the flux-limited diffusion approximation (the default value for both electrons and ions is 0.4). Radiation is transported according to the photon energy, i.e., ultra-violet and soft X-rays have very short mean free paths, while the more energetic photons' harder X-rays will penetrate deeply into the material. The absorption and emission coefficients are determined self-consistently from the atomic physics model of choice or may be supplied by the user in tabular form.

2.1.2 Atomic Spectroscopy Codes

Theoretical atomic data are important for X-ray radiation produced by plasmas. R. Cowan's code [61], HULLAC [140], and FAC [92] are the most popular codes that can perform atomic calculations. R. Cowan's code [61] is based on the non-relativistic approximations with relativistic corrections introduced as perturbations. HULLAC [140] and FAC [92] are fully relativistic atomic codes developed based on the Dirac equation.

In this work, the relativistic configuration interaction atomic code FAC is used. Since for atoms with Z between 20 and 60 inner shell radial functions are altered sufficiently by relativistic effects, it is safer to use a relativistic atomic structure theory than a non-relativistic one [224]. Furthermore, for $Z > 60$ relativistic effects and electron correlation are strongly coupled making it necessary to use a code based on relativistic theory [224].

The energy levels of an atomic ion with N electrons are obtained by diagonalizing the Hamiltonian matrix. Leaving aside the influence of spin and relativistic effects, the Hamiltonian can be

written as [15]:

$$\hat{H} = \hat{H}_{\text{kinetic}} + \hat{H}_{\text{elec-nucl}} + \hat{H}_{\text{elec-elec}} = \left(\begin{array}{c} \hat{H}_{\text{kinetic}}: \text{Kinetic energy of the } i\text{th electron} \\ \sum_{i=1}^N -\frac{\hbar^2}{2m^2} \nabla_i^2 \\ \underbrace{-\frac{Ze^2}{4\pi\epsilon_0 r_i}}_{\hat{H}_{\text{elec-nucl}}: \text{Potential energy of the } i\text{th electron in the electric field created by the nucleus}} \underbrace{e^{-\lambda_{TF} r_i}}_{\text{Screening effect due to the nucleus-electron interaction}} \end{array} \right) + \quad (2.1.2.1)$$

$$\underbrace{\sum_{i \neq k}^N \frac{1}{4\pi\epsilon_0} \frac{e^2}{|\vec{r}_i - \vec{r}_k|}}_{\hat{H}_{\text{elec-elec}}: \text{Mutual coulomb interaction between electrons}} \underbrace{e^{-\lambda_e |\vec{r}_i - \vec{r}_k|}}_{\text{Screening effect due to the electron-electron interaction}}.$$

Distance of the i th electron from the nucleus

In a partially filled subshell which contains several electrons, their spins and orbital angular momenta can combine in several different ways, to give different values of the total angular momentum, with different energies. In order to deal with this problem, it is necessary to consider the spin-orbit interaction as well as the residual Coulomb interaction between the outer electrons. Then, the Hamiltonian can be written as follows [16]:

$$\hat{H}_0 = \sum_{i=1}^N \left(-\frac{\hbar^2 \nabla_i^2}{2m^2} - \frac{Ze^2}{4\pi\epsilon_0 r_i} e^{-\lambda_{TF} r_i} + U_i(r) \right)$$

$$\hat{H} \approx \underbrace{\hat{H}_0 + \sum_{i \neq k}^N \frac{1}{4\pi\epsilon_0} \frac{e^2}{|\vec{r}_i - \vec{r}_k|} e^{-\lambda_e |\vec{r}_i - \vec{r}_k|}}_{\hat{H}_1: \text{Residual coulomb interaction}} - \sum_{i=1}^N \underbrace{U_i(r)}_{\text{Single-electron potential}} + \sum_{i=1}^N \underbrace{\xi_i(r)}_{\xi_i(r) = \frac{1}{2m^2 c^2} \frac{1}{r} \frac{\partial v}{\partial r}} \underbrace{\hat{L}_i \cdot \hat{S}_i}_{\hat{H}_2: \text{Spin orbit interaction}}. \quad (2.1.2.2)$$

If $\hat{H}_1 \gg \hat{H}_2$, \hat{H}_2 can be treated as a perturbation on $\hat{H}_0 + \hat{H}_1$. Then, this leads to a scheme called LS (or Russell-Saunders) coupling, which applies in the case of light atoms. If $\hat{H}_2 \gg \hat{H}_1$, the spin-orbit interaction is better described by the j-j coupling [286], which usually takes place for high- Z atoms.

A set of eigenstates for the Schrödinger equation can be defined as [15, 20]:

$$\begin{array}{ccc} \text{Hamiltonian operator} & & \text{Energy "eigenvalue" for the system} \\ \uparrow & & \uparrow \\ \hat{H} \Psi_i & = & \epsilon_i \Psi_i \\ \downarrow & & \\ \text{Atomic state wave function} & & \end{array} \quad (2.1.2.3)$$

This gives spectroscopy information about the excited states, e.g., the "eigenvalue" ϵ_i gives the energy level value of the i th state.

The atomic state wave functions can be expanded in terms of complete orthogonal basis functions ($\Phi_i(\vec{r}_i)$) [92]:

$$\Psi_i = \sum_j C_j \Phi_j(\vec{r}_i) \quad (2.1.2.4)$$

where C_i are the mixing coefficients obtained from diagonalizing the total Hamiltonian. The basis functions ($\Phi_i(\vec{r}_i)$) are expanded in antisymmetric sums of products of N one-electron wave functions (φ), which can be used in LS or j-j coupling schemes.

In the non-relativistic LS approximation, the single particle wave-function (φ) has the following

form [61]:

$$\varphi_i(\vec{r}_i) = \frac{1}{r} \underbrace{P_{n_i l_i}(r)}_{\text{Radial function}} \underbrace{Y_{l_i m_{l_i}}(\theta, \phi)}_{\text{Angular function}} \underbrace{X_{m_{s_i}}(\sigma)}_{\text{Spin function}} \quad (2.1.2.5)$$

where n is the principal quantum number, l is the angular momentum quantum number, m_l is the magnetic quantum number, and m_s is the electron spin quantum number.

In the true relativistic theory, the single particle wave-function (Dirac spinors: φ_{nkm}) has the following form [75, 92]:

$$\varphi_{nkm} = \frac{1}{r} \underbrace{\begin{pmatrix} P_{nk}(r) \chi_{km}(\theta, \varphi, \sigma) \\ iQ_{nk}(r) \chi_{-km}(\theta, \varphi, \sigma) \end{pmatrix}}_{\text{Spin-angular function}} \quad (2.1.2.6)$$

where $\rho_{nk}(r) = (P_{nk}^2(r) + Q_{nk}^2(r))$ defines the radial density distribution. Here, n is principal quantum number and m is the z-component of the angular momentum j . k is the relativistic angular quantum number, which is related to the orbital and total angular momentum as follows:

$$k = (l - j)(2j + 1). \quad (2.1.2.7)$$

The flexible atomic code (FAC) is used here to calculate the required atomic data such as collisional excitation coefficients, spontaneous emission coefficients, and energy levels. FAC employs a fully relativistic approach based on the Dirac equation. It is a configuration interaction program for calculating atomic collisional and radiative processes, including (i) energy levels, (ii) radiative transitions and the inverse process of (iii) photo-excitation, (iv) collisional excitation and (v) ionization by electron impact and its inverse process (vi) collisional de-excitation and (vii) three-body recombination, (viii) radiative recombination and its inverse process (ix) photo-ionization, (x) auto-ionization and its inverse process and (xi) dielectronic capture.

Due to some limitations of FAC in handling the calculation of ionic distributions, the online FLYCHK code from the NIST was used, too. The FLYCHK code was used to calculate ionic level populations by a solving multi-level rate equation in zero dimension.

2.1.3 Boundary Conditions for Ar Target

Calculations are performed by considering a neutral gas target, Ar^0 , considering an electronic flux-limit multiplier of 0.05 and a multi-group radiation transport of 50 groups (in HYADES). The plasma is created using $\lambda = 1054$ nm Nd:glass laser (IR pulse). The pump pulse is incident at an angle of 90° (normal incidence) to the target. Here, the considered geometry is planar (1D Cartesian) geometry. The initial gas density of neutral Ar^0 at all zones (irradiated area) is considered the same, which is 4 mg/cm^3 ($6 \cdot 10^{19} \text{ cm}^{-3}$).

2.2 Optical Codes

2.2.1 Ray-tracing in Optics Design

For design and analysis of the beam propagation (ray tracing) through optical elements, optical design codes are also used. ZEMAX [345] and OSLO [229] are examples of commercial optical design codes. KuBERT from "Kubisch BERN Ray Tracing" is an optical design code developed at University of Bern. In this thesis, KuBERT is used for optical design and analysis. Namely, physics inside KuBERT as an optical ray tracing code works based on Snell's Law (Eq. 2.2.1.1), considering optical pass equation (Eq. 2.2.1.2), and diffraction grating equation (Eq. 2.2.1.3).

Snell's law is an equation used to give the relationship between the angles of incidence and refraction referring to light passing through a boundary between two different media:

$$n_1 \sin \theta_1 = n_2 \sin \theta_2 \quad (2.2.1.1)$$

where n_1 and n_2 denote the refractive indexes on the each side of the interface. θ_1 and θ_2 are the incident and exit angle of the ray at the interface, respectively. At reflective surfaces incident

angle equals exit angle is applied.

If the refractive index varies along the path, the optical path length (OPL) is given by:

$$\text{OPL} = \int_a^b n(s) ds \quad (2.2.1.2)$$

where $n(s)$ is the local refractive index as a function of distance along the path. In a homogeneous medium, the optical path length is simplified to $\text{OPL} = nd$, where d is traveling distance of light. Output beams of all possible diffraction orders at a grating can be estimated by:

$$\sin(\theta_1) + \sin(\theta_2) = m\lambda/d \quad (2.2.1.3)$$

where m ($m = 0, \pm 1, \pm 2, \dots$) is diffraction order, λ is Wavelength, and d is line-space of the grating.

2.2.2 Ray-tracing across Plasmas

The general solution for finding how the light propagates inside the plasma region is obtained by solving the Helmholtz equation. In the frequency domain, the Helmholtz equation inside the plasma is as follow:

$$\nabla^2 E + k_0^2 n^2 E = 0 \quad (2.2.2.1)$$

where k_0 is wave number in free space and n is refractive index of the plasma. It is important to note that in the plasma region the refractive index is position-dependent, thus Eq. 2.2.2.1 does not have an exact solution. In order to solve the propagation of light inside a plasma, an applicable modeling is ray-tracing which can approximate the propagation in the plasma region via an eikonal approach. In fact, the eikonal equation describes the kinematic propagation of high frequency waves [44, 328]. In addition, the eikonal approach is very general and it can be derived in a systematic way for a medium whose properties change slowly in time and space. The electric field component of a monochromatic wave can be written as follows:

$$E(\vec{r}, t) = E(\vec{r}) e^{-i\omega t} \quad (2.2.2.2)$$

where ω is the angular frequency. The Wentzel-Kramers-Brioullin (WKB) approximation is used when the wavelength λ of waves is much smaller than the electric field characteristic length scale $|E|/|\nabla E(\vec{r})|$ [136], namely in cases the field amplitude changes are small. The zeroth order electric field approximation $E(\vec{r}) = E_0 e^{ik_0 S(\vec{r})}$ is considered (all other variations in E is neglected), where $S(\vec{r})$ is the eikonal function. The electric field expression is applied to the Helmholtz equation, and then the eikonal equation is deduced [44, 136, 337], where $|\nabla S(\vec{r})|^2 = n^2(\vec{r})$:

$$\nabla S(\vec{r}) = n(\vec{r}) \hat{s} = n(\vec{r}) \frac{d\vec{r}}{ds} \quad (2.2.2.3)$$

by taking derivative in s ,

$$\frac{d}{ds} (\nabla S(\vec{r})) = \frac{d}{ds} \left(n(\vec{r}) \frac{d\vec{r}}{ds} \right) \quad (2.2.2.4)$$

considering Eq.2.2.2.3 and the chain rule, one obtains:

$$\begin{aligned} \frac{d}{ds} (\nabla S(\vec{r})) &= \frac{d\vec{r}}{ds} \cdot \nabla (\nabla S(\vec{r})) = \\ \left(\frac{\nabla S(\vec{r})}{n(\vec{r})} \right) \cdot \nabla (\nabla S(\vec{r})) &= \frac{1}{2n(\vec{r})} \nabla (\nabla S(\vec{r}) \cdot \nabla S(\vec{r})) = \frac{1}{2n(\vec{r})} \nabla (n^2(\vec{r})) = \nabla n(\vec{r}). \end{aligned} \quad (2.2.2.5)$$

Then, the ray equation is derived as follow:

$$\frac{d}{ds} \left(n(\vec{r}) \frac{d\vec{r}}{ds} \right) = \nabla n(\vec{r}) \quad (2.2.2.6)$$

where ds is the element of distance along the ray, r is the position vector for a ray point, and n is the refractive index of the medium. Defining $dl = ds/n(\vec{r})$, ray equation will be derived as follows:

$$\frac{d^2 r}{dl^2} = n(r) \nabla n(r). \quad (2.2.2.7)$$

By solving numerically or analytically of eikonal equation [104], the ray trajectory inside a plasma is analyzed.

Since the refractive index depends on the electron density, beams in a plasma are refracted if they pass through a region with an electron-density gradient (see Fig. 1.9). In this work, ray trajectories of short-wavelength-signal and IR-pump pulse in the LPP are presented including ray-tracing modeling study on the eikonal theory.

2.2.3 *Boundary Conditions*

For the calculation, only a Mo planar target (see Fig. 2.6) was chosen along with an electronic flux-limit of 0.05 and a multi-group radiation transport of 50 groups which are logarithmically interpolated the photon energy domain in the range of 1 eV to 10 keV. In addition, it is considered that the peak of first pre-pulse arrives at the target at 2.4 ps. The pre-pulses and main-pulse have a Gaussian pulse shape. Furthermore, the total energy of the pulse train is 2.5 J. The time precision for the computation is considered 0.5% of ps.

2.3 Experimental Equipment

Main themes here:

- *Laser for the Plasma Generation*
- *Measurement Methods*
- *Diagnostics*

2.3.1 Terawatt Pump Laser & Soft X-ray Plasma Laser

The experimental measurements were realized at the self-developed "BEAGLE" TW-laser source (Fig. 2.2). The terawatt drive laser beam is used to irradiate a metallic tin target and induce a plasma, which acts as gain medium to amplify spontaneous emission (ASE). The drive beam is a 1054-nm (IR) Nd:glass laser with a pulse duration of 1.2 ps and an energy delivered onto the target, which was limited to 2.5 to 3 J for the tin laser. The oscillator feeds pulses of approx. 200 fs at a repetition rate around 100 MHz, having energies of a few nJ. A Pockels cell gates one pulse to the pulse stretcher and amplification stage. The pulse stretcher consists of a grating pair of 1740 grooves/mm. The pulse is, prior to amplification, stretched to 1 ns. The pre-amplification is done in a regenerative amplifier with a total of ca. 50 round-trips, 7.1 ns round-trip time, and overall gain of approx. 10^6 with output in the mJ level. This is a compact and effective way of pre-amplification. Pulse contrast is approx. 1000:1. A set of amplification Nd:glass rods, with diameters 10 mm, 16 mm, 25 mm, 45 mm contributes to the generation of a Joule-level pulse, which is finally compressed with another grating pair. Pulse compression is done with a double-pass grating compressor with one grating tilted by 0.09° , such that a travelling wave at the speed of light is attained even at an incidence angle of 45 degrees. Pre-pulses induced in the regenerative amplifier are suppressed by means of Pockels-cell gating on the amplifier chain. The spatial beam profile is homogenized and image-relayed by means of four evacuated spatial filters at 10^{-4} mbar to avoid the formation of hot spots. Two pre-pulses and a main pulse of identical duration are delivered at 45 degrees onto the target. The spatial overlap is checked adjusting the position of a set of beamsplitters with 0.25%, 8%, and 100% reflectivity, respectively.

The 1054 nm Nd:glass laser, with two pre-pulses with identical pulse duration as the collinear main pulse ($\tau = 1.2$ ps), delivered 2.5–3 J on a metallic (e.g. Mo, Pd, Sn) planar target over a 12-mm line focus at 40–50 degrees (triple grazing-incidence pumping or TGRIP). The results were compared to single orthogonal-incidence pre-pulse ("classical" transient collisional-excitation, TCE). The main advantage of our TGRIP scheme is the precision in adjusting the pre-pulse with the main pulse overlap, even with a tight line focus. The double pre-pulse generates a pre-plasma, that is the stepwise excited prior to main pulse ignition.

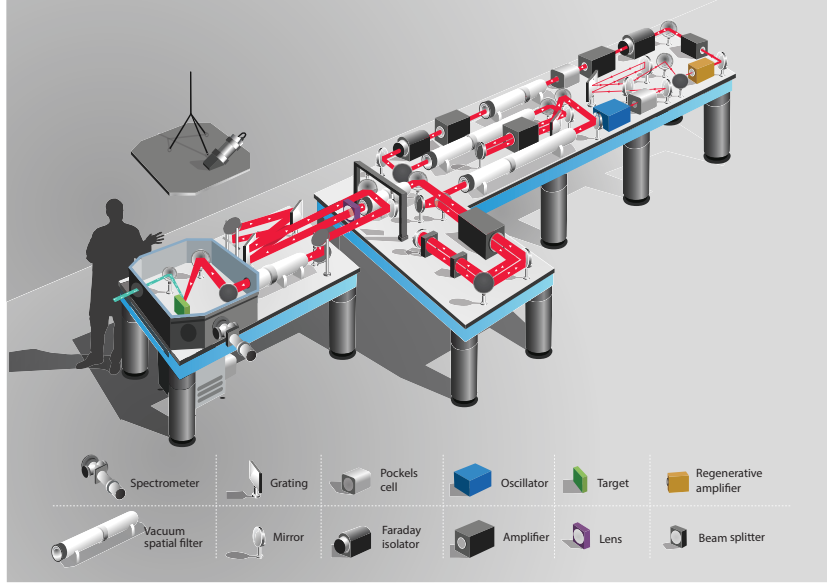


Fig. 2.2: Artist's view of the self-developed Beagle TW laser system. The architecture is based on chirped-pulse amplification (CPA) of a few nJ pulse. Key elements are shown in the legend.

2.3.2 Near and Far-field XUV Characterization

Fig. 2.3 shows the implemented setup for the measurement of the pointing stability and the divergence in the far field. Nd:Glass laser is incident on the target with an angle of 50° from the surface. XUV radiation is created and amplified in the plasma column. The radiation propagates to a spherical multilayer mirror, working as "micro-collimator", placed at a distance to the plasma equal to the mirror's *focal length*. The micro-collimator had a 250 mm radius of curvature (R). The mirror was coated with a Mo/Y multilayer. The incoming XUV radiation is directed to the CCD by using a turning mirror which was flat and coated with Mo/Y multilayer. Fig. 2.4 shows the setup used for near field imaging.

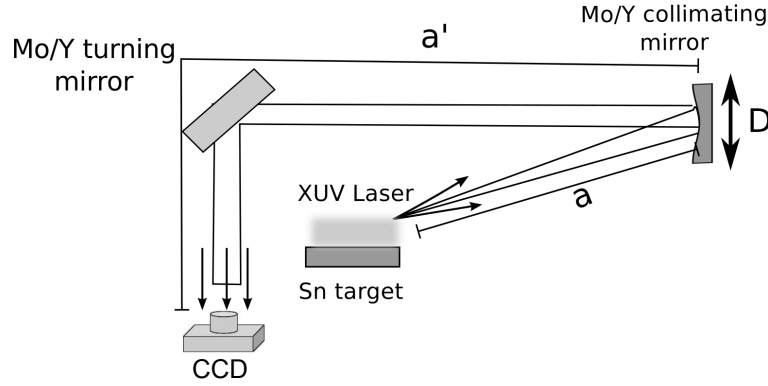


Fig. 2.3: Experimental setup for far-field characterization of the plasma-driven laser illumination. The optical collimation is obtained by adjusting the position of the collimating mirror to use it as a micro-collimator, in order to improve the pointing stability and divergence. The optimum collimation is acquired for distance set as $a=R/2 = 250\text{mm}/2$. Sketch not to scale.

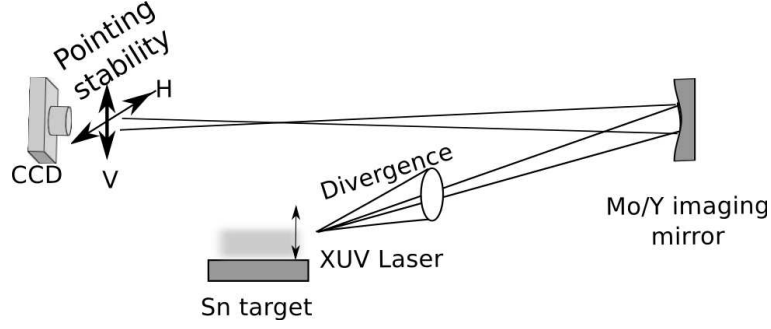


Fig. 2.4: Experimental setup for near-field characterization of the plasma-driven laser illumination. Sketch not to scale.

The signal-to-noise ratio was measured as a function of the illumination fluence. The obtained experimental calibration is shown in Fig. 2.5, between the illumination (top axis) and the signal-to-noise ratio (SNR). The observed SNR was fitted as a function of fluence, F (in counts per unit surface) with the following curve:

$$SNR = \frac{4096}{1 + 7 \cdot \exp(-4.6 \cdot 10^{-7} \cdot F[cts/cm^2])} \quad (2.3.2.1)$$

The amplitude of 4096 is explained by the 12-bit digitization ($2^{12} = 4096$ counts).

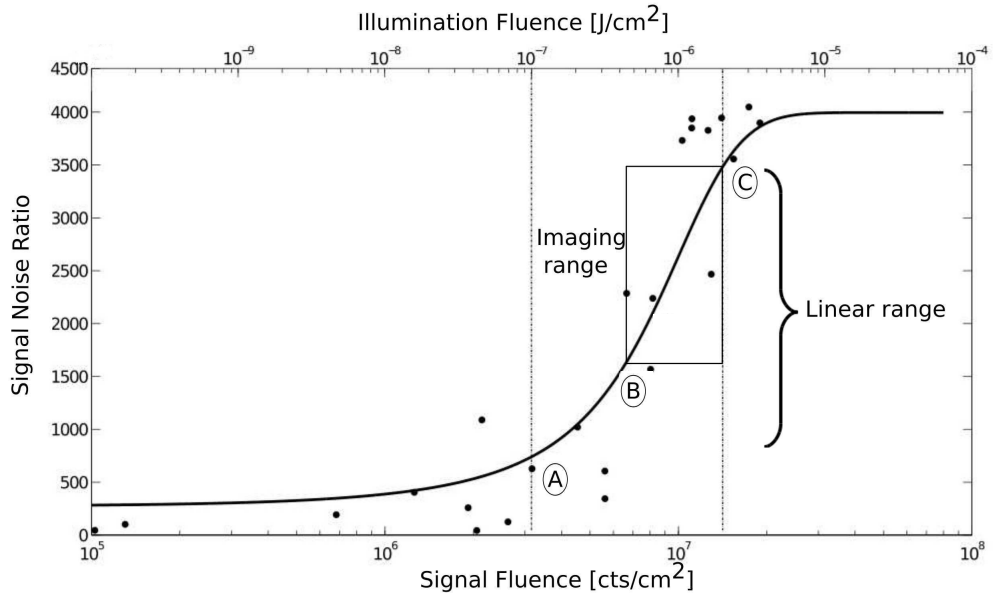


Fig. 2.5: Signal-noise ratio as a function of fluence, and illumination (top-axis). Points (•) are experimental data. The fitting is a sigmoid curve ($R^2=0.94$) given in eq. 2.3.2.1. Point (A) is the threshold of the linear range, (B) is the threshold for imaging with $SNR > 0.5$ and (C) is the saturation level. See discussion in the text.

2.3.3 Spatial Coherence Characterization

The Young double slit experiment was performed to determine the spatial coherence of the XUV Laser. Different double-slit masks were used. Tab. 2.1 shows the slit width and the slit separation used. The two pre-pulse schemes (TGRIP and TCE) were compared. Results obtained with the TCE scheme were published before [45]. The visibility (γ) to obtain the coherence degree was calculated using the following definition:

$$\gamma = \left| \frac{I_{max} - I_{min}}{I_{max} + I_{min}} \right| \quad (2.3.3.1)$$

Where I_{max} and I_{min} are referred to the maximum and minimum intensity in the diffraction patterns obtained after the illumination on the double slit masks. Some patterns obtained with the TGRIP are in Fig. 4.3. The coherence width, w_{coh} , was obtained as: $\frac{\lambda}{\theta}$, where λ is 12 nm, the wavelength, and θ is the angle subtended by the separation of the slits and the distance to the source. That step is needed to normalize the distance for the measured coherence degree obtained with different setups. The coherence width is considered for the slit separation where γ falls to $1/e$.

Number of slit	Separation [μm]	Minimum width [μm]	Maximum width [μm]	Slit length [μm]	Pre-pulse
1	9.9	3.2	3.6	3	GRIP
2	17.8	3.7	4.2	3	TCE
3	19.5	4.1	4.8	3	GRIP
4	25.2	3.8	4.9	3	TCE
5	33.0	2.8	4.1	3	TCE
6	40.6	2.8	4.1	3	TCE
7	51.0	3.8	4.2	3	TCE/GRIP

Tab. 2.1: Parameters used in the double-slit experiment for the spatial coherence measurement.

2.3.4 Target Chamber & Microscopy

Planar diamond-machined metallic targets were irradiated with fresh surface at every shot. The target chamber was operated at ca. 10^{-4} mbar and connected to the diagnostics chamber at 10^{-6} mbar by means of a vacuum gate and with a cold finger to prevent condensation on the CCD detector. The XUV was detected using a 16-bit 1024x1024-pixel back-illuminated x-ray CCD (Andor Camera) with a pixel size of $13\mu\text{m}$. The chip was cooled to -20 degrees C for low background level. The optical setup for XUV microscopy was optimized using self-developed optics software for raytracing.

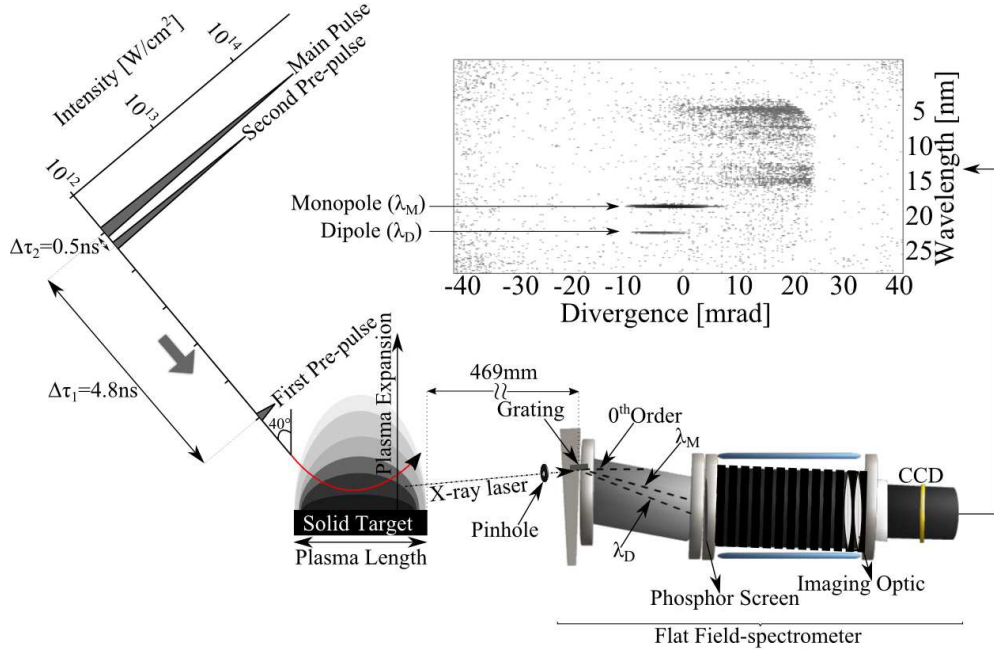


Fig. 2.6: Schematic of the flat field-spectrometer used to acquire spectra of X-ray laser produced by plasma.

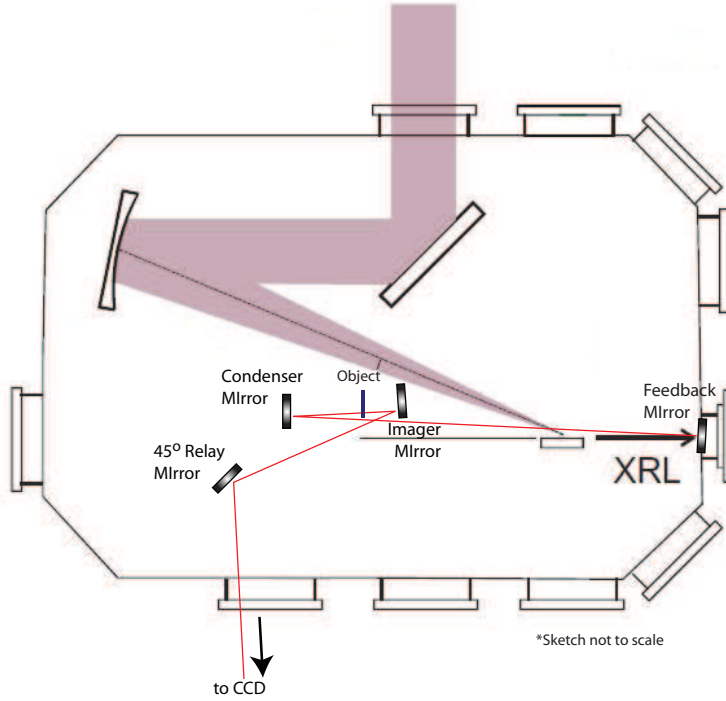


Fig. 2.7: Experimental setup for the generation of an X-ray laser (XRL) by focusing an intense pulse on a target material. The X-ray light was also used for actinic microscopy, and the optical setup of the self-developed microscope is shown. Sketch not to scale.

For the beam characterization, a CCD with $9\ \mu\text{m}$ pixel size (Star Camera) was used which had a front phosphor screen for XUV-to-visible conversion. In front of the XUV CCD detector a 150-nm-thick layer of zirconium was used to block the off-band radiation. Such setup produced an infinity correction and collimated the incoming XRL pulses, whatever its fluctuating divergence or line-of-sight. The *raw* image, before the micro-collimator, was captured by a spectrometer. The horizontal axis was the dispersion dimension of the spectrometer. Pointing stability and divergence were measured with and without the micro-collector.

Spectral characteristics of the XUV laser have been determined using an on-axis, time-integrating spectrometer (Fig. 2.6) that provided 2D images of angle- and wavelength-dispersion. The spectrometer consists of a $1200\ \text{mm}^{-1}$ flat field Hitachi grating (radius of curvature 5649 mm), working at grazing-incidence of 3° . The grating disperses the radiation onto a 40-mm-diameter P20 phosphor screen, imaged onto a cooled CCD camera with a pixel size of $25\ \mu\text{m}$. The spectral range is between 5 and 25 nm with a resolution of approx. 0.1 nm limited by slitless operation of the spectrometer.

The self-developed XUV microscope (Fig. 2.7) is composed of four Mo/Y multilayer mirrors ($R = 48\%$ centered at 12 nm): (i) a planar mirror, (ii-iii) a condenser & objective spherical pair with focal lengths of 120 mm, (iv) a 45 degrees planar mirror directing the rays to the CCD detector, through a 150 nm Zr foil that provides 60% transmission in the 7 to 14 nm and blocks radiation at longer wavelengths. The CCD detector was located at 1650 mm from the objective, which resulted in a 12x magnification. The illuminated field of view was approx. 100 by $50\ \mu\text{m}$ and the resolution below $1\ \mu\text{m}$, limited by magnification of the available optics. The images were obtained with one single shot, since the photon flux of ca. 10^{11} photons/shot was enough for good signal to noise ratio.

A particular transmission imaging sample (Fig. 2.8) was used to evaluate the resolution of optical instruments ("Siemens star"). It consisted of a pattern of transmitting spokes on a dark background, where the spoke were etched by means of e-lithography tapering from 200 nm at their touching tips to $10\ \mu\text{m}$. When displayed on an optical device with given resolution, even a printer or PC display, the spokes appear to merge into a central disk, which gives the overall resolution of the imaging setup. Our Siemens stars were fabricated using a Si₃N₄ membrane with a thickness of 100 nm and a Cr absorber layer of 20 nm.

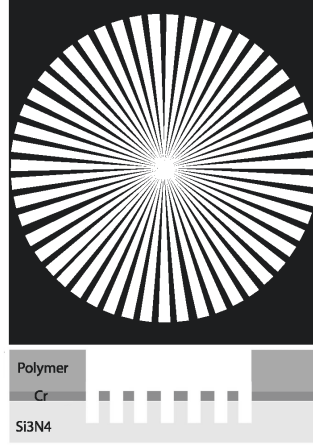


Fig. 2.8: Reference sample for the imaging experiments. A Siemens star has a radially modulated spatial frequency. The spokes touch only at the tip. Depending on the cut-off resolution of the tested imaging system, the merging of the spokes appear as a smaller or larger central disc.

2.3.5 Conditions for the Two-color Laser

In the in-house set-up a planar target is used, i.e., the plasma is created by a $\lambda = 1054$ nm Nd-glass chirped pulse amplification (CPA) laser system [24] with a pulse duration of 1.2 ps (FWHM) and Gaussian pulse shape. The beams including two pre-pulses and a main-pulse are irradiated at an incident angle of 40° degrees with respect to the target normal, which leads to a line focus [23, 33]. Two 0.5% and 16% pre-pulses (which are produced by inserting two beam splitters) irradiated the target 4.8 ns and 0.5 ns before the arrival of the main pulse for Mo. They arrived 5 ns and 0.2 ns before the arrival of the main pulse in the case of the Pd target. The pre-pulses were collinear with the main pulse. The total optimized-energy of the pulses in the experiment fluctuates in the range 2.5 ± 0.1 J for Mo and 2.6 ± 0.1 J for Pd on a line focus of $12 \text{ mm} \times 65 \text{ } \mu\text{m}$, see Fig. 2.6.

3. OPTIMIZATION OF PLASMA X-RAY LASING

3.1 Line Focusing & Plasma Column

Published in Bleiner et al. *Appl. Optics* 50 (36), 6689, 2011. Main themes here:

- Methods for Line Focus Generation
- Grazing-Incidence Pumping (GRIP) Method
- Limits of Alternative Line-Focus Methods

A focal spot, shaped as a narrow stripe ("line focus") of approx. 10 mm in length by 50 μm in width, induces the formation of a plasma column above the irradiated target. The plasma column is functional to the generation of an Extreme Ultra-Violet (EUV, i.e. $\lambda = 10 - 50$ nm) or soft X-ray coherent radiation ($\lambda = 1 - 10$ nm) by means of amplified spontaneous emission (ASE) in single-pass amplification along the column's length. Besides cylindrical lenses, parabolic and spherical reflectors have proved more efficient in generating a line focus by means of geometrical aberrations, i.e. either utilizing (i) astigmatism or (ii) spherical aberration.

Astigmatism is observed when the tangential and sagittal foci do not coincide. A tilt of the focusing mirror, centrally illuminated, leads to astigmatism (Fig. 3.1.a), with a change in the tangential focus as given by:

$$f_T = (R/2)\cos\vartheta \quad (3.1.0.1)$$

and a change in the sagittal focus as given by:

$$f_S = (R/2)/\cos\vartheta \quad (3.1.0.2)$$

where R is the radius of curvature of the mirror and ϑ is the tilt angle. The focal spots appear stretched over a certain length as a thin stripe of light.

On the other hand, *spherical aberration* is the variation of focus location with illumination aperture. A spherical mirror can thus induce a line focus when illuminated with a pencil of light

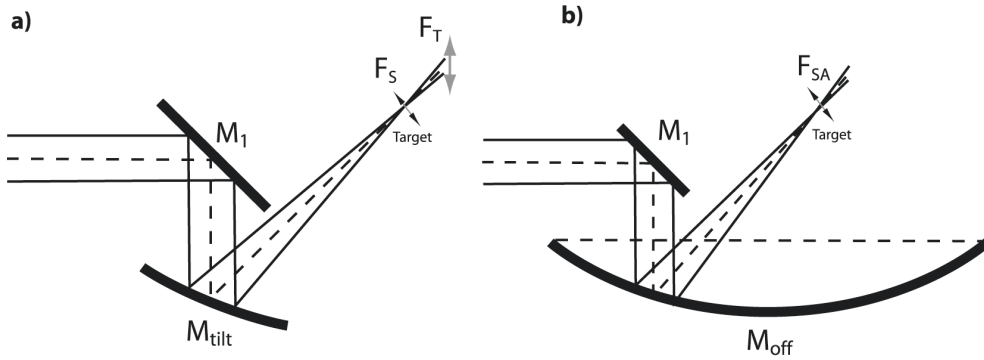


Fig. 3.1: Schematic of the focusing setup simulated for the case of 45 deg. GRIP angle. A) Astigmatic line focus by reflector tilting of 22.5 degrees, with tangential (black, length parallel to the page) and sagittal (red, length normal to the page) foci with the target at the latter position; B) Off-axis illumination of the non-tilted spherical reflector to exploit its spherical aberration.

on an off-axis region (Fig. 3.1.b). In the particular case of illumination beam parallel to the mirror-symmetry axis, the line focus is produced along such optical axis itself.

The two frames of reference to generate a line focus, i.e. (i) that of exploiting astigmatism and (ii) that of using spherical aberration, are equivalent and produce the same irradiance distribution on the target. This is easily understood if a reference system transformation is applied. Fig. 3.2 permits to visualize the equivalence between astigmatic focusing and spherical-aberration focusing. The former geometry implies tilting a small reflector (thick traces in Fig. 3.2) with respect to the illuminating chief ray, until the required target grazing-incidence angle (in the following just "GRIP angle") is attained.

This geometry leads to a sagittal line-focus on the target located at the distance given by eq. 3.1.0.2. To keep the target fixed at the center of Fig. 3.2 the tilted mirror is shifted backwards for decreasing GRIP angle ("i") according to the distance of the sagittal focus. If, on the other hand, the tilted mirror is regarded as a segment of a large reflector (thin traces in Fig. 3.2) having its optical axis (dash-point line) parallel to the chief ray, the line-focus can be explained as due to spherical aberration in a large-aperture-illumination.

In Fig. 3.2, such a line-focus lies along the optical axis, and in order to keep the target fixed in space the spherical collectors are shifted accordingly. Hence, one notices that the traces of the large reflectors overlay with the profiles of the tilted reflectors, showing that the tilt-alignment of a small reflector adjusts its surface to match the virtual extension of the large sphere with optical axis aligned with the target.

In general, it is important to generate a homogeneous plasma column, which may be done by optimizing the line-focus irradiance distribution. The latter is a function of GRIP angle. In X-ray laser science exploiting ASE, there is an interest to generate line foci at low GRIP angle to maximize the output. This is accomplished exploiting internal refraction along the plasma column [155], and thus exploiting almost the full amplification length. On the other hand, a large GRIP angle is beneficial for scaling-down the output wavelength. In fact, due to the $\sin^2 \vartheta_{GRIP}$ dependence of the optical penetration depth into a plasma [166], a large ϑ_{GRIP} permits depositing the energy deeper into the plasma, at higher electron densities, which is required for soft X-ray lasing. Hence a first issue to address here is the trade-off of the GRIP angle versus amplification-length.

Furthermore, the use of mirrors has shown advantages in terms of intensity throughput, wavefront distortion, and maximum power limitation with respect to cylindrical lenses. A parabolic mirror is practical in an experimental setup for alignment reasons. Our investigations confirmed that a parabolic mirror produces systematically a wider line focus than that from a spherical mirror. A wider line focus can make easier the overlapping of pre-pulses to the main pulse. On the other hand, spherical mirrors may produce significantly hotter and denser plasma conditions at comparable drive beam energy by means of tighter focusing. Therefore, in the rest of this paper we will restrict the discussion on the use of spherical reflectors, which are the only ones that can be operated in both focusing approaches introduced above (paraboloids have no spherical aberration).

Aim of this study was to investigate the parameter-dependent characteristics of the line focus obtained with a spherical reflector, and relate them to the laser plasma column for ASE. More specifically, the study considered the angle of incidence (GRIP), the profile of the driver beam, and the beam diameter. We will show results obtained with an in-house code, and validate the computational results with experimental data.

3.1.1 Parametric Study

Two different focusing approaches were simulated as shown in Fig. 3.1. In the astigmatic line focus ("A"), the reflector was a spherical mirror that was tilted to the incoming laser beam (Fig. 3.1.a). The tilt angle was half the GRIP angle on the target. The position of the target was chosen in order to minimize the width of the sagittal focus in agreement with eq. 2. The orientation of the sagittal focus lies perpendicular to the plane of the page. The line-focusing using spherical aberration ("B") was simulated with the same spherical reflector radius of curvature (ROC) as in "A", i.e. $ROC = 1219.2$ mm, but non-tilted and whose optical axis was coincident with the target orientation (Fig. 3.1.b). The reflector was illuminated parallel to the optical axis at off-axis distance corresponding to specific GRIP angles on the target. Experimental data were acquired using a modified target mount to allocate a CCD detector.

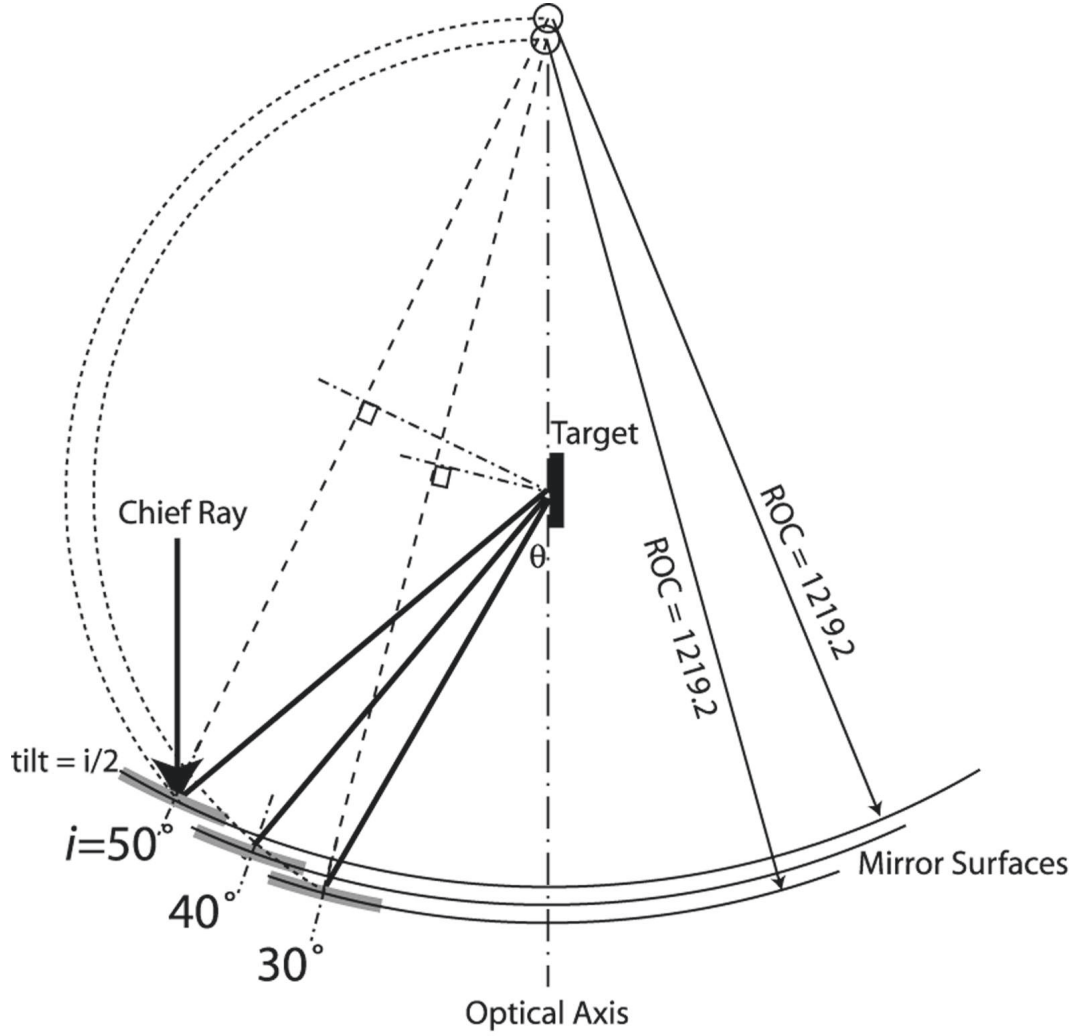


Fig. 3.2: Geometry of the line focus generation with a spherical reflector oriented for three grazing incidence angles on the target. In the sketch the target position is kept fixed and the reflector is moved correspondingly. The radius of curvature (ROC) is taken as in the Bern X-ray laser facility. The sketch visualizes the equivalence between the two discussed line focusing techniques.

The laser was delivered at 45 deg. and attenuated using the transmission of a highly reflecting plane mirror followed by neutral density filters. The measurements are combined from several images taken at different camera positions along the line focus, as the detector width was smaller than the length of the focal line.

The pump TW pulse was delivered with a 45 deg. turning mirror toward a focusing spherical reflector whose radius of curvature was 1219.2 mm, i.e. a focal length of $f = 609.6$ mm (24 inches). The driver laser was simulated as a super-Gaussian beam, i.e. characterized by a radial intensity profile given by the following relation:

$$I(r) = I_o \exp(-2(r/r_o)^{2N}) \quad (3.1.1.1)$$

where I_o is the peak intensity, r_o is the beam radius, and N is the super-Gaussian exponent, that for $N = 1$ provides a TEM00 gaussian profile. As given in Tab. I the default value was $N = 6$ (flat-top profile).

Fig. 3.3 summarizes the parametric study for a line focus produced exploiting astigmatism ("A") and spherical aberration ("B"). The plots consistently show the physical equivalence of the line focus irradiance distributions under the two frames of reference. These line irradiance distributions were generated under different parameter configurations, as explained below, where the area was kept constant at 1J shot energy. In Fig. 3.3.top one can observe the effect of GRIP angle on the irradiance distribution and line-focus length. The profiles become shallower with increasing GRIP angle. The fact that the energy is stretched over a longer line length at increasing GRIP angle explains the reduction of peak irradiance (signal integrals are constant). Fig. 3.3.mid shows the influence of the driver beam profile indicated as exponent of the super-Gaussian profile. One notices that the higher the super-Gaussian order, the steeper is the profile. Finally, Fig. 3.3.bottom shows the effect of the beam width. It is evident that the line focus length scales up with the beam diameter. Narrow beams lead to higher irradiation peaks as a consequence of the concentration of the delivered energy over shorter line focus lengths. This effect is indeed complementary to that of the GRIP angle.

It is noteworthy to compare the obtained line focus lengths, computed under these configurations, with existing analytical models. Ref. [324] has derived a trigonometric expression for the line focus length (L) as a function of GRIP angle (ϑ) and beam width (d), with the reflector focal length (f) as parameter, which is as follows:

$$L = \frac{f}{\sqrt{1 - (\sin \vartheta + \frac{d}{4f})^2}} - \frac{f}{\sqrt{1 - (\sin \vartheta - \frac{d}{4f})^2}} \quad (3.1.1.2)$$

The predicted line focus length is consistent with what is obtained with our raytracing computations. Fig. 3.5 shows such a comparison between raytracing and analytical model. Fig. 3.5.a shows the dependence on the GRIP angle. The raytracing code provides consistent results among the two focusing approaches, showing data point overlapping between tilt (astigmatism) and off-axis (spherical aberration). Analytical and numerical results are slightly mismatched because the analytical expression from the analytical model of ref. [324] should refer to the full line length on the target surface, whereas the raytracing results provide the FWHM line focus length. Furthermore, the analytical expression assumes a fully flat-top beam whereas the ray-tracing computations used a super-Gaussian profile. Fig. 3.5.b shows the dependence on the beam width.

The irradiance distributions in Fig. 3.3 show that by changing one parameter multiple profile characteristics are modified. For instance, an increase in GRIP angle alters the leading and the trailing edges, the overall length, etc.. For small beam diameters the profile structure is not

Parameter	Default Value	Range of Study
Angle of incidence	45°	25 to 55°
Mirror shape	spherical	fixed
Beam diameter	80mm	20 to 100mm
Mirror radius	1219.2	fixed
Beam profile	Super-Gaussian, N=6	N=1,2,10

Tab. 3.1: Parameter settings

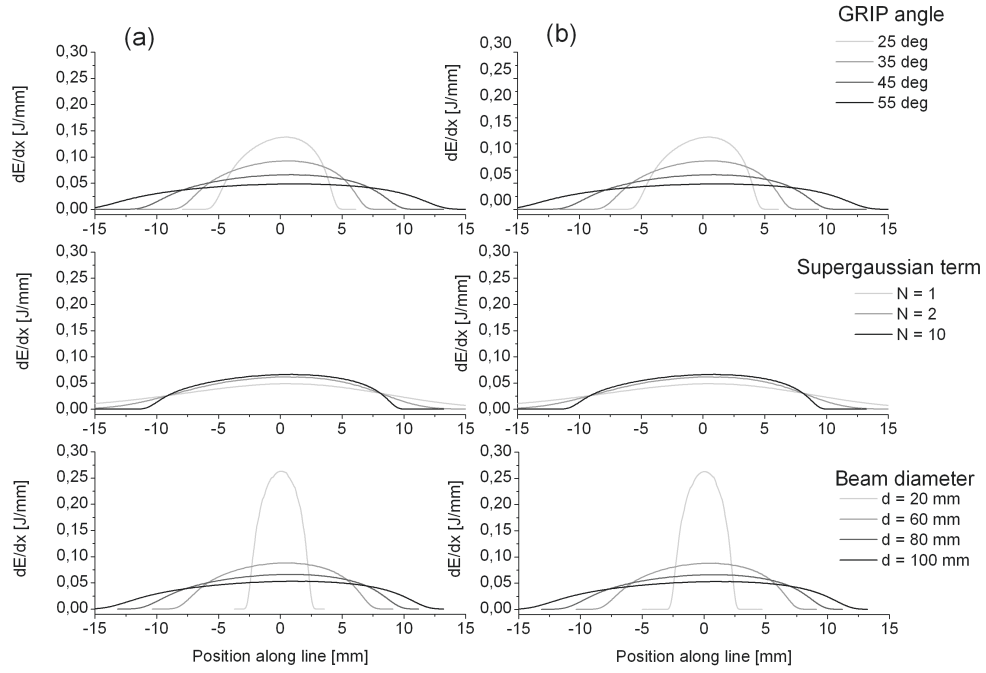


Fig. 3.3: Calculated line focus profiles produced by means of (A) sagittal focus with tilt-induced astigmatism and (B) using the off-axis spherical aberration, as a function of GRIP angle (top), driver beam spatial profile (mid), driver beam diameter (bottom).

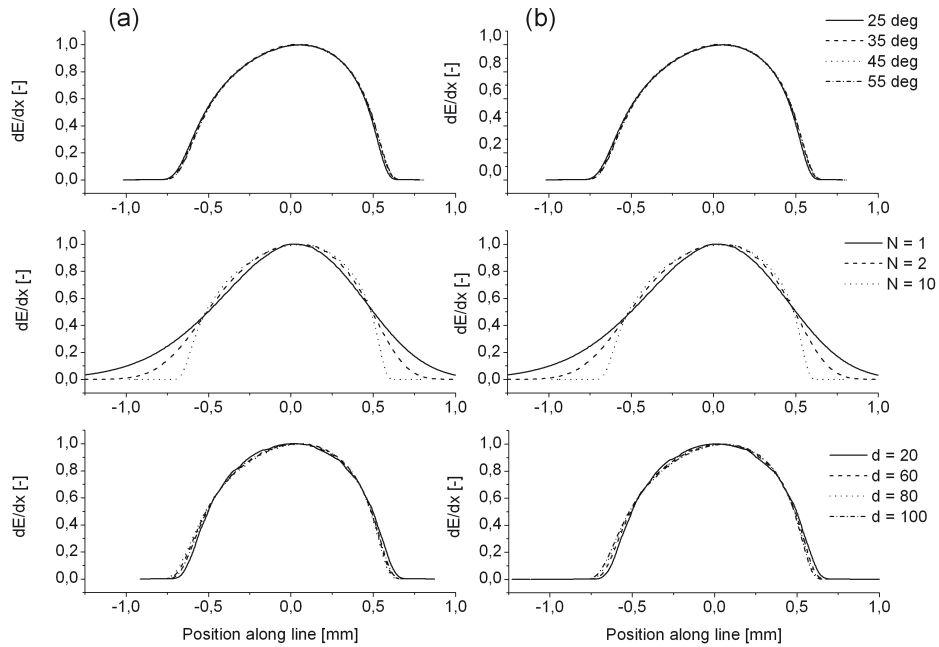


Fig. 3.4: Width- and peak-normalized line focus irradiance profiles produced by means of sagittal focus with tilting-induced astigmatism (A) and using the off-axis spherical aberration (B), as a function of GRIP angle (top), beam profile (mid), beam diameter (bottom).

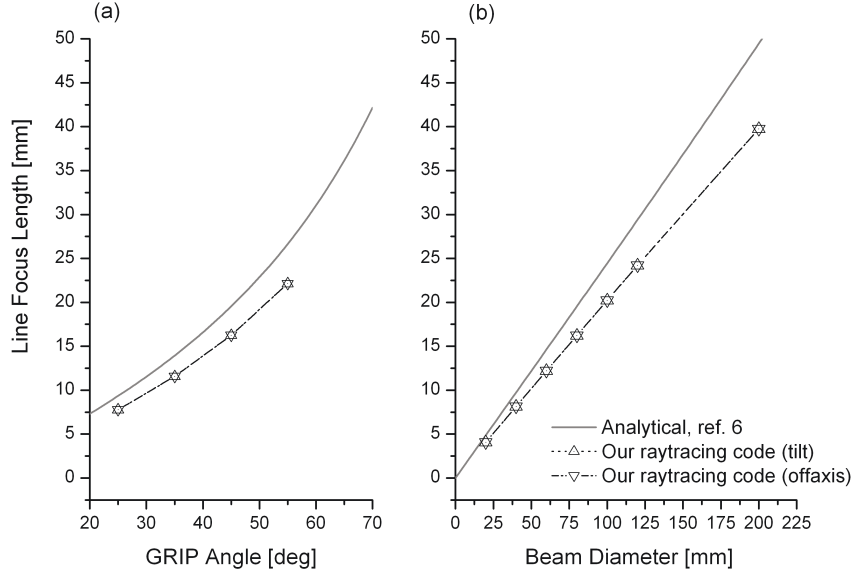


Fig. 3.5: Line focus length as a function of incidence angle at 80 mm diameter (A) and as a function of beam diameter for 45 degrees incidence (B), determined with various computational methods discussed in the text.

changed but only scaled, except when changing the beam profile. With increasing beam diameter the line-focus profile becomes increasingly asymmetric. To highlight this aspect, FWHM- and height-normalized distributions were computed from the data shown in Fig. 3.3, and shown in Fig. 3.4.

In these plots the FWHM is always equal to 1 (i.e. from -0.5 to 0.5) and the irradiance values of each curve range from background level up to 1.0. In physical terms, this corresponds to changing pairs of parameters, e.g. GRIP angle and beam width, such that the line-focus length remains constant at various GRIP angles. One notices, that the profiles for the case of the variation of the GRIP angle (Fig. 3.4.top) and the variation of beam diameter (Fig. 3.4.bottom) change is insignificant. This indicates that the irradiance distribution structure is not modified by these parameters, only the distributions are re-scaled to different extents. The change of the beam Gaussian profiles is, on the other hand, causing a significant re-modulation in distribution bandwidth, especially noticeable at the edges (Fig. 3.4.middle). This suggests that one can consistently optimize the line-focus irradiance profiles by operating on angle and beam width, and preferably homogenizing the driver beam profile (e.g super-Gaussian $N > 6$).

3.1.2 Amplification Length

The parameter-dependent optimization of the line-focus irradiance distributions affects the peak irradiance versus the amplification length. The optimum is obviously dictated by the threshold for lasing, i.e. by the minimum plasma temperature and density required. It is clearly necessary to keep the line-focus irradiance higher than such threshold value, but also not much higher to prevent loss of inversion due to further ionization or collisional de-excitation in a over-hot/dense plasma. Any excess beam energy, with respect to the threshold requirements, may be instead used for extending the line-focus length. Increasing the line-focus length as much as possible is advantageous to increase the amplification-length (as long as the pump irradiance is above the threshold value). The threshold value can be inferred from the relation between driver-beam irradiance and the optimum plasma temperature/density for EUV lasing.

The line-focus length can be increased, as shown above, with a larger GRIP angle until the decrease in peak irradiance matches the lasing threshold. The optimization of the GRIP angle extent should thus produce increasingly stronger X-ray laser emission. For further increase of the GRIP angle the peak irradiance along the line focus drops beneath the threshold value.

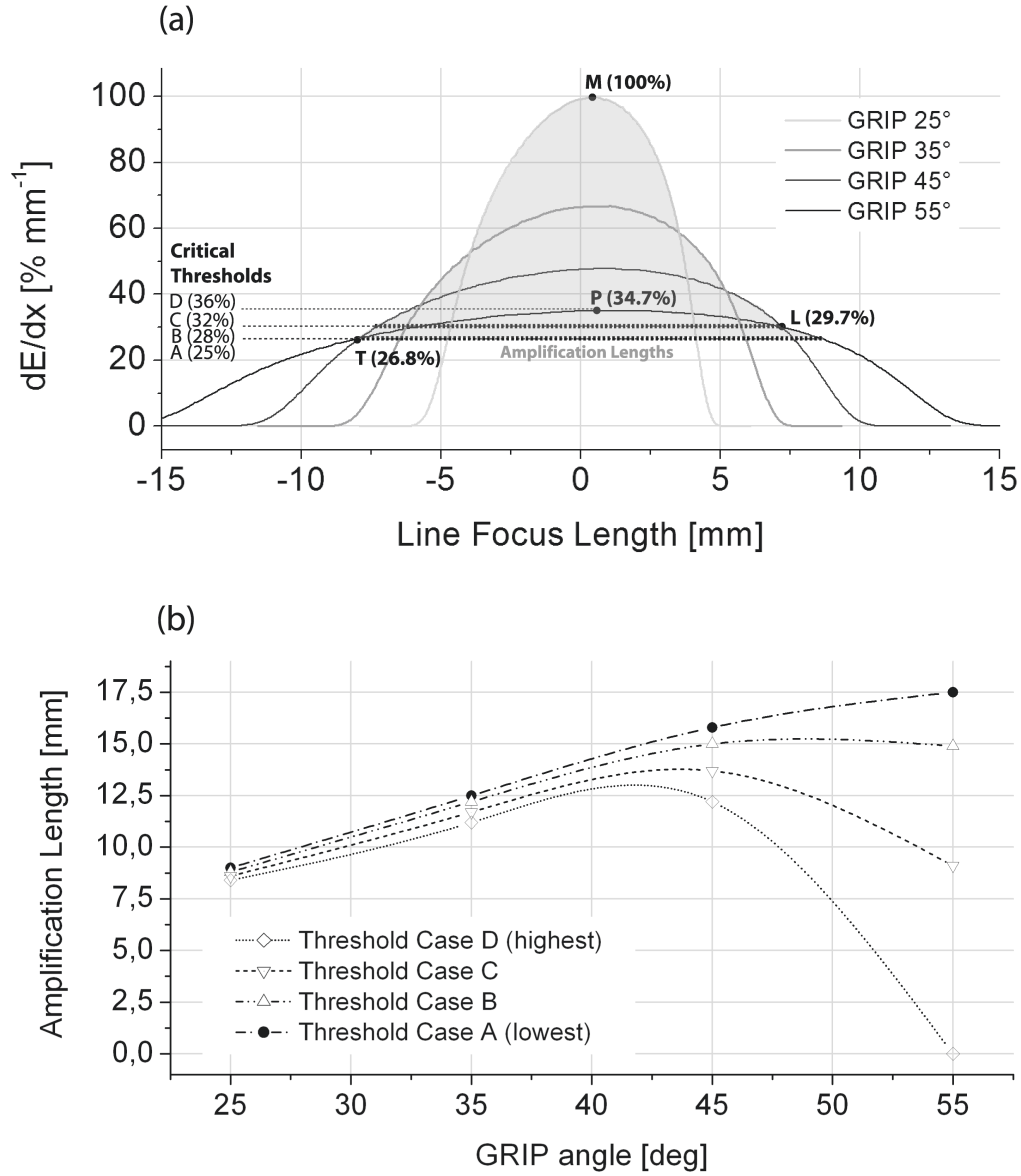


Fig. 3.6: (a) Normalized line-focus irradiance distributions as a function of GRIP angle from Fig. 3.a. One can define four important cases for a lasing threshold, as explained in the text (cases are labeled as A, B, C, D). (b) Depending on in-which of these ranges is the lasing threshold, the amplification-length will have a maximum or not, as a function of GRIP angle.

Analyzing the structure of the line-focus irradiance distributions shown in Fig. 3.3.a, one notices that two GRIP curves cross each other at specific points on their trailing and leading edges. The leading-edge cross point (let's call it "L") is higher than the trailing-edge one (let's call it "T") , as shown in Fig. 3.6.a. This is due to the skewness of the profiles. Considering that the skewness is gradually mitigated at increasing GRIP, also the height gap between the two cross points is consistently reduced at large GRIP angle.

Let's consider, as depicted in Fig. 3.6.a, a horizontal line that delimits the irradiance threshold for X-ray lasing. The amplification-length is the segment joining the GRIP curve trailing and leading edges along the threshold line (i.e. the irradiance above the threshold contributes to ASE gain). If such a threshold is very low all GRIP curves shown are mainly in the lasing range. If the threshold is raised the shallowest curve will gradually get below the cut-off value. More specifically, one can define four important cases depending on the height of the threshold, namely:

Case A) The threshold is at the point T;

Case B) The threshold is between point T and point L;

Case C) The threshold is between point L and the curve peak value (P);

Case D) The threshold is at or above P.

If the lasing threshold is consistent with case 'A', then the irradiance is still above lasing threshold even at the largest possible GRIP angle. As shown in Fig. 3.6.b the corresponding amplification-length has no topping value. If the lasing threshold matches with case 'B', although the peak of the $\vartheta = 55^\circ$ is above the threshold-limit, the amplification length reaches a plateau value (Fig. 3.6.b).

If the threshold is raised to match with case 'C' , the amplification length increases with increasing GRIP angle up to a optimum value. For larger GRIP angles the amplification length is reduced (Fig. 3.6.b). Finally, if the threshold-limit matches with case 'D' the amplification-length will increase with comparable rate as in the cases above (Fig. 3.6.b) but beyond a certain maximum value the drop of amplification length is more pronounced.

The model explained here above is in consistent agreement with experimental data we have published previously [117]. In that work we have indeed observed an analogous behavior to what shown in Fig. 3.6.b for the case of Pd target irradiated with 2 J and 5 J. The irradiance distribution profiles obtained at 2 J and large GRIP angle were possibly closer to the lasing threshold-limit, which is confirmed by an optimum value at $\vartheta_{GRIP} = 35^\circ$. In the case at 5 J, all studied GRIP profiles were largely above the lasing threshold, which did not provide any specific optimum bound.

For the cases analyzed here, i.e. with the set of curves at GRIP angles of 25, 35, 45, and 55 degrees we have used the $\vartheta_{GRIP} = 25^\circ$ peak height (point M) as normalization value and computed the other curves accordingly in a percent scale (Fig. 3.6.a). In this respect, the T and the L points are identified as crossing points among the $\vartheta_{GRIP} = 45^\circ$ and the $\vartheta_{GRIP} = 55^\circ$ curves at ordinate values as follows: T is at 26.8%, L is at 29.7%, P is at 34.7%. The discussion is here based on the arbitrarily chosen four GRIP curves but it can be generalized considering any set of N GRIP-distributions and the crossing between any arbitrarily spaced N-th and (N-1)-th GRIP curves.

3.1.3 GRIP Technique by Tilting the Target

GRIP angle adjustment has been also proposed by tilting the target instead of moving the focusing optics [332]. The characteristics of the line-focus under these focusing conditions are therefore investigated. Although such an inclination of the target correlates with the GRIP angle, it should be noticed that the beam profile typically evolves along the direction of propagation.

At the sagittal focus a line-focus is 'naturally' generated. The latter evolves in the sagittal and tangential planes, such that the aspect ratio is inverted and a 90° rotated line-spot is produced at the tangential focus. By tilting the sample additional aberration and coma are induced. The spot diagrams obtained for the four GRIP angles discussed above are shown in Fig. 3.7 with a tilt angle of the target of 2° with respect to the nominal value.

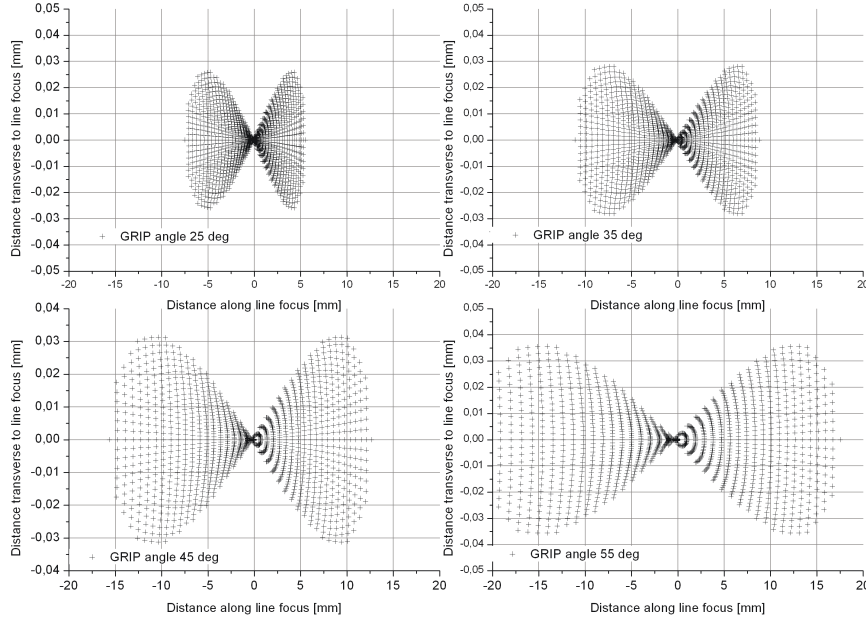


Fig. 3.7: (a) Spot diagram obtained by ray-tracing with an additional target tilt of 2° to obtain the indicated GRIP angles.

The spot diagrams of Fig. 3.7 are indeed gauge-invariant and when plotted non-dimensionally they look identical. The most distinguishing feature is the bi-lobed ('propeller-like') shape, which indicates a variation of focal irradiance across the spot. The trailing and leading edges are thus characterized by lower irradiance than the central part. This effect is exacerbated at large GRIP angles, with the conclusion that at large target tilt the plasma column is characterized by increased longitudinal gradients in temperature and density. In ref. [Wang], this effects are not observed for the specific experimental setup chosen. In fact, the target was tilted over a relatively wide angular range of 12° , while the incidence angle on the focusing mirror was kept constant at 7° . An adjustable cylindrical lens before the compressor was used to keep the length of the line focus constant and to avoid the formation of a bi-lobed line-focus. Raytracing validation.

Having so far compared computational results, e.g. of analytical versus raytracing simulations, we turn now to a comparison with the experimental results (Fig. 3.7). We show the specific case of 45 degrees angle of incidence and a beam of 60 mm (FWHM) in diameter, which is what our experimental setup permitted to acquire. One notes that our ray-tracing code captures the profile quite faithfully throughout. The measurement was unfortunately affected by high frequency noise and lower frequency fluctuations that are smoothed-out computationally. The predictive value of our computation is however validated, and with it the extent of implications discussed for optimized line focusing in Soft X-ray Amplified Spontaneous Emission plasma lasing.

3.1.4 Summary on Line Focusing

Line-focus irradiation is important for the generation of a plasma column to sustain amplified spontaneous emission (ASE) for laboratory-scale soft X-ray lasers. The adjustment of the drive beam parameters and irradiation scheme is important to obtain saturated output, even at short wavelength which demands conflicting conditions in terms of GRIP angle. In this work we performed a parametric study of line focus generation using in-house written ray-tracing software, and comparing the obtained results to experimental measurement of the line focus. For the calculations, two beam focusing approaches were compared, i.e. (i) exploiting astigmatism

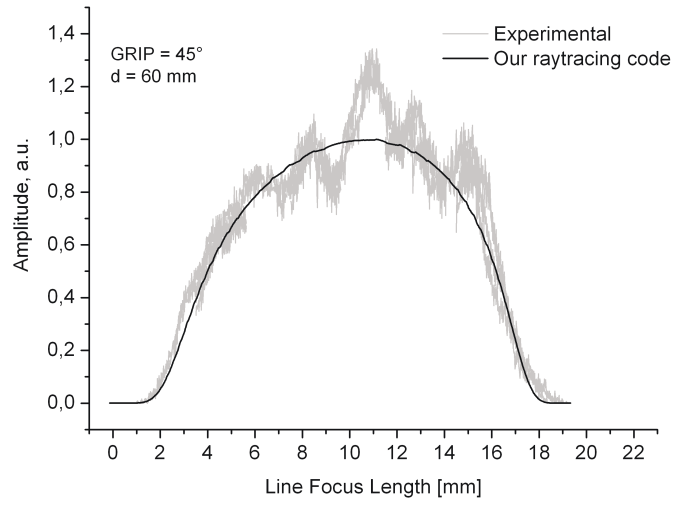


Fig. 3.8: Comparison of experimental and computational results. The experimental curve was obtained with a GRIP angle of 45 degrees, a beam diameter of 60 mm (FWHM), and a super-Gaussian profile of order $N = 6$.

of a tilted spherical reflector or (ii) using spherical aberration from off-axis spherical mirror illumination. In both cases the line-focus length was shown to increase with larger grazing incidence angle, in agreement with literature data. Computed irradiance distributions were shown to have a close match with experimental data of line-irradiance profiles. We demonstrated that the amplification-length is optimized at the largest GRIP angle for which the irradiance is still above the lasing threshold. Therefore, a "*sledgehammer approach*", i.e. high-peak irradiation at short line foci, may lead to non-optimum X-ray lasing. The delivering of the drive pulses at GRIP angle induced by tilting the target, instead of the focusing setup, was shown to deteriorate the line focus characteristics.

3.2 Pump-Pulse Shaping

Unpublished. Main themes here:

- *Effects of Pump Pulse Shape*
- *Pulse Profile*
- *Pulse Fluence vs. Power*

Since for laser-produced plasmas, gas targets have several advantages over solid targets, such as the less steep density gradients, lack of debris, high repetition rate, and long unbroken operation, XUV lasing in Ne-like Ar^{+8} target (as a model for gas targets) was investigated in this part of the research. Here, the effect of pump-pulse shape on the XUV collisionally excited laser-produced Ne-like Ar^{+8} plasma operating at the wavelength $\lambda = 46.9$ nm in the $2p^5 3p^1(J=0) \rightarrow 2p^5 3s^1(J=1)$ laser transition was investigated.

To begin with, the gain calculation due to collisional-pumping of XUV lasing in the laser-produced plasma was investigated by considering a three-level model, as shown in Fig. 3.9.

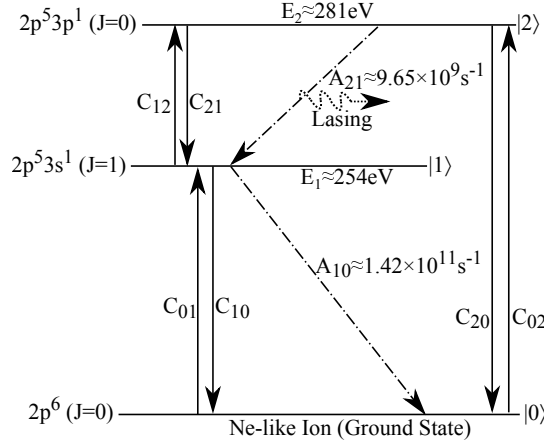


Fig. 3.9: Grotrian scheme and the transitions for the lasing of the Ne-like Ar^{+8} . The energy levels schematically are composed of the upper $|2\rangle$ and lower $|1\rangle$ lasing levels and the ground $|0\rangle$ level.

The level populations of Ne-like Ar^{+8} are computed by solving rate equations of a three-level laser model. Due to the selection rule ($\Delta J = 0, \pm 1$ and $J=0 \rightarrow 0$) the transition from lower level ($J=0$) to upper level ($J=0$) is only achieved by the electron collisional excitation (monopole), as shown in Fig. 3.9.

If n_2 and n_1 are the upper and lower laser state populations and σ_{stim} is the cross section for the stimulated emission, the small signal gain is found as follows:

$$g_0 = n_2 \sigma_{stim} F \quad (3.2.0.1)$$

where F is the population inversion factor, defined as follows:

$$F = 1 - \left(\frac{\gamma_2}{\gamma_1} \right) \frac{n_1}{n_2} \quad (3.2.0.2)$$

where γ_i, γ_j are the degeneracies of the i -th, j -th levels.

The upper and lower laser state populations were calculated as follows:

$$\begin{aligned} n_1 &= \frac{(C_{21}n_e + C_{20}n_e + A_{21})(C_{01}n_en_0) + (A_{21} + C_{21}n_e)(C_{02}n_en_0)}{(C_{21}n_e + C_{20}n_e + A_{21})(C_{10}n_e + C_{12}n_e + A_{10}) - (A_{21} + C_{21}n_e)(C_{12}n_e)}, \\ n_2 &= \frac{(C_{12}n_e)(C_{01}n_en_0) + (C_{10}n_e + C_{12}n_e + A_{10})(C_{02}n_en_0)}{(C_{21}n_e + C_{20}n_e + A_{21})(C_{10}n_e + C_{12}n_e + A_{10}) - (A_{21} + C_{21}n_e)(C_{12}n_e)}. \end{aligned} \quad (3.2.0.3)$$

3.2.1 Calculation with Gaussian vs. Flat-top Pulse

The XUV gain, in the cases where Gaussian and super-Gaussian pump-pulses are used to irradiate a neutral Ar^0 gas target, is investigated. A functional of a Gaussian and a super-Gaussian (flat-top) pulse is as follows:

$$I(t) = I_0 \exp \left(-\frac{1}{2} \left| \frac{t - t_0}{c} \right|^n \right) \quad (3.2.1.1)$$

where $n = 2$ for a Gaussian pulse and $n > 2$ for a super Gaussian pulse, I_0 is the peak of intensity and t_0 is the position of the center of the peak. The parameter c is related to the full width at half maximum (FWHM) of the peak according to $\text{FWHM} = 2\sqrt{2 \ln 2} \, c \approx 2.3c$.

3.2.2 Calculation of Effect of Pump-pulse Clipping on XUV Lasing

The XUV gain of a clipped Gaussian pump-pulse irradiating an Ar^0 target is investigated in Fig. 3.10a with three pump-pulses that have identical pump-laser intensity of $I_L = 10^{12} \text{ W/cm}^2$. In the case 1, the pulse is clipped in a way that the peak intensity at $t = 0$ reaches the target. In case 2 the pulse is clipped in a way that the peak intensity at $t = 5$ ps reaches the target. In the case 3, the peak intensity at $t = 20$ ps reaches the target. Fig. 3.10b shows the calculated gain coefficients for case 1, 2, and 3. Considering case 3 as a reference, it shows that the clipping cannot improve the gain for the short pulse 10 ps at the same pump-laser intensity. Comparison of Fig. 3.10a and Fig. 3.10b shows that for peaks of identical intensity but different fluences, the pulse with the highest fluence has highest XUV gain.

Fig. 3.10c shows three pulses that have a same fluence $j_L \approx 10 \text{ J/cm}^2$ and pulse duration of 10 ps. In the case 1, the pulse is clipped in a way that peak intensity at $t = 0$ reaches the target. In the case 2, the pulse is clipped in a way that peak intensity at $t = 5$ ps reaches the target. In the case 3, the peak intensity at $t = 20$ ps reaches the target. Fig. 3.10d shows the calculated gain coefficients for case 1, 2, and 3. Considering case 3 as a reference, it shows that shaping improves the gain by as much as 60% at the same fluence. Comparison of Fig. 3.10c and Fig. 3.10d shows that if the fluence is identical but the peak intensities are different, the pulse that has the highest peak intensity has highest XUV gain.

3.2.3 Calculation of Effect of Pump-pulse Rise-time on XUV lasing

The XUV gain is produced by irradiating an Ar^0 gas target with Gaussian or flat-top pump-pulses. Thus, the influence of pulse rise time on the XUV gain medium is investigated. The rise time is considered to be the time taken for a pulse to rise from 10% peak intensity to 90% of its peak value. Indeed, the rise time in super Gaussian pulses is faster than a Gaussian pulse as shown in Fig. 3.11.

Fig. 3.11a shows a Gaussian pulse ($n = 2$) and 5th ($n = 5$) and 10th ($n = 10$) order of Super-Gaussian pulses with the same laser intensity 10^{12} W/cm^2 . For $\text{FWHM} = 10$ ps Fig. 3.11b shows that at the constant laser intensity the effect of rise time on the XUV gain is as low as 3% (considering the Gaussian pulse as a reference).

Fig. 3.11c shows Gaussian pulse and 5th and 10th order of Super-Gaussian pulses with the same energy fluence $j_L \approx 10 \text{ J/cm}^2$. Fig. 3.11d shows that at a constant fluence for Super-Gaussian pulses the gain increases to as high as 40% (considering the TEM00 Gaussian pulse as

a reference). Comparison of Fig. 3.11 shows that XUV gain medium depends on instantaneous intensity of the pump-pulse instead of its average intensity.

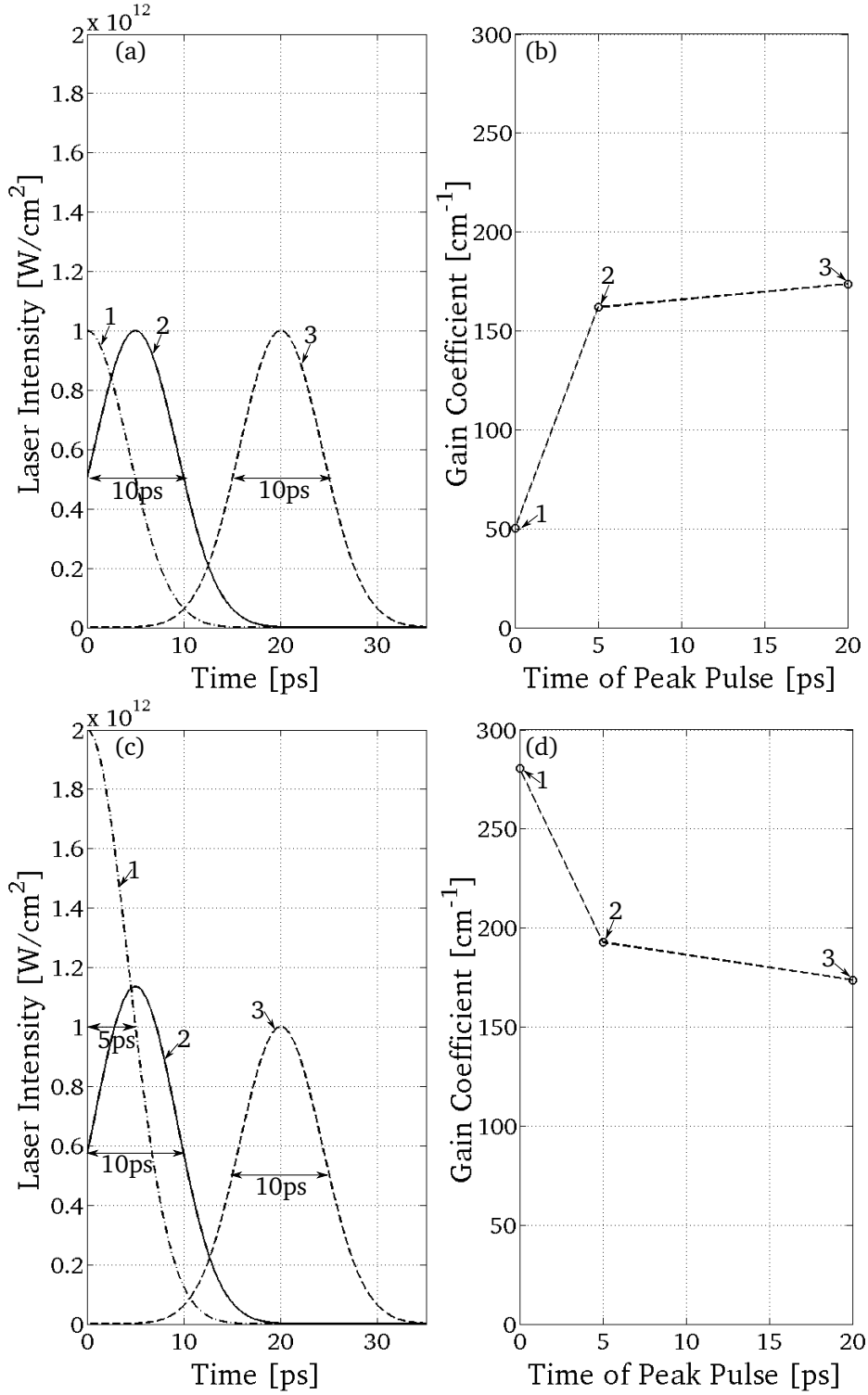


Fig. 3.10: (a) Pulses with a constant pump-laser intensity and (b) effect of pulse delays at a constant pump-laser intensity on the gain coefficients. (c) Pulses with a constant fluence and (d) effect of pulse delays at a constant fluence on the gain coefficients.

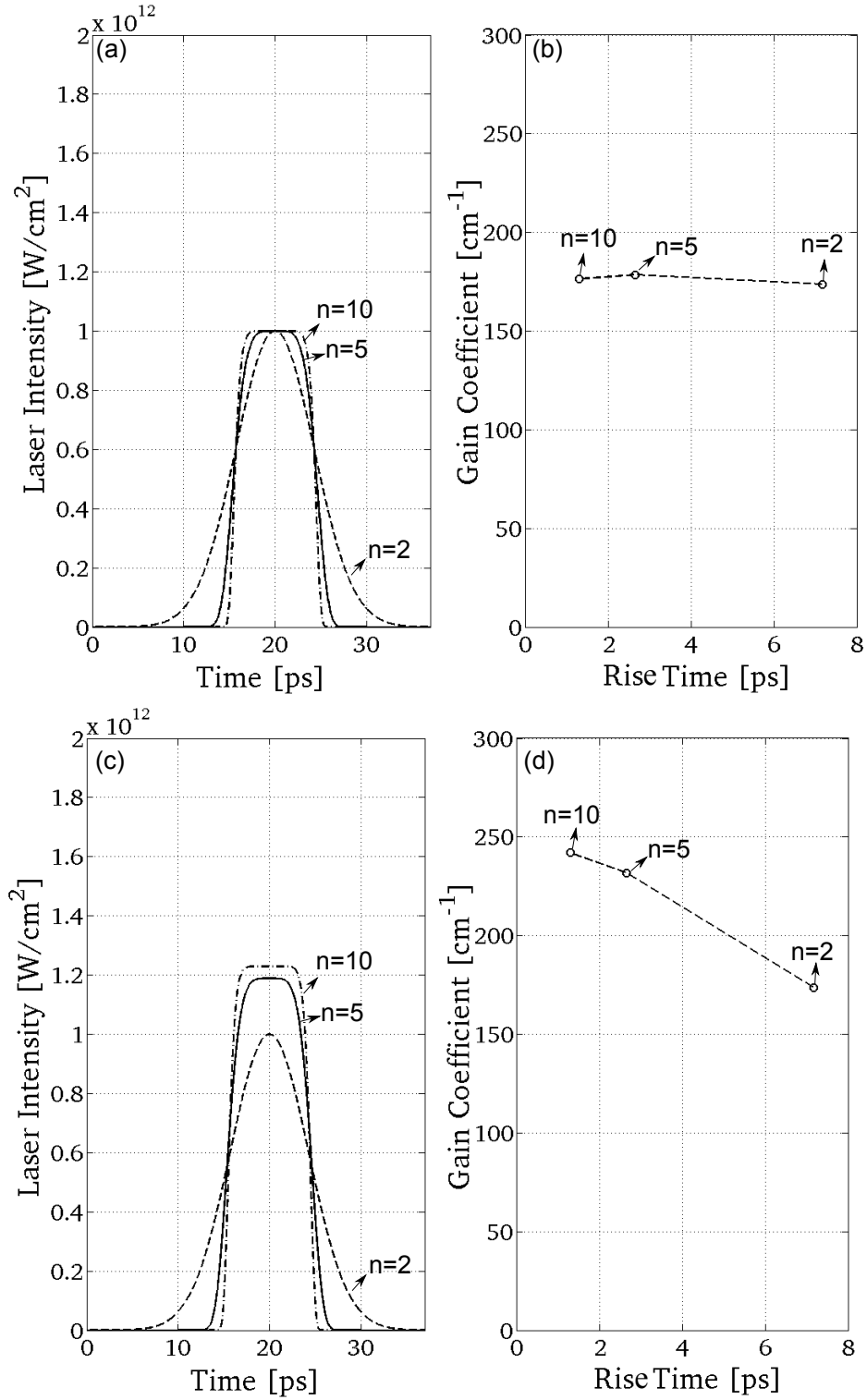


Fig. 3.11: (a) Gaussian pulse ($n = 2$) and 5th ($n = 5$) and 10th ($n = 10$) order of Super-Gaussian pulses with the same pump-laser intensity and (b) effect of these pulses on the XUV gain coefficient of the Ne-like Ar^{+8} . (c) Gaussian pulse ($n = 2$) and 5th ($n = 5$) and 10th ($n = 10$) order of Super-Gaussian pulses with the same fluence and (d) effect of these pulses on the XUV gain coefficient of the Ne-like Ar^{+8} .

3.2.4 *Summary on Pulse Shaping*

It was found that the pump pulse clipping in time cannot improve the gain in the case where the pump-laser intensity remains at a fixed value. Meanwhile, it is found that shaping in time can improve the gain for the case of a constant fluence.

It is demonstrated that there is negligible XUV gain improvement, 3%, by considering a super-Gaussian pump-laser instead of a classical Gaussian pump-laser at the same intensity. Shaping a Gaussian into a super Gaussian pump-pulse, at a constant fluence, the XUV gain is increased by up to 40%.

If the peak intensity of the pulses are the same and the energy fluences are different, the pulse that has the highest energy fluence produces a plasma with the highest XUV gain. If the fluence of the pulses are the same and the peak intensities are different, the pulse that has the highest peak intensity produces a plasma with the highest XUV gain.

3.3 Pump Pulse Timing

Published in Masoudnia et al. Photonics, 2, 164-183, 2015. Main themes here:

- *Time-scales for Atomic Processes*
- *Time-scales for Energy Deposition*
- *Effect of Pump Pulse Duration & Delay*

A few ways have been proposed to increase the efficiency of laser-irradiated solid targets for plasma-driven X-ray lasing [78]. The main drawback of solid targets is the presence of steep density gradients, which causes the refraction of the pump and signal pulses, limiting the gain. A solution to the strong density gradients we studied was using Hohlraum targets, as discussed in ref. [205].

Alternatively, gas targets have several advantages over solid targets, such as the shallow density gradients, lack of debris, high repetition rate and long unbroken operation [72, 77, 99, 100, 102]. For the first time, the generation of laser radiation with Ar^0 gas at a wavelength of 46.9 nm producing a gain of 0.6 cm^{-1} was observed in a capillary discharge by Rocca *et al.* [248]. In the laser-produced gas targets, the possibility of having a high repetition rate will lead to high average power for soft X-ray lasers.

Tab. 3.2 summarizes the operating conditions used experimentally in the lasing of the Ne-like Ar^{+8} ions at $\lambda = 46.9 \text{ nm}$ in the $2p^5 3p^1(J=0) \rightarrow 2p^5 3s^1(J=1)$ laser transition. In refs. [77, 99, 100, 102, 186], the plasma is produced with a long pulse ($\Delta\tau_{MP} = 450 \text{ ps}$), a combination of a long ($\Delta\tau_{PP} = 600 \text{ ps}$) and a short pulse ($\Delta\tau_{MP} = 6 \text{ ps}$) and double-short pulses ($\Delta\tau_{PP} = \Delta\tau_{MP} = 1.5 \text{ ps}$). Here, "short pulse" means a pulse with a pulse-duration shorter or in the order of the lifetime of the upper level (lasing level). On the other hand, the "long pulse" has a pulse duration longer than the lifetime of the upper level. The lifetime of the upper level, taking into account the radiative decay (without considering collisional processes) in Ne-like Ar^{+8} , is $\approx 100 \text{ ps}$ (Figure 3.9).

Tab. 3.2 shows also the gain due to the collisional excitation calculated by fitting the Linford formula [182] to the experimental data. It shows that the highest gain coefficient is 18.7 cm^{-1} , achieved in the case of plasma driven with double short-pulses [186]. As the population inversion only persists as long as the plasma parameters are close to optimum, then for long pumping, the plasma will destroy the gain, and most of the possible inversions would be lost by spontaneous emission.

Tab. 3.2: Reported experimental operating conditions in the lasing of the Ne-like Ar^{+8} plasma at $\lambda = 46.9$ nm. Legend: $\Delta\tau_{PP}$ is pulse duration of the pre-pulse, $\Delta\tau_{MP}$ is pulse duration of the main pulse, Δt is time delay between two pulses, λ_P is pump laser's wavelength, I_{PP} is pre-pulse-laser intensity, I_{MP} is main-pulse-laser intensity, ρ_0 is initial gas density of Ar^0 , and g is the gain coefficient.

$\Delta\tau_{PP}$ [ps]	$\Delta\tau_{MP}$ [ps]	Δt [ps]	λ_P [nm]	I_{PP} [W/cm ²]	I_{MP} [W/cm ²]	ρ_0 [mg/cm ³]	g [cm ⁻¹]	Ref
-	450	-	1315	-	$5 \cdot 10^{12} - 3 \cdot 10^{13}$	0.15	1.65	[99, 100]
600	6	500–2100	1054	$2 \cdot 10^{11}$	$5 \cdot 10^{13}$	4	11	[77, 101, 102]
1.5	1.5	1200	1054	$7 \cdot 10^{14}$	$4.7 \cdot 10^{15}$	0.166	18.7	[186]

Tab. 3.2 indicates that the time delays between pulses are in the range of 500–2100 ps, which is needed to achieve the optimum ionization level. The wavelength of pump lasers are either 1054 nm or 1315 nm, and the initial Ar^0 mass densities are in the range of 0.15–4 mg/cm³. In refs. [99, 100], a pulse with intensity in the range of $5 \cdot 10^{12} - 3 \cdot 10^{13}$ W/cm² is used to ionize the plasma up to the required ionization stage to produce a lasing plasma. In ref. [99], a pulse with lower intensity of $2 \cdot 10^{11}$ W/cm² produced a pre-plasma, and then, a pulse with higher intensity of $5 \cdot 10^{13}$ W/cm² produces the lasing plasma. In [186], double pico-second pulses with intensity $7 \cdot 10^{14}$ W/cm² and $4.7 \cdot 10^{15}$ W/cm² rapidly produce the pre-plasma and heat it.

3.3.1 Theory

The main computational steps of the approach used in our study are (i) calculation of the ionization time and (ii) transition time and (iii) calculation of the pumping and relaxation time. These are needed to quantify the optimum timing for the pump pulses.

3.3.1.1 Ionization Time

The ionization time as derived from the McWhirter's criterion [217] is: $t[s] = 10^{12}/n_e$ [cm⁻³]. For this calculation, McWhirter [217] considered two processes: (i) collisional ionization; and (ii) radiative recombination. However, Pert [234] pointed out that McWhirter's criterion is overestimated by up to a factor of 10. Here, our analysis for estimating the ionization time includes the following processes: (i) collisional ionization; (ii) three-body; (iii) radiative; and (iv) dielectronic recombination.

The ionization time can be obtained by considering a two-level system, in which transitions take place from one level to the other, and the solution characterized by an initial transient phase, during which an ion in charge state $+Z$ (Ar^{+Z}) will be ionized to the succeeding charge state ($\text{Ar}^{+(Z+1)}$) [217]. Solving the rate equations at the steady state, where $\text{Ar}^{+(Z+1)} \propto \text{Ar}^{+Z}(1 - e^{-tn_e(S_Z + \alpha_{Z+1} + n_e\beta_{Z+1} + D_{Z+1})})$, gives the ionization time between two adjacent states as follows:

$$t_{\text{Ar}^{+Z} \rightarrow \text{Ar}^{+(Z+1)}} [s] = \frac{1}{n_e(S_Z + \alpha_{Z+1} + n_e\beta_{Z+1} + D_{Z+1})} \quad (3.3.1.1)$$

where n_e is expressed in cm⁻³ and the collisional ionization rate S_Z from charge state Z to $Z + 1$ [217] in cm³s⁻¹. The terms α_{Z+1} , β_{Z+1} and D_{Z+1} are, respectively, the radiative, collisional three-body and dielectronic recombination rates applied to the ionic charge level $Z + 1$ in cm³s⁻¹, cm³s⁻¹/cm⁻³ and cm³s⁻¹, respectively. It is noteworthy that Equation (3.3.1.1) gives the ionization time (characteristic time) when $\text{Ar}^{+(Z+1)}$ has $\approx 63\%$ of the Ar^{+Z} population.

3.3.1.2 Plasma Energy Dissipation Time

The characteristic timescale for radiative cooling is of the same order as the time it takes for the plasma to reach thermal equilibrium [131]. The equilibrium time t_{eq} of the plasma is predicted as follows [272]:

$$t_{eq}[s] \approx 3.16 \cdot 10^{-10} \frac{A}{Z^2} \left(\frac{kT_e}{100} \right)^{3/2} \left(\frac{10^{21}}{n_{ion} \log \left[\left(\frac{3}{2\bar{z}^2} \right) \cdot \left(\frac{(kT_e)^3}{\pi e^6 n_e} \right)^{1/2} \right]} \right) \quad (3.3.1.2)$$

where A is the atomic weight of the ions, Z is the atomic number, \bar{z} is the average charge state, kT_e is the electron temperature in eV, n_e is the electron density in cm^{-3} and n_{ion} is the ion density.

3.3.1.3 Atomic Level Transition Times

Due to the selection rules, the transition from ground level ($J = 0$) to the upper level ($J = 0$) is only achieved by the monopole collisional excitation (Figure 3.9).

The level transition times considering a three-level system ($|0\rangle, |1\rangle, |2\rangle$) are obtained as follows:

$$\begin{aligned} \tau_{02}[s] &= \frac{1}{n_e C_{02}} \\ \tau_{01}[s] &= \frac{1}{n_e C_{01}} \\ \tau_{12}[s] &= \frac{1}{n_e C_{12}} \\ \tau_{20}[s] &= \frac{1}{n_e C_{20}} \\ \tau_{10}[s] &= \frac{1}{A_{10} + n_e C_{10}} \\ \tau_{21}[s] &= \frac{1}{A_{21} + n_e C_{21}} \end{aligned} \quad (3.3.1.3)$$

where n_e is in cm^{-3} , A_{ij} in s^{-1} and C_{ij} in $\text{cm}^3 \text{s}^{-1}$. Here, τ_{02} is the transition time from the ground level $|0\rangle$ to the upper level $|2\rangle$, τ_{01} is the transition time from the ground level $|0\rangle$ to the lower level $|1\rangle$, etc. In the transition time from the upper level $|2\rangle$ to the lower level $|1\rangle$ and from the lower level $|1\rangle$ to the ground level $|0\rangle$, the radiative decays (A_{21} and A_{10}) are also allowed. In fact, the τ_{10} and τ_{21} depend on both radiative decay and collisional de-excitation if both are of the same order of magnitude. Otherwise, the τ_{10} and τ_{21} depend only on the largest one, which means a shorter time.

The electron collisional excitation rates (C_{ij}^e , with $j > i$) between (i, j) -levels depend on the electron temperature:

$$C_{ij}^e[\text{cm}^3 \text{s}^{-1}] = 1.6 \cdot 10^{-5} \frac{\langle g_{ij} \rangle}{(kT_e)^{1/2}} \frac{f_{ij}}{\Delta E_{ij}} e^{(-\Delta E_{ij}/kT_e)} \quad (3.3.1.4)$$

where f_{ij} is the oscillator strength, ΔE_{ij} is the excitation energy and $\langle g_{ij} \rangle$ is the Gaunt factor. For calculating the collisional de-excitation rate (C_{ji}^d), considering detailed balancing, one has that:

$$C_{ji}^d[\text{cm}^3 \text{s}^{-1}] = \frac{\gamma_i}{\gamma_j} C_{ij}^e e^{(\Delta E_{ij}/kT_e)} \quad (3.3.1.5)$$

where γ_i and γ_j are the degeneracy of the i th and j th levels, where the degeneracy of each level is $2J + 1$ (statistical weight).

3.3.1.4 Pumping & Relaxation Time

The populations of the Ne-like levels are computed in a three-level model [52, 227] as in Fig. 3.9. Oliva *et al.* have shown [227] that a three-level model has good agreement with experimental data. In their model, they took into account only Doppler broadening, while collisional broadening should also be treated. Here, in our calculation, we take into account both Doppler broadening and collisional broadening. If n_2 and n_1 are the upper and lower laser level populations (Figure 3.9) and σ_{stim} is the cross-section for the stimulated emission, the small signal gain at $\lambda = \lambda_0$ (λ_0 is 46.9 nm for a Ne-like Ar^{+8} laser) was found as in Eq. 3.2.0.1.

We recall that F is the population inversion factor, defined in Eq. 3.2.0.2. Here, we compute the value of the gain at the center of line profile $\lambda = \lambda_0$. The cross-section σ_{stim} is given by:

$$\sigma_{stim} = \frac{\pi r_0 f_{12} \lambda}{\Delta \lambda_x} \frac{\gamma_1}{\gamma_2} \varphi_x(\lambda) \quad (3.3.1.6)$$

where $\Delta \lambda_x$ is the spectral line width and $\varphi_x(\lambda)$ is the normalized line shape profile. Line shape $\varphi_x(\lambda)$ is given by the convolution integral,

$$\varphi_x(\lambda) = \int_{-\infty}^{+\infty} \varphi_G(\lambda) \varphi_L(\lambda_0 - \lambda) d\lambda. \quad (3.3.1.7)$$

Assuming that Doppler broadening (φ_G) and collisional broadening (φ_L) act on a line profile simultaneously; then, the resulting measured line shape is a Voigt profile. In a plasma, Doppler broadening due to the thermal motion of ions produces a Gaussian-shaped line function, where $\Delta \lambda_D = \frac{\sqrt{2kT_{ion}/M}}{c} \lambda$ is the Doppler width, where kT_{ion} is the ion temperature and M is the ion mass. The value of the spectral bandwidth for the FWHM of this Gaussian intensity is given by [115]:

$$\Delta \lambda_G = 2\sqrt{2 \ln 2} \Delta \lambda_D. \quad (3.3.1.8)$$

The formula for the electron impact broadening is used to estimate the Lorentzian profile [342]:

$$\Delta \lambda_L = 2 \cdot 10^{-16} w n_e \left[1 + 1.75 \cdot 10^{-4} \alpha n_e^{1/4} \left(1 - 6.20 \cdot 10^{-4} n_e^{1/6} T_e^{-1/2} \right) \right] \quad (3.3.1.9)$$

Here, T_e in eV and n_e are in cm^{-3} ; where α is the ion broadening parameter and w is an electron impact width. The FWHM of the Voigt profile can be estimated with an accuracy of 0.02% as [326]:

$$\Delta \lambda_V \approx 0.5346 \Delta \lambda_L + \sqrt{0.2166 \Delta \lambda_L^2 + \Delta \lambda_G^2} \quad (3.3.1.10)$$

The populations of the lower (n_1) and upper (n_2) laser level can be obtained by solving the stationary rate equations of a three-level model:

$$\begin{aligned} \frac{dn_1}{dt} &= -R_1 + P_1 \\ \frac{dn_2}{dt} &= -R_2 + P_2 \end{aligned} \quad (3.3.1.11)$$

where:

$$\begin{aligned} R_1 &= n_1 [n_e (C_{12} + C_{10}) + A_{10}] \\ R_2 &= n_2 [n_e (C_{21} + C_{20}) + A_{21}] \\ P_1 &= n_e [n_0 C_{01} + n_2 C_{21} + n_2 A_{21}] \\ P_2 &= n_e [n_0 C_{02} + n_1 C_{12}]. \end{aligned}$$

Here, R_1 and R_2 stand for the *relaxation* rates from the lower level and upper level, respectively, while P_1 and P_2 stand for the *pumping* rates to the lower level and upper level, respectively. The pumping rate to the lower level P_1 includes both collisional excitation from the ground level and collisional de-excitation and radiative decay from the upper level to the lower level. Meanwhile, the pumping rate to the upper level P_2 includes collisional excitation from the ground level and the lower level to the upper level. Here, n_0 is the population in the ground level, i.e., $2p^6$ in the Ne-like system. The quasi-neutral approximation implies that $n_0 = n_e/Z$, where Z is the ion charge. In other words, the population of Ne-like Ar^{+8} at $n_e = 10^{18} \text{ cm}^{-3}$ is considered $n_0 = 1.25 \cdot 10^{17} \text{ cm}^{-3}$.

At a specific electron temperature and density, the pumping time from the Ne-like ground level and the relaxation time to the Ne-like level can be calculated as follows:

$$t_{pumi} = \frac{n_i}{\frac{dn_i}{dt}|_{pumi}} \quad (3.3.1.12a)$$

$$t_{reli} = \frac{n_i}{\frac{dn_i}{dt}|_{reli}} \quad (3.3.1.12b)$$

where i can be considered either as one or two, corresponding to the lower level and upper level, respectively (Figure 3.9). Additionally, the $\frac{dn_i}{dt}|_{pumi}$ and $\frac{dn_i}{dt}|_{reli}$ can be considered as follows: $\frac{dn_i}{dt}|_{pumi} = P_i$ and $\frac{dn_i}{dt}|_{reli} = R_i$, where R_i and P_i are tabulated in Equation (3.3.1.11).

Taking into account Equation (3.3.1.12), the pumping time to the upper (t_{pum2}) and lower level (t_{pum1}) and the relaxation time from the upper level (t_{rel2}) and lower level (t_{rel1}) can be calculated.

Equation (3.3.1.12a) shows that the pumping time to the upper level (t_{pum2}) and lower level (t_{pum1}) depends on the population of the upper and lower levels (n_2 and n_1). Besides, Equation (3.3.1.12b) shows that the relaxation time from the upper level (t_{rel2}) and lower level (t_{rel1}) does not depend on the population of the upper and lower levels (n_2 and n_1).

3.3.2 Calculation of Time-scale(s) for Plasma Lasing

The characteristic times are: (i) the ionization time of a neutral Ar^0 ; (ii) the ionization time up to Ne-like Ar^{+8} ; (iii) the transition time among excited levels; and (iv) the pumping time and relaxation time among excited levels of Ne-like Ar^{+8} .

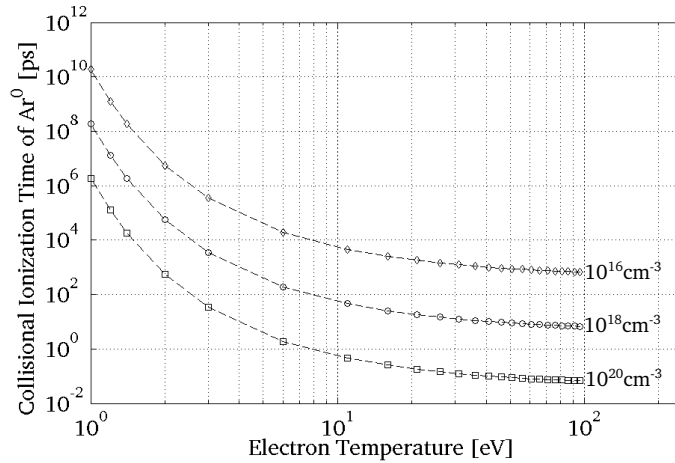


Fig. 3.12: Collisional ionization time of the neutral Ar^0 as a function of the initial electron temperature for a selection of electron densities.

3.3.2.1 Ionization Time of Neutral Ar^0

In this section, the electron impact ionization time of neutral Ar^0 using the collisional ionization rate recommended by Voronov [330] was calculated. Figure 3.12 shows that the collisional ionization time of a neutral Ar^0 is dependent on the initial electron temperature and density of the pre-plasma. It shows that the ionization time of a neutral Ar^0 by electron impact scales down linearly with electron density. For $T_e < 10$ eV, the electron impact ionization time of the neutral Ar^0 will decrease as high as 6 orders of magnitude increasing the electron temperature. Then for $T_e \geq 10$ eV, the electron impact ionization time of the neutral Ar^0 decreases by a factor of 7 for an increase in electron temperature by one order of magnitude. The characteristic time is thus of the order of a few ps for ordinary operating conditions.

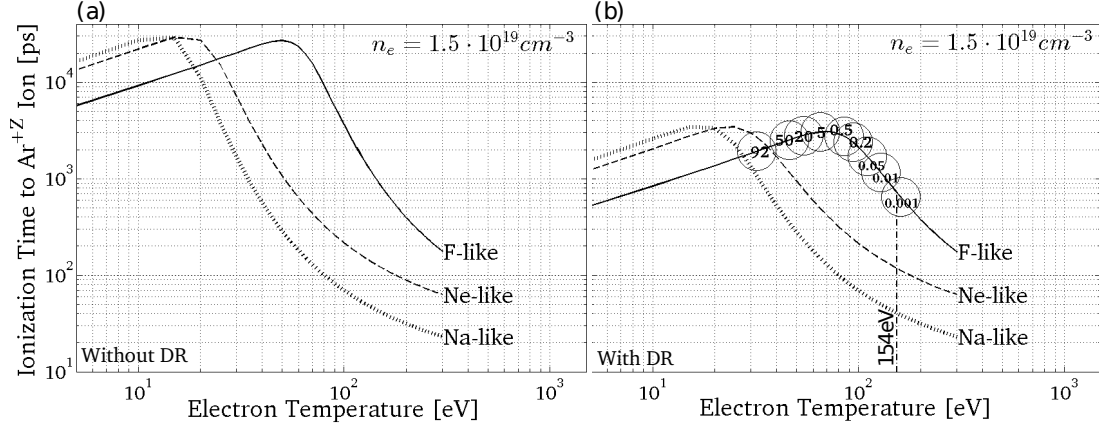


Fig. 3.13: Time required to achieve the Ar^{+Z} ion for the following steps: (i) $\text{Ar}^{+6} \rightarrow \text{Ar}^{+7}$ (Na-like); (ii) $\text{Ar}^{+7} \rightarrow \text{Ar}^{+8}$ (Ne-like); and (iii) $\text{Ar}^{+8} \rightarrow \text{Ar}^{+9}$ (F-like), as a function of temperature at a constant electron density $n_e = 1.5 \cdot 10^{19} \text{ cm}^{-3}$. The ionization time without (a) and with (b) taking the dielectronic recombination into consideration is shown. The ionic fractions of Ar^{+8} at each specific electron temperature are given on the curve $\text{Ar}^{+8} \rightarrow \text{Ar}^{+9}$ (F-like).

3.3.2.2 Ionization Time up to Ne-Like Lasing Stage

The ionization time for achieving Ar^{+8} was calculated with Eq. (3.3.1.1), which includes the following important processes: (i) collisional ionization; (ii) three-body; and (iii) radiative, and (iv) dielectronic recombination.

Figure 3.13 shows the time required for the ionization stage from Ar^{+6} to Ar^{+7} , and from Ar^{+7} to Ar^{+8} and from Ar^{+8} to Ar^{+9} for different electron temperatures without (a) and with (b) considering the dielectronic recombination at optimum electron density. Elton [90] has reported optimum electron density and temperature for the lasing of Ne-like Ar^{+8} , which are $n_e = 1.5 \cdot 10^{19} \text{ cm}^{-3}$ and $T_e = 154 \text{ eV}$, respectively. Dielectronic recombination has a stronger effect on the ionization time of Ar^{+Z} to have Ar^{+8} at cold temperatures less than 50 eV. At these temperatures, the ionization time to achieve Ar^{+8} without (a) considering dielectronic recombination is higher than with (b) considering the effect of dielectronic recombination was as high as a factor of 30 different. At electron temperatures $T_e > 50$, the effect of dielectronic recombination on the yield of Ar^{+8} is negligible, and the difference is as low as 14%. However, it has an effect on the over-ionization rate for Ar^{+9} .

The vertical line cross of the optimum electron temperature is shown in Figure 3.13b. It shows that the times required for the ionization from Ar^{+6} to Ar^{+7} , Ar^{+7} to Ar^{+8} and Ar^{+8} to Ar^{+9} are, respectively, 41 ps, 121 ps, and 691 ps.

Inside the circles of Figure 3.13b, the ionic abundance of Ar^{+8} when the equilibrium state is reached at specific electron temperatures is given (curve: Ar^{+8} to Ar^{+9}). It shows that by increasing the electron temperature, the ionic abundance decreases. Besides, it shows that the plasma requires time to produce Ne-like ions. With increasing electron temperatures, the time required for ionization time between levels to be achieved is getting shorter, and the abundance of Ne-like ions is getting smaller, which can result in a low conversion efficiency in X-ray laser-produced plasmas. For example, at an electron density $n_e = 1.5 \cdot 10^{19} \text{ cm}^{-3}$ and electron temperatures $T_e = 32 \text{ eV}$, the abundance of Ar^{+8} is 92% and at $T_e = 110 \text{ eV}$ the abundance of Ar^{+8} is 0.05%. Under these conditions, the ionization time of Ar^{+7} to achieve Ne-like Ar^{+8} are $3ns$ ($T_e = 32 \text{ eV}$) and $0.9ns$ ($T_e = 110 \text{ eV}$), respectively.

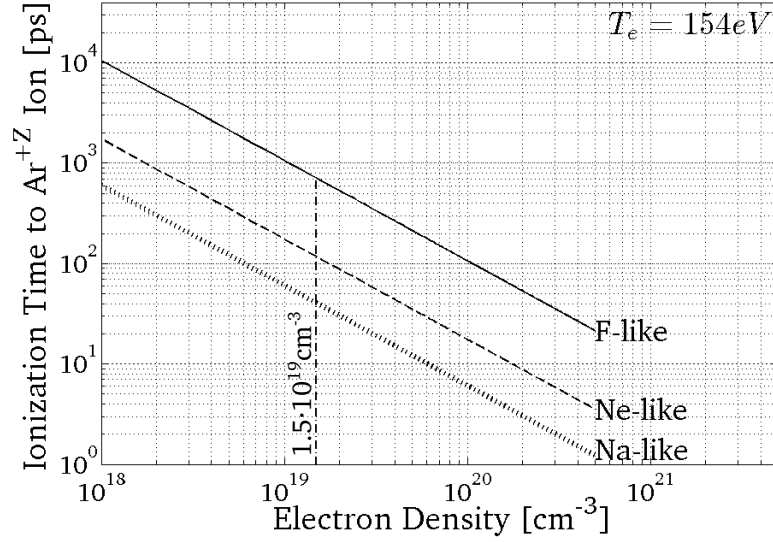


Fig. 3.14: Ionization time to achieve the Ar^{+Z} ion as a function of the electron density at the optimum electron temperature for the following: (i) $\text{Ar}^{+6} \rightarrow \text{Ar}^{+7}$ (Na-like); (ii) $\text{Ar}^{+7} \rightarrow \text{Ar}^{+8}$ (Ne-like); and (iii) $\text{Ar}^{+8} \rightarrow \text{Ar}^{+9}$ (F-like).

Fig. 3.14 shows the time required for the ionization from Ar^{+6} to Ar^{+7} , Ar^{+7} to Ar^{+8} and Ar^{+8} to Ar^{+9} versus electron densities at the optimum electron temperature. It shows that by increasing the electron density by a factor of 10, the ionization time between levels decreases by a factor of 10, as well (the ionization time scales down linearly with electron density).

Fig. 3.15 shows the total ionization time required to achieve a given ionic stage ($\text{Ar}^0 \rightarrow \text{Ar}^{+Z}$) at constant values of the electron density and temperature of Ne-like Ar^{+8} (Eq. (3.3.1.1)). A "total" ionization time, $\sum_{n=1}^Z t_{\text{Ar}^{+n} \rightarrow \text{Ar}^{+(n+1)}}$, comes from the consideration that Ar^0 cannot ionize directly to Ar^{+8} , but stepwise it should first ionize to Ar^{+1} , then to Ar^{+2} , and so forth. In Figure 3.15, the dashed ellipse shows the range for the pulse duration or the time delay required to achieve Ne-like Ar^{+8} . The characteristic t_{ion} to reach Ar^{+8} is 210 ps and to reach Ar^{+9} is 920 ps at the optimal values. This big difference in the ionization time to reach Ar^{+8} and Ar^{+9} is due to the closed shell configuration at the stable Ne-like electron configuration. The pre-pulse durations and the time delay from the literature are indicated with circles. Fig. 3.15 shows also that the pulse durations or the time delay between pulses are compatible with the total ionization time for having Ne-like Ar^{+8} .

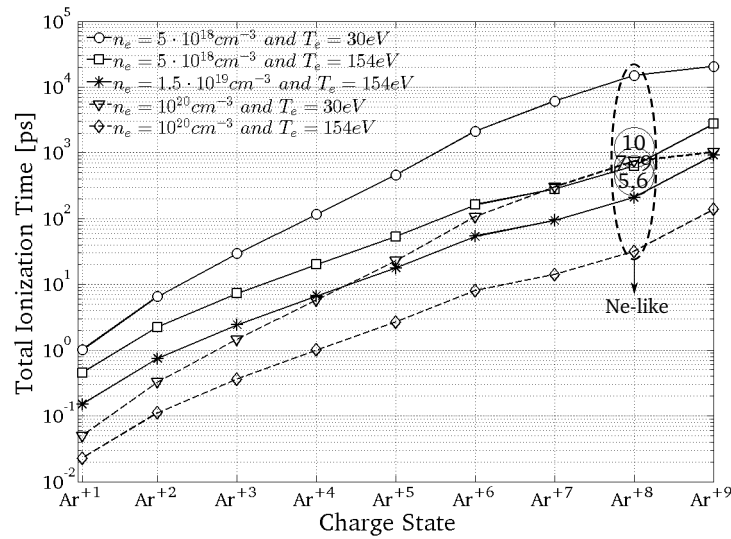


Fig. 3.15: Total ionization time to ionization stages ($\text{Ar}^0 \rightarrow \text{Ar}^{+Z}$) at different electron densities and temperatures. The dashed ellipse shows Ne-like Ar^{+8} .

The lasing can be efficient if the pulse duration or the time delay between pre-pulses is comparable with the time required to reach the desired ionic stage (Ar^{+8}), as shown in Figure 3.15.

The characteristic time for radiative cooling is thus ≈ 820 ps, which is ≈ 4 times longer than the total ionization time to achieve Ne-like Ar^{+8} (Tab. 3.3).

By fitting a set of data (Fig. 3.15), we can obtain the required total ionization time for having Ne-like Ar^{+8} , with the electron temperature and electron density dependency as follows:

$$t_{ion}[s] \simeq \frac{(1.4 \pm 0.4) \cdot 10^{13}}{n_e T_e^{1.61}} \quad (3.3.2.1)$$

where n_e is in cm^{-3} and T_e is in eV. Eq. (3.3.2.1) is obtained for a variety of ranges of electron temperatures and electron densities. In Eq. (3.3.2.1), $+0.4$ stands for $T_e < 45$ eV and -0.4 stands for $T_e \gtrsim 45$ eV. It is worth noting here that earlier work on Ne-like Ar^{+8} ionization time scaling [202] did not include any temperature dependence.

3.3.2.3 Transition Time among Ne-Like Levels

Transitions times between Ne-like levels were calculated by considering transient collisional excitations and radiative decays. Fig. 3.16a shows the transition time between levels composed of an upper level $|2\rangle$ and a lower level $|1\rangle$ and the ground level $|0\rangle$ at the optimum electron density in the electron temperature range of $T_e = 10$ eV to 2'000 eV. It shows that by increasing the temperature by a factor of five, the transition time from the upper to the lower laser level (τ_{21}) and the transition time from the upper level to the ground state (τ_{20}) are increasing by a factor of 1.8 and 2.4, respectively.

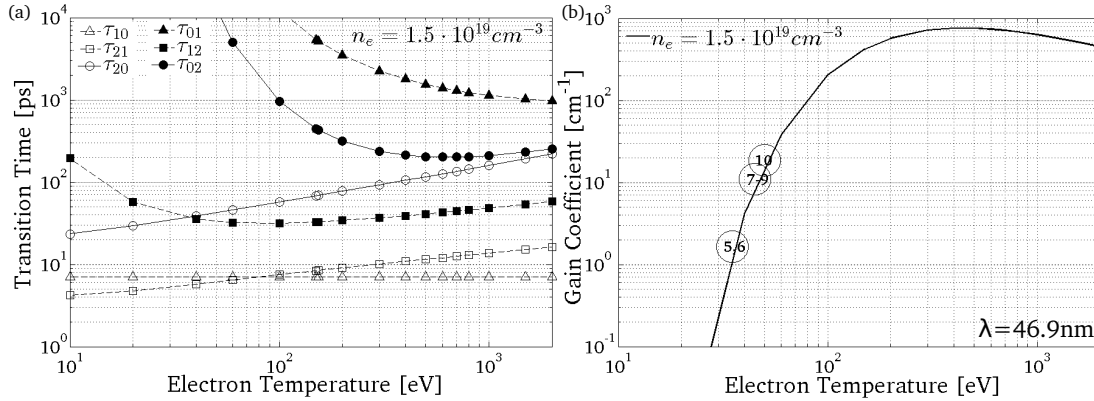


Fig. 3.16: (a) Transition time between Ne-like Ar^{+8} levels at the optimum electron density of $1.5 \cdot 10^{19} \text{ cm}^{-3}$ as a function of temperature. (b) Gain coefficient of the Ne-like Ar^{+8} laser at a wavelength $\lambda = 46.9 \text{ nm}$. Benchmarking data [77, 99–102] from the literature (circles) from experiments for gain coefficients of Ne-like Ar^{+8} laser-produced plasma are given.

It is shown that the transition time from the ground level to the upper level (τ_{02}) and the transition time from the lower to upper level (τ_{12}) are decreasing with increasing the temperatures up to 600 eV and 100 eV, respectively. However, τ_{02} and τ_{12} start to increase for $T_e > 600$ eV and $T_e > 100$ eV, respectively.

Fig. 3.16b shows the calculated gain coefficient of a Ne-like Ar^{+8} at a wavelength $\lambda = 46.9 \text{ nm}$ at the optimum electron density as a function of electron temperature. At $T_e = 50$ eV, the gain coefficient is 15 cm^{-1} , while τ_{21} is faster than τ_{10} by 10%. Then, a comparison of Figs. 3.16a,b shows that in the transient electron collisional excitation scheme, inversion (gain formation) happens because the collisional excitation and de-excitation processes of the upper and lower levels occur at different rates. The previous claim [11] of the faster radiative decay of the lower level than the upper level ($A_{10} > A_{21}$) is thus one aspect of the lasing.

It is shown that at the optimum electron density with increasing the temperatures up to 400 eV, the gain is increasing. If the temperature increases from 35 eV to 400 eV, the gain

increases by almost 3 orders of magnitude. At $T_e \approx 35$ eV, the gain coefficient is $\approx 1 \text{ cm}^{-1}$. From $T_e > 400$ eV, the gain starts to decrease.

In Fig. 3.16b, the benchmarking data are shown (Tab. 3.2). The experimentally measured gain is always lower than the gain calculated by the atomic calculation. In the experiments, the gain along its propagation path through the plasma suffers from a finite gain lifetime, traveling-wave velocity mismatch or inhomogeneous plasma conditions. All of these effects decrease the measured gain coefficient in the experiment.

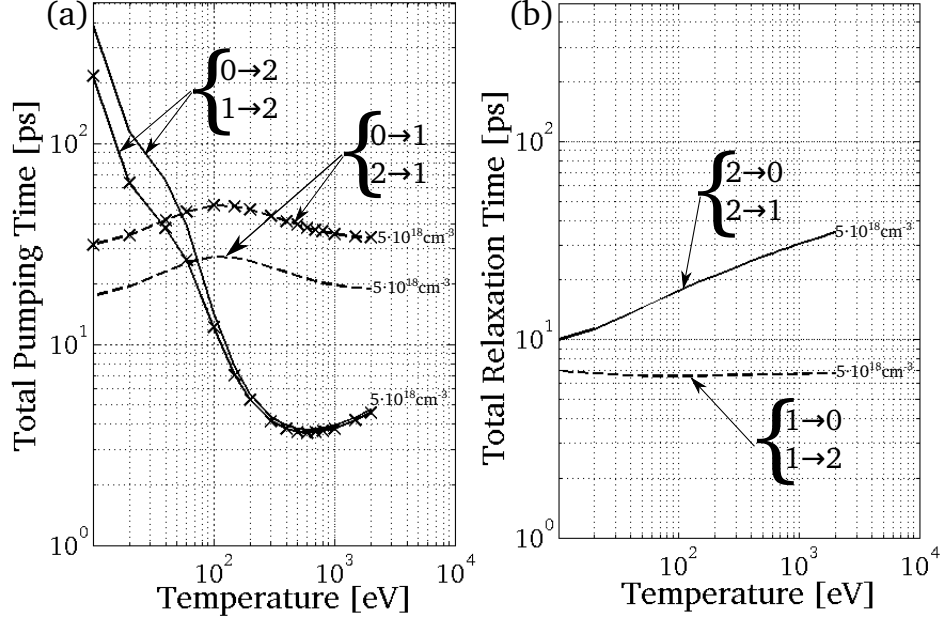


Fig. 3.17: (a) Total pumping time to the upper level $|2\rangle$ and lower level $|1\rangle$ at an electron density of $5 \cdot 10^{18} \text{ cm}^{-3}$, considering an inversion factor of 10% (curve with marker) and 50% (curve without marker). (b) Total relaxation time of the upper (solid line) and lower (dashed line) levels of Ne-like Ar^{+8} .

3.3.2.4 Pumping Time vs. Relaxation Time among Ne-Like Levels

Since the time it takes to maintain the inversion is equal to the upper level lifetime, the optimum value of the pulse duration of the main pulse must be comparable to the relaxation time of the upper level (t_{rel2}). Indeed, if the pulse duration of the main pulse is much longer than the lifetime of the upper level, most of the possible inversions would be lost by spontaneous emission without amplification.

Fig. 3.17 shows that the pumping to the upper and lower laser level, as well as the relaxation from the upper and lower level occur at different time scales. In Fig. 3.17a, for plotting the pumping time to the lower and upper level, the optimum value of the upper level population was considered $n_2 = 3 \cdot 10^{-4} n_0 (\lambda_{21})^{0.5}$, where λ_{21} is the X-ray wavelength in angstroms. The population of the upper and lower level is calculated with considering $F = 50\%$ and $F = 10\%$. These values of $F = 50\%$ and $F = 10\%$ are conservative values. It was obtained that the relaxation time does not depend on the upper and lower level population, i.e., the relaxation time for both $F = 10\%$ and $F = 50\%$ are the same.

Fig. 3.17a shows that at temperatures higher than 36 eV, corresponding to $F = 10\%$, the pumping time to the upper level is faster than the pumping to the lower level as high as a factor of ≈ 10 . Besides, it is shown that at temperatures higher than 72 eV, corresponding to $F = 50\%$, the pumping time to the upper level is faster than the pumping time to the lower level as high as a factor of ≈ 7 .

Fig. 3.17b shows that at an electron density of $5 \cdot 10^{18} \text{ cm}^{-3}$, the relaxation time from the lower level is faster than the upper level by a factor of as high as 5.2. It is shown that the relaxation time from the upper level with increasing of the electron temperature at a constant electron density is getting slower. For an electron density of $5 \cdot 10^{18} \text{ cm}^{-3}$ and electron temperatures in

the range of 10 → 2000 eV, the relaxation time from the upper level is in the range of 10 → 35 ps.

Fig. 3.15 and 3.17 show that at a low electron temperature, $T_e = 30$ eV and the electron density $n_e = 5 \cdot 10^{18} \text{ cm}^{-3}$, the time scale in which the relaxation time from the upper level ($t_{rel2} \approx 12$ ps) and the lower level ($t_{rel1} \approx 7$ ps) occurs is much lower than the time required to achieve Ne-like ions ($t_{ion} \approx 15000$ ps) and the time required to generate a population inversion ($t_{pum2} \approx 60$ ps).

Tab. 3.3 shows that at an optimum electron density of $1.5 \cdot 10^{19} \text{ cm}^{-3}$ and increasing the electron temperature by a factor of five, the relaxation time from the upper level is getting slower by a factor of ≈ 1.7 ($T_e = 154$ eV is an optimum electron temperature [90]). Meanwhile, at a constant electron temperature of $T_e = 30$ eV, increasing the electron density, the relaxation time from the upper level is getting faster. Increasing the electron density by a factor of ≈ 3 , the relaxation time from the upper level is faster by a factor of ≈ 3 .

Tab. 3.3: Summary of the effects of the electron temperature and density on t_{ion} (total ionization time to achieve Ne-like ions), t_{pum2} (total pumping time to the upper level) and t_{rel2} (total relaxation time from the upper level) at a wavelength $\lambda = 46.9$ nm in the $2p^5 3p^1(J=0) \rightarrow 2p^5 3s^1(J=1)$ laser transition at $F > 0$.

$n_e [\text{cm}^{-3}]$	$T_e [\text{eV}]$	$t_{ion} [\text{ps}]$	$t_{pum2} [\text{ps}]$	$t_{rel2} [\text{ps}]$	t_{pum2}/t_{rel2}
$1.5 \cdot 10^{19}$	30	5000	15	4.5	3.3
$1.5 \cdot 10^{19}$	154	211	2.3	7.5	0.3
$5 \cdot 10^{19}$	30	1500	8.0	1.4	5.7

Tab. 3.3 summarizes the effect of the electron temperature and density on t_{ion} , t_{pum2} and t_{rel2} time scales. It shows that the ratio of t_{pum2} to t_{rel2} is smaller for larger electron temperatures. The data in Tab. 3.3 show that, with increasing electron density at fixed temperature, both values of t_{rel2} and t_{pum2} are decreasing. Meanwhile, by increasing electron temperature at fixed density, the values of t_{rel2} and t_{pum2} , respectively, increases and decreases.

Based on our calculation (using Equation (3.3.1.12)), we can estimate the total relaxation time from the upper level (t_{rel2}) and the total pumping time to the upper level (t_{pum2}) for $T_e \lesssim 300$ eV:

$$\begin{aligned} t_{rel2} [s] &\simeq \frac{(2.8 \pm 0.2) \cdot 10^7}{n_e T_e^{-0.27}} \\ t_{pum2} [s] &\simeq \frac{(2.2 \pm 0.3) \cdot 10^{10}}{n_e T_e^{1.23}} \end{aligned} \quad (3.3.2.2)$$

where n_e is in cm^{-3} and T_e is in eV. Equation (3.3.2.2) is retrieved by fitting the data points by considering a dependence to electron density and temperature and taking into account Ne-like Ar^{+8} as a ground level (see Figure 3.9). So far, the electron density and temperature influence the total ionization time required to obtain Ne-like Ar^{+8} and also affect the time scales of t_{pum} and t_{rel} . In the next section, we show how the pulse duration can influence the quantity of the electron density and temperature in the X-ray-produced plasma.

3.3.3 Calculation of the Effect of Pulse Duration on Hydrodynamic Parameters

In order to determine the dependence of the pulse duration on the electron density and temperature of the laser-produced plasma, we studied the evolution of the electron density and temperature produced by pulses of different durations.

Fig. 3.18 shows calculated maximum electron temperature and maximum electron density as a function of time in the direction of plasma expansion. During the short laser pulse, little expansion occurs ($L_{\text{expansion}} = v_{\text{expansion}} \cdot \Delta\tau_p$). This allows the direct deposition of a remarkable amount of the laser energy on the plasma, which means a higher electron temperature. It is found that the electron density and temperature are respectively a factor of ≈ 2.1 and ≈ 5 times higher in the case of a shorter pulse of $\Delta\tau_p = 0.1$ ps in comparison to the long pulse of $\Delta\tau_p = 1000$ ps.

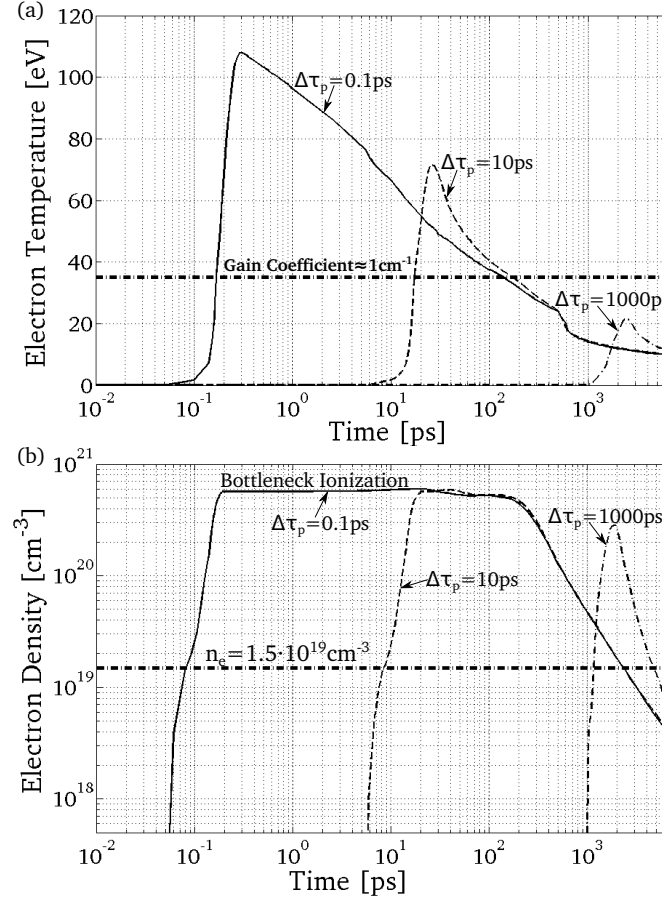


Fig. 3.18: (a) Time-dependent electron temperature and (b) electron density produced with pulses with durations of 0.1 ps, 10 ps, and 1000 ps and energy fluence $j_L \approx 10 \text{ J/cm}^2$.

Figure 3.18 and the data in Table 3.3 show that in the case of a shorter pulse, the time required to produce Ne-like Ar^{+8} and the t_{pum2} and t_{rel2} time scales will be shorter and closer together.

Fig. 3.18a shows that the plasma produced by the long pulse $\Delta\tau_p = 1000$ ps is below the area with the gain coefficient of 1 cm^{-1} . In Figure 3.18b, the line cross of the optimum electron density ($1.5 \cdot 10^{19} \text{ cm}^{-3}$) corresponding to the gain coefficient of $\approx 1 \text{ cm}^{-1}$ at the electron temperature 35 eV is shown.

Fig. 3.18b shows that in the case of the plasma produced with the pulse duration of 0.1 ps, there is a bottleneck in the ionization level at $0.2 \text{ ps} \lesssim t \lesssim 4 \text{ ps}$, which means that the plasma required more time to expand and cool so that the recombination rate increases and the average charge state concomitantly decreases. Figure 3.18a shows that electrons can lose energy emitting radiation and by conduction, so the temperature drops. Ne-like Ar^{+8} has a closed shell, making removal of an additional electron more difficult. This significantly increases the threshold for further electron ionization, which can also be considered an ionization bottleneck for a plasma at a specific temperature.

Fig. 3.18b shows that the electron density is always less than $n_{ec} \approx 10^{21} \text{ cm}^{-3}$, where n_{ec} is the critical electron density and also a turning point in the normal incidence for the pump laser with a wavelength $\lambda = 1054 \text{ nm}$. Figure 3.18b shows that the plasma produced by a gas target can limit the refraction of the pump-pulse, which means the time delay between pulses cannot be an issue in order to smear-out the electron density gradient.

3.3.3.1 Optimum pump-Laser Intensity for Achieving Ne-like Ar^{+8}

The optimum pump-laser intensity at the focus point of the laser on the target in order to have Ne-like Ar^{+8} was calculated. Fig. 3.19 shows the optimum laser intensity required to have Ne-like Ar^{+8} at different pulse durations and Ar^0 mass densities, obtained from the hydro-code.

It shows that with increasing the initial gas density by a factor of 10, the required laser intensity is decreased by a factor as high as ≈ 7 . When charged particles are accelerated in the electric field of the laser, they can ionize neutral gas molecules by collisions. Then, the process is dependent on the initial gas density (pressure).

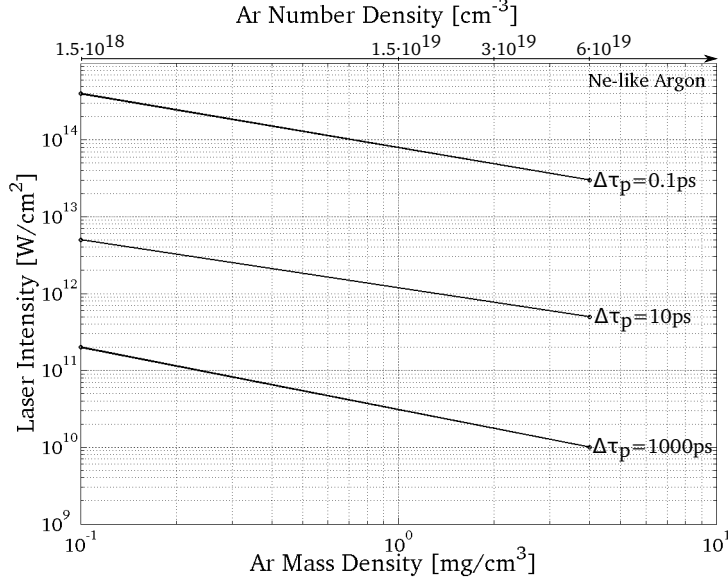


Fig. 3.19: Optimum laser intensity for having Ne-like Ar^{+8} as a function of Ar^0 density at different pulse durations. The top axis is the number density (cm^{-3}).

Based on the results in Figure 3.19, the following scaling-laws can be obtained:

$$\begin{aligned}
 I_{opt} [W/cm^2] &\approx \Delta\tau_p^{-1.13} \left(\frac{5.81 \cdot 10^{12}}{\rho_0^{0.72}} \right), \quad \Delta\tau_p < 1ps \\
 I_{opt} [W/cm^2] &\approx \Delta\tau_p^{-1.01} \left(\frac{1.24 \cdot 10^{13}}{\rho_0^{0.59}} \right), \quad 1 \leq \Delta\tau_p \leq 100ps \\
 I_{opt} [W/cm^2] &\approx \Delta\tau_p^{-0.31} \left(\frac{2.78 \cdot 10^{11}}{\rho_0^{0.79}} \right), \quad \Delta\tau_p > 100ps
 \end{aligned} \tag{3.3.3.1}$$

where the optimum pump-laser intensity (I_{opt}) for having Ne-like Ar^{+8} is dependent on the pulse duration and initial Ar^0 density. In Equation (3.3.3.1), $\Delta\tau_p$ is the pulse duration in ps and ρ_0 is the initial Ar^0 mass density in mg/cm^3 .

3.3.4 Summary on Pulse Duration & Timing

In this study, we systematically investigated the optimum time configuration of pump pulses. In Section 3.3.2.2, we studied a neutral Ar^0 ionization time scale for achieving Ne-like Ar^{+8} , finding that the dielectronic recombination has an important effect at temperatures less than 50 eV. For $T_e \lesssim 50$ eV, without considering dielectronic recombination, the ionization time is overestimated as high as a factor of 30. For $T_e > 50$, this difference reduces to 14%.

The total ionization time in order to achieve Ne-like ions is obtained by Equation (3.3.2.1).

In Section 3.3.2.3, we showed that in the transient electron collisional pumping scheme, lasing happens because the collisional excitation processes of the upper and lower levels occur at different rates, and not simply because of the faster rate of the radiative decay of the lower level. Thus, even if the transition time of the upper level $|2\rangle$ to the lower level $|1\rangle$ is faster than the transition time from the lower level $|1\rangle$ to the ground state $|0\rangle$, the plasma gain medium is formed.

In Section 3.3.2.4, we demonstrated that at low temperatures ($T_e = 30$ eV) and at a certain electron density ($n_e = 1.5 \cdot 10^{19} \text{ cm}^{-3}$), both the total relaxation time from the upper level (4.5

ps) and total pumping time to the upper level (15 ps) are much shorter than the time required to achieve Ne-like ions (5000 ps).

In Section 3.3.2.4, we showed that the ratio of the pumping time for the population inversion to the relaxation time from the upper level can be as high as a factor of 10 for $T_e \gtrsim 20$ eV, depending on the electron density.

We found that at temperatures higher than 36 eV ($F = 10\%$) and 72 eV ($F = 50\%$), the upper level will be pumped faster than the lower level by a factor as high as 10.

It is shown that at a constant electron density ($1.5 \cdot 10^{19} \text{ cm}^{-3}$), increasing the temperature by a factor of five ($30 \rightarrow 154$ eV), the ionization time to achieve Ne-like ions and the pumping time to the upper level are decreasing, by a factor of 24 and 6.5, respectively. Meanwhile the relaxation time from the upper level increases by a factor of 1.7 (Table 3.3).

It is found that at a constant electron temperature (30 eV), increasing the electron density by a factor of 3.3 ($1.5 \cdot 10^{19} \rightarrow 5 \cdot 10^{19} \text{ cm}^{-3}$), all time scales including ionization time, pumping time and relaxation time to the upper level are decreasing, by a factor of 3.3, 1.9 and 3.2, respectively (Equation (3.3.2.2)).

Both the pumping time to the upper level $|2\rangle$ and relaxation time from the lower level $|1\rangle$ are estimated. It was found that for an electron density higher than $5 \cdot 10^{18} \text{ cm}^{-3}$, at electron temperatures in the range $10 \rightarrow 2000$ eV, the relaxation time from the upper level is as high as $\tau_{rel2} \leq 35$ ps. The most effective lasing happens with short pulses with a pulse duration comparable to the total relaxation time from the upper level, namely $\Delta\tau_p \leq 35$ ps.

In Section 3.3.3, we studied the effect of the pulse duration on the electron temperature or density for plasma lasing. The optimum time scale required to achieve Ne-like ions, as well as the time required to generate a population inversion depends on the combined effect of the temperature and density (Table 3.3).

In Section 3.3.3.1, formulas for calculating optimum pump-laser intensity for producing the Ne-like Ar^{+8} are obtained. This equation can be used for different pulse durations and considering different initial gas densities of Ar^0 .

3.4 Laser-produced Plasma Conditions

Published in Masoudnia et al. NIMS B, 323, 59-70, 2014. Main themes here:

- *Optimum Electron Density & Temperature for Lasing*
- *Analytical Models for Plasma Lasing*
- *Numerical Models for Plasma Lasing*

Since the mid 1980s with the Ne-like ions [103, 178, 207] and later in the 1990s with the Ni-like ions [64, 146, 160, 167, 181, 186, 319], short-wavelength lasers in the extreme UV and soft X-ray domains were demonstrated by means of amplified spontaneous emission (ASE) across a hot and dense plasma. Such table-top systems are commonly referred to as "X-ray plasma laser" (XPL), despite of the effective spectral range is mostly in the XUV. In order to obtain strongly amplified X-ray emission, a laser-pump pulse is delivered onto a target material to generate a plasma column with: (i) sufficient population of the lasing Ne- or Ni-like ions, (ii) sufficient electron density, leading to an efficient monopole collisional pumping rate from the ground state to the upper laser level, and (iii) suitable electron temperature to efficiently populate the inversion.

The X-ray-lasing plasma-medium, especially considering the highly ionized atoms, has transient lifetimes as low as a few tens of ps at the best, such that so-called bottleneck ionization from closed-shell electron configurations is required [273]. Ions that fulfill these requirements are the above-mentioned Ne-like ($Z = 10$) or Ni-like ($Z = 28$) iso-electronic shells, e.g., Ni-like tin (Sn^{+22}). Despite lasing in Ni-like ions has proven more difficult to achieve than using Ne-like lasers [197], Ni-like plasmas are attractive due to the higher quantum efficiency and characteristic laser emission wavelengths shorter than 10nm [66, 81].

The realization of the XPL requires knowledge about the optimum electron temperature and density across the plasma medium. Too soft temperature and density conditions can result in an insufficient population of Ni-like ions and/or a failure to achieve population inversion. Too hard conditions can collisionally destroy a population inversion. Furthermore, the *generation of shorter-wavelengths* demands that the pump energy pulse is deposited deeper in the plasma medium, in order to reach the required higher electron densities. In the case of the grazing-incidence pumping (GRIP) scheme a shallow turning point, due to refraction of the pump laser beam out of the plasma column, limits the penetration depth. Thus, the pump energy may not be deposited efficiently in the deep high-gain zone. Therefore the *penetration depth* for the optimum electron density and temperature, which is related to the *atomic number* (Z) and the *angle of target irradiation*, is important for Ni-like plasma lasing.

A series of papers [90, 119, 180] examined computationally the optimum electron density and temperature for the *Ne-like* XPL and went on to develop scaling laws which were a function of the atomic number. For Ni-like ions however analogous scaling laws are still not available, and the extrapolation of models applied to the Ne-like needs validation. Yan et. al. [343], pointed out a *heuristic affinity* (diagonals on the periodic table) between the optimum conditions for a given *Ne-like* ion and its "affine" *Ni-like* plasma-lasing radiator. For instance, Ne-like Cu is claimed to have similar optimum conditions to those for Ni-like Sn. However, the degree of heuristic affinity between the Ne-like and Ni-like XPLs is generally weaker for elements with higher atomic number [343].

Tab. 3.4: Summary of main experimental parameters for the generation of Ni-like plasma-driven X-ray lasers. Data from refs. [1, 2, 7, 79, 147, 152, 156, 194, 195, 208–210, 213, 214, 255, 301, 348]. Legend: FPP is first pre-pulse, SPP is second pre-pulse, TPP is third pre-pulse, MP is main pulse, E_P is the total energy of all pump pulses, λ_P is the wavelength of the pump-laser, n_e is the optimum electron density, T_e is the optimum temperature, and λ_X is the X-ray laser wavelength.

Lasing Ion	FPP[ps]	SPP[ps]	TPP[ps]	MP[ps]	E_P [J]	λ_P [nm]	n_e [cm ⁻³]	T_e [eV]	λ_X [nm]	Ref.
Mo^{+14}	200	—	—	1.5	0.15	800	$3 - 5 \cdot 10^{19}$	—	18.9	[156]
Pd^{+18}	600	—	—	1	5-7	1054	$9 \cdot 10^{19}$	400	14.7	[79]
Pd^{+18}	600	—	—	0.5 – 27	5.5	1054	$1 - 2 \cdot 10^{20}$	400 – 450	14.68	[301]
Ag^{+19}	350	350	—	8	0.978	800	$2 \cdot 10^{20}$	—	13.9	[147]
Ag^{+19}	600	—	—	1	0.02	1060	$2 \cdot 10^{20}$	250	13.9	[234]
Ag^{+19}	75	75	—	75	-	1050	$5.7 \cdot 10^{20}$	700	14	[346]
Cd^{+20}	120	120	—	8	1.365	1064	$2.8 \cdot 10^{20}$	—	13.2	[255]
Sn^{+22}	200	200	—	1.2	0.3	800	$3 \cdot 10^{20}$	512	11.9	[152]
Te^{+24}	210	210	—	5	4.2	800	$4 \cdot 10^{20}$	600	10.9	[7]
Nd^{+32}	100	100	100	1000	250	532	$2.8 \cdot 10^{20}$	820	7.9	[153]
Sm^{+34}	75	75	—	75	-	1050	10^{21}	700	7	[348]
Sm^{+34}	200	—	—	200	-	1060	$8 \cdot 10^{20}$	500 – 600	—	[213]
Sm^{+34}	285	—	—	2	0.3	1060	10^{21}	1000	7.2	[234]
Eu^{+35}	—	—	—	1000	kJ	530	$2 \cdot 10^{20}$	600	6.58, 7.1	[194]
Eu^{+35}	—	—	—	-	-	530	$3 \cdot 10^{20}$	700	6.57, 7.08	[208]
Gd^{+36}	200	—	—	200	-	1060	$9 \cdot 10^{20}$	500 – 600	—	[213]
Yb^{+42}	—	—	—	—	—	—	$1.5 \cdot 10^{21}$	1000 – 1500	5.609, 5.026	[67]
Yb^{+42}	—	—	—	1000	kJ	530	10^{21}	900	5.026, 5.61	[195]
Ta^{+45}	200	—	—	200	-	530	$2 \cdot 10^{21}$	1200 – 1400	4.4	[213]
Ta^{+45}	80	—	—	20	-	530	$4 \cdot 10^{21}$	1500	4.48	[210]
W^{+46}	—	—	—	—	-	—	$3.5 \cdot 10^{21}$	1400 – 1800	4.32	[67]
W^{+46}	—	—	—	—	-	—	$2 \cdot 10^{22}$	800	4.28	[2]
W^{+46}	—	—	—	550	-	530	$2.5 \cdot 10^{21}$	860	4.31	[209]
Au^{+51}	—	—	—	—	-	—	$6 \cdot 10^{22}$	1500	3.51	[1]

Table 3.4 summarizes the operating conditions used in generating the Ni-like plasma as well as the identified optimum electron temperature and density that would maximize the XPL gain and lead to saturation. As shown in Table 3.4, the indicated electron density and electron temperature can vary not only with the target material but also with the irradiation conditions. This makes it difficult to attribute specific plasma-medium optimum conditions to a given output wavelength (or target material). This lacuna on the quantitative prediction of the optimum Ni-like plasma-medium conditions using a general scaling law deserves attention.

A widely adopted treatment involves the radiation field to be solved from a radiative transfer equation using Maxwell-Boltzmann population distributions computed within the frame of local thermodynamic equilibrium (LTE). The assumption of high electron density is important in this case in order to ensure a collisional regime. The quantitative assessment as to whether LTE has been fulfilled is often based on McWhirter's approach [138], which imposes the electron density for LTE to hold as follows:

$$n_e \geq 1.6 \cdot 10^{12} E_{exc}^3 T_e^{\frac{1}{2}} \quad (3.4.0.1)$$

where n_e is the electron density measured in cm⁻³, E_{exc} is the excitation potential in eV, and T_e is the electron temperature in K. To fulfill the LTE condition for the Ni-like Sn XPL, n_e has to be greater than $\sim 1.9 \cdot 10^{21}$ cm⁻³, i.e., at the electron temperature of $1.16 \cdot 10^6$ K (100 eV) and the excitation of ~ 104 eV (e.g., Sn^{+22} , $\lambda \sim 11.9$ nm XPL). Besides, thermalization implies long time-scales on the order of ns. In the LTE model, the laser pulse couples to the free electrons by inverse Bremsstrahlung, and collisions between the oscillating free electrons and background heavy particles (atoms and ions) are necessary to preserve momentum and thus achieve Saha equilibrium ($T_e = T_i$). The thermalization time between electrons and ions is quantitatively predicted as follows [273]:

$$t_{ei}[s] \approx 3.16 \cdot 10^{-10} \frac{A}{Z^2} \left(\frac{kT_e}{100} \right)^{3/2} \left(\frac{10^{21}}{n_i \log \left(\left(\frac{3}{2\bar{z}^2} \right) \cdot \left(\frac{(kT_e)^3}{\pi e^6 n_e} \right)^{1/2} \right)} \right) \quad (3.4.0.2)$$

where A is the atomic weight of the ions, Z is the atomic number, \bar{z} is the average charge state, kT_e is the electron temperature in eV, n_e is the electron density in cm^{-3} , and n_{ion} is the ion density which we can use plasma neutrality condition: $n_e = \bar{z}n_i$.

The requirement to operate in a non-thermalized regime, which is typical in a lasing context with population inversion, can be modeled with a collisional-radiative rate equation treatment. This demands accurate knowledge on the specific coefficients. Such a non local thermodynamic equilibrium (NLTE) model can improve in accuracy by adding specific rate equations for accounting specific processes such as dielectronic recombination (DR), but at the cost of computational load. In the NLTE model, the population distribution at any point does not depend only upon local plasma parameters, unlike in the LTE model, but also upon the mixing collisional processes of local nature with radiative processes of non-local nature. Consideration of the dielectronic recombination process has proven to be essential for accurate predictions on the ionization.

The indicated electron densities in the cited benchmarking literature were found not to fulfill the McWhirter's density criterion [138], which indicates that XPL optimum conditions are indeed better interpreted within a NLTE regime. NLTE kinetics have been extensively studied for plasmas which are produced by a ultrashort pulse laser [58].

The aim of this study was to develop scaling laws for predicting the optimum electron temperature and density for the $3d^9 4d^1 (J=0) \rightarrow 3d^9 4p^1 (J=1)$ transition in *Ni-like ions* plasma. The considered transition is the closest one to the main transition observed experimentally. In fact, detailed calculations [66] showed multiple possible transitions between the $J=0$ and the $J=1$ states. For reasons of simplicity, and for easier comparison with experiments, we investigated a three-level system with one laser transition. A more detailed theoretical analysis of multi-line $J=0 - 1$ transitions will be subject of a future publication.

The logical steps of our modeling are summarized in Fig. 3.20. Results are benchmarked against literature data. We begin with a "top-down" approach, verifying the applicability of existing models, based on consistency and scope. Thus, in Sect. 3.4.2, scaling-laws for Ni-like ions based on heuristic affinity conditions of Ne-like ions in XPL and their affine Ni-like ions are presented. In Sect. 3.4.3, optimum temperature and density conditions were derived extrapolating different theoretical models for Ne-like ions to the case of Ni-like lasing ions. In Sect. 3.4.5.1 and in Sect. 3.4.5.2, a "bottom-up" approach was adopted: the temperature and density that maximizes the abundance of Ni-like ions was numerically modeled considering either the LTE or the NLTE model for describing the physical processes. In Sect. 3.4.5.2, conditions' shift while considering the dielectronic recombination are shown. In Sect. 3.4.5.3, a conclusive comparison between LTE and NLTE models is done.

Following the study of analytical predictive laws, our focus progressed toward the numerical computation of the salient plasma processes. Such processes were thus explored to identify the "optimum lasing conditions" as a function of operating parameters. Thus, in Sect. 3.4.6.1, the electron temperature that maximizes collisional pumping from ground and lower laser states to the upper state was calculated. In Sect. 3.4.6.2, the limiting electron temperature for the population inversion across the plasma medium for Ni-like plasma lasers is discussed. In Sect. 3.4.6.3, the electron temperature and density for the lasing across the plasma medium for Ni-like plasma lasers were obtained. In Sect. 3.4.7, a comparison of scaling-laws (which were obtained in Sect. 3.4.4-3.4.6.3) for Ni-like plasma lasers is made.

After the analysis on what plasma conditions are ideal for the sake of lasing, we conclude the work showing how to achieve these. In Sect. 3.4.8, the optimization of pumping conditions such as the irradiation intensity and irradiation angle in the plasma medium are discussed. Optimum irradiation intensity and irradiation angle are important for experimental optimization conditions.

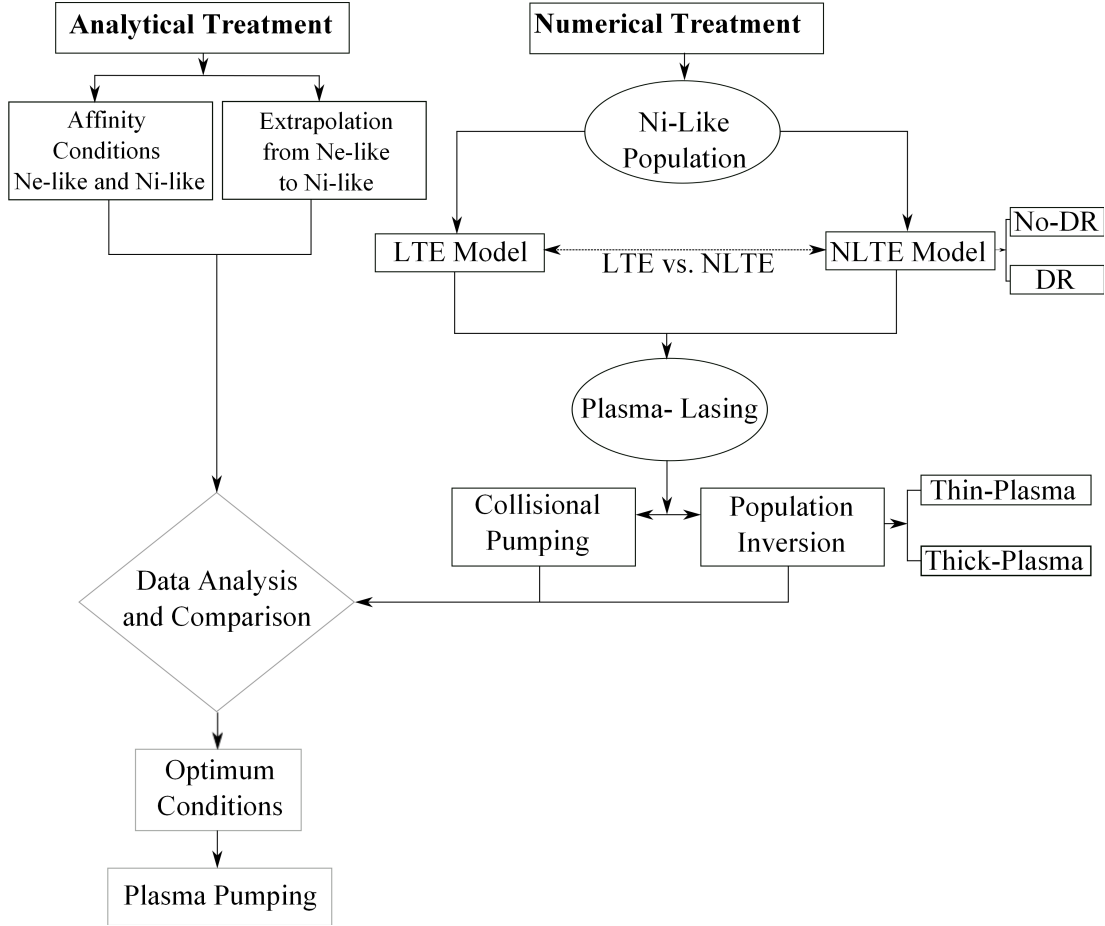


Fig. 3.20: Flow-chart of the study of the optimum electron density and temperature for plasma-lasing, comparing alternative computational approaches.

3.4.1 Theory

If n_2 and n_1 are the upper and lower laser state populations and σ_{stim} is the cross section for stimulated emission, the small signal gain is found as in Eq. 3.2.0.1. To map the optimum electron temperature and density, one can map the gain with the criterion $F \geq 0$ (Eq. 3.2.0.2), while varying the plasma electron temperature and density for a Ni-like radiator of atomic number Z . The populations of the Ni-like levels (Fig. 3.21. a) are computed by solving the rate equation of a three-level model as follows:

$$\frac{dn_1}{dt} = n_2(n_e C_{21} + A_{21} + \varepsilon n_e C_{01}) - n_1(n_e C_{12} + G_{10}(\tau_c) A_{10} + n_e C_{10}) = 0 \quad (3.4.1.1)$$

where ε is n_0/n_2 , A_{ij} are spontaneous emission coefficients, and C_{ij} are collisional coefficients. The escape factor $G_{10}(\tau_c)$ is the relative local flux of photons from the expanding plasma [168]. In Eq. 3.4.1.1, we considered that the plasma is at ionization equilibrium, at a temperature where the recombination rate to the excited laser state is negligible and the inversion of the $J=0 \rightarrow 1$ transition is created uniquely by means of monopole collisional pumping from the ground level [66, 208]. On the other hand, the recombination processes have a significant effect on the $J=2 \rightarrow 1$ lasing transition [113].

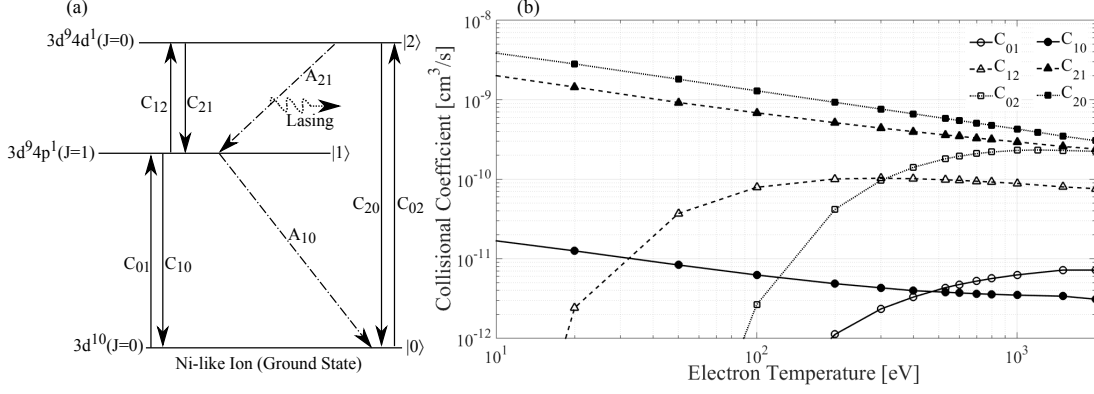


Fig. 3.21: (a) Laser levels and transitions for a Ni-like ion (see also Table 3.5). For simplicity main upper $|2\rangle$ and lower $|1\rangle$ lasing states are shown, along with the ground $|0\rangle$ state. (b) Calculated collisional coefficients as a function of the electron temperature for Ni-like Sn. Increasing the temperature the collisional excitation coefficients increased (empty markers) while the de-excitation coefficients decreased (full markers).

In order to include the high temperature cut-off effect of electron collisional excitation from the ground state to the upper state (C_{02}), a value of $\varepsilon \neq 0$ is needed. The electron collisional excitation rates (C_{ij}^e) between levels depends on the electron temperature as in Eq. 3.3.1.4. For calculating the collisional de-excitation rate (C_{ji}^d), considering detailed balancing [137], one has Eq. 3.3.1.5. For a Doppler-broadened spectral line, the opacity τ_c , i.e., physically the number of line optical depths at the central wavelength λ_c of a plasma with thickness d , is given by,

$$\tau_c = 1.1 \cdot 10^{-16} \lambda_c n_0 d f_{10} \left(\frac{\mu}{kT_{ion}} \right)^{1/2} \quad (3.4.1.2)$$

where μ is the atomic mass, n_0 is the populations of absorbing ions (at ground level) in cm^{-3} , f_{10} is the oscillator strength for the lower state to the ground state transition, kT_{ion} is the ion temperature in eV. In addition, λ_c is in \AA , and d is the plasma size along the line of sight in cm. The radiation is attenuated by a factor of $\exp(-\tau_c)$, resulting from absorption in the plasma. The opacity of the plasma affects both the escape probability of the observed spectral emission as well as the overall population dynamics of the plasma. The issue of radiation trapping due to the plasma opacity must be considered. In fact, optimum plasma conditions, kT_{e-opt} and n_{e-opt} , require low opacity for de-population of the lower laser level. Opacity can be reduced by shortening the depth of plasma. If $\tau_c \ll 1$, the plasma is optically thin and almost no self-absorption takes place, whereas for $\tau_c \gg 1$ significant absorption in a optically thick plasma occurs. For the Doppler-broadened lines and $\tau_c \leq 4.5$, McWhiter [138] has shown that the escape factor is bounded as follows:

$$\exp(-\tau_c) \leq G(\tau_c) \leq (1 - \exp(-\tau_c)) / \tau_c. \quad (3.4.1.3)$$

For the larger values of τ_c , Holstein [135] has shown that the escape factor scales as follows:

$$G(\tau_c) = 1 / \left(\tau_c (\pi \ln(\tau_c))^{1/2} \right). \quad (3.4.1.4)$$

In order to obtain the temperature that maximizes the ionic abundance and reach to Ni-like ions in a NLTE plasma for Ni-like, we use the rate equation of CR model to estimate ionization charge states in NLTE as follows [118, 273]:

$$\frac{n_{Z+1}}{n_Z} = \frac{S_Z}{\alpha_{Z+1} + n_e \beta_{Z+1} + D_{Z+1}} \quad (3.4.1.5)$$

where S_Z is a collisional ionization coefficient corresponding to an ionic stage $+Z$ is given by [138]:

$$S_Z [\text{cm}^3 \text{s}^{-1}] = 2.43 \cdot 10^{-6} \xi_Z T_e^{-3/2} \left(\frac{\exp(-u)}{u^{7/4}} \right) \quad (3.4.1.6)$$

where T_e is electron temperature in eV, ξ_Z is the number of electrons in the outermost layer corresponding to the ionic charge state Z , and u is χ_Z/T_e , which χ_Z is ionization potential in eV. The terms α_{Z+1} , β_{Z+1} , and D_{Z+1} are respectively the radiative, collisional three-body, and dielectronic recombination coefficients applying to the ionic charge state $Z + 1$, which corresponding coefficients are tabulated as follows [164]:

$$\alpha_{Z+1}[cm^3 s^{-1}] = 5.2 \cdot 10^{-14} (Z + 1) u^{1/2} \left(0.429 + 0.5 \ln(u) + 0.469 u^{-1/2} \right) \quad (3.4.1.7)$$

$$\beta_{Z+1}[cm^6 s^{-1}] = 2.97 \cdot 10^{-27} \frac{\xi_Z}{(T_e \chi_Z^2 (4.88 + 1/u))}. \quad (3.4.1.8)$$

The dielectronic recombination coefficient is often neglected [48, 276]. Following the work of Eidmann [86], we account for it by using $D_Z = \rho \alpha_Z$ with ρ as a free parameter, e.g., $\rho \approx 10$ for $kT_e < 1000$ eV.

In a high-density plasma, plasma effects were taken into account, considering that the potential lowering is given as follow:

$$\Delta\chi[eV] = -Z Ry \min\left(\frac{2a_0}{\lambda_D}, \frac{3a_0}{2R_0}\right) \quad (3.4.1.9)$$

where Z is the ion charge, Ry is Rydberg energy, a_0 is the Bohr radius, λ_D is the Debye radius, and R_0 is the ion-sphere radius. Within the calculation due to our electron temperature and density range, the value of ionization potential lowering $\Delta\chi[eV] \approx 1.95 \cdot 10^{-10} Z \sqrt{n_e/T_e}$ is considered (n_e in cm^{-3} and T_e in eV).

In Eq. 3.4.1.5, if we have $n_e \beta_{Z+1} \ll \alpha_{Z+1} + D_{Z+1}$, then Eq. 3.4.1.5 will be density independent as in the corona equilibrium (CE) model. It is investigated [120] that the CE model can be safely applied to laser-produced plasmas with electron densities less than or equal to $10^{22} cm^{-3}$ for estimating e.g., the abundance of high- Z ions and the average ionic charge state relevant to X-ray line radiation studies.

Collisions increase as the density of a plasma is increased. At sufficiently high densities, collisional processes become more important than radiative processes in determining excited state population (LTE model). In the LTE, the number of particles in the two states described by as the Saha equation. The LTE model is applicable to the high density regime. The ion balance in Eq. 3.4.1.5 embodies the Saha equilibrium as follows:

$$\frac{n_{Z+1}}{n_Z} = \frac{S_Z}{n_e \beta_{Z+1}}. \quad (3.4.1.10)$$

The total abundance of an element is given by:

$$n_{tot} = \sum_{i=0}^Z n^i. \quad (3.4.1.11)$$

Where n^i is the population of ion X^{+i} , where Z is the atomic number of X . The fractional abundance of charge state i is given by:

$$f^i = \frac{n^i}{n_{tot}}. \quad (3.4.1.12)$$

This leads to the normalization:

$$\sum_{i=0}^Z f^i = 1. \quad (3.4.1.13)$$

For X-ray lasing to occur, a population inversion is needed, which happens when C_{12} and C_{02} are dominating over the other transitions. When population inversion happens, spontaneous emission from the upper level to the lower level happens and a seed photon is generated. Amplified spontaneous emission (ASE) of such photons at the carrier wavelength, along the plasma column, creates the X-ray laser beam.

3.4.2 Experimental Affinity Ne-Like to Ni-Like Ions

Ref. [343] claimed a heuristic affinity between a given Ne-like X-ray laser and a Ni-like X-ray laser radiator based on five cases, i.e., $\text{Fe}^{+16} \rightarrow \text{Ag}^{+19}$, $\text{Co}^{+17} \rightarrow \text{Cd}^{+20}$, $\text{Ni}^{+18} \rightarrow \text{In}^{+21}$, $\text{Cu}^{+19} \rightarrow \text{Sn}^{+22}$, and $\text{Zn}^{+20} \rightarrow \text{Sb}^{+23}$ which permitted to extrapolate to other pairs such as $\text{Sc}^{+11} \rightarrow \text{Mo}^{+14}$ and $\text{Nb}^{+31} \rightarrow \text{Sm}^{+34}$. The electron temperature for Ni-like ions was studied here considering Eq. 3.4.3.1 and the affinity between Ne-like X-ray lasers and homologous Ni-like X-ray lasers [343] as below:

$$kT_{e-\text{opt}}[\text{eV}] \simeq 2.42 (Z - 27)^{1.7}, \quad 28 \leq Z \leq 79. \quad (3.4.2.1)$$

The electron density for Ni-like ions was obtained considering Eq. 3.4.3.2 and the affinity between Ne-like X-ray lasers and their homologous Ni-like X-ray lasers [343] as below:

$$n_{e-\text{opt}}[\text{cm}^{-3}] \simeq 1.45 \cdot 10^{14} (Z - 27)^{4.65}, \quad 28 \leq Z \leq 79. \quad (3.4.2.2)$$

Similarly, the electron density to optimize the gain coefficient for Ni-like ions was obtained by considering Eq. 3.4.3.3 and the affinity between Ne-like X-ray lasers and their homologous Ni-like X-ray lasers [343] as below:

$$n_{e-\text{opt}}[\text{cm}^{-3}] \simeq 3.9 \cdot 10^{12} (Z - 27)^{6.7}, \quad 28 \leq Z \leq 79. \quad (3.4.2.3)$$

3.4.3 Scaling-laws for Neon-like Plasma Lasers

The optimum plasma conditions in Ne-like XPL have been well characterized previously. Elton [90] considered that the optimum electron *temperature* should be 1/3 of the ionization energy of the ions, which modeled $T_{e-\text{opt}}$ as follows:

$$kT_{e-\text{opt}}[\text{eV}] = 5.7 (Z - 9)^{1.5}, \quad Z \geq 10 \quad (3.4.3.1)$$

where Z is the atomic number of Ne-like ions. Gupta et al. [119], estimated the optimum electron temperature for the Ne-like to be T_e that maximizes the Ne-like XPL gain. They found the T_e that maximizes the Ne-like ions abundance, maximizes the Ne-like XPL gain as well. Elton also considered the optimum value of the electron *density* to occur when the plasma has 1/2 of the electron density required for collisional equilibrium, such that $n_e C_{21} = A_{10}$. The following expression as the optimum electron density for Ne-like ions has been proposed:

$$n_{e-\text{opt}}[\text{cm}^{-3}] = 4 \cdot 10^{15} (Z - 9)^{3.75}, \quad Z \geq 10. \quad (3.4.3.2)$$

Li et al. [180], derived another Z -scaling law for the optimum temperature, under the condition $kT_e = \Delta E_{20}/2$, where ΔE_{20} is excitation energy from the ground state to the upper laser level of Ne-like ions. The optimum electron density to optimize the gain coefficient for Ne-like ions has been given as follows [180]:

$$n_{e-\text{opt}}[\text{cm}^{-3}] = 0.57 \cdot 10^{14} (Z - 8.8)^{6.1}, \quad Z \geq 10. \quad (3.4.3.3)$$

3.4.4 Scaling-laws for Nickel-like Plasma Lasers

In order to predict the Ni-like plasma optimum conditions two approaches are investigated, namely (i) analytical scaling-laws and (ii) numerical solutions, both validated against a selection of literature data. Considering analytical laws for Ni-like lasers, we begin with discussing scaling-laws' extrapolation from Ne-like systems. The heuristic affinity model proposed in Ref. [343] is also discussed. Regarding numerical modeling, we computed the optimum temperature and density for sufficient radiator's population within the LTE and NLTE model. Further, optimum density and temperature leading to a strong monopole collisional pumping and population inversion is addressed, see Fig. 3.21. Finally, the analytical and numerical solutions are compared.

A number of approaches to derive analytical scaling laws for optimum plasma conditions to obtain Ni-like lasing were compared. To begin with we indicate the specific approaches and adopted models. Below (Sect. 3.4.7) we will compare the predicted values from the various scaling laws and comment on their accuracy to agree with benchmarking data from the literature.

Adopting different models for Ne-like ions found in the literature, we extrapolated for the case of Ni-like ions. From Elton's criterion, namely that the optimum temperature should be approximately 1/3 of the *ionization* energy of Ni-like ions, we considered the ionization potentials from Ref. [51, 173], thus obtaining the following power-law formulas for the optimum electron temperature of Ni-like ions:

$$kT_{e-opt}[eV] \simeq 2.75 (Z - 27)^{1.6}, \quad 28 \leq Z \leq 79. \quad (3.4.4.1)$$

Following the Li criterion [180], we alternatively considered that the optimum temperature should be 1/2 of the *excitation* energy from ground state to upper state of Ni-like ions. With this assumption, we obtained the following power-law scaling for the optimum electron temperature namely,

$$kT_{e-opt}[eV] \simeq 2.15 (Z - 27)^{1.6}, \quad 28 \leq Z \leq 79. \quad (3.4.4.2)$$

Considering the optimum electron density as 1/2 of the electron density required for collisional equilibrium, finally the optimum electron density based on this criterion is obtained for two Z ranges as follows:

$$\begin{aligned} n_{e-opt}[cm^{-3}] &\simeq 1.85 \cdot 10^{15} (Z - 27)^{3.8}, \quad 28 \leq Z < 53 \\ n_{e-opt}[cm^{-3}] &\simeq 1.5 \cdot 10^{13} (Z - 27)^{5.4}, \quad 53 \leq Z \leq 79. \end{aligned} \quad (3.4.4.3)$$

3.4.5 Nickel-like Ion Population

To obtain strongly amplified X-ray emission, it is necessary to have a sufficiently intense laser pump pulse irradiating the target in order to generate a plasma column with a sufficient population of the Ni-like ions. Here, we present the optimum temperature for a sufficient population of the Ni-like ions using both the LTE and NLTE models (see Fig. 3.21). In the NLTE model, we consider the effect of dielectronic recombination on Ni-like ions abundance.

3.4.5.1 LTE Numerical Description

The LTE condition based on McWhirter's criterion [138] is only applicable when the collision rate is significantly larger than radiative decay rate. Solving Eq. 3.4.1.10 a scaling law for the electron temperature to maximize ionic abundance at $n_e = 10^{21} cm^{-3}$ is obtained as follows, for two atomic ranges respectively:

$$\begin{aligned} kT_{e-max}[eV] &\simeq 1.42 (Z - 27)^{1.35}, \quad 28 \leq Z < 53 \\ kT_{e-max}[eV] &\simeq 0.875 (Z - 27)^{1.52}, \quad 53 \leq Z \leq 79. \end{aligned} \quad (3.4.5.1)$$

Fig. 3.22 shows the ion fractional abundance versus electron temperature at $n_e = 10^{21} cm^{-3}$ in LTE for a selection of Ni-like radiators. Such optimum values of the electron temperature can be approximated as follows:

$$\begin{aligned} 0.77 \lesssim T_{e-opt}/T_{e-max} \lesssim 1.25, \quad 28 \leq Z < 53 \\ 0.8 \lesssim T_{e-opt}/T_{e-max} \lesssim 1.2, \quad 53 \leq Z \leq 79. \end{aligned} \quad (3.4.5.2)$$

In the LTE model the electron density will affect the temperature required to maximize the Ni-like ionic fraction. Henceforth, the electron temperature that maximizes the Ni-like ion abundance can be approximated as follows:

$$\begin{aligned} kT_{e-max}[eV] &\simeq 10^{-2} n_e^{0.1025} (Z - 27)^{1.35}, \quad 28 \leq Z < 53 \\ kT_{e-max}[eV] &\simeq 9.74 \cdot 10^{-3} n_e^{0.093} (Z - 27)^{1.52}, \quad 53 \leq Z \leq 79. \end{aligned} \quad (3.4.5.3)$$

The Saha equation, which determines the degree of ionization of the plasma is only valid in LTE systems where thermal collisional processes impose a Maxwell-Boltzmann (MB) distribution.

In the case of a short-pulse laser-generated plasma, the plasma evolution time is short for electrons to thermalize during the laser pulse duration (Eq. 3.4.0.2). Indeed, in ultrafast processes the assumption of LTE is violated. Hence, we investigated the optimum conditions for a Ni-like plasma also in the NLTE condition considering collisional, radiative, and dielectronic recombination processes.

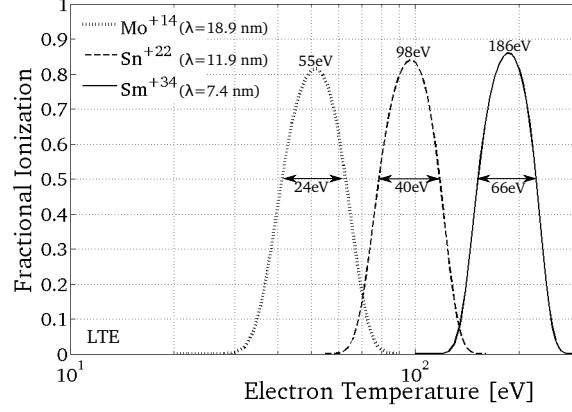


Fig. 3.22: Ion fractional abundance in a selection of Ni-like plasma lasers versus electron temperature at the electron density $n_e = 10^{21} \text{ cm}^{-3}$ for the LTE model. Increasing the atomic number of the lasing ions, the required temperature also increased. Values at the top indicate the temperature of maximum ionic abundance. Full width of distributions is given at 50% of fractional ionization.

3.4.5.2 Non-LTE Numerical Description

For lasing, the pump pulse has to deposit enough energy into the plasma to reach the Ni-like ionization stage while also generating the population inversion necessary, in far from equilibrium kinetics. Solving Eq. 3.4.1.5, a scaling law for the electron temperature to maximize ionic abundance at $n_e = 5 \cdot 10^{20} \text{ cm}^{-3}$ (see Eq. 3.4.0.1) in the NLTE plasma in the absence of dielectronic recombination (dielectronic recombination) for Ni-like ions was found to be:

$$\begin{aligned} kT_{e-max}[\text{eV}] &\simeq 9.8 \cdot 10^{-2} (Z - 27)^{2.4}, \quad 28 \leq Z < 53 \\ kT_{e-max}[\text{eV}] &\simeq 3.02 \cdot 10^{-2} (Z - 27)^{2.75}, \quad 53 \leq Z \leq 79. \end{aligned} \quad (3.4.5.4)$$

Moreover, a scaling law at $n_e = 5 \cdot 10^{20} \text{ cm}^{-3}$ in the NLTE plasma *with* including the dielectronic recombination for Ni-like ions was found to be:

$$\begin{aligned} kT_{e-max}[\text{eV}] &\simeq 8.5 \cdot 10^{-2} (Z - 27)^{2.6}, \quad 28 \leq Z < 53 \\ kT_{e-max}[\text{eV}] &\simeq 3.2 \cdot 10^{-2} (Z - 27)^{2.91}, \quad 53 \leq Z \leq 79. \end{aligned} \quad (3.4.5.5)$$

Fig. 3.23 shows the ion fractional abundance in NLTE as a function of electron temperature at the electron density of $5 \cdot 10^{20} \text{ cm}^{-3}$ *with* and *without* considering dielectronic recombination. One notes that with increasing atomic number, the peak abundance of Ni-like ion in the plasma decreases. This suggests a reduction of lasing population at short wavelengths by high- Z targets. The range of optimum values of T_e in Fig. 3.23 is defined as follows:

$$\begin{aligned} 0.7 \lesssim T_{e-opt}/T_{e-max} &\lesssim 1.4, \quad 28 \leq Z < 53 \\ 0.8 \lesssim T_{e-opt}/T_{e-max} &\lesssim 1.3, \quad 53 \leq Z \leq 79. \end{aligned} \quad (3.4.5.6)$$

Fig. 3.23 shows the temperature shift for peak population that is required to compensate for dielectronic recombination. The change in temperature range at 50% fractional ionization, with and without dielectronic recombination, is also shown. It is shown that considering dielectronic recombination, a larger temperature-shift for higher- Z elements occurs and the lasing populations are also broader.

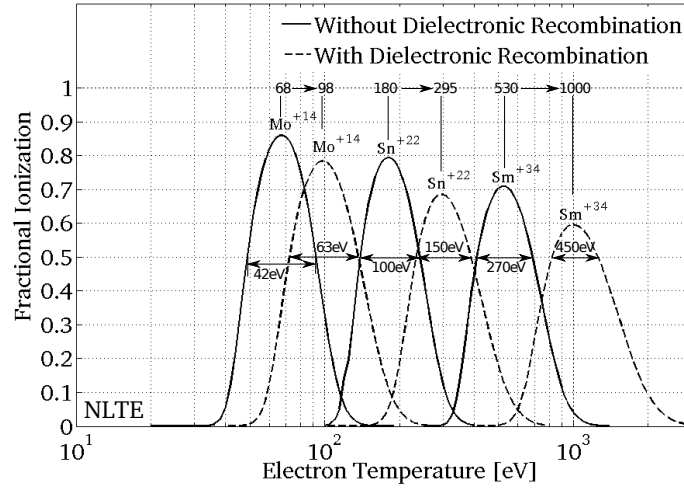


Fig. 3.23: Ion fractional abundance for NLTE in a selection of Ni-like plasma lasers, as a function of electron temperature. The electron density was $n_e = 5 \cdot 10^{20} \text{ cm}^{-3}$, and results with and without considering the dielectronic recombination (dielectronic recombination) are shown. Taking into account dielectronic recombination, the temperature that maximizes ionic abundance increased. Increasing the atomic number, the abundance of Ni-like ions decreased. Values at the top indicate the temperature of maximum ionic abundance.

3.4.5.3 LTE vs. Non-LTE frameworks

Comparison of Fig. 3.22 and Fig. 3.23 shows that increasing the atomic number (Z) the temperature difference at the peak abundance of Ni-like ions increases. However, the lasing process across the plasma medium is influenced by the average ionization degree, rather than population peaks.

Fig. 3.24 summarizes the average Sn ionization degree (\bar{z}) as a function of the temperature at different electron densities, for different modeling approaches. Fig. 3.24. a is obtained by solving Eq. 3.4.1.5. It is shown that for temperatures above 300 eV, the electron density will not affect the generation of Ni-like ions ($\bar{z} = 22$ for Sn). The ionization is also virtually independent of the temperature fluctuation, which is possibly due to bottleneck ionization. Fig. 3.24. b shows NLTE results while using the FLYCHK code, which implements a more complete CR treatment. In Fig. 3.24. a and Fig. 3.24. b, the results are in substantial agreement for the low and middle density values considered. The agreement with the $n_e = 10^{22} \text{ cm}^{-3}$ case is limited to the low temperatures like the LTE model. For comparison, results from the widely adopted LTE (collisional) approach are shown. Fig. 3.24. c is obtained by solving Eq. 3.4.1.10. It shows that at high density the average ionization drops in the 95 – 140 eV temperature range. The differences between the various densities are less strong for $T_e > 100 \text{ eV}$. A cross-over of the three curves is also noticed at approximately 25 eV because pressure ionization becomes important as the temperature becomes softer. Fig. 3.24. d shows results adopting the Saha equation in FLYCHK. The drop in ionization while considering the high density curve is confirmed, but it persists throughout the entire temperature range considered. It is noteworthy that the predicted temperature for Ni-like Sn within the LTE framework is factor of 3 lower than for the NLTE.

In the framework of a XPL generated by means of multiple pulses, i.e., pre-pulses/main pulse, the kinetics of the plasma medium is not only dictated by the pulse duration, but also by the pre-pulse and main-pulse delay. Delays of several ns between the pre-pulses could provide sufficient thermalization time to adopt a LTE regime, even if the individual pulses are ps-pulses. On the other hand, delays of tens of ps between the pre-pulse and the main pulse may demand a NLTE treatment. In this respect, a hybrid approach may provide the most realistic predictions. In the analysis above, we showed the predictions as obtained by the "pure states", i.e., collisional or coronal. We stress that the effective prediction must be tailored to the specific experimental cases.

3.4.6 Gain Across the Laser-produced Plasma

The condition discussed above for attaining a Ni-like lasing population is necessary but it is not sufficient. For lasing one needs population inversion within the Ni-like ion levels (see Fig. 3.21). The optimum collisional pumping temperature leading to inversion will be presented in this section. Moreover, the optimum density and temperature for lasing across the plasma medium for Ni-like radiators is studied considering both optically thick and thin plasmas.

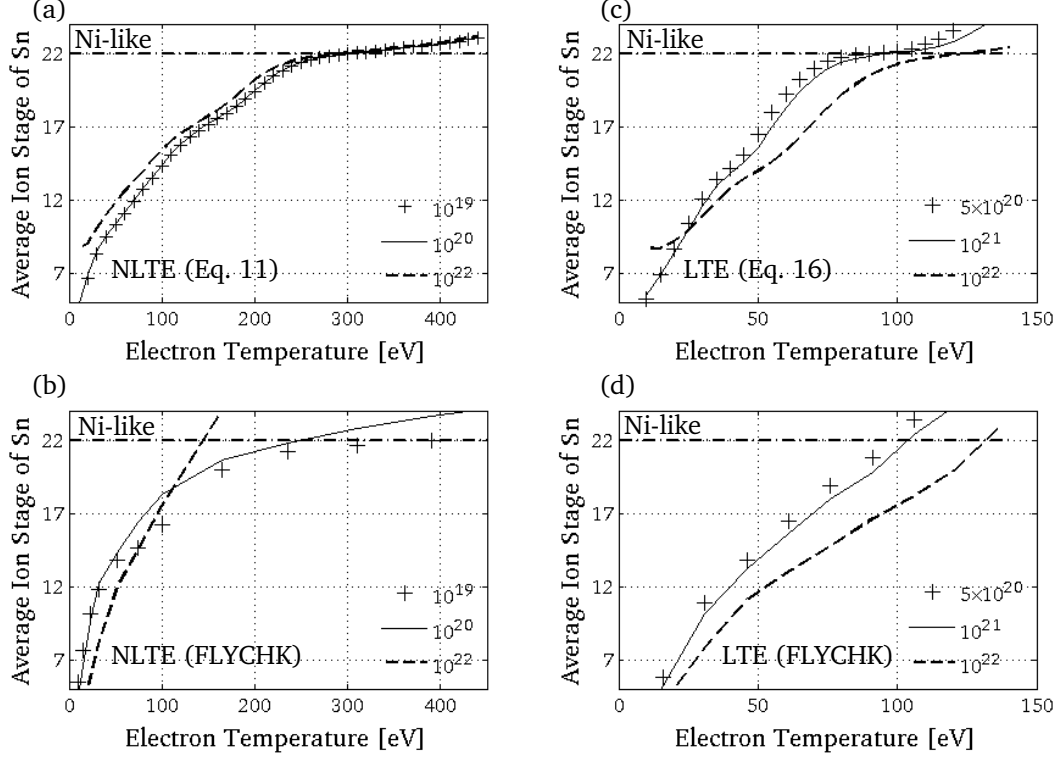


Fig. 3.24: Sn ionization in the plasma as a function of temperature at different electron densities. (a) NLTE solving Eq. 3.4.1.5, (b) NLTE from the collisional-radiative model in the FLYCHK public code, (c) LTE solving Eq. 3.4.1.10, and (d) LTE from the Saha equation using the FLYCHK code. Eq. numbers in the figure as given in the original publication [205].

3.4.6.1 Collisional Pumping

Fig. 3.21. b summarizes calculated collisional coefficients for population (open symbols) and de-population (full symbols) of the upper laser level, as a function of the electron temperature. It shows that with increasing temperature the collisional de-excitation decreases meanwhile the collisional pumping increases, especially in the first hundreds of eV. Further, the dominant pumping is collisional from the coefficient C_{02} . Due to the selection rule the transition from lower level ($J=0$) to upper level ($J=0$) is only achieved by monopole collisional excitation (see Fig. 3.21. a), that is why the effect of self photo-pumping (dipole excitation) is not considered.

Fig. 3.21. b shows that the values of C_{02} and C_{12} increase with increasing temperature, but at a specific temperature starts to decrease, i.e., $kT_e \sim 1370$ eV and $kT_e \sim 300$ eV respectively. This may be explained by noting that collisional de-excitation may tend to destroy population inversion at excessive temperatures.

Fig. 3.25 shows the monopole collisional pumping coefficient (C_{02}) for a selection of Ni-like lasing ions. The coefficients (C_{02}) increase with increasing temperature, but above the maximum temperatures start to decrease. Calculated collisional pumping rates from the ground state to upper lasing level (C_{02}) is in agreement with calculation in Daido et al. [66]. We derived the temperature for which monopole collisional pumping coefficients of Ni-like ions are maximum to

be:

$$kT_{e-opt}[eV] \simeq 12.5(Z - 27)^{1.5}. \quad (3.4.6.1)$$

Fig. 3.25 confirms that for the pumping of a X-ray Ni-like laser, a temperature of several hundreds eV is required, but temperatures close to the keV range suppress the pumping mechanism and the C_{02} rate starts to decrease. The inversion temperatures are indicated in Fig. 3.25, and vary between 0.72 and 2.58 keV from Mo to Sm.

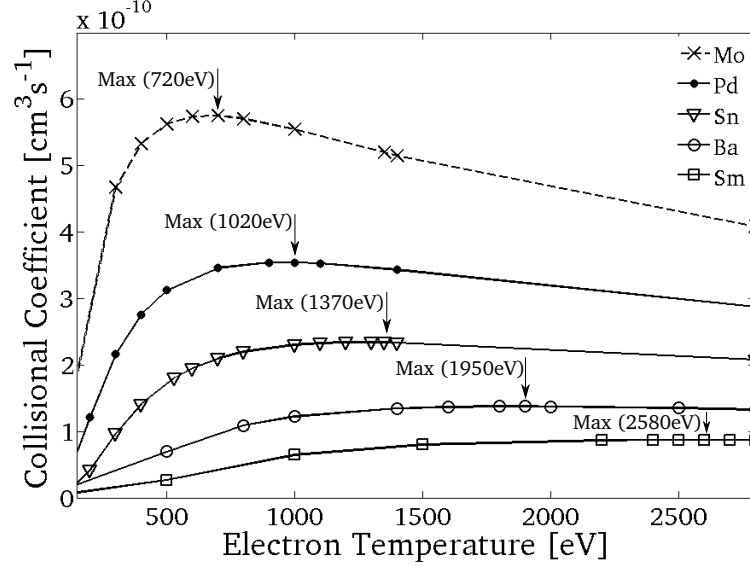


Fig. 3.25: Calculated monopole collisional pumping coefficients (C_{02}) as a function of the electron temperature for a selection of Ni-like targets. The coefficients (C_{02}) increased while increasing the temperature, but above the indicated inversion temperatures they decreased. The calculated coefficients are in agreement with values in Daido et al. [66].

The inversion temperature can be predicted as a power law formula as follows:

$$kT_{e-opt}[eV] \simeq 2.75(Z - 27)^{1.5}. \quad (3.4.6.2)$$

So far, we obtained multiple Z scaling laws for the optimum electron temperature and density in the XPL plasma. In the following step, we computationally analyze the limiting condition for having positive inversion factor.

Finally, a comparison of Fig. 3.22, Fig. 3.23, and Fig. 3.25 shows that at the temperature that the value of C_{02} can be maximum the ionic fraction of Ni-like ions is negligible. When the temperature of plasma increases, the temperature that maximizes the ionic fraction of Ni-like ions will be shifted to the larger values [86]. Indeed, when the electron temperature increases, the effect of the dielectronic recombination will increase as well.

3.4.6.2 Population Inversion

Achieving XPL requires a high electron temperature to sufficiently produce a population inversion. During the heating of the plasma with the main pulse, both the 4p (lower) and 4d (upper) laser levels are populated by electron collisional excitation (Fig. 3.21. a). The 4p-3d spontaneous decay is faster than the 4d-4p laser transition so that a population inversion builds up. Table 3.5 gives the calculated energies for the upper and lower level for a selection of Ni-like ions, and the relative radiative life times calculated with FAC. Additionally, it presents XPL wavelengths from FAC and the relative error, which is calculated as $\epsilon = \frac{\lambda_{FAC} - \lambda_X}{\lambda_X}$. Furthermore, Table 3.5 shows that with increasing atomic number the ratio of upper/lower radiative life-times (t_{21}/t_{10}) are increasing.

Tab. 3.5: Calculated Ni-like 4d-4p laser levels above the ground state, and radiative lifetimes for both the 4d \rightarrow 4p (t_{21}) and 4p \rightarrow 3d (t_{10}) transitions for a selection of Ni-like ions. The lasing wavelengths obtained computationally with the FAC code (λ_{FAC}) and their relative accuracy ($\epsilon = \frac{\lambda_{FAC} - \lambda_X}{\lambda_X}$) with respect to the experimental wavelengths (see λ_X in Tab. 3.4) are given.

Z	Ion	E_2 [eV]	E_1 [eV]	t_{21} [ps]	t_{10} [ps]	λ_{FAC}	ϵ
42	Mo ⁺¹⁴	322	250	29	11	17.2	-9%
46	Pd ⁺¹⁸	460	371	28	7	13.9	-5%
47	Ag ⁺¹⁹	498	405	27	7	13.3	-4%
48	Cd ⁺²⁰	537	440	27	6	12.8	-3%
50	Sn ⁺²²	619	514	26	5	11.8	-1%

Considering the steady state in a three-level model, lower (n_1) and upper (n_2) laser state populations can be calculated as follows:

$$\begin{aligned} n_1 &= \frac{(C_{21}n_e + C_{20}n_e + A_{21})(C_{01}n_en_0) + (A_{21} + C_{21}n_e)(C_{02}n_en_0)}{(C_{21}n_e + C_{20}n_e + A_{21})(C_{10}n_e + C_{12}n_e + A_{10}) - (A_{21} + C_{21}n_e)(C_{12}n_e)} \\ n_2 &= \frac{(C_{12}n_e)(C_{01}n_en_0) + (C_{10}n_e + C_{12}n_e + A_{10})(C_{02}n_en_0)}{(C_{21}n_e + C_{20}n_e + A_{21})(C_{10}n_e + C_{12}n_e + A_{10}) - (A_{21} + C_{21}n_e)(C_{12}n_e)}. \end{aligned} \quad (3.4.6.3)$$

Here n_0 is the electron population density in the ground state, i.e. 3d¹⁰ in the Ni-like system. For having population inversion ($\gamma_1 n_2 > \gamma_2 n_1$), the following equation must be satisfied:

$$\gamma_1 n_e \beta + \gamma_1 A_{10} C_{02} > e^{\frac{\Delta E_{12}}{kT_e}} \gamma_1 n_e \beta + \gamma_2 A_{21} (C_{01} + C_{02}) \quad (3.4.6.4)$$

where $\beta = C_{01}C_{12} + C_{10}C_{02} + C_{02}C_{12}$. In order to find the upper limit for obtaining population inversion, we find the limit where Eq. 3.4.6.4 is not valid. In fact, it is not valid at a temperature $kT \rightarrow \infty$ (e.g., for Ni-like Sn, $C_{01} > 14 \cdot C_{02}$ with considering $\gamma_2 = 1, \gamma_1 = 3$, and $A_{10} \approx 5 \cdot A_{21}$). When $kT \rightarrow \infty$, values of C_{02} and C_{12} will be negligible, i.e., $n_2 \rightarrow 0$.

3.4.6.3 Amplified Spontaneous Emission

Considering Eq. 3.4.1.1, a ratio between n_2 to n_1 can be obtained. Then by using this ratio, considering the inversion factor F , and $n_2 \gg n_0$ ($\varepsilon \rightarrow 0$), the following expression for n_e can be obtained:

$$n_e [cm^{-3}] \simeq \frac{3(1-F)G_{10}(\tau_c)A_{10} - A_{21}}{3C_{12}(e^{\frac{\Delta E_{12}}{kT_e}} - (1-F))} \quad (3.4.6.5)$$

Considering an optically thin plasma ($G_{10}(\tau_c) = 1$), Eq. 3.4.6.5 can be written as a Z -scaling law with temperature dependence as follows:

$$n_e [cm^{-3}] \simeq 1.8 \cdot 10^{13} (Z - 27)^3 (kT_e)^{1.5}. \quad (3.4.6.6)$$

The Eq. 3.4.6.6 was obtained by substituting C_{12} into Eq. 3.4.6.5, setting $F = 0$, and $kT_e > \Delta E_{12}$ due to the fact that the temperature of the lasing plasma is approximately 3 to 9 times higher than the energy difference between upper and lower level. Furthermore, Eq. 3.4.6.5 shows that for a non-zero inversion factor ($F \neq 0$) the electron density of an optically thin lasing-plasma will be limited to an electron density lower than Eq. 3.4.6.6.

In the present work, we considered that the highest temperature for Ni-like lasing is that one for which $C_{02} \approx C_{21}$. Increasing temperature, the value of C_{12} starts to decrease earlier than the value of C_{02} (see Fig. 3.21). Considering this condition, we calculated the electron temperature in the plasma which effectively influences the XPL gain achieved. We computed that plasma-lasing of Ni-like ions is feasible within a limited electron density and temperature for which a gain criterion $F > 0$ holds. One such limit is set by the electron collisional excitation population and based on our calculations restricts the lasing operation to temperatures of the following value:

$$kT_{e-opt} [eV] \simeq 13(Z - 27)^{1.5}. \quad (3.4.6.7)$$

when C_{12} and C_{02} start to decrease, the population of the upper level (n_2) also will decrease. Substituting Eq. 3.4.6.7 in the Eq. 3.4.6.6, at this temperature electron collisional coefficients between laser levels limit the electron density of an optically thin plasma as follows:

$$n_{e-opt}[cm^{-3}] \simeq 8.4 \cdot 10^{14} (Z - 27)^{5.25}. \quad (3.4.6.8)$$

Fig. 3.26 shows that increasing the optimum Z -normalized electron density is associated with a $(kT_e)^{1.5}$ of the Z -normalized electron temperature. Fig. 3.26 shows the modest increase of the electron density with the temperature, assuming an optically thin plasma ($G_{10}(\tau_c) = 1$) and by allowing the escape factor $G(\tau_c)$ to become less than unity with increasing opacity on the resonance lines. When A_{10} becomes $G(\tau_c)A_{10}$, the value of spontaneous emission rate from lower level to ground state decreases ($G(\tau_c) < 1$), which means the beginning of the destruction of the population inversion between lower and upper levels (lasing levels).

Using $\lambda_{21}[nm] = \frac{1240.6}{\Delta E_{21}[eV]}$ and the scaling of the excitation energy from the ground state (Ni-like ion) to the upper laser level of Ni-like ions as follows:

$$\Delta E_{21}[eV] \simeq 4.4(Z - 27). \quad (3.4.6.9)$$

one obtains the scaling of λ as $(Z - 27)^{-1}$. Considering $\mu = 2Z$, $n_0 = n_i$, $n_i = n_e/\bar{z}$, assuming that the ion charge (\bar{z}) is proportional to the atomic number (Z) (e.g., for Ni-like Mo $\bar{z} = Z/3$), $T_i = T_e/3$, the oscillator strength for the lower state to the ground state transition can be written as:

$$f_{10} \simeq 1.2 \cdot (Z - 27)^{-1}. \quad (3.4.6.10)$$

Considering the value n_e from Eq. 3.4.6.6, we can define the reduced depth as follows:

$$\Delta[cm] \simeq 0.192 \cdot 10^4 d(Z - 27)Z^{-1/2}(kT_e). \quad (3.4.6.11)$$

Hence, τ_c and $G(\tau_c)$ can be expressed independently of Z by specifying the reduced depth Δ instead of the plasma-depth-scale d . Then, τ_c will be defined as $\tau_c \approx 0.0255\Delta[cm]$. It is noteworthy that $\Delta = 100$ cm corresponds to a plasma X-ray laser size (depth) $d \approx 31\mu m$ and $d \approx 11\mu m$ for Ni-like Sn at the electron temperatures of 500 eV and 1434 eV, respectively. In addition, $\Delta = 100$ cm matches to $\tau_c \approx 2.55$ and $G(\tau_c) \approx 0.36$. With increasing the opacity, the value of escape factor will decrease as well. It is also notable that due to a general scaling law for all Ni-like elements, we just analyze up to $G(\tau_c) \approx 0.36$ because the ratio of A_{10} to A_{21} is closer for middle Z -elements (e.g., for Ni-like Mo ≈ 2.6).

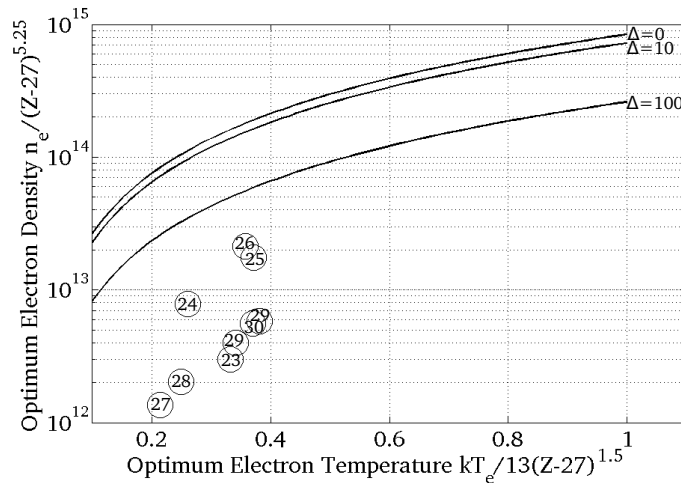


Fig. 3.26: Optimum Z -normalized electron density versus electron temperature for the population inversion threshold ($F = 0$) with considering opacity for a reduced depth $\Delta[cm] = 0.192 \cdot 10^4 d(Z - 27)Z^{-1/2}(kT_e)$. As Δ increases, inversions are achieved only at lower densities. It also shows the indicated electron density and temperature from some papers [79, 152, 194, 208, 210, 348] for Ni-like XPL, which are below the population inversion threshold.

Fig. 3.26 shows that the population inversion ($F > 0$) is limited by collisional de-population to the electron density below the boundary curve. Moreover, it shows that inversions are achieved at lower densities when Δ increases. Every value of Δ corresponds to an appropriate value of the escape factor $G(\tau_c)$. In Fig. 3.26, for executing the effect of the escape factor the coefficient $\frac{3G(\tau_c)A_{10}-A_{21}}{3A_{10}-A_{21}}$ has been multiplied by the Eq. 3.4.6.6 (the Eq. 3.4.6.6 has been obtained with considering $G(\tau_c) = 1$).

Further, in Fig. 3.26 the indicated electron density and temperature from some other works [79, 152, 194, 208, 210, 348] for Ni-like XPL are shown. Their indicated electron density and temperature are below the boundary curves.

3.4.7 Comparison Analytical vs. Numerical Models

Fig. 3.27 shows calculated optimum temperatures derived from the models presented above as a function of atomic number. Theoretical predictions in Fig. 3.27 are compared to data from references [1, 2, 7, 79, 152, 194, 195, 208–210, 213, 214, 234, 301, 348] for Ni-like XPL. The range of predicted values is quite large over more than 1.5 orders of magnitudes. The most remarkable underestimation came from Eq. 3.4.5.3 while the highest overestimate came from Eq. 3.4.6.7.

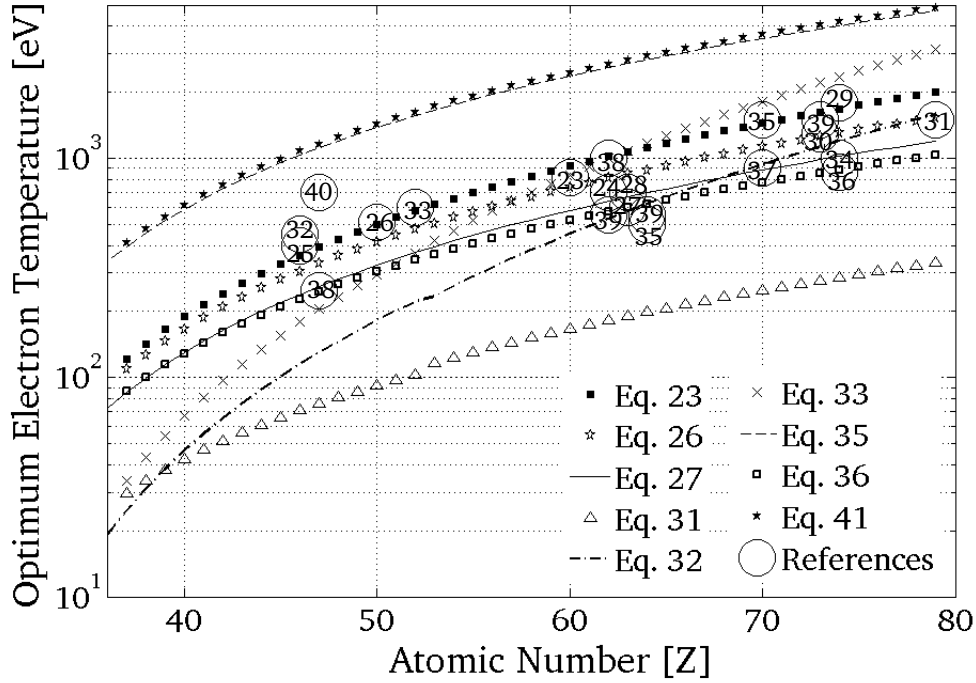


Fig. 3.27: Comparison of predicted optimum electron temperature, using the various models discussed in the text, and benchmarking data from the literature [1, 2, 7, 79, 152, 194, 195, 208–210, 213, 214, 234, 301, 348] (numbered circles) for Ni-like plasma lasers. Equations numbering and references as in the original publication [205].

The best prediction was from Eqs. 3.4.2.1, 3.4.4.1, 3.4.4.2, 3.4.6.2. Eqs. 3.4.5.5, 3.4.6.1 converged towards correct values at high Z , but their suitability at Z below 50 – 60 is poor. This indicates an incorrect Z -dependent regression of the predicted values.

Fig. 3.28 shows calculated optimum densities as a function of atomic number Z . In this context, the predictions turn out to be much less accurate than in the case of temperature. The highest predictions were from Eq. 3.4.2.3 and Eq. 3.4.6.8, which provide estimates which are up to two orders of magnitude too large. The best predictions came from Eq. 3.4.2.2 and Eq. 3.4.4.3. None of the models provided underestimates for the optimum electron density.

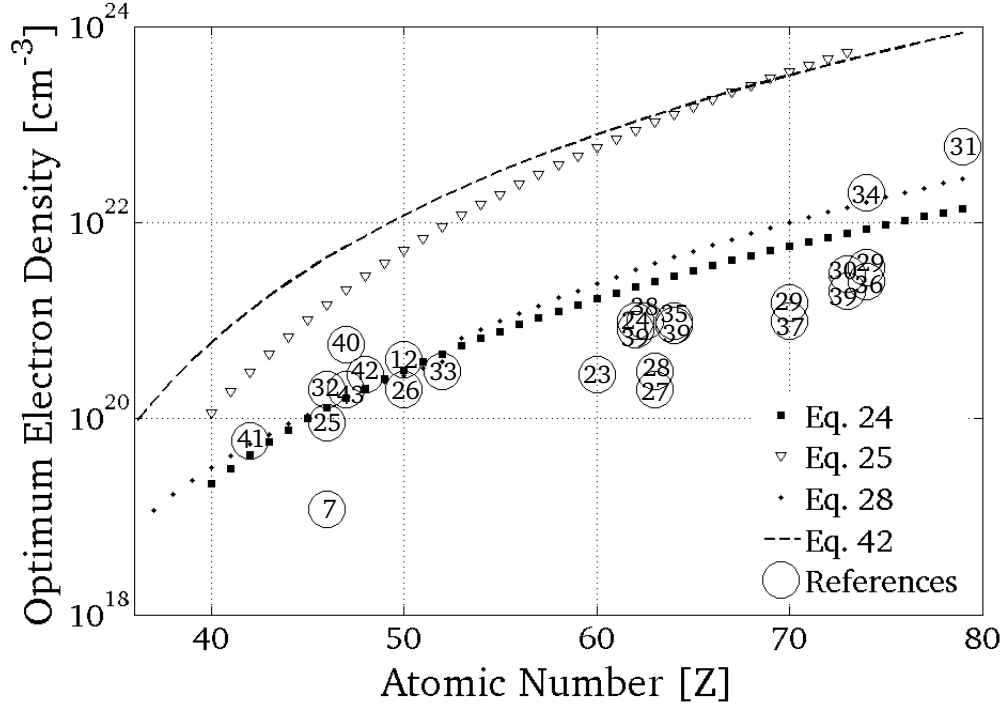


Fig. 3.28: Comparison of predicted optimum electron density, using the various models discussed in the text, and benchmarking data from the cited literature (numbered circles) for Ni-like plasma lasers. Equations numbering and references as in the original publication [205].

3.4.7.1 Optimum Electron Temperature and Density

For Ni-like lasing plasmas, a sufficient population of Ni-like ions is needed along with a population inversion between upper and lower levels. The temperature that satisfies these two conditions and maximizes monopole collisional pumping, while accounting for the fact that we are in a NLTE regime, is defined for two different atomic number ranges by the following scaling laws (Eq. 3.4.6.1):

$$\begin{aligned} kT_e[\text{eV}] &\simeq (0.36 \pm 0.15) \cdot [\text{Eq. 3.4.6.1}], \quad 28 \leq Z < 53 \\ kT_e[\text{eV}] &\simeq (0.4 \pm 0.17) \cdot [\text{Eq. 3.4.6.1}], \quad 53 \leq Z \leq 79. \end{aligned} \quad (3.4.7.1)$$

It is noteworthy that these ranges of the optimum temperature are also the best fitting of the electron temperatures from the existing literature and our scaling laws for the Ni-like lasing-plasma (see Fig. 3.27). The best fitting of the electron density from the literature and our scaling laws for Ni-like lasing-plasmas is approximated by the following Z -scaling law:

$$n_e[\text{cm}^{-3}] \simeq (1.4 \pm 1.2) \cdot 10^{13} (Z - 27)^{5.25}, \quad 28 \leq Z \leq 79. \quad (3.4.7.2)$$

The creation of a plasma with a value of kT_e and n_e around the optimum value is essential for operation of an XPL. The density as a function of temperature can be approximated by the following scaling laws:

$$\begin{aligned} n_e[\text{cm}^{-3}] &\simeq (0.64 \pm 0.52) \cdot 10^{13} (Z - 27)^{4.5} (kT_e)^{0.5}, \quad 28 \leq Z < 53 \\ n_e[\text{cm}^{-3}] &\simeq (1.1 \pm 0.4) \cdot 10^{12} (Z - 27)^3 (kT_e)^{1.5}, \quad 53 \leq Z \leq 79 \end{aligned} \quad (3.4.7.3)$$

where kT_e is in eV.

Tab. 3.6: Optimum irradiation intensity for a selection of Ni-like ions in the NLTE and LTE models for a Nd:glass as the pump-laser ($1\omega \equiv 1054\text{nm}$).

Ni-like ion	$I_{NLTE}[\text{W.cm}^{-2}]$	$I_{LTE}[\text{W.cm}^{-2}]$
Mo ⁺¹⁴	$2.6 \cdot 10^{14}$	$1.5 \cdot 10^{14}$
Sn ⁺²²	$8.0 \cdot 10^{14}$	$2.6 \cdot 10^{14}$
Sm ⁺³⁴	$2.7 \cdot 10^{15}$	$5.0 \cdot 10^{14}$

3.4.8 Plasma Gain-Medium Pumping

The plasma electron temperature is a function of the pump-laser intensity, as given by the following relation for optimized pump intensity: $I_{opt}[\text{W.cm}^{-2}] = 3 \cdot 10^{12} \frac{T_e[\text{eV}]}{\lambda^2[\mu\text{m}]} [139]$.

Tab. 3.6 summarizes the calculated optimized pump-laser intensity ($1\omega \equiv 1054\text{ nm}$) for a selection of Ni-like laser targets, following the predicted optimum temperatures discussed above. Table 3.6 illustrates that higher laser intensities are required in the case of NLTE in comparison to LTE.

The pump laser wavelength as well as the electron density can be adjusted to optimize the irradiation angle for XPL operation. Only for irradiation angles that do not exceed the plasma critical density is one able to theoretically obtain efficient short-wavelength scalability. Indeed, knowing the optimum electron density can help one optimize the optimum irradiation angles ($\theta_{opt} = \arcsin \sqrt{\frac{n_{opt}}{n_{cpump}}}$).

Knowing the optimum electron density, one can estimate feasible X-ray refraction angles in the lasing region ($\phi_r = \sqrt{\frac{n_{opt}}{n_{cXPL}}}$) [110]. The critical electron density at the frequency of the propagating ray for both a pump laser and an XPL is $n_c[\text{cm}^{-3}] = \frac{1.1 \cdot 10^{21}}{\lambda^2}$, where λ is in μm .

Fig. 3.29 shows the turning point (maximum penetration into the plasma) versus the irradiation angle (or grazing-incidence angle) for the first ($1\omega \equiv 1054\text{ nm}$) and the second ($2\omega \equiv 527\text{ nm}$) harmonics of the Nd:glass pump laser. Fig. 3.29 shows the optimum electron density versus atomic number of the different elements for Ne-like (Eq. 3.4.3.2) and Ni-like (Eq. 3.4.7.2) XPL ions.

As long as the optimum conditions are below the turning point boundary, the former are accessible for the pump laser. For Ni-like XPL ions the irradiation angle is significantly higher than that for the Ne-like, since amplification with high- Z targets requires higher electron density, found at larger depth within the plasma.

In Fig. 3.29, the fitting curve from Eq. 3.4.7.2 indicates that from $Z = 59$ (Pr target) the optimum electron density for lasing (which depends on the electron temperature, laser intensity, opacity, etc.) lies beyond the turning boundary for the pump laser operating at its fundamental wavelength (1ω). So beyond that point, non-optimized pumping for some rare earth elements (REE) targets is to be expected, unless one opts to use the second harmonic of the pump laser (2ω) at sub-normal irradiation. For some high- Z targets the optimum electron density at which lasing can occur lies in the electron density larger than $\approx 10^{21}\text{ cm}^{-3}$ and so here irradiating the target with a 2ω pump can be a solution.

Furthermore, in Fig. 3.29 the fitting curve from Eq. 3.4.7.2 indicates that from $Z = 68$ (Er target) the optimum electron density for lasing lies beyond the turning boundary for the 2ω . For these targets irradiating with a shorter wavelength pump can be a solution. Similarly, for the case of Ne-like ions at $Z = 37$ (Rb) the optimum electron densities cut off the turning boundary for the 1ω pump (see Fig. 3.29).

Tab. 3.7: Optimum electron density (Eq. 3.4.7.2, n_e), grazing-angle (θ_{opt}), and laser divergence (ϕ) for a selection of Ni-like ions.

Ni-like ion	$n_e[\text{cm}^{-3}]$	$\theta_{opt}[\text{deg}]$	$\phi[\text{mrad}]$
Mo ⁺¹⁴	$2.0 \cdot 10^{19}$	8.2	2.5
Pd ⁺¹⁸	$7.0 \cdot 10^{19}$	15.4	3.7
Sn ⁺²²	$2.0 \cdot 10^{20}$	27.0	5.1
Ce ⁺³⁰	$9.5 \cdot 10^{20}$	78.0	8.0

In addition it is worth mentioning that the shortest X-ray laser wavelengths produced by Ne-like Rb, Ni-like Pr, and Ni-like Er are 16.5 nm, 8.2 nm, and 6.48 nm, respectively. Tab. 3.7 shows the optimum electron density based on the fitting curve (Eq. 3.4.7.2), the optimum irradiation angle for a Nd:glass laser ($\lambda = 1.054 \mu\text{m}$) as a pump-laser, and a feasible X-ray refraction angle for a selection of Ni-like ions.

Table 3.7 shows that for targets with low atomic number the irradiation angle should be smaller in order to afford the optimum electron density for lasing. It also shows that for targets with high Z -number the irradiation angle should be larger. Nevertheless, the increase of irradiation angle causes a shortening of the light pass (the gain zone) longitudinally inside the laser-produced plasma. Additionally, Tab. 3.7 shows that feasible X-ray refraction from Ni-like laser-produced plasma is increasing for high- Z targets.

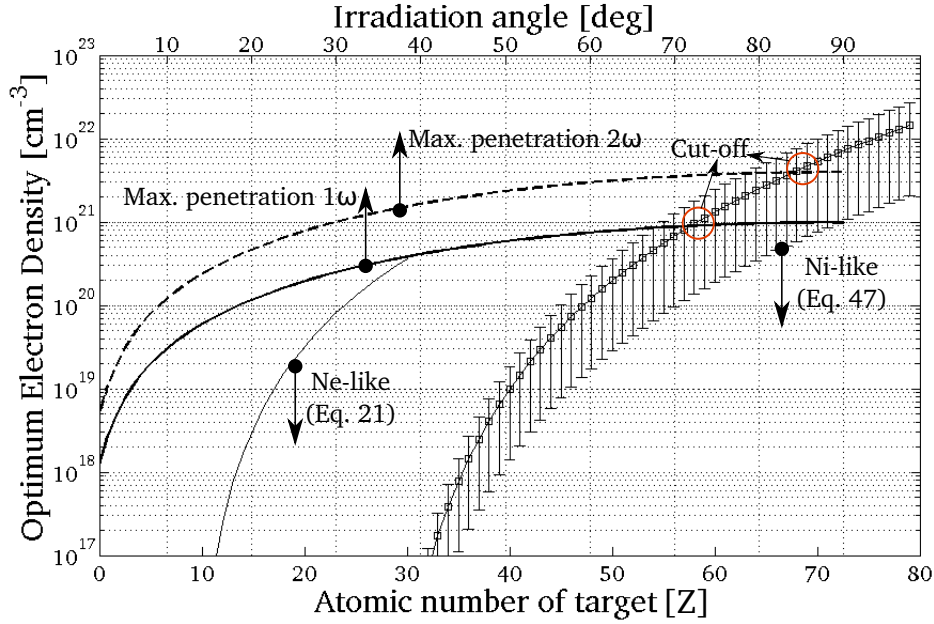


Fig. 3.29: Maximum pump penetration as a function of irradiation (grazing) angle of 1ω and 2ω Nd:glass harmonics (top axis). In addition, optimum electron densities for Ne-like ions (Eq. 3.4.3.2) and Ni-like ions (Eq. 3.4.7.2) as a function of atomic number (bottom axis) are shown. For $Z \geq 59$ (Pr) at 1ω or for $Z \geq 68$ (Er) at 2ω the optimum density cannot be reached by the pump because the curves show a cross-over (red circles).

3.4.9 Summary on Laser-produced Plasma Conditions

The optimum electron density and temperature for the Ni-like ions supporting short-wavelength laser gain across a plasma were quantitatively predicted with scaling laws as a function of the atomic number (Eq. 3.4.2.1- 3.4.4.3). The temperature that maximizes ionic abundance with two physical models, i.e., LTE and NLTE, was obtained (Eq. 3.4.5.3- 3.4.5.5) and compared to benchmarking temperatures from the literature.

It was found that in the plasma medium with increasing the atomic number, the abundance of Ni-like ions is decreasing. This suggests more stringent conditions for achieving a high-gain at shorter wavelengths, as produced using high- Z targets.

If one increases the Z -number, the difference between temperatures that maximize radiators abundance in the LTE and NLTE model grows. A shift of approximately a factor of 2 in the temperature for optimum ionic abundance was obtained with and without considering dielectronic recombination. The shifted temperature is larger for high- Z ions. This restricts the feasibility of laser amplification for high- Z radiators. The effect of the DR process is stronger for high- Z radiators, since higher temperatures are needed which enhances the recombination rates. Furthermore, a comparison between optimum temperatures for maximizing either the Ni-like ion population ($T_{ion,opt}$) or the ion level monopole-collisional-pumping ($T_{pump,opt}$) was done. Such optimum temperatures showed a Z -dependent ratio, namely $T_{ion,opt}/T_{pump,opt}$ was a factor of

$0.1-0.23$ for the mid- Z radiators ($Z < 53$) and $0.26-0.7$ for the high- Z ones. This would indicate that although high- Z radiators require more stringent optimum conditions, the attainment of optimum radiator population that are concomitantly laser-prone is somewhat more likely.

This work showed that for targets with high- Z the pump "grazing" angle should be large, such that the penetration depth into the plasma ensures the optimum electron density for plasma-lasing. Above a certain threshold a cross over takes places between the penetration depth and the location of the optimum density, with the latter lying beyond the turning point. Indeed, it was shown that for $Z \geq 59$ the optimum electron density for lasing cannot be reached using 1ω pumping. This suggests that for scaling the XPL wavelength below 6.8 nm a 2ω pump is required.

3.5 Saturation of Gain for Plasma-lasing

Published in Bleiner Appl. Phys. Lett. 101 (8), 2012. Main themes here:

- *Gain-Length Product at Saturation*
- *Effect of Plasma Column Geometry*
- *Experimental Validation of Modeling*

The generation of coherent short-wavelength photons by means of single-pass amplified spontaneous emission (ASE) across a laser-induced plasma column, commonly referred to as *X-ray laser* (XRL), has been demonstrated experimentally under various pumping mechanisms such as electron collisions [134], recombination[161], inner-shell photo-ionization [76, 263]. The temperature and electron density of the plasma gain-medium has been shown to be critical in various computational and experimental studies [90].

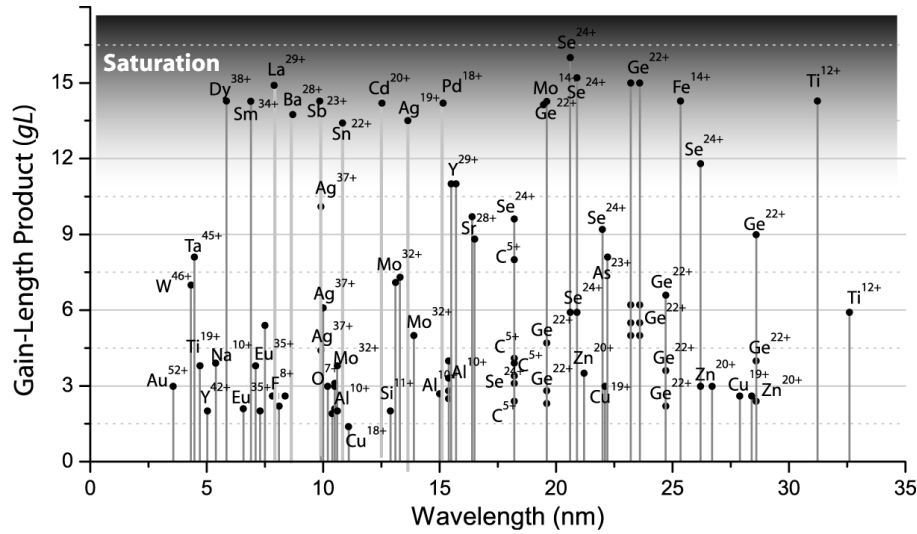


Fig. 3.30: Selection of ionic radiators used for coherent short-wavelength radiation along a laser-produced plasma column.

Traveling-wave excitation (TWE) is accomplished when irradiating the target at an angle, in order to cascade the deposition of the pump pulse. In fact, the path-difference for the pulse-front's various radial points to reach the inclined target provides a cascade-effect in laser-plasma generation. A traveling-wave is a non-dispersive "plasma perturbation" whose phase is a linear function of propagation space and time. The propagation speed of the "hot and dense plasma perturbation" is then matched to the speed of ASE propagation, obtaining a "hot plasma bath" jacketing the growing radiation field. In first approximation, e.g. neglecting line-broadening effects, gain-guiding [105, 318], etc., the ASE speed is the speed of light in vacuum. The TWE

speed is thus temporally/spatially matched with the ASE speed at grazing irradiation angle $\theta_{gr} \sim 0$, when the TWE speed (v_T) is $v_T/c = 1/\cos\theta_{gr} \approx 1$.

A large number of radiators have been reported to produce saturated short-wavelength lasing at different G_{sat} (Fig. 3.30), such that the attribution of a specific gain-length product for saturation is still debated. The ASE saturation process is typically characterized using the generalized Linford formula [318], which shows an exponential signal growth as a 1D function of plasma column length. In this regime, the signal has no significant effect on the extent of the population inversion. The spatial rate of signal output has thus constant slope, namely $\frac{dI}{dz} = g_o(\nu) \cdot I(z)$, where I is the signal intensity, z is the plasma column length, ν is the frequency, and the small signal gain is $g_o = \sigma_{ul} \cdot \Delta N_{ul}$, i.e. the product of cross-section for stimulated emission σ_{ul} between levels *up* and *low*, and the population inversion ΔN_{ul} . At *saturation*, the ASE gain drops to *half* of the small signal gain, as can be inferred from the general gain equation, when $I(z) \rightarrow I_{sat}$:

$$\frac{dI(z)}{dz} = \frac{g_o(\nu)}{1 + \gamma(\nu) \frac{I(z)}{I_{sat}}} \cdot I(z) \quad (3.5.0.1)$$

where $\gamma(\nu)$ is the spectral line-shape. The ASE is accomplished over a frequency width given by the homogeneous linewidth, centred at the nominal emission frequency. The value of the gain-length product at which the laser reaches saturation, $G_{sat} = g_{sat} \cdot L$, is thus crucial information. The growing signal during single-pass TWE, i.e. from a "seed" of background spontaneous emission (I_o), can be thus described as a function of propagation length as follows:

$$I(L) = I_o \cdot \exp[\sigma_{ul}(N_u - (g'_u/g'_l)N_l)] \cdot z \quad (3.5.0.2)$$

where g' indicates the transition coefficients (not the gain). In a hot plasma column for short-wavelength amplification, considering that the inversion lifetime is very fast compared to the amplification process, one can assume that $\Delta N_{ul} \approx N_u$. Furthermore, the length-scale l of background signal generation must be shorter than the plasma-column gain length, otherwise for $l > z$ bare spontaneous emission dominates. For plasma active volumes of isotropic geometry, any direction is likely to lead to lasing, which randomize the direction, like in so-called "random lasers" [281]. This condition is equivalent to have a low gain-length product, since the radiation characteristics would not differ significantly from the bare spontaneous emission basis. Another condition is required, i.e. that within the spontaneous seed length-scale l , the gain must be $g_l \geq 0$. Obviously, this condition is necessary to prevent self-suppression of the "noise seed" by accidental absorption whenever $g_l < 0$.

In this work, the attention is focused on the geometry of the plasma column, which is shown to be influencing the saturation gain-length product. To begin with, we will derive a scaling-law to show that G_{sat} is a non-dimensional function of plasma-column geometry, and henceforth laser focusing characteristics. Depending on the symmetry of the active volume, whether rectangular or cylindrical, an initial "black box" *Ansatz* will be developed into a set of specific scaling-laws. Finally, the scaling-law will be validated with experimental data taken from the literature, whenever complete information on the measured gain-length product for plasma-based short-wavelength laser and the focal spot was found.

3.5.1 Gain-length Product for Saturation

The plasma-column is in first approximation a "black-box" characterized by a amplification length z (Fig. 3.31). The TWE framework permits a treatment scoped to a local active-volume of length-scale l , and transverse lengths x (width) and y (height), where stimulated emission is favored. This is an important physical consideration, which simplifies the treatment. If the entire plasma-column would ignite concomitantly, ASE propagation must be treated considering the space/time-dependent cooling dynamics. This is the case in *quasi steady-state* (QSS) pumping [268] and *transient collisional excitation* (TCE) with long pre-pulse [82]. In these frameworks, yet not in TWE, concomitant and contending "hot spots" of ASE co-evolve, resulting in a "multi-mode" bi-directional large-divergence output. On the other hand, TWE favours co-moving amplification in a "low-mode" uni-directional regime. The resulting homogeneous illumination output is crucial in the perspective of using coherent short-wavelength plasma radiation for laboratory-scale applications in imaging or spectroscopy.

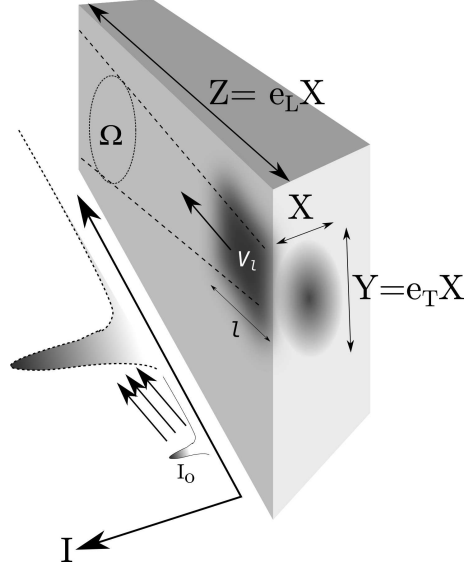


Fig. 3.31: Geometry of the plasma gain-medium with longitudinal (e_L) and transverse (e_T) aspect ratios, showing short-wavelength signal amplification from an initial spontaneous emission "seed" (I_o), within the propagation aperture (Ω). X and Y are the transverse length-scales of the active volume, l is the active volume length, whereas z is the plasma column length-scale. The aspect ratios are thus ratios of the various length scales.

The amount of "usable" spontaneous noise seed I_o , generated within the active volume V_l , is obtained from the fraction of the whole 4π -sr radiated energy that propagates within the output aperture Ω . Such energy can be written as follows:

$$E_o(V_l) = \frac{\Omega}{4\pi} (n_u V_l) h\nu_{ul} \quad (3.5.1.1)$$

or as radiated intensity:

$$I_o(V_l) = E_o(V_l) \frac{A_{ul}}{XY} \quad (3.5.1.2)$$

where n_u is the number density of the upper level population, A_{ul} is the radiative rate, and $h\nu_{ul}$ is the photon energy. The noise seed intensity amplifies exponentially while propagating as TWE along the distance z , and saturates if the following condition holds:

$$I_o \cdot e^{G_{sat}} = \frac{h\nu_{ul}}{\sigma_{ul}(\nu)\tau_{ul}} \quad (3.5.1.3)$$

Since depopulation is only by means of *radiative decay*, the lifetime and the radiative rate are related through the equation $\tau_{ul} = A_{ul}^{-1}$. Combining eqs. 3.5.1.2 and 3.5.1.3 one obtains an explicit expression of the gain-length product at saturation (G_{sat}) as a function of plasma active volume geometry. This reads, after simplification considering that $V_l = XY \cdot l = XY \cdot 1/n\sigma$, as follows:

$$G_{sat} = Ln[4\pi \frac{z^2}{XY}] \quad (3.5.1.4)$$

Depending on the geometry of the plasma "black box" one can then derive specific scaling-laws for G_{sat} .

For a *rectangular geometry* one can use the three given dimensions as characteristic length-scales x, y, z . Thus eq. 3.5.1.4 becomes:

$$G_{sat,rect} = 2.53 + 2Ln(z) - Ln(xy) \quad (3.5.1.5)$$

where in a simple case of *square cross-section* with $X=Y$ the expression simplifies to:

$$G_{sat,sqr} = 2.53 + 2Ln(\frac{z}{x}) \quad (3.5.1.6)$$

In the case of cylindrical geometry, with *elliptical cross-section*, one can exploit the fact that $XY = \pi/4 \cdot hw$, where h is the cross-section height-axis and w is the cross-section width-axis. These considerations leads to:

$$G_{sat,ell} = 2.77 + 2Ln(z) + Ln(HW) \quad (3.5.1.7)$$

In the case of *circular cross-section*, eq. 3.5.1.7 further simplifies, considering that $XY = \pi/4 \cdot d^2$ where d is the cross-section diameter. This leads to the following expression:

$$G_{sat,ell} = 2.77 + 2Ln\left(\frac{z}{d}\right) \quad (3.5.1.8)$$

Finally one can generalize eqs. 3.5.1.5–3.5.1.8 with the following expression:

$$G_{sat} = k_{geom} + 2Ln\left(\frac{z}{\sqrt{xy}}\right) \quad (3.5.1.9)$$

where k_{geom} assumes the exact values of $Ln(16)$ for cylindrical geometry, or $Ln(4\pi)$ for a rectangular geometry. The logarithmic term can be further worked-out by defining the longitudinal aspect ratio as $e_L = z/x$ and the transverse aspect ratio as $e_T = y/x$. Noting that $xy = e_T \cdot x^2$ then the following substitutions apply:

$$G_{sat} = k_{geom} + 2Ln\left(\frac{z}{\sqrt{e_T \cdot X^2}}\right) = k_{geom} + 2Ln\left(\frac{e_L}{\sqrt{e_T}}\right) \quad (3.5.1.10)$$

This provides a general scaling-law in a non-dimensional framework, which provides information on the critical value for saturation of the gain-length product. Considering that a large number of radiators have been reported to produce saturated short-wavelength lasing at different G_{sat} (Fig. 3.30), eq. 3.5.1.10 may explain the difference as non-conflicting results. These were thus possibly due to different laser pump focusing characteristics.

3.5.2 Experimental Validation

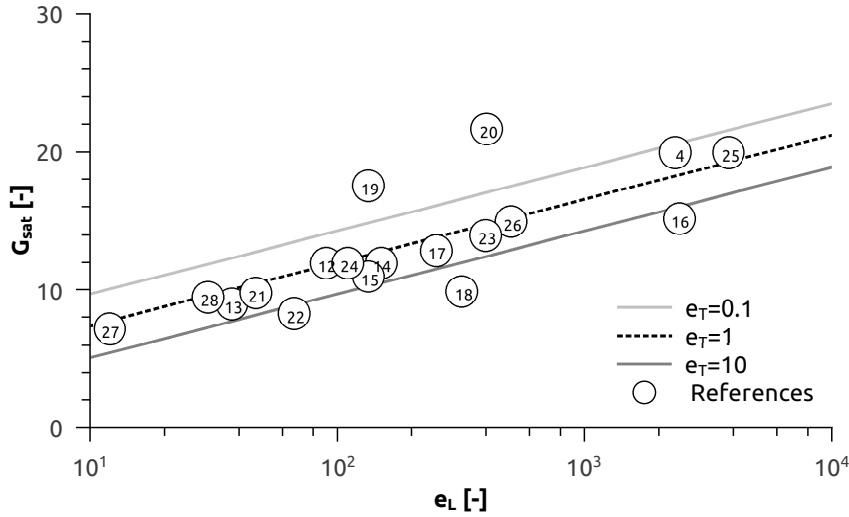


Fig. 3.32: Gain-length product at saturation (G_{sat}) as a function of longitudinal plasma aspect ratio (e_L) (eq. 3.5.1.10) for transverse aspect ratios of $e_T = 0.1, 1, 10$. Predicted trends are compared with experimental data for benchmarking. Data point label indicates the corresponding reference, as numbered in [26].

Fig. 3.32 compares theoretical predictions using the derived relation, Eq. 3.5.1.10, with experimental data from the literature. The focusing of the pump pulse largely influences the plasma-column aspect ratio, which explains the data scatter. The longitudinal aspect ratio is typically easily determined from the line focus dimensions. The transverse aspect ratio is more

difficult to characterize, since this involves precise information on the active volume's width and height. Considering the laser-plasma expansion dynamics influences the height, this may be a further source of data uncertainty. Finally, the references chosen for Fig. 3.32 did not all implement a travelling Wave Excitation (TWE) scheme, as explained in the next section. In spite of this, the good agreement indicate that the proposed scaling-law, derived within the assumptions valid for TWE, has a more general validity in predicting the saturation G_{sat} .

3.6 Traveling-wave Plasma-Excitation

Published in Bleiner et al. Appl. Optics 51, (36) 8848, 2012. Main themes here:

- *Theory of Fourier Optics*
- *Chirped Pulse Amplification (CPA) Method*
- *Pumping with a Back-Tilted Pulse-Front*

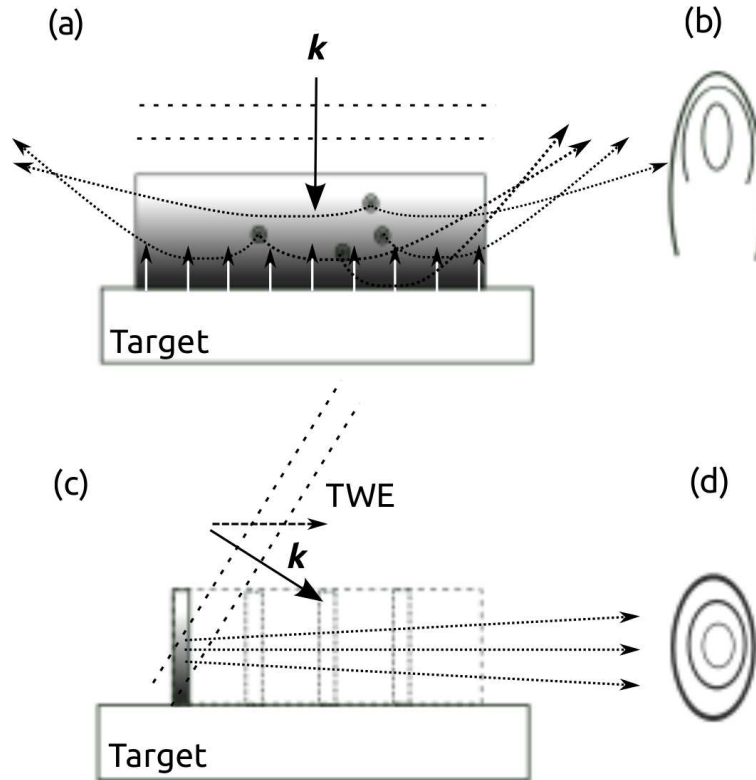


Fig. 3.33: Schematic of the laser-produced plasma column generation. In (a) a normal-incidence irradiation is shown, such that a plasma column develops "hot spots" from which beamlets amplify in a refractive medium. In (b) the beam profile is visualized. In (c) a TWE scheme is shown, which homogenizes the profile (d) of the output short-wavelength beam.

High-power laser-irradiation of matter generates hot and dense plasmas. Among the various applications, laser-produced plasmas are used as gain media to generate short-wavelength coherent light, by means of amplified spontaneous emission (ASE). The ASE process is accomplished as a high-gain single-pass along a "plasma-column" that must remain hot and dense as long as the propagating ASE front is growing till saturation. Normal-incidence irradiation (the angle is here defined between the target surface and the beam) leads to multiple counter-propagating

ASE trajectories across the entire volume of the plasma-column (Fig. 3.33.a). This splits the output between both plasma-column endings, and causes degradation of the beam collimation, due to the spread in trajectories within the output aperture. A further difficulty for single-shot normal-incidence pumping is related to the plasma lifetime. In fact, a longer plasma-column demands increasingly more pump energy, such that the plasma remains in a hot and dense quasi-steady state (known as QSS) for the entire ASE propagation [82].

A turnaround to the limitations described was introduced with transient collisional excitation (TCE), i.e. using multiple short pulses, and in particular with so-called *traveling-wave excitation* (TWE). Here the pump beam is inclined to the target (Fig. 3.33.c), such that the pump irradiates the target with a certain temporal spread between the pulse-front's leading and trailing edge. In fact, the leading edge induces the plasma a few tens of ps in advance to the trailing edge, for a plasma-column of 10-15 mm. The cascaded pulse-front deposition produces a propagating "plasma surge" that preserves its hot and dense conditions throughout, regardless the column length. Further, the TWE propagation efficiently bunches the gain towards one of the plasma-column endings. For a given irradiation angle ϑ , the nominal TWE speed is obtained as a vectorial projection of the speed of light along the plasma-column, i.e. $v_{TWE} = c / \cos \vartheta$. Ideally, the v_{TWE} must remain close to the speed of light such that the "plasma surge" and the ASE front propagate in superposition, and feedback is thus maximized. However, such a speed-matching condition is obtained for small irradiation angles of $\vartheta < 25^\circ$, considering as high as 10% deviation from $v_{TWE} \approx 1c$.

On the other hand, for *shorter wavelengths* amplification the pump pulse must be deposited deeper into the plasma, where higher electron density is found to collisionally pump higher energy states. Upon penetration across the inhomogeneous plasma medium, the pump pulse refracts away because the plasma refractive index is smaller than 1. The *turning-point* plasma density (n_{TP}), attained by pump penetration into the plasma, is computed as $n_{TP} = n_c \sin^2 \vartheta$, where n_c is the plasma critical density. Henceforth, for small irradiation angles the pump meets its turning point already at a small fraction of the critical density. For cutting-down the ASE wavelength one must thus choose large irradiation angles, in order to get as close as possible to the dense high collisional-pumping region. The latter requirement of *large* irradiation-angle poses a *trade-off* with TWE close to $1c$ that requires a *small* angle.

In this paper we investigate a technique to overcome such trade-off, by means of decoupling the TWE speed versus turning-point dependency. This is essential to permit efficient plasma-based lasing below the $\lambda = 10\text{nm}$ limit in laboratory-scale installations. The basic idea integrates with existing components of a common pump systems for realizing ASE lasing. In fact, in chirped-pulse amplification (CPA) a stretched-pulse is amplified and then recompressed using a grating pair (compressor) [5, 54, 106, 238]. The two compressor gratings must be perfectly parallel to achieve optimum recompression over the entire beam diameter. If the two gratings are not parallel aligned, a residual angular dispersion "leaks-out" in the propagating "compressed" pulse. Angular dispersion causes a tilting of the pulse-front. Indeed, in our approach the grating pair was intentionally misaligned, in order to tailor a controlled amount of pulse-front *back-tilt*, and with that compensate the TWE increase at larger ϑ (Fig. 3.34). In fact, the TWE depends

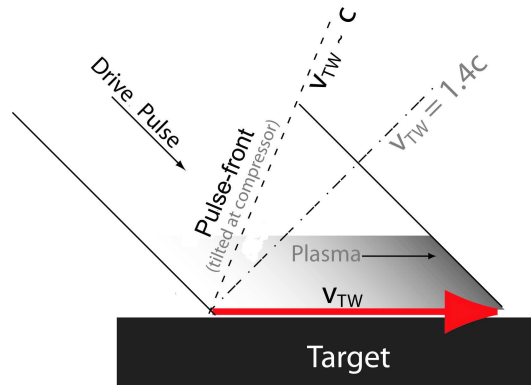


Fig. 3.34: Schematic of the pulse-front back-tilt technique to match the ASE speed with the propagation speed of the plasma traveling-wave at large angle of irradiation (here 45°).

on the pulse-front slope (envelope of amplitude), whereas the optical penetration depends on the wave-front slope (envelope of phase). Differently from the literature [109], we present a direct attempt of pulse-front tilt using the CPA setup already implemented in the pump setup, thus avoiding introducing additional components for *ad-hoc* pulse-front tilt, which may degrade throughput.

Aim of this work was thus to evaluate quantitatively the possibility of pulse *back*-tilt at large irradiation angle, in order to match the TWE speed to c . A one-dimensional Fourier optics code was written for computing the parametric dependence between the compressor misalignment and the pulse characteristics. Experimental data on the pulse structure and TWE speed were used for benchmarking.

3.6.1 Fourier Optics Theory & Model

Fourier optics considers, within the paraxial approximation, a set of superposed plane waves in order to obtain the natural modes of the propagation medium itself[114], i.e. the E field characteristics over space ($k_{x,y}$) and time. Specific transfer functions are deployed to compute the evolution of the electric field across a certain "optical element". The latter can be a lens, mirror, grating, etc. but also free space. Combination of multiple elements in an optical setup are handled with the product of the individual transfer functions.

The pulse coming from the stretcher into the compressor was modelled as a Gaussian beam with the following relation:

$$E_{stret}(k, \omega) = \left(\frac{1}{w_o} \right) \exp \left[-\frac{1}{4} (k_x \cdot w_o)^2 \right] \times \quad (3.6.1.1)$$

$$\exp \left[(\omega - \omega_o) \left(\frac{1}{4} \frac{1}{\Delta\omega} \right)^2 \right] \times$$

$$\exp \left[-i \frac{\phi_2}{2} (\omega - \omega_o)^2 \right]$$

The first term of eq. 3.6.1.1 is the axially symmetric spatial profile with Gaussian distribution in the wave-vector domain. The second term is the frequency distribution, around the central frequency ω_o . The third term is the pulse chirp.

Fig. 2.3 sketches-out the unfolded two-grating structure of the compressor as a four-grating compressor, i.e. showing grating elements (G_1 till G_4) symmetrically centred about a roof folding-mirror (M). In line of principle, both the four-grating system of Fig. 2.3 and our experimental system with two-grating in double-pass optical geometry are possible. The differences are in the factor of 2 footprint and in the fact that in the two-grating folded-design a tilt of the second grating is consistently produced in the fourth grating as well, by means of the symmetry condition. At the front-end, the imaging/focusing element (F) is shown, which reduces the pump beam to a 10–15-mm line focus.

To begin with, the free-space propagation (FSP) transfer function is expressed as follows, with propagation in the z -axis:

$$E_{FSP}(k_x, \Omega) = E_o(k_x, \Omega) \exp \left[-ikz - \frac{iz}{2k} k_x^2 \right] \quad (3.6.1.2)$$

where the FSP is applied on the input field E_o . A pulse impinging on a grating is then recomputed with the grating-dispersion (GD) transfer function, which is expressed as follows:

$$E_{GD}(k_r, \Omega) = \frac{1}{b} E_o \left(\frac{k_r + \gamma \Omega}{b}, \Omega \right) \quad (3.6.1.3)$$

where $b = \cos \alpha / \cos \beta_o$ is the beam-width change upon diffraction, where α is the angle of incidence on the grating, β_o is the angle of diffraction for the central frequency, $\gamma = \frac{2\pi M}{\omega_o G \cos \beta_o}$ is the coupling through the linearized grating equation, with M the diffraction order and G the grating constant, and $\Omega = \omega - \omega_o$ is the relative frequency with respect to the central frequency ω_o .

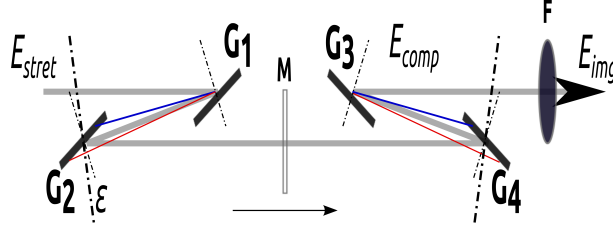


Fig. 3.35: Schematic of the compressor setup for the 1D Fourier optics computation. G is indicating the gratings, M is the folding mirror, F is the imaging optics, ϵ is the G_2 tilt angle.

In a CPA compressor, the pulses are transformed by FSP and GD such that the emerging field is computed by combination of the eqs. 3.6.1.2 and 3.6.1.3 as much as the experimental setup requires (Fig. 3.35). In the context of our double-pass compressor, a four grating system with symmetry about a folding mirror, gives the following field *amplitude* after the last compressor grating (indices refer to the specific element number as in the illustration):

$$\begin{aligned}
 E_{comp}(k_r, \Omega) &= \frac{1}{b_1 b_2 b_3 b_4} \times \\
 E_o \left(\frac{1}{b_1 b_2} \left(\frac{1}{b_3 b_4} (k_x - \gamma_4 \Omega + b_4 \gamma_3 \Omega) - \gamma_2 \Omega + b_2 \gamma_1 \Omega \right), \Omega \right) \times \\
 \exp \left[-\frac{i\Delta}{2k} \left[\left(\frac{k_x - \gamma_4 \Omega + b_4 \gamma_3 \Omega}{b_2 b_3 b_4} - \frac{\gamma_2 \Omega}{b_2} \right)^2 + \left(\frac{k_x - \gamma_4 \Omega}{b_4} \right)^2 \right] \right] \times \\
 \exp \left[-\frac{id}{k} \left(\frac{k_x - \gamma_4 \Omega + b_4 \gamma_3 \Omega}{b_3 b_4} \right)^2 \right] \times \exp [-2ik(d + \Delta)]
 \end{aligned} \tag{3.6.1.4}$$

The spectral *phase* of the propagating pulse can be expressed as a Taylor series, as follows:

$$\phi(\Omega) = \phi_o + \phi_1 \Omega + \phi_2 \frac{\Omega^2}{2} + \phi_3 \frac{\Omega^3}{6} + \dots \tag{3.6.1.5}$$

The second order phase term (*chirp*) of a grating compressor is obtained from eq. 3.6.1.4 as follows:

$$\phi_2 = -\frac{i\Delta}{k} \gamma_1^2 \Omega^2 \tag{3.6.1.6}$$

which for the present case provided values of $-1.02 \cdot 10^4$ (Ti:sapphire) and $-3.11 \cdot 10^2$ (Nd:glass). An analytical expression has been reported in the literature [73] as follows:

$$\phi_2 = \frac{\lambda_o}{2\pi c^2} \left(\frac{\lambda_o}{G} \right)^2 \frac{L}{\cos^3 \beta_o} \Omega^2 \tag{3.6.1.7}$$

with the orthogonal grating separation L . Eq. 3.6.1.7 provides values in perfect agreement with the result obtained by means of Fourier optics in eq. 3.6.1.6.

The third-order term may be also important in some cases, and Diels et al. [73] provided an analytical expression to evaluate the third-order contribution versus the second-order term, as follows:

$$R_{\phi 3/2} = \frac{\Delta\omega}{\omega_o} \left[1 + \frac{\frac{\lambda_o}{G_1} \left(\frac{\lambda_o}{G_1} + \sin \alpha_1 \right)}{1 - \left(\frac{\lambda_o}{G_1} - \sin \alpha_1 \right)^2} \right] \tag{3.6.1.8}$$

Finally, the compressed pulse is imaged on the target by means of focusing optics[32]. The target is some distance away from the last grating and the transfer function of an imaging/focusing component with the focal length f is as follows:

$$E_{img}(r, \Omega) = E_{comp}(x, \Omega) \exp \left[\frac{ik}{2f} r^2 \right] \tag{3.6.1.9}$$

The computations were performed for the two most popular pump laser systems, namely the Nd:glass with a wavelength of $1054 \pm 2\text{nm}$ (i.e. carrier wavelength and bandwidth) and for a Ti:sapphire laser with a wavelength of $800 \pm 10\text{nm}$. The Gaussian beam waist radius was $w_o = 66\text{mm}$ and focused using a $f=609.6\text{mm}$ spherical mirror under a irradiance angle (defined between the target and the beam) of 48° . The compressor had gratings with $G^{-1} = 1740\text{lpmm}$, and the chirped pulse stretch per bandwidth was 296 ps/nm , as in our experimental setup. The roof mirror had a half-distance $d = 1360\text{mm}$. The angle of incidence of the stretched pulse on the first grating was 60.8° . The imaging system had a magnification of 5:1 ($m=0.2$).

3.6.2 Calculation of Tilted Pulse-front Characteristics

The characteristics of the compressed pulse were computed as a function of grating misalignment. It was critical to quantify benefits of misalignment, i.e. the pulse back-tilt, versus the drawback, i.e. the pulse broadening. Pulse broadening causes loss of peak irradiance (power per unit surface). Variable irradiance as a function of beam radius leads to a transversely inhomogeneous plasma-column in temperature and density. Inhomogeneities cause refraction and self-absorption, thus hindering the amplification process. Henceforth, we begin discussing quantitatively how much peak power loss is generated at the uncompressed pulse boundary in a Nd:glass or Ti:sapphire pump.

Fig. 3.36 summarizes the relative pulse broadening as a function of grating tilt. The uncompressed pulse duration is normalized to the computed Fourier-limited pulse duration at the centerline (point of best compression), i.e. $\tau_o = 0.82\text{ ps}$ (Nd:glass), $\tau_o = 0.09\text{ ps}$ (Ti:sapphire). It is noted that short wavelength and small bandwidth mitigate the broadening effect, and in the present case the best compromise is provided by the Nd:glass laser. Ideally, one would like this dependence to be moderate, in order to prevent drastic changes in pulse peak power across the beam diameter. The quantification of this effect was done for a normalized pulse energy and considering the effective pulse duration in ps at the pulse boundary, which is the point of worst re-compression, in a Nd:glass and Ti:sapphire pump. Fig. 3.37 shows the ratio of the latter versus the former laser system as a function of grating tilt. One notes that the ratio increases and plateaus at approx. factor of 2, indicating that pulse broadening in a uncompressed Ti:sapphire causes as twice as much peak power deterioration than in a Nd:glass. The fact that the trend levels-off indicates that the chosen range of study for the tilt is reasonable to provide complete overview on the parametric change.

Concerning the effective control on the pulse-front slope, Fig. 3.38 summarizes the pulse tilt as a function of second compressor grating tilt. Ideally, one would like the sensitivity to be moderate, in order to facilitate the task of compressor alignment with larger tolerance. However, for the purpose of TWE velocity-matching, it would be desirable to achieve a remarkable sensitivity between pulse-front tilt and grating misalignment. One notes that the calculated dependence is a function of laser system, with the Nd:glass showing a more remarkable influence. This is in agreement with what discussed in Pretzler et al. [238] that showed that the pulse tilt was a linear function of the angular chirp times the wavelength. This indicates that a better TWE velocity-matching at large irradiation angle is achieved with the Nd:glass laser pump.

Fig. 3.39 indicates that substantial pulse back-tilt is mostly achieved through the imaging element, proportionally to the magnification, when compared with Fig. 3.38. In fact, for a given beam width, a shorter line focus means a steeper back-tilt of the pulse-front. This drastically enhances the pulse-tilt that was possible to induce after the compressor (Fig. 3.38). Therefore, it is concluded that TWE velocity-matching should be accomplished with minimal compressor misalignment and maximal imaging magnification. The misalignment of the compressor in fact causes concomitant degradation of the pulse compression, as shown above (Fig. 3.36).

Finally, the combined effect on the TWE speed is shown, as a function of compressor misalignment, in Fig. 3.40. The nominal TWE speed at irradiation angle 48° is $1.5c$ but for a compressor grating tilt of -0.5° a reduction of TWE speed down to $1.2c$ is computed for the $\lambda = 1054\text{nm}$ pump (Nd:glass).

The Beagle laser, which uses a Nd:glass pump, was used for experimental benchmarking. The system, in the current setup, has a beam of 133 mm in diameter that is focused onto the target over a line-focus of 12 mm . This configuration gives an imaging ratio of 11:1 ($m=0.09$). Fig. 3.41 shows, for the University of Bern system, the calculated interrelation between pulse-front tilt and concomitant pulse uncompression, expressed as duration at the boundary (worst

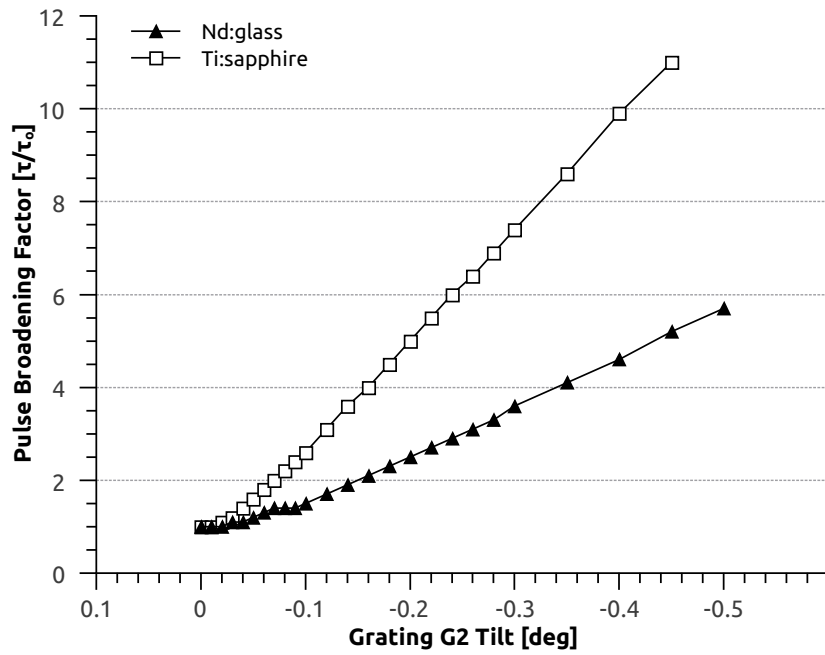


Fig. 3.36: Pulse broadening at the beam boundary as a function of compressor misalignment.

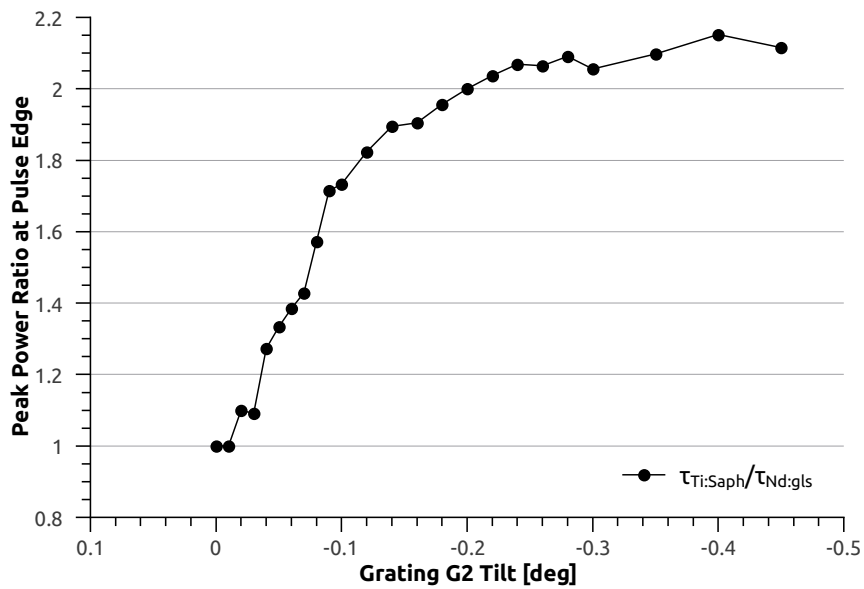


Fig. 3.37: Ratio of peak power in a uncompressed Ti:sapphire versus Nd:glass pulse as a function of compressor misalignment.

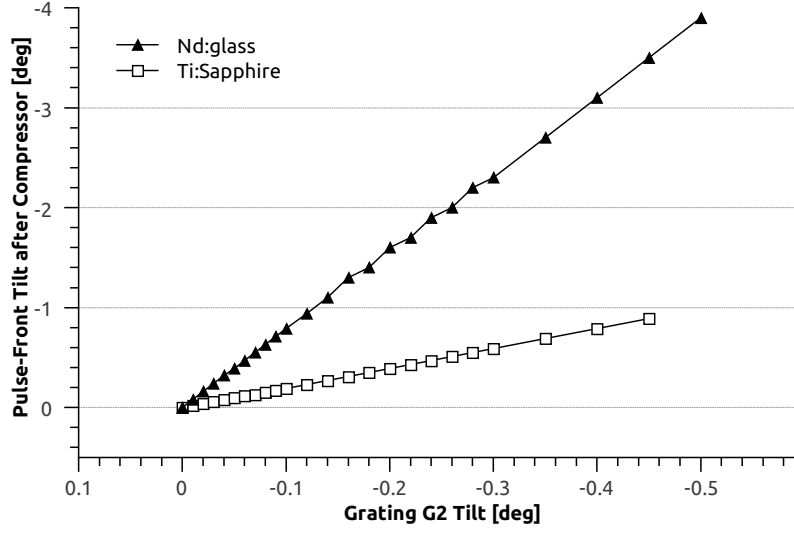


Fig. 3.38: Pulse-front back-tilt right after the compressor (E_{comp} in Fig. 3.35) as a function of compressor misalignment, and for a selection of laser pumps.

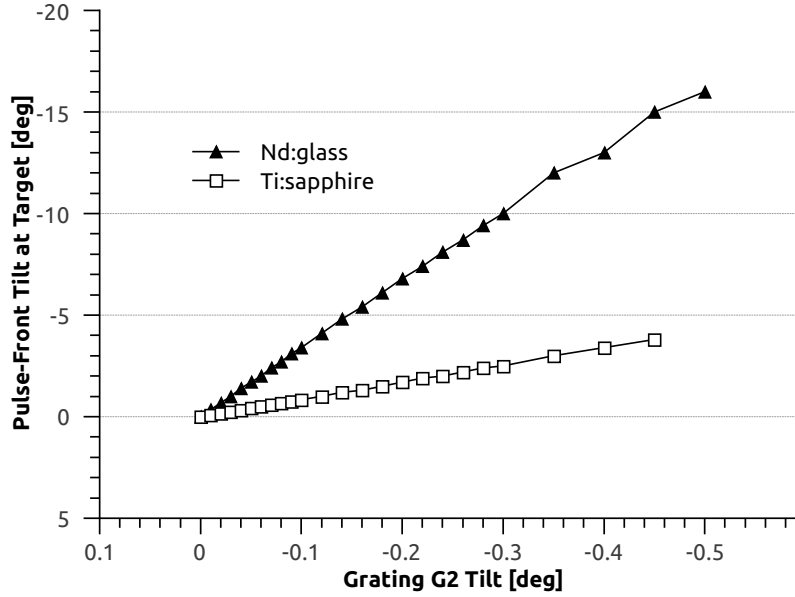


Fig. 3.39: Pulse-front back-tilt at the target (E_{img} in Fig. 3.35) as a function of compressor misalignment, and for a selection of laser pumps.

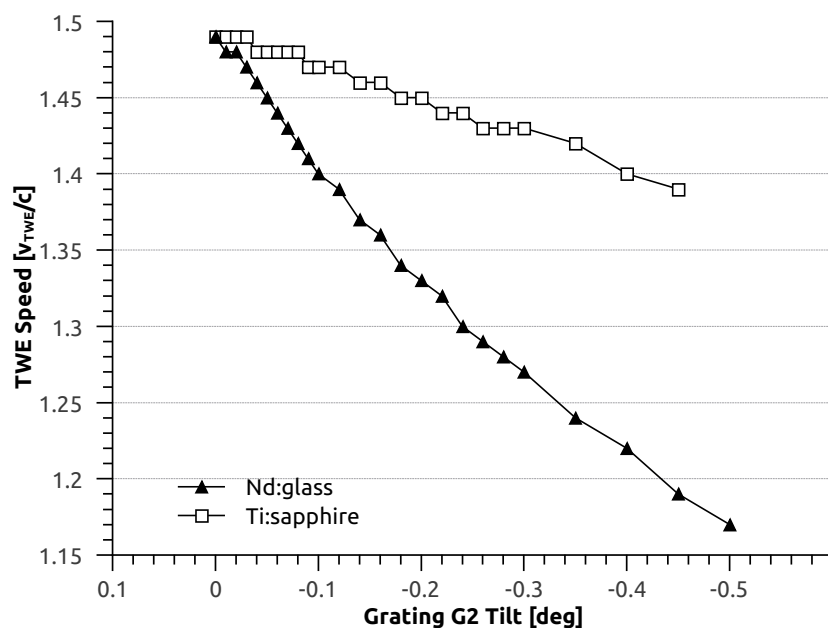


Fig. 3.40: Traveling-wave excitation speed along the line-focus, after speed-matching with compressor-grating tilt, for a irradiation angle of 48° on the target.

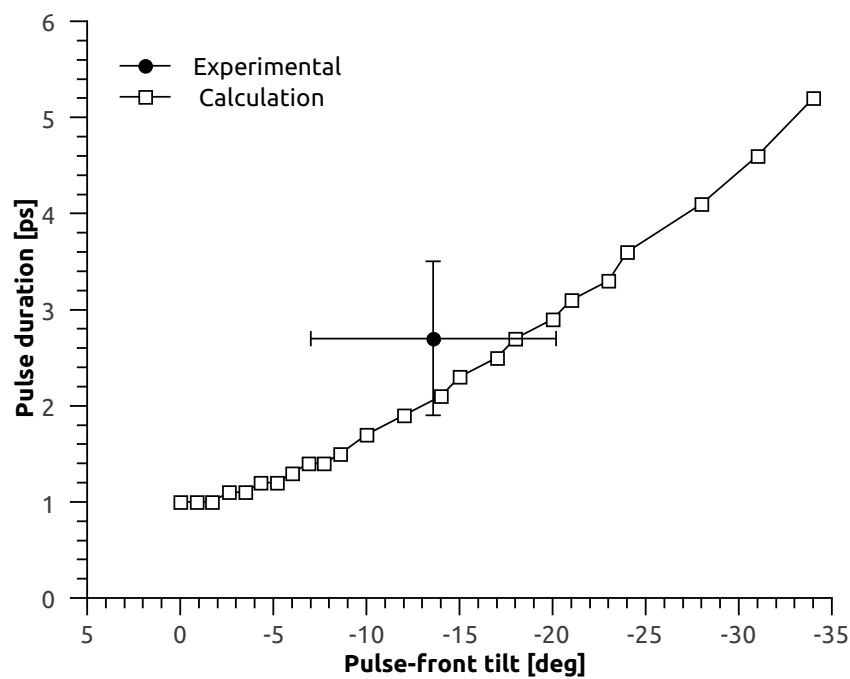


Fig. 3.41: Pulse-front tilt after the misaligned compressor versus concomitant pulse uncompression.

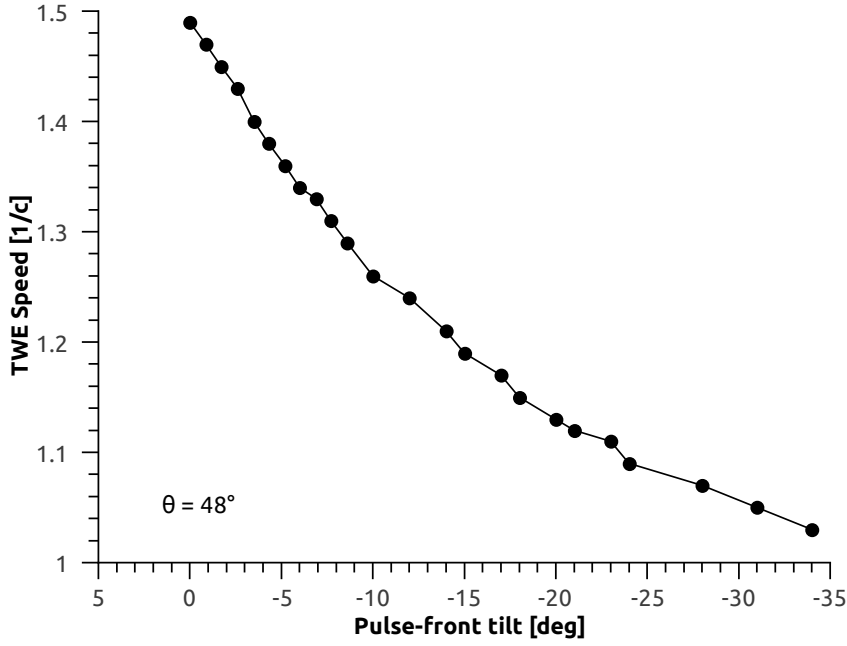


Fig. 3.42: TWE speed obtained with a 11-fold imaging, showing feasibility of 1c speed-matching even at an angle of irradiation of 48° . For comparison, Fig. 3.40 shows a more modest compensation since a factor of 2 lower magnification was there considered.

case). The experimental data are also shown. The pulse duration data were obtained using an auto-correlator. The pulse-tilt data were obtained determining the TWE speed using a streak camera connected to the leading and trailing edges of a line focus with optical fibres. This allowed determining the delay of pulse-front delivery at the leading and trailing edge, and thus the pulse-front slope ($\zeta = 58.6^\circ \pm 6.6^\circ$). Considering that for this experiment an angle of irradiation of 45° was used, the excess slope on the target ($\zeta = 13.6^\circ$) was attributed to the compressor misalignment and imaging.

Fig. 3.42 shows the calculated TWE speed dependency to the pulse-front tilt for the experimental 11-fold imaging setup. The result shows that with a significantly higher front-end magnification (11-fold) than what discussed in the rest of the paper (5-fold), it is possible to obtain complete TWE speed-matching. This result is indeed possible for a compressor misalignment that is not dramatically degrading the pulse duration at the beam boundary, and thus preserving a reasonable transverse profile in the plasma-column.

3.6.3 Summary on Travelling-Wave Excitation

Pulse-front tilt to compensate TWE velocity at large target-irradiation angle, needed for short-wavelength lasing, was shown to be effective only if coupled with a strong front-end imaging/focusing component. The study shows that with a approx. 10-fold front-end magnification it is possible to obtain *complete* TWE speed-matching, for less than half degree compressor-grating tilt. The alternative technique of using large compressor tilting and modest imaging magnification is negatively affecting the performance. Indeed, concomitant pulse broadening at the beam boundary can be very large, depending on wavelength and bandwidth. Variable irradiance as a function of beam radius, consequence of transverse pulse broadening, leads to a transversely inhomogeneous plasma-column in temperature and density. Inhomogeneities cause refraction and self-absorption, thus hindering the amplification process across the plasma length. It is noted that short wavelength and small bandwidth mitigate the broadening effect, and in the present case the best compromise is provided by the Nd:glass laser.

4. ADVANCED ANALYTICS

4.1 Implementing Plasma-lasers in Nano-imaging

Published in Ruiz et al. Appl. Phys. B 115.3, 311-324 (2014). Main themes here:

- *Plasma-Laser Specs & Imaging Requirements*
- *Design of an EUV Objective for Aberration-Free Imaging*
- *Experimental Demonstrator & 4 Modes of Operation*

Short-wavelength illumination is crucial for the progress of microscopy and for its *enabling character*, i.e. beating the micrometer resolution limit of present-day table-top systems, and accessing imaging at the nano-scale in the own lab. It is well-known that shorter wavelengths push down the diffraction limit, since the ultimate resolved structure is given by $0.61\lambda/NA$, with λ the illumination wavelength and NA the numerical aperture of the imaging system. In commercial microscopes working in the visible the ultimate resolution is $\lambda/2$. For contrast, using $\lambda = 5\text{--}50$ nm available from plasma sources, a few research groups have demonstrated proof-of-principle extreme ultraviolet (EUV) microscopy systems, with resolutions down to 50–80 nm [47]. Such nano-imaging systems have been proposed for enabling actinic nano-inspection of EUV lithography masks, as shown at synchrotrons [112], or for cutting-edge material science applications [96], *in the own lab*. Optimization and high-duty research are however not possible at synchrotron sources, due to the limited and discontinuous accessibility. Table-top systems are therefore desirable.

The basic elements of a microscope are the following ones:

- photon source (and collector/condenser)
- sample holder
- objective
- detector

Our study was restricted to the light source and the imaging optics, since CCDs in the X-ray and EUV ranges are well established compact, and commercially available, components. On the other hand, short-wavelength compact photon sources as well as the related multi-layer optics are still subject of fundamental research, which we believe should not be carried out separately, in order to provide integrated specifications for turnkey systems.

Most of the reported nano-inspection systems have been demonstrated in conjunction with large-footprint sources, such as the synchrotron. The miniaturization of the EUV sources for own-lab operation and daily access is a technology-enabling achievement, if happens without deterioration of the state-of-art performance. The EUV laser (also known as “X-ray laser” or XRL), generated using a laser-plasma gain-medium, is a well-debated platform for enabling nano-scale microscopy in the own lab. Amplified spontaneous emission (ASE) along the plasma column leads to as high as 10^{11} coherent photons, i.e. 1–10 μJ at wavelengths as low as 8–23 nm (depending on the target material), with just 1–3 Joules of pump energy on the target. Such pump energies are nowadays easy to achieve on table-top setups, for instance by means of chirped-pulse amplification [226]. The plasma-laser is more performing when *pump pre-pulses* on the solid target are used for generating a pre-plasma, then irradiated with a

main pump pulse inducing ASE conditions across a hot/dense plasma-column. The decoupling of the ion-ensemble-formation, and their population inversion permits more flexibility in the optimization. The optimization of pre-pulse delivery is indeed subject of ongoing research, in order to enhance the conversion efficiency as well as the laser output characteristics [325]. **Transient collisional excitation (TCE)** [161] is accomplished with a 0.5–0.8 ns pre-pulse, orthogonal to the target, followed within its temporal duration by a short 10–50 ps main pulse. **Grazing-incidence pumping (GRIP)** [78] showed further improvements delivering the short main pulse at $10^\circ - 30^\circ$ grazing incidence. Our laboratory introduced a dual pre-pulse followed by the main pulse all at GRIP (TGRIP) [117]. This specific geometry of the **triple GRIP** permits a more accurate alignment of the pre-pulses with the main pulse. The use of two pre-pulses of good pedestal contrast permitted a stricter control of the atomization, ionization, and population inversion stages. Whether the TGRIP scheme proves to be more suitable than classical TCE for imaging application in terms of profile and reproducibility is still not addressed in the literature and is subject of this study. The aim of this study was to provide constraints on the illumination and imaging characteristics of a plasma-based short-wavelength laser using TGRIP and to obtain critical tolerances for a table-top nano-scale microscope using design-adapted Schwarzschild objectives. The parameters discussed above were analysed and quantified combining computational studies and experimental data. Given that the observed *raw* characteristics of a plasma-laser were insufficient to provide reproducible illumination on a microscope entrance pupil, we present technical solutions on pre-pulse delivery and light collimation for fully compensating the EUV laser output randomness and provide stable and homogeneous light filling on the sample.

4.1.0.1 Pointing Stability

The reproducibility of the illumination is a critical aspect in advanced analytical technologies. In particular this applies to a nano-science system, where any *minimal* misalignment, consequence of the spatial and temporal fluctuations of the source, can immediately and significantly degrade the imaging. Regarding the *temporal* fluctuations, since the ASE process develops from noise, there may be some concerns on the pointing stability and divergence of a plasma-based source. For comparison, in a fourth-generation accelerator source such as the "LCLS" free electron laser (XFEL), a pointing stability with a $0.25\mu\text{m}$ (Tab.4.1) beam precision at the sample plane has been reported [323], which corresponds to a μrad angular tolerance over a km-length system. A footprint reduction of factor 1000, from a km-size facility to a table-top one, brings an advantage in angular tolerance, for a comparable field of view. Indeed, for a mm shot to shot pointing stability a mrad tolerance is sufficient for a table-top system versus a μrad as in the case of the XFEL.

Concerning *spatial* fluctuations the lack of illumination uniformity of XRL spot may become a reason of concern for applications [246], especially when compared to the excellent figures-of-merit of the synchrotron. Therefore, besides a quantification of the impact of spot uniformity on the imaging quality, optical strategies were developed in this work, in order to compensate for intrinsic plasma-related randomness, and fully exploit the "table-top potential".

4.1.0.2 Condenser

In the case of a spontaneous emission EUV plasma source ($4\pi\text{sr}$ emission), a required component in the microscope is the condenser. The condenser gathers light on a smaller surface and thus enhances the fluence (light per unit surface) to the benefit of illumination contrast. If the fluence is too low, the contrast (or "visibility") is indeed modest, whereas a too strong illumination can generate flare effects, i.e. raising the amplitude baseline of the acquired images, or even damage the sample. The question of the optimal fluence on the sample is still not quantitatively investigated in this context and is subject of this work, in order to pinpoint the ideal NA for the condenser. The NA of the condenser and objective are ideally matched, in order to maximize the light collection efficiency into the imaging front-end. Thus, the definition of the optimum fluence is functional to define the condenser NA, and then the objective NA.

Nevertheless, the enhancement in brightness that a collimated source brings, e.g. EUV laser, as compared to a spontaneous EUV source emitting over $4\pi\text{sr}$, does impact the imaging throughput with as fast as one full image per single shot. Indeed, several groups have shown

Light Source	Free electron laser	Laser-plasma	Capillary discharge
Divergence	$< 10^{-2}$ mrad	5 mrad	7-14 mrad
Pointing stability	$0.25 \mu\text{rad}$	0.5 mrad	25 mrad
Spatial coherence	100 %	$< 20\%$	50 %
Temporal coherence	10 %	100%	100 %
Spectral bandwidth	$> 0.1\%$	$10^{-3}\%$	$10^{-3}\%$
Peak brilliance*	$> 10^{30}$	10^{27}	20^{25}
Wavelength range	Hard X-Ray/ XUV	XUV	EUV

Objective	Schwarzschild	Fresnel Zone Plate
Spherical aberration (Seidel coeff.)	< 0.001	< 0.001
NA	0.15-0.30	0.066
Obscuration	15-18%	0%
Magnification	20-30X	660X
Efficiency	20%	10%
Resolution	< 150 nm	20-100 nm

Tab. 4.1: Typical specifications for laser-like X-ray sources, such as free-electron laser [323], short-wavelength plasma-laser and capillary discharge [252] (top table) and different XUV microscopy objectives. (*)Peak brilliance given as $\text{ph/s} \cdot \text{mm}^2 \cdot \text{mrad}^2$ 0.1% BW

that a partial enhancement of the coherence has a dramatic effect on the improvement of the visibility. The issue is here to investigate whether a collimated source has a primary fluence that makes the condenser redundant.

4.1.0.3 Repetition rate

The operation of high *peak*-brightness imaging sources is in pulse mode, and to keep the *average* brightness also high the pulse repetition rate is another critical parameter to consider. It also influences the number of accumulated counts per image, the statistics, and the measurement throughput. The former can be overcome if high peak brightness is there, such that even a single-shot is sufficient for a high contrast acquisition as shown in the next section. If the imaging is done using photo-emission of charged particles (e.g. PEEMS), it is however believed that a low peak brightness with high repetition rate is important to mitigate space charge artifacts. Simulations have however indicated that for angle-resolved studies, high pump brightness can help to preserve the pristine characteristics due to the generation of a sheath boundary layer in the charged particle bunch. On the other hand single shot imaging is advantageous to overcome problems of sample vibrations, as possibly due to instrumentation in the lab, e.g. pumps. XRL based on solid state pump laser technology presently offer repetition rates up to a few Hertz [322]. Research to scale-up the repetition rate of XRL towards the 100 Hz, especially in combination with sub 10 nm emission, is ongoing worldwide.

4.1.0.4 Coherence Degree

Finally, concerning the objective the use of either multilayer optics or zone plates for short-wavelength imaging suffers from poor efficiency, alignment sensitivity and high cost. Furthermore, lab-scale microscopy is difficult to push below the 100-nm-resolution, for which reason lensless methods based on coherent diffraction imaging (CDI) have been proposed by *Miao et al* [221] and more recently holography techniques have been also used for the same purpose [50]. In order to enable lensless imaging in the lab, a table-top high brightness source with coherence width larger than the sample size is required. Whether the plasma-laser can combine brightness and coherence length is investigated here, and quantitative information of the possible sample sizes for CDI experiments is provided.

4.1.0.5 Objective

As mentioned, the investigations on the source should be combined with those on the imaging optics, in order to match the respective characteristics. Objectives for short-wavelength spontaneous sources have been realized using the (inverse) Schwarzschild design (properly speaking a Cassegrain design) i.e. two multilayer-coated mirrors working as a primary large concave

mirror with a central hole and a secondary smaller convex mirror. The classical Schwarzschild alignment of a concave and convex pair addresses third-order aberration issues that a single spherical mirror of large NA suffers from. Few groups using Schwarzschild objectives have achieved high resolution below 100 nm [223]. Pros and cons in conjunction with plasma sources are investigated in this work.

The illumination into the primary is annular, since the secondary mirror obscures the axial region at the end of which is the hole on the primary. Such central obscuration is about 15-20% depending on the objective's NA. A further side-effect of the central obscuration is observed, if illuminated with coherent light, since the border of the secondary mirror will cause diffraction fringes. Therefore coherent sources would have better imaging performance with objectives without central obscuration. Such alternative designs are considered here as known as "Partial Schwarzschild" or "Yolo" or "Schiefspiegler" objective [122]. The main disadvantage of these designs is that due to the tilting of the mirrors third order aberrations occur, as shown quantitatively here.

One approach to reach spatial nano-resolution is to use short wavelength as the source illumination in microscopes. However, due to the high absorption of extreme ultraviolet radiation (XUV) in most materials, the types of optical elements which can be used are limited to: Fresnel Zone Plate and multilayer mirrors. The advantage of the latter is that they are more efficient than the former. For instance, the typical throughput of a Fresnel Zone Plate is 10%, while multilayer mirror reflect typically 40-70%. In this sense, the Schwarzschild objectives based on extreme ultraviolet radiation (XUV) are an interesting tool for high resolution imaging. They are made up of a concave primary and a convex secondary mirror, which have an identical center of curvature, is an interesting tool for extreme ultraviolet imaging. The relation of radius of curvature (ROC) between mirrors accomplishes the aplanatic solution for optical aberrations, such the total system is free of third order aberrations. Moreover, by eliminating these aberrations, i.e., spherical aberration, coma and astigmatism, one increases the field of view. This on-axis configuration of the Schwarzschild allows a high numerical aperture (NA) and hence the resolution of smaller details without compromising the magnification. Among all this potential, Schwarzschild objectives are inexpensive compared to other reflective objectives which use three or four mirrors.

4.1.1 Optical Theory & Model

The modeling of the Schwarzschild objective was done with OSLO [229], which uses the ray tracing for the analysis of the aberrations. The ray is defined by its entrance pupil coordinates (x, y) and the images coordinates (x_0, y_0) . The distortions are measured by using the Seidel aberration function. The aberrations are defined according to the ray displacement on the wavefront shape emerging from the exit pupil and they are expressed in term of an aberration polynomial:

$$W(x, y, x_0) = A_1 + A_2 + A_3 + B_1 + B_2 + B_3 + B_4 + B_5 + B_6 + \dots \quad (4.1.1.1)$$

Where

$$\left. \begin{aligned} A_1 &= a_1(x^2 + y^2) && \text{(defocus)} \\ A_2 &= a_2xx_0 && \text{(tilting)} \\ A_3 &= a_3x_0 && \text{(phase shift)} \\ B_1 &= b_1(x^2 + y^2) \\ B_2 &= b_2xx_0(x^2 + y^2) \\ B_3 &= b_3x^2x_0 \\ B_4 &= b_4x_0^2(x^2 + y^2) \\ B_5 &= b_5xx_0^3 \\ B_6 &= b_6x_0^4 \end{aligned} \right\} \quad \text{(wavefront aberrations)}$$

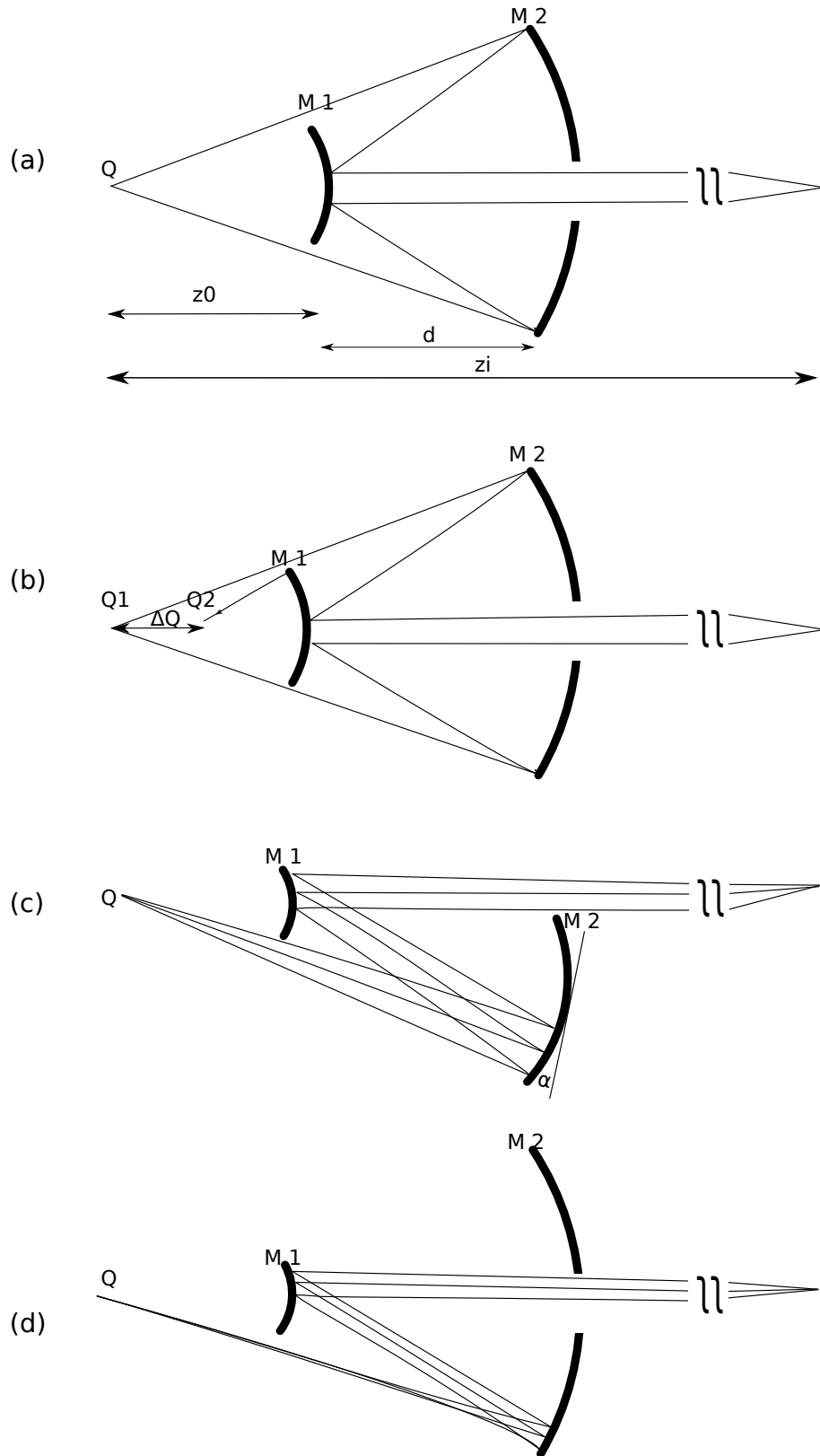


Fig. 4.1: Sketch of the modified Schwarzschild objectives studied. (a) Classical Schwarzschild objective. (b) Eccentric Schwarzschild. (c) Partial Schwarzschild. (d) Off-axis Schwarzschild.

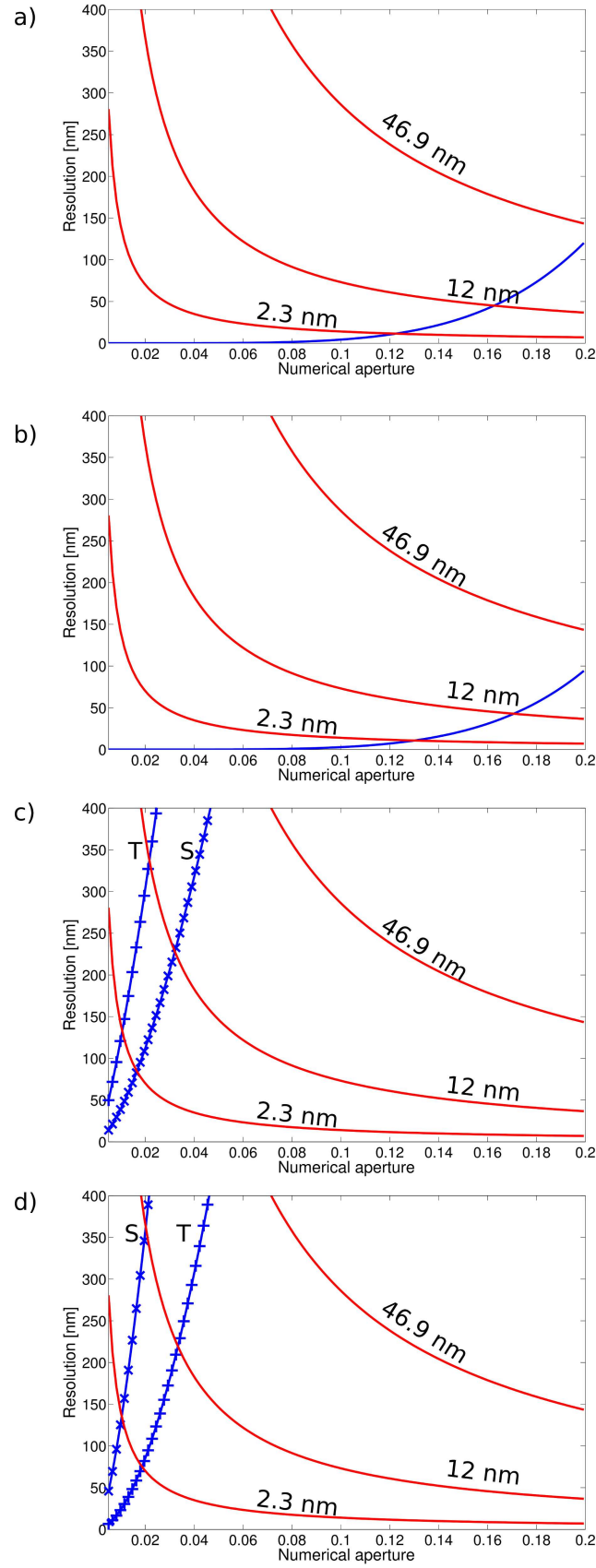


Fig. 4.2: Calculated resolution as limited by diffraction (red lines) at three wavelengths, i.e. 12 nm, 2.3 nm (water-window radiation) and 46.9 nm (capillary-discharge laser), and as limited by third-order aberrations (blue lines) as a function of the numerical aperture for the four studied objectives: (a) classical, (b) eccentric, (c) partial and (d) off-axis Schwarzschild. In a) and b) astigmatism is fully corrected while in c) and d) the symbol 'T' refers to the tangential and the 'S' refers to the sagittal plane.

a_1 represents the coefficient of defocus corresponding to the paraxial optics, a_2 is the coefficient containing the information about the tilting, a_3 is the coefficient which refers to a phase shift. The coefficients b_1 to b_6 express the wavefront aberrations: spherical, coma, astigmatism, Petzvel radius and distortion. The aberrations are consequence of the deviation of the wavefront whose is consequently deteriorated in the quality of the Airy disc.

For a discussion where we mention the spherical, coma or astigmatism coefficient, the pupil entrance is expressed in polar coordinates. The image of a point which is not limited by diffraction is limited by the aberrations, specified as the ratio of the geometrical spot size and the magnification. The spot size is defined as the RMS (root mean square) spot radius in each main plane (tangential and sagittal). The tolerance for the resolution limited by the aberrations is given by the so-called Strehl ratio, defined as the ratio of the observed peak intensity at the image plane compared to the theoretical maximum peak intensity of a perfect optical system [300]. According to the Maréchal criterion we used the limit of the tolerance at 80% of the Strehl ratio. For the optimization of the objective the software uses a standard optimization algorithm called *damped least squares* [229]. The divergence, pointing stability and signal-noise ratio were modeled with a self-written MATLAB code, which evaluated directly and individually the experimental images obtained in our lab. This code gives position coordinates for each pulse. A second self-written code calculates the pointing stability in mrad as the standard deviation of all the coordinates. The divergence was calculated for the horizontal and the vertical axis. Each axis is defined by a so-called quasi-Gaussian profile. The dimensions of the beam shape were determined for a width of those profiles at $1/e^2$. The data are post-processed in terms of statistical analysis including the average, the measurement of uncertainty and the standard deviation. The pointing stability was given as the 1σ precision. In order to understand the effect of the source profile homogeneity (illumination noise density), we added white Gaussian noise. The inhomogeneity has a Gaussian distribution. We defined the probability of finding a deviation δ from the mean ($\delta = 0$) as:

$$p(\delta) = \frac{1}{\sigma\sqrt{2\pi}} e^{-\frac{\delta^2}{2\sigma^2}} \quad (4.1.1.2)$$

Where σ is the standard deviation. The intensity was normalized attributing the maximum intensity (white) to the value 0 and minimum intensity (black) to 255 in the gray scale. Visibilities at different profiles have been calculated using Eq. 2.3.3.1. Four different geometries based on Schwarzschild design were studied and listed here below.

The *classical* Schwarzschild is a design with the primary and the secondary mirror having identical center of curvature. By using a primary concave and a secondary convex mirror the spherical, coma and astigmatism aberrations up to the third order are compensated (See Fig. 4.1a). For full NA illumination of the primary mirror a spontaneous source is required, or the expansion of a collimated beam.

The *eccentric* design is a modification of the above system consisting of offset centers of curvature for primary and secondary mirrors (Fig. 4.1b). It implies that the object-to-center-of-curvature distance (ΔQ) is optimized for superior imaging performance, i.e. minimization of aberration spot size, and for the positioning tolerance.

Fig. 4.1c shows the *partial* Schwarzschild. It uses two spherical mirrors but the primary is offset from the obscuration range and tilted in order to project the incoming pencil of light to the secondary. Both mirrors have common center and the secondary is in the same axis as the object and the image, which results in an illumination cone tilted by the *angle* α with respect to the optical axis.

The *off-axis*-illumination Schwarzschild is a special case of the "partial" design. From the point of view of a plasma-laser, the illumination has such small aperture that this design matches with this specification. The "off-axis" uses the same configuration as the "classical", but employs only a portion of the primary mirrors (Fig. 4.1d). This is indeed not a new optical designs but the case of the "classical" illuminated with a laser source.

4.1.2 Characterization of the XUV Plasma-laser

4.1.2.1 Spatial coherence measurement

For the measurement of the coherence of the plasma X-ray laser, we based on the Young double slit experiment. Different double-slit masks were used. Tab. 2.1 shows the slit width and the slit separation used. The two pre-pulse schemes (TGRIP and TCE) were compared. Results obtained with the TCE scheme were published before [45]. The visibility (γ) to obtain the coherence degree was calculated using Eq. 2.3.3.1. Some patterns obtained with the TGRIP are in Fig. 4.3. The coherence width, w_{coh} , was obtained as: $\frac{\lambda}{\theta}$, where λ is 12 nm, the wavelength, and θ is the angle subtended by the separation of the slits and the distance to the source. That step is needed to normalize the distance for the measured coherence degree obtained with different setups. The coherence width is considered for the slit separation where γ falls to $1/e$.

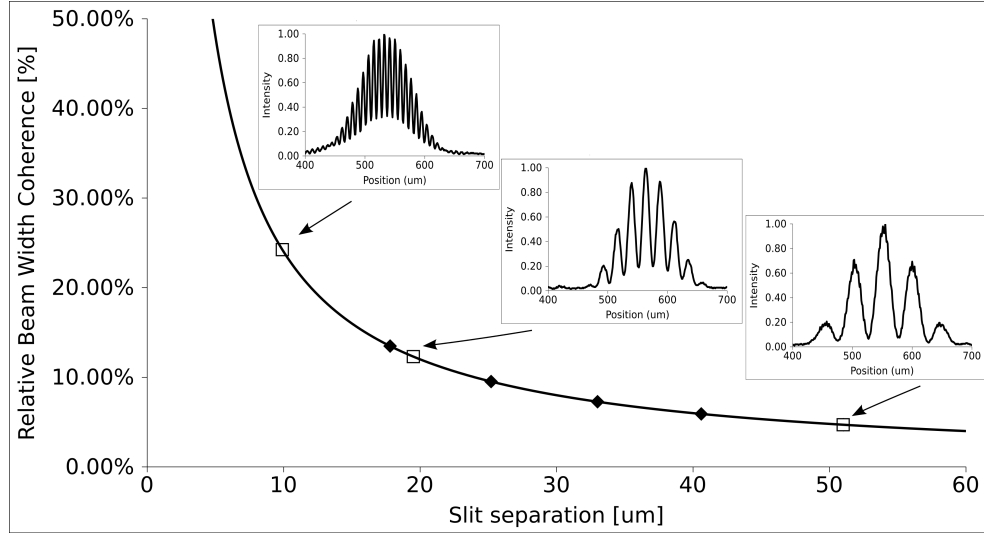


Fig. 4.3: Relative coherence width as a function of slit separation for TCE (◆) and TGRIP (□) prepulse scheme. No significant difference was found between the schemes.

4.1.2.2 Fluence for EUV imaging

In order to know the minimum fluence limit of table-top nano-imaging the signal-to-noise ratio was measured as a function of the illumination fluence. The obtained experimental calibration is shown in Fig. 2.5, between the illumination (top axis) and the signal-to-noise ratio (SNR). The observed SNR was fitted as a function of fluence, F (in counts per unit surface) with Eq. 2.3.2.1.

4.1.2.3 Pointing Stability and Divergence at TGRIP vs. TCE Pumping

The pointing stability of a laser is affected by several factors: plasma hydrodynamics, ASE development from noise, energy fluctuations, *etc.* The *unaided* plasma-driven laser emission showed an experimental divergence of 5.0 ± 1.0 mrad (defined as twice the beam NA). Such value would imply a beam diameter of 4–6 mm over 1 m free propagation up to a microscope entrance pupil. The latter must be filled homogeneously and reproducibly (no shot missing it). The pointing stability of the plasma-laser spot centroid was measured as 0.5 mrad (corresponding to a diameter of 0.5 mm over 1 m for the centroid X/Y spread), which is excessive for a stable feeding of the entrance pupil of a microscope. These experimental results were confirmed by a companion computational study published elsewhere [176].

Near field plasma imaging was carried out to visualize the source spot under the two different prepulse schemes explained above, namely TGRIP and classical TCE. Those data coming from TCE were obtained somewhere else [304]. The data analysis was, however, extracted specifically for this study. In the classical TCE scheme multiple concomitant *hot spots* inside the plasma gain-medium contributed to the superposition of contending beamlets ("modes"), with an irregular "multi-mode" spot profile (Fig. 4.4b). Fig. 4.4a shows that the TGRIP scheme instead

converts the spot profile to a more uniform low-mode one (quasi-Gaussian). The improved spot uniformity (low spot noise) is advantageous for imaging applications, which is intuitive, but also confirmed quantitatively in the imaging quality analysis reported below with a Siemens star.

Fig. 4.5 compares the divergence and pointing stability of the two pre-pulse schemes. The divergence was determined as vertical and horizontal principal axes. One notes that our TGRIP scheme gives a factor of 3 more collimated divergence, in both horizontal and vertical direction than the classical TCE scheme. The pointing stability was also improved, by a factor of approx. 2.5, in the TGRIP scheme.

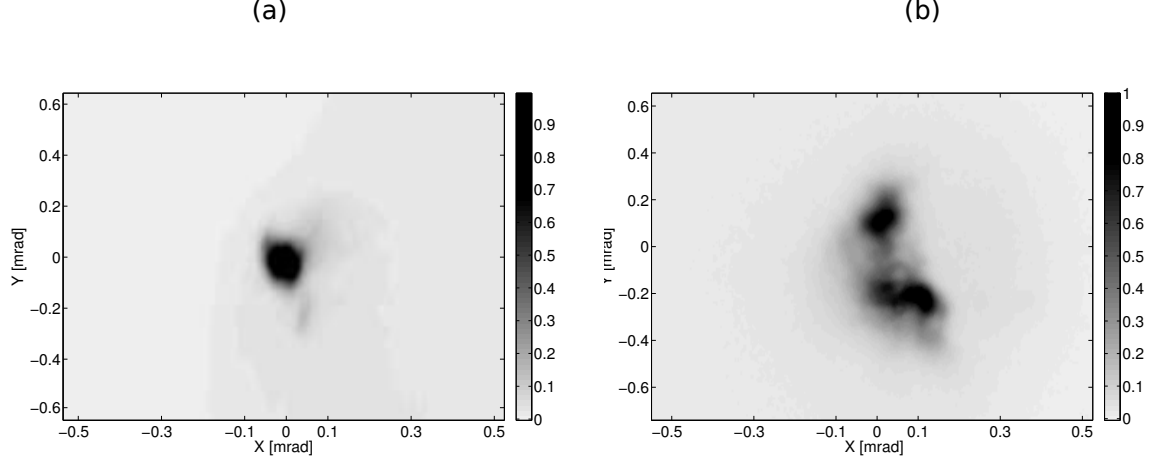


Fig. 4.4: Near-field illumination spot of the plasma-laser source obtained with (a) TGRIP (b) TCE scheme. The comparison shows a more uniform low-mode (quasi-Gaussian) spot for TGRIP than for TCE. See discussion in the text for details.

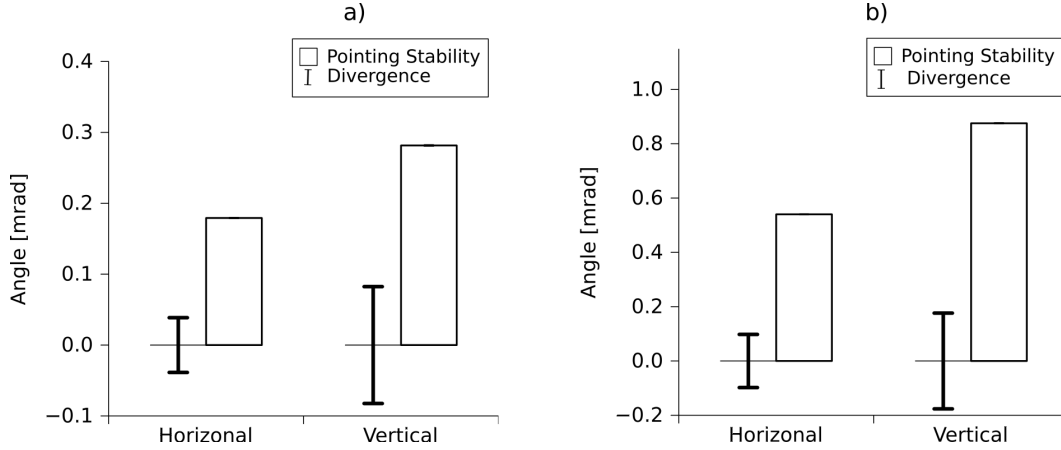


Fig. 4.5: Pointing stability and divergence for (a) TGRIP (b) TCE pumping scheme pre-pulse. The TGRIP scheme gives a factor of 3 more collimated divergence than the TCE scheme. The pointing stability was approx. factor of 2.5 improved in the TGRIP scheme.

Finally, the results obtained for the spatial coherence measurement of BeAGLE were shown above in Fig. 4.3. The spatial coherence for TGRIP and TCE once normalized to the same propagation distance (1m away from the source), show no mismatch of the respective regression curves. This indicates that the pre-pulse scheme has no relevant effect on the coherence degree of the plasma laser beam-lets. However, in the TGRIP the latter combine in a consistent bundle. Therefore, CDI experiments with sample as wide as tens of a micrometer are possible in a table-top plasma-based system, which is however out of the scope of this paper, and becomes subject of ongoing work.

4.1.2.4 Micro-collimator for beam matching

Even considering the spot uniformity improvement discussed with the TGRIP pre-pulse scheme, the obtained line-of-sight (pointing) reproducibility was clearly insufficient for a routine nano-inspection EUV microscope. Therefore, a further technical solution was investigated. In order to improve the pointing stability and collimation of the illumination, the setup was modified implementing an original projection scheme using a micro-collimator with focal length (f) equal to the source distance (a). Fig. 4.6a shows the calculated divergence of the beam as a function of mirror position as well as the experimental case in our laboratory. One notes that the divergence could be manually optimized down to 0.5 mrad whereas nano-positioning devices would be required for better adjustment. However, given the low curve slope approaching the condition $a = f$, the benefit would be insignificant. The collimated beam was also stabilized in pointing angle because whatever the angular input, the beam was systematically parallelized to the mirror's axis. Indeed Fig. 4.6b shows that the inclined illumination of the collimating mirror (on-axis illumination is not possible because it would project the light back on its source) had a limiting value at approx. 4.5° (in Fig. 4.6b data are in mrad), with the same considerations made above about alignment tolerances.

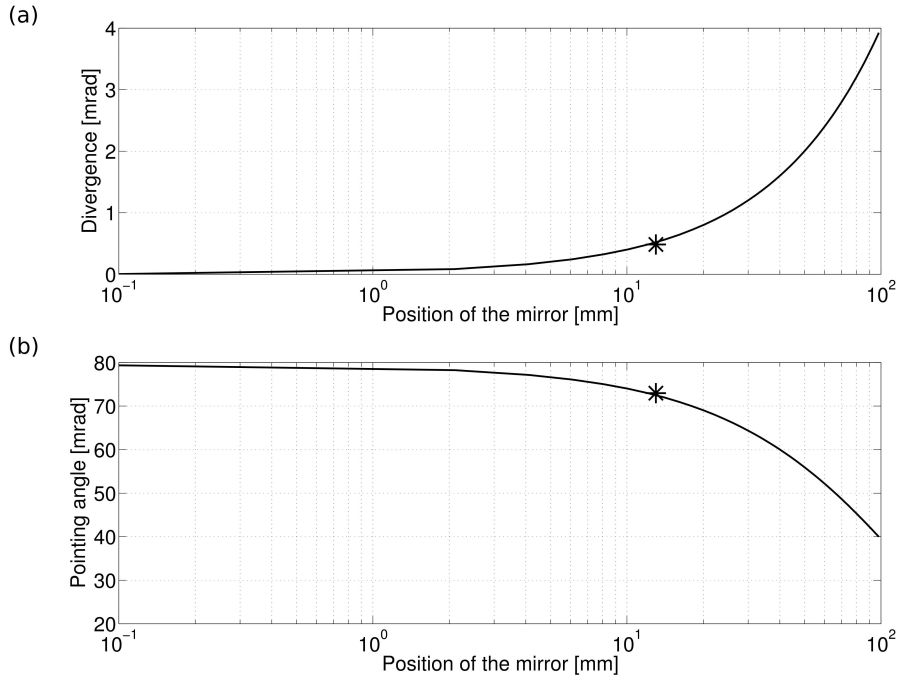


Fig. 4.6: Calculated (a) divergence and (b) pointing angle of the plasma-laser beam as a function of the micro-collimator mirror position. The experimental value obtained at our facility by manual adjustment is indicated by the star.

The collimated beam was directed on a CCD for the far-field mapping of the spot. Fig. 4.7 shows that the pointing stability improved by a factor of 5 (from approx. 0.5 mrad to 0.1 mrad) and the divergence a factor of 10 (from 5 ± 1.0 mrad to 0.5 ± 0.1 mrad) when our collimation scheme was implemented. These results showed an increase of source stability and also brightness, by means of reducing the étendue, since brightness is defined as power/étendue. Étendue is the area of the source per solid angle at the entrance pupil of the objective. The new correction can be theoretically understood by considering the Gaussian-mirror-equation, with the following given specifications:

$$\frac{1}{f = 125\text{mm}} = \frac{1}{a = 125\text{mm}} - \frac{1}{at \rightarrow \infty} \quad (4.1.2.1)$$

where a is the distance from the object to the mirror, at is the distance from the object to the detector and f is the focal length of the mirror equal to $R/2$, with R the radius of curvature of the micro-collimator. The formula can be recast to explain the functionality of the

micro-collimator as follows:

$$\beta = \left(\frac{1}{f = 150\text{mm}} - \frac{1}{a = 125\text{mm}} \right) \cdot D \quad (4.1.2.2)$$

where for small divergence angles $-a' \approx D/\beta$ can be used, with β the divergence (twice the NA) and D the diameter of the illuminated part on the micro-collimator. In Fig. 4.6a one observes that the divergence decreases when the distance between the plasma source and the micro-collimator (a) is approaching to the focal length of the collimator.

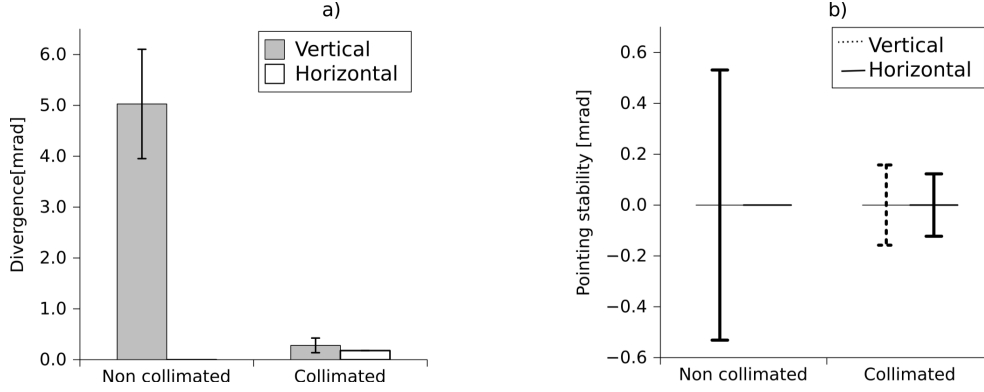


Fig. 4.7: (a) Plasma-laser beam divergence and (b) pointing stability with and without the micro-collimator. The figure (a) shows an improvement of a factor 10 in the divergence and (b) a factor of 5 in the pointing stability.

4.1.2.5 Optimum fluence for quality nano-imaging

The obtained control on the peak-brightness of the EUV laser questioned whether a condenser was *at all* required, or as it is customary for spontaneous EUV plasma sources. To address this point we analyzed the results plotted in Fig. 2.5, showing the output signal-to-noise ratio versus the input fluence. The dark current in our experimental data was less than 100 counts. The fitting carried out using eq. 2.3.2.1 showed an agreement with the experimental data points as high as $R^2 = 0.94$. Since the output of the plasma-laser is in the range of a few μJ and the area of the CCD chip is of the order of 1 cm^2 , the raw (no optics in-between) illumination fluence is within the linear range, i.e., $\approx 10^{-6}\text{ J/cm}^2$. In Fig. 2.5 the linear range, marked with two dashes lines between points A and C, starts at 10^{-7} J/cm^2 up to 10^{-6} J/cm^2 . Accounting for a 10–20% imaging optics throughput, the illumination however may degrade below the linear range (approx. 10^{-7} J/cm^2). To overcome such threshold, if it is not possible by controlling the beam size to maximum 1–2 mm at the sample position, one can accumulate signal with multiple-shot imaging.

Fig. 4.8 provides a computational analysis of the imaging performance of a quarter of a Siemens star reference sample, as a function of sample-related illumination amplitude (net signal) and illumination uniformity (spot noise). The illumination amplitude is investigated at reference values of 10% (bottom row), 25% (central row), 100% (top row), for the case of null background (Fig. 4.8a). The illumination noise is investigated at reference values of 0% (RHS column), 10% (centre column) and 90% (LHS column). The visibility (γ) of the Siemens star spokes is computed following eq. 2.3.3.1 and is reported at the corner of each snapshot. The total illumination amplitude on the detector (net sample-related signal + background) is given at the bottom of each box. Fig. 4.8b provides the same analysis for the case with flare, i.e. with background equal to 50% of the dynamic range. It is to remind that 100% corresponds to full dynamic range.

The scientific discussion focuses on the optimization of the illumination amplitude (fluence) and reduction of flare, but as shown here is critical to understand the effect of the illumination homogeneity. Indeed this provides a rationale for the importance for imaging applications of the improved spot homogeneity following our TGRIP scheme, as shown above. The baseline level affects the off-field image, the peak-to-valley contrast, as well as the residual dynamic

range. However, for a virtually flat-field illumination, a non-zero baseline level can enhance the visibility of nano-scale features. The latter can remain unresolved only if spot noise degrades the illumination. Therefore, a threshold for *high quality nano-imaging* is set at point B in Fig. 2.5, namely when $SNR > 0.5$ of linear range.

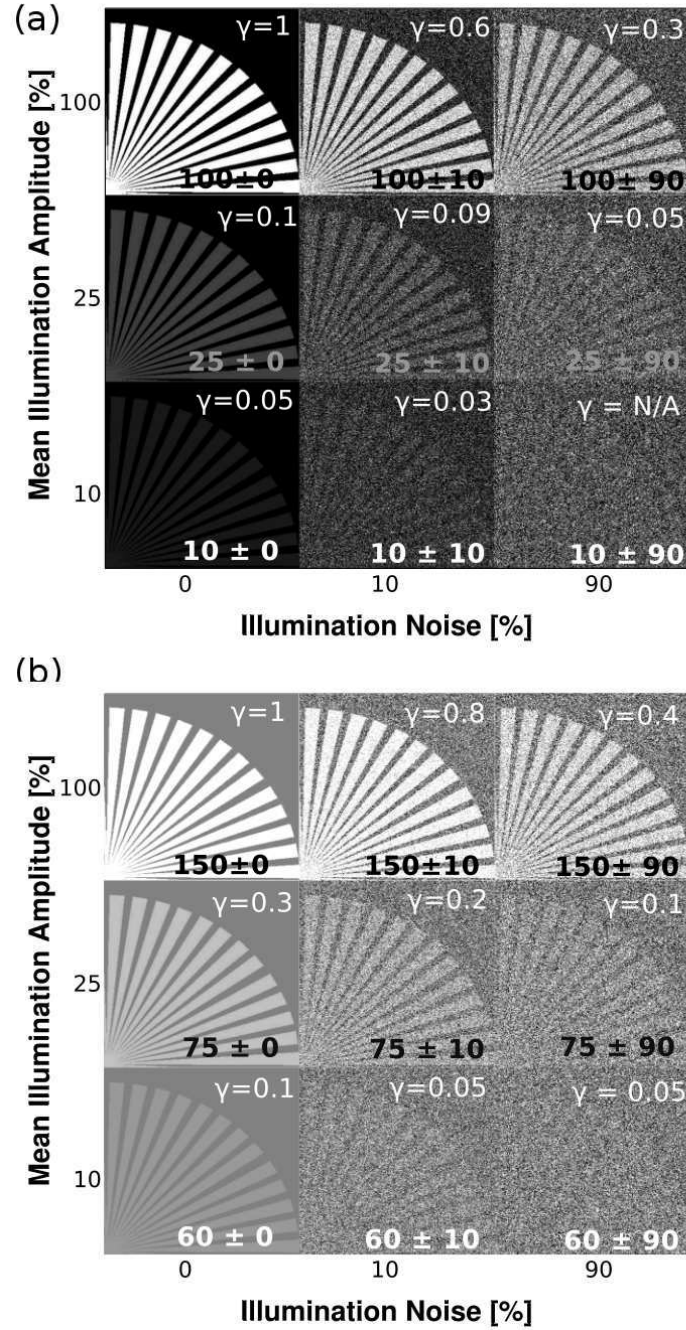


Fig. 4.8: Calculated imaging performance on a quarter Siemens star by changing the illumination noise at three steps of 0%, 10%, 90% (x axis) and the mean of the net illumination amplitude on the spokes at 10%, 25% and 100% (y axis). The spokes visibility (γ) obtained for each box is given as well as the total illumination amplitude arriving at the detector. All values are in percent with respect to the full dynamic range (saturation level is at 100%).

From the presented computational analysis one concludes that the imaging optimization benefits more from enhanced illumination homogeneity than comparable increase in spot intensity. Indeed, one can compare the corresponding quarter Siemens star visibility degradation with

spot noise and note how an inhomogeneous (noisy) spot degrades the imaging, even at high illumination amplitude. The experimental images of the Siemens star with a single concave-mirror objective (see next section) showed a visibility of $\gamma = 0.68$ at the amplitude of 90% of full dynamic range. Such results can be improved by increasing the signal uniformity, rather than suppressing the background leaking between the Siemens star spokes.

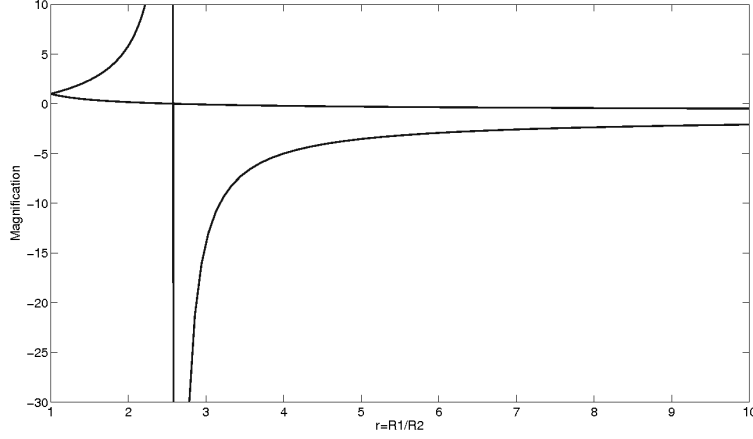


Fig. 4.9: Aplanatic condition for Schwarzschild as a function of magnification and mirror's radii ratio $r=R_1/R_2$. The simulation agrees with results from ref. [142].

4.1.3 Performance of the Four Objective Designs for Nano-scale Imaging

The spatial resolution is well-known to be limited by diffraction, which motivates the use of multilayer optics that can be operated with short-wavelength sources. It is however to be reminded the importance to choose a high NA to enlarge the high frequency cut-off of collected wave-vectors. However, large NA can be prone to more significant third-order aberrations, as discussed above. Fig. 4.2 compares the performance of the Schwarzschild designs introduced in the Sec.4.1.1. The Strehl ratio of 80% is at the cutoff of the resolution limited by diffraction and the resolution limited by aberrations. The latter changes in the four configurations of the Schwarzschild with the position and inclination of primary or secondary mirror. Magnifications above 15X in Schwarzschild are possible for a ratio of primary to secondary mirror radii of curvature (R_1/R_2) between 2.5-3 [142] (Fig. 4.9). Based on this criterion we choose the radii of curvature for all the designs as $R_1 = 100$ and $R_2 = 36$ mm ($r=2.8$) for primary and secondary mirror, respectively, which correspond to a magnification of 30X.

The *classical Schwarzschild* has an aperture limited by the diffraction and aberration resolution of 0.16 (Fig. 4.1a) which corresponded to 45 nm resolution. The produced obscuration by the secondary mirror is 15%. The reflectance of each mirror is 45% thus the total reflectance of the Schwarzschild, taking in account the obscuration too, is 17.2%. Increasing the NA involves increasing the diameter of primary mirror or decreasing the distance z_0 between the object and the mirror (see Fig. 4.1). Both alternatives imply also a potential increase of the aberrations, specially for classical and eccentric designs. Fig. 4.2 shows that the resolution and numerical aperture are linked with an inverse relationship. For NA higher than 0.15 there is no-significant increase in the resolution. Resolution limited by aberration links also with the aperture.

The *eccentric Schwarzschild* was adjusted to separation of the centers of curvature of the primary and secondary mirror in the range of 150-200 μm , which allows increasing the NA to 0.17 by keeping the same Seidel coefficients but not the obscuration which increases to 18%. The free-third-order aberration of both optics, classical and eccentric can be understood in Fig. 4.10a and b where is shown the wavefront and the ray analysis. The wavefront indicate a peak-to-valley of 0.125 μm and 0.110 μm respectively at the entrance pupil. In the ray analysis we observe that the aberrations are not significant for 0.5 mm field of view. In order to have a good compromise of obscuration and resolution, we propose a 0.15 eccentric model, which has not a significant improvement in resolution (50 nm) and it is only limited by diffraction.

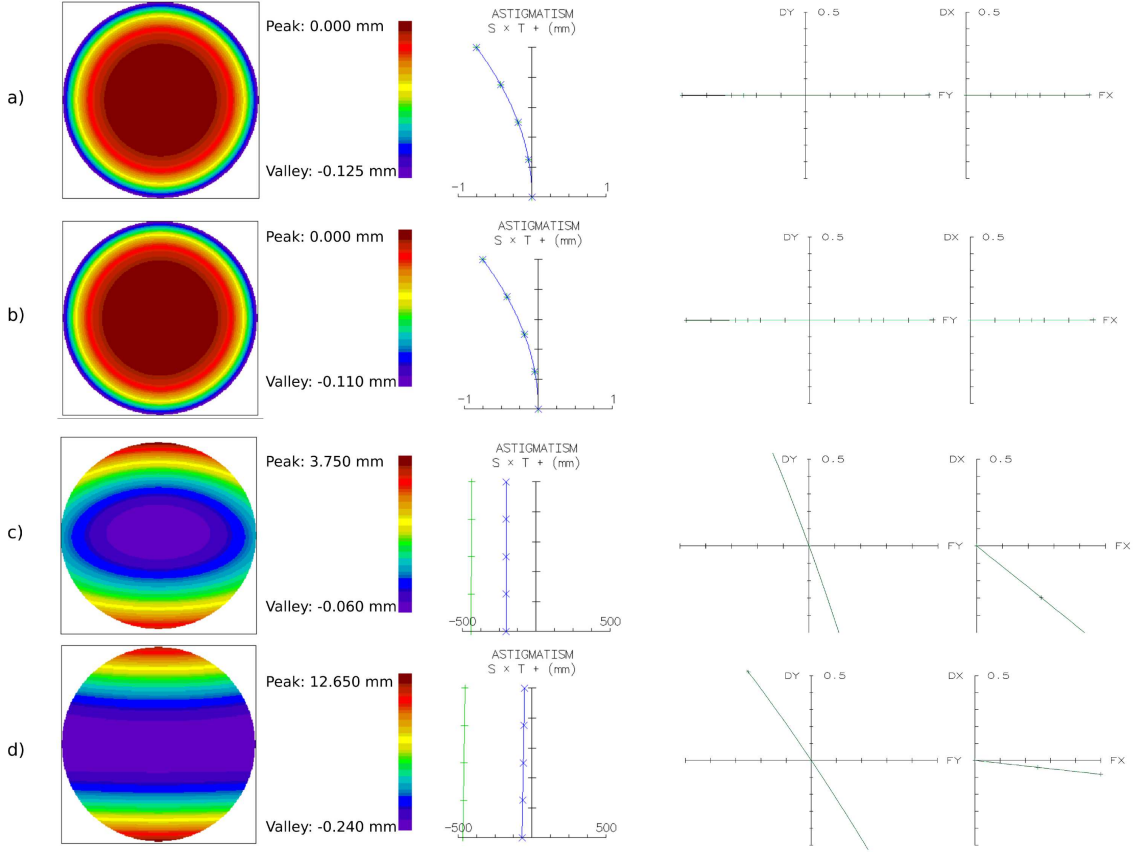


Fig. 4.10: Wavefront (left), astigmatism analysis (centre) and ray analysis (right) for the (a) classical, (b) eccentric, (c) partial and (d) off-axis Schwarzschild. (a) and (b) are free of third-order aberrations. We observe in (c) coma and astigmatism aberration due to the inclination of the rays through the partial and off-axis optics, (d) is affected by coma.

The *partial Schwarzschild* has higher spherical aberrations for the same NA as the classical or eccentric models. The Airy disc is not symmetric with respect to the optical axis and the aberrations have a notably difference in the horizontal and the vertical direction. For instance in a $NA = 0.025$ the tangential resolution is 325 nm whereas the sagittal resolution is 230 nm. In Fig. 4.10c we observe this asymmetry, which is basically astigmatism, in the wavefront surface. The value of the coefficients for the *third* order coma and astigmatism is smaller than $|10^{-6}|$. The major aberration contribution is done by orders higher than *fifth* and by the spherical aberration.

The *off-axis Schwarzschild*'s simulations showed a resolution of 250 nm for a non-significant spherical aberrations. The illumination incises on the primary mirror out of the optical axis. The objective can be employed with a laser source by using a scanning beam while the "classical", "eccentric" and "partial" designs are more relevant with spontaneous sources since they can be used with a full-field beam. Coma aberration is observed in this design (see Fig. 4.10d). The value of the *third* order coefficients are approx. 10^{-5} for coma and astigmatism. They both are generated as a result of the inclined incident beam on the optics. The aperture of 0.03 is perfectly compatible with BeAGLE since the results of the measurement had shown smaller divergence.

4.1.4 XUV Microscopy Demonstrator

The Schwarzschild objective built in this work consists of two spherical multilayer mirrors coated with 90 layers of Ruthenium and Boron carbide (Ru/B_4C). The multilayer is optimized to

operate at $\lambda = 12$ nm. The images, after a magnification of approximately 30X, are detected using a $13\mu\text{m}^2$ -pixel X-ray CCD, which allows observing approximately 0.5 mm-field of view. The total numerical aperture (NA=0.15) was obtained after a compromise of the diffraction-related and geometrical aberrations. By using the equation: $\text{RES} = \frac{0.61 \cdot \lambda}{NA}$, one obtains the theoretical resolution of the Schwarzschild objective $\approx 50\text{nm}$. However, such resolution is not possible if the two mirrors are not precisely aligned. To render a good alignment of the two multilayer mirror, they are mounted in the "Schwarzschild-shell" which is provided of three pico-motors. They are used to compensate the misalignments due to the mechanical positioning.

In this section, the different parts of the design process of the Schwarzschild objective are discussed naming as: i) details of the main parameters of the optics, and ii) description of the Schwarzschild housing shell (section 4.1.4).

The deposition of the layers was done in Fraunhofer institute using Nussy-3, a magnetron sputtering system, which was used for the first time in 2013 to build a Mo/Si/ B_4C multilayer mirror. The system is used for the deposition of a laterally graded multilayer, as in the case of the Schwarzschild mirrors. For this purpose, it is equipped with six rectangular magnetrons with the size of 250 mm x 125 mm each. By adjusting the rotation speed of the substrates and the source power, Nussy-3 allows adjusting the layer thickness with sub-Angstrom precision.

The Schwarzschild objective designed here is made of two multilayer mirrors coated with Ru/ B_4C on a substrate made of fused silica. The mirrors are optimized for $\lambda = 12$ nm, since this is the central wavelength of a plasma-based X-ray laser using a Sn-target. The reflectivity of both is approximately 50% (see Fig. 4.11). The primary mirror has a concave curvature and the secondary has a convex curvature. The main parameters are summarized in Tab. 4.2

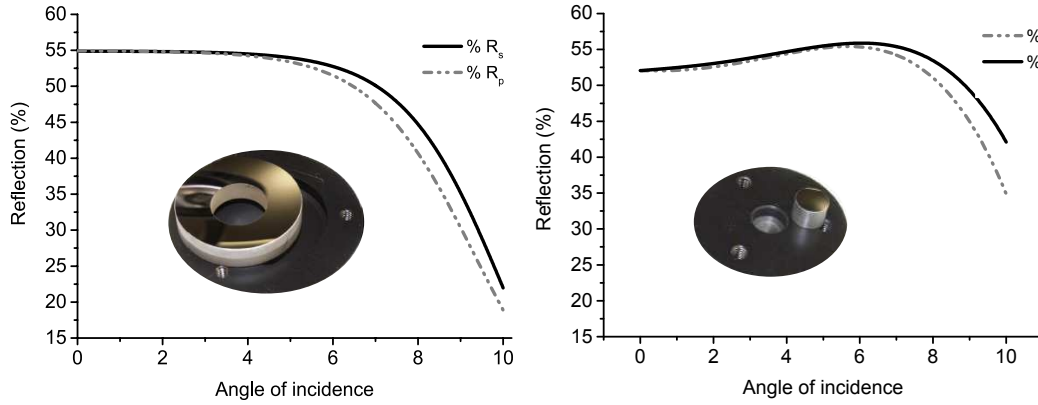


Fig. 4.11: Reflectivity curves at $\lambda=12$ nm versus the angle of incidence of a) primary multilayer mirror for s and p-polarization; b) secondary multilayer mirror for s and p-polarization of the Schwarzschild objective.

	Primary mirror	Secondary mirror
Radius of curvature	100 mm	-36 mm
Diameter	38.1 ± 0.1 mm	8.6 ± 0.1 mm
Inner hole	17.0 ± 0.1 mm	none
Incidence angle	1.2° to 2.5°	3.0° to 7.0°
Thickness	8.0 ± 0.1 mm	6.3 ± 0.1 mm
Reflectivity	<55%	<55%
Surface roughness RMS	< 0.15 nm	< 0.15 nm

Tab. 4.2: Parameters of the multilayer mirrors fabricated for the Schwarzschild objective. Metrology performed at the Physikalische Technische Bundesamt (PTB) Berlin.

The roughness of the mirrors was characterized at the National Metrology Institute of Germany (PTB) in Berlin (beamline BESSY II). The roughness of the surface was measured as $\lambda/14=0.9$ nm. The experimental results at the primary mirror showed a RMS roughness of 0.10 nm in the central part and 0.13 nm at 15 mm from the center. The secondary mirror showed a RMS=0.3nm. A second measurement was realized with an ion beam sputtering at the mirror to

improve considerably the roughness of this mirror. The final value was 0.12nm at the centre position and 0.13nm out of the centre.

The roughness and the scatter of the light are related exponentially as is shown in the following equation:

$$S = R_0 \left[1 - e^{-\left(\frac{4\pi R_0 \cos \theta_i}{\lambda}\right)^2} \right] \quad (4.1.4.1)$$

where S is the Total Integrated Scatter (TIS, the total amount of light scattered by a surface), R_0 is the RMS roughness of the surface, θ_i is the angle of incidence on the surface and λ is the wavelength of light.

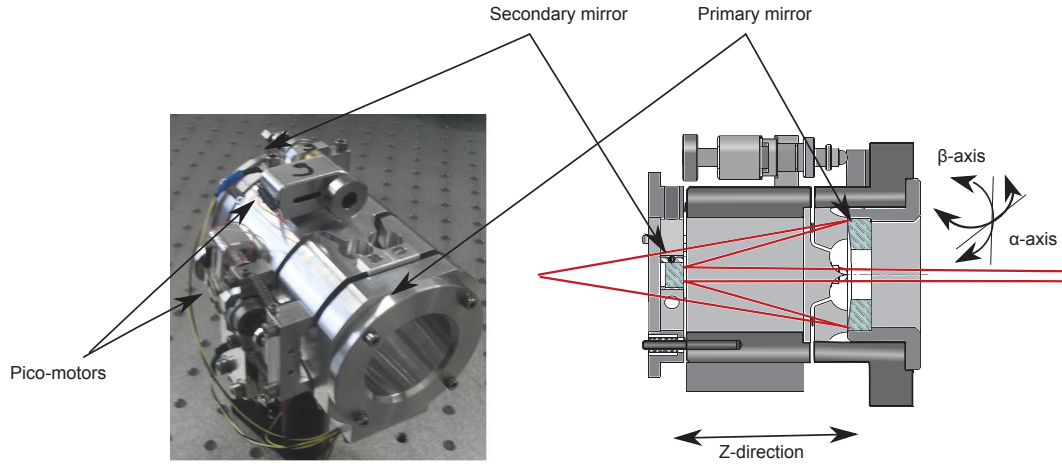


Fig. 4.12: a) Photograph of the Schwarzschild demonstrator. b) Transversal cross-cut view of the Schwarzschild shell and mirrors (in green), with optical path of marginal rays.

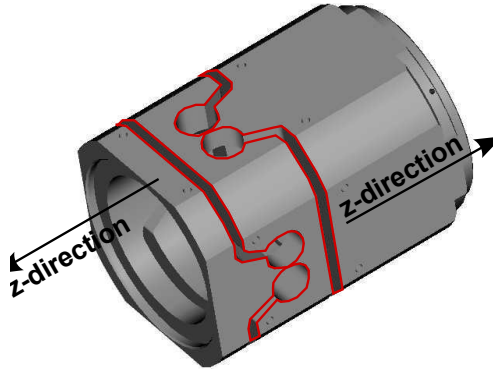


Fig. 4.13: The flexure gimbal (in red) of the Schwarzschild objective shell permits rotational movements by applying a force in the z-direction.

Fig. 4.12 shows the Schwarzschild objective developed in this work. To provide stability to the microscope, the Schwarzschild objective is mounted on an aluminum structure (Fig. 4.12.a) equipped with three vacuum-compatible picomotors. The positioning has a resolution better than 30-nm along the 12.7 mm of travel path. The principle of movement relies on the basic difference between dynamic and static friction. One advantage of these picomotors is that they can hold the position even whereas no power is applied.

One of the picomotors moves the primary mirror along the z-axis (Fig.4.12), which is used to adjust the distance between mirrors. In the classical configuration of the Schwarzschild objective (for concentric center of curvature of both mirrors) this distance is $d=64$ mm. However,

if the primary mirror decreases the distance respect to the secondary mirror, the numerical aperture increases; this condition only works for a few microns, for shorter distances the spherical aberration is not compensated. It has been found [142] that the resolution of the Schwarzschild improves to 43 nm. This configuration is known as *eccentric Schwarzschild*.

The other two picomotors control the tilt of the primary mirror along the alpha and beta axes, ensuring that both mirrors are parallel the axis α and β . The Schwarzschild shell contains 2 modified flexure gimbals used to performance the rotational movement. Each gimbal is made of two hollow circles with a diameter of 12.1 mm (Fig. 4.12b). Between the circles there is a bridge of 0.5 mm. A gap starts out of each circle and it divides the shell in two parts, uniquely linked by the said bridge. These two picomotors can apply a force in a direction parallel to the z-axis, producing a rotational movement, and thus tilting the primary mirror.

Fig. 4.14 shows the results obtained computationally for the angular (Fig. 4.14a) and distance tolerances (Fig. 4.14b). By using the motors, the goal is to obtain better resolution than 100 nm (dash line). An angular misalignment higher than $\pm 0.15^\circ$ produces lower resolution than this limit. The same effect is observed in distance misalignment higher than $\pm 20\mu\text{m}$.

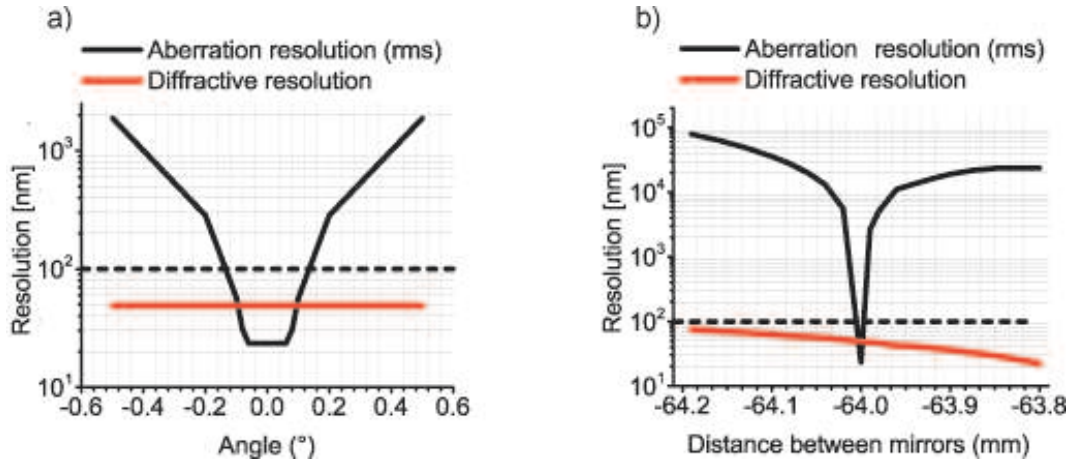


Fig. 4.14: Tolerances in the alignment of the Schwarzschild. a) Angular tolerances b) distance between mirrors. For the desirable resolution of <100 nm, the tolerances are $\pm 0.15^\circ$ and 0.02 mm respectively.

4.1.5 Summary on XUV Imaging Optics

The TGRIP plasma gain-medium generation scheme was shown to give a factor of 3 more collimated laser output than a classical TCE short-wavelength plasma laser as well as better uniformity. The pointing stability was approx. factor of 2.5 also improved in the TGRIP scheme. Additionally, we have demonstrated a simple method to control both divergence and pointing stability using a micro-collimator. The insertion of a micro-collimator in the setup improved by a factor of 5 (from approx. 0.5 mrad to 0.1 mrad) the pointing stability and the divergence a factor of 10 (from 5 ± 1.0 mrad to 0.5 ± 0.1 mrad). The coherence degree found from the visibility modulation was shown to remain unchanged in the TGRIP versus TCE schemes. The measured coherence length of several tens of micrometers allows for coherent diffraction imaging, in order to have a lensless sub-50-nm nano-imaging tool. Ongoing work in this field will be subject of a future publication. The measured fluence to noise relationship showed that optimum brightness in the linear range is within the specifications of plasma-laser output. Within this range the contrast may be degraded by the illumination inhomogeneity (spot noise). Experimental images obtained by a single EUV laser shot showed to be at optimum theoretical conditions.

The development of the appropriate optics for EUV plasma-laser involved the study of the obscuration and the aberrations. Classical and eccentric Schwarzschild are free of *third* order aberration. High resolution smaller than 50 nm are possible with both optics. However the position of the secondary mirror produces an obscuration of 15% and 18%. The partial Schwarzschild is devoid of such problem of obscuration at the cost of adding the spherical aberrations and off-axis introduces coma. By restricting the numerical aperture the two latter

can be used in EUV laser microscopes by using a scanning beam. Tab.4.3 summarizes the main parameters of the Schwarzschild studied in this work.

Objective Mode	<i>Classical</i>	<i>Eccentric</i>	<i>Partial</i>	<i>Off-axis</i>
NA	0.16	0.17	0.02	0.02
Resolution (theory)	45nm	43nm	365nm	330nm
Obscuration	15%	18%	none	none
Magnification	30X	31X	25X	30X
Efficiency	17.2%	16.8%	20.2%	20.2%

Tab. 4.3: Comparison of the critical parameters for the different microscope designs studied here.

4.2 Table-top Nano-imaging by Plasma-Lasers

Published in Bleiner et al. Opt. Comm. 284, 4577-4583, 2011. Main themes here:

- *Analysis of the Imaging Performance*
- *The Siemens Star Imaging Reference Sample*
- *Experimental Resolution*

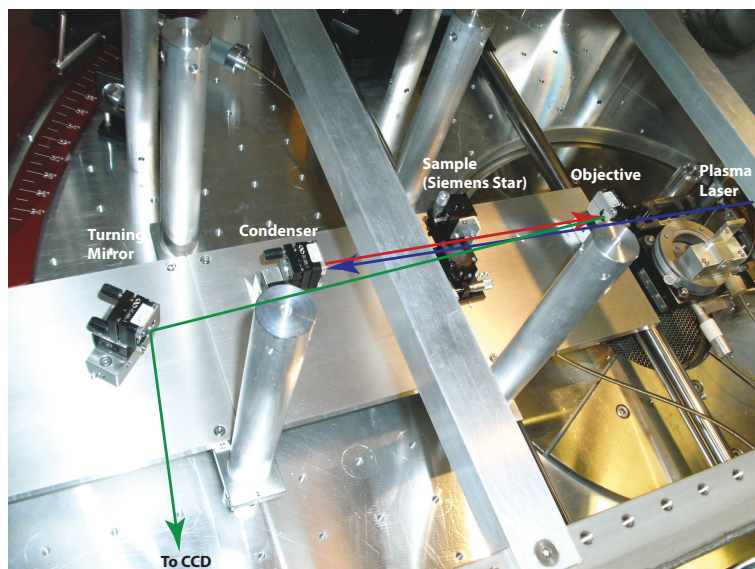


Fig. 4.15: Experimental demonstrator for XUV microscopy with the plasma X-ray laser.

The semiconductor industry has drastically invested to prepare the transition to Extreme Ultraviolet (EUV) lithography using 13.5-nm plasma sources. The main challenges have been related to the average power that laboratory-scale sources could attain, presently demonstrated to just a few Watts, and the uptime, limited to a few hours. If the former is an issue that seems to be addressable by using more powerful and multiplexed drivers, it is nevertheless coupled with a consistent increase of debris that can rapidly hamper the source functionality and limit the uptime. Nevertheless a 1 to 100 kHz repetition rate is expected to provide demo-level average power of a few tens of Watts and enable EUV lithography by 2017. The latter, however, requires also rapid mask inspection to make sure that printable defects are below a critical density, and guarantee a profitable wafer yield of 80-100 good wafer/hour.

Mask inspection devices, operating at EUV wavelengths, are thus an important enabling tool for the overall implementation of EUV lithography. A main difference between inspection and printing tools is that the former do not need excessive average power, important for high throughput, rather should provide the brightness for high contrast imaging. Unfortunately, high magnification degrades illumination. Thus high photon flux in a narrow angle (brightness

or spatial coherence) is important. Moreover, high resolution attained with short wavelength sources relaxes requirements on large NA, which otherwise introduces aberrations.

Brightness is the bandwidth power per unit solid angle, and is therefore enhanced in a conjunct effort to enhance (i) the number of in-band photons emitted (ii) within a narrow collimation angle. Spontaneous emission is a 4π sr irradiation, requiring collection optics. The use of collector optics determines the effective source numerical aperture (NA). Large NA collection maximizes the photon flux but deteriorates the source projection by poorer collimation. Amplified spontaneous emission (ASE) is, on the contrary, characterized by a pronounced directionality of light propagation. In this respect, ASE laser sources have implicitly higher brightness thanks to the primary collimated emission of the photon bunch.

Brightness is important for high contrast imaging, because directionality of light reduces image shadowing effects. Thus, bright-to-dark transitions at the feature's border can be as steep as the morphology dictates. High brightness demands high spatial coherence. The longitudinal coherence, or monochromaticity, is important to have sharp diffraction-limited images. The transverse coherence, or collimation, should not be excessive, in order to avoid occurrence of speckle interference and to enable full aperture illumination (full field).

Typically, high brightness at EUV is a characteristic of large-scale facilities, such as synchrotrons and free-electron lasers (FEL). The excessive cost-of-ownership of such large facilities has bottlenecked their access in research and prevented implementation in the industry. Therefore, the need for high brilliance lab-scale EUV sources is strategic for either boosting research or enabling industrial productivity.

Plasma sources generated by laser irradiation of a target material have been proposed to fill this gap. Laser-driven plasma sources are based on optical energy conversion from a pump IR pulse. The latter irradiates a target material and induces a hot and dense plasma that radiates in the desired bandwidth. The target material largely contributes with the characteristic spectrum of the atomic ensemble. For EUV lithography application, Sn has been identified as the most efficient target material. The spontaneous emission spectrum has been investigated previously [12], showing an unresolved transition array (UTA) around 13.5 nm from the emission of several ionization stages between Sn^{5+} and Sn^{13+} (Fig. 1.18). Depending on the form of the target, i.e. whether gaseous, mass-limited, or solid, the occurrence of Bremsstrahlung as well as debris can vary, degrading the source cleanliness. The UTA emission is Lambertian (i.e. radiance according to a cosine distribution) and thus requires large collection optics (300-600 mm in diameter) to be directed to the intermediate focus. Provided that good thermo-mechanical stability is accomplished, the collection optics is aged as a consequence of the exposure to ionizing radiation as well as fast ion debris.

Alternatively, for very hot (e.g. > 200 eV) and dense (e.g. $> 10^{20} cm^{-3}$) plasma conditions induced along a line focus (plasma column), the closed-shell Ni-like Sn ion sustains amplified spontaneous emission (ASE) of the $4d_1S_0$ to $4p_1P_1$ lasing transition at 11.97 nm. The laser emission is inherently of high brilliance because directional and subtended within a few milliradians of solid angle. The radiation characteristics are such that small optics (1 inch or less) can be used and positioned away from the zone of debris showering.

In this study we report on imaging capabilities of a compact footprint EUV laser facility to the imaging obtained with spontaneous emission. The compactness of the EUV laser source demonstrates that high brightness imaging is now accessible on a laboratory scale.

4.2.1 Imaging Optimization

The setup is shown in Fig. 4.15. Computational pre-studies were done to define (i) the optimum design for the given optical elements available, and (ii) a sensitivity study to define how much impact on performance was to be expected by any potential experimental mismatch upon assembling the setup. Fig. 4.16 summarizes major findings. An "E"-shaped mask was imaged consistently with the experimental constraints given above, and the calculated images are shown.

The condenser adjustment shows (Fig. 4.16.a,b) a sensitive impact on the illumination even for 1% axial offsetting from optimum. In fact, the condenser produces an image of the source that ideally should fall at the sample plane. A closer positioning of the condenser to the sample with respect to the optimum position can enlarge the field of view with concomitant deterioration of the illumination. It should be also noted that given the horizontal tilt between the condenser and the objective, to allow transport of the light beyond the mirror pair, a slight astigmatism is

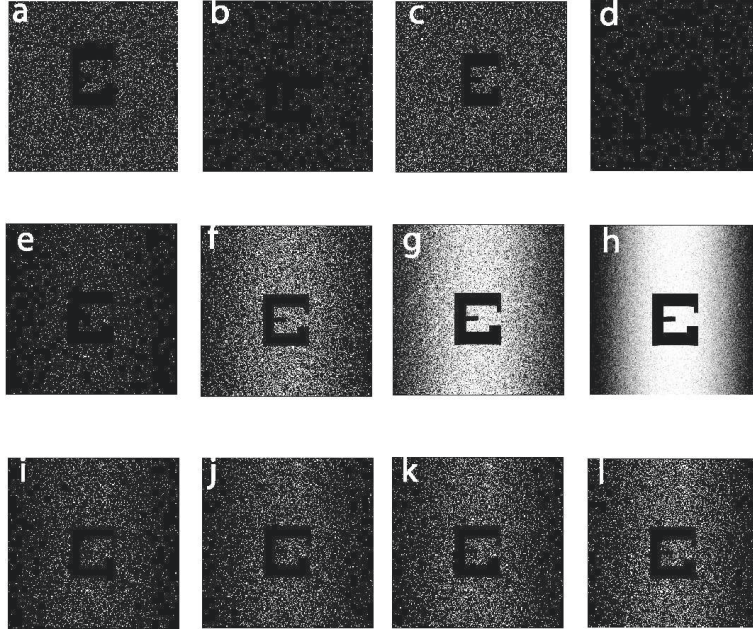


Fig. 4.16: Calculated images by means of ray-tracing, with the EUV microscope specifications given in the experimental section. Legend: a) condenser 2 mm back from reference position, b) condenser 2 mm ahead of reference position, c) objective 2 mm back from reference position, d) objective 2mm ahead of reference position, e) 10^5 rays exposure (rays to photons ratio is 13:1), f) 10^6 rays exposure, g) 10^7 rays exposure, h) 10^8 rays exposure, i) 2 shots of frame e), j) 3 shots of frame e), k) 4 shots of frame e), l) 5 shots of frame e).

observed. This can be exploited to maximize the photon flux within the width of the detector, i.e. 13.6 mm. The mirror was adjusted for best sample illumination, i.e. 615 mm from the first planar mirror, and optimum range is within 1%.

The objective adjustment (Fig. 4.16.c,d) has also an influence on the illumination, since it controls the projection of the source. For maximized illumination the mirror-pair distance was matched to the source distance to obtain an infinite-corrected projection. Concomitantly, the objective performs the 12x imaging of the sample. The mirror was thus adjusted for best CCD illumination, i.e. the condenser-to-objective distance was 266 mm. Mirror tilt was also investigated (not shown in Fig. 4.16). The observed effects were (i) an obvious horizontal stretching of the image, and (ii) the formation of a vertical illumination stripe. The maximum recommended tilt angle, also to avoid drastic loss of multilayer reflectivity, was 5 degrees. We have finally chosen to operate at 3 degrees tilt angle.

Last issue that was subject of ray-tracing investigations was the influence of photon counts (Fig. 4.16.e-h) on the imaging quality. In fact, we wanted to validate that our four optical elements (Fig. 4.15) design would not cause a drastic loss of illumination. Further, we have investigated whether with a repeated number of EUV shots we could compensate for illumination loss. In the raytracing computation the conversion was approx. 13:1 rays-to-photons. As Fig. 4.16 summarizes, one notes that for more than 10^4 collected photons across the full field-of-view, the image contrast is good. Our table-top laser source is expected to provide above 10^{10} photons/shot. Considering that a spontaneous emission laser plasma source offers factor of 10^6 less brightness/pulse, due to the emission over 4π sr, we conclude that good contrast at single-shot operation can be obtained with a EUV laser source only. Thus one single shot was found to be sufficient to produce high-contrast images. We investigated the benefit of accumulating additional shots to enhance signal-to-noise ratio (Fig. 4.16.i-l). The results indicate that the optimization of the beam collimation is much more significant than accumulation of sequential shots. Moreover, considering that in the present system the repetition rate is extremely low (1 shot every 12 minutes), accumulation is also very time-consuming and can be practically restricted to just a few shots as shown in Fig. 4.16.i-l.

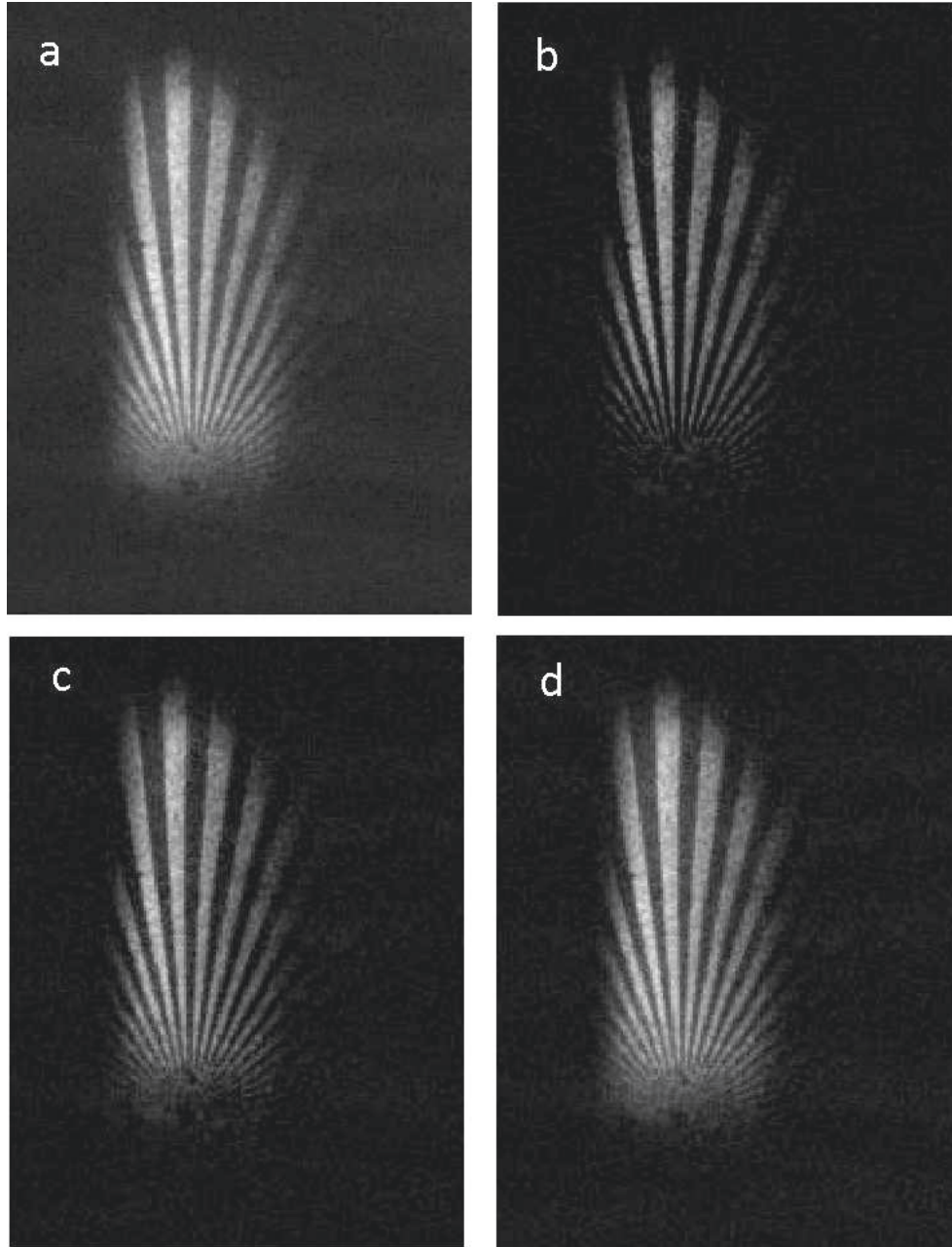


Fig. 4.17: Contrast improvement applying different background correction criteria, versus the unprocessed EUV image. Legend: a) unprocessed image, and background correction from b) 10 pixel rolling ball radius c) 30 pixel rolling ball radius d) 50 pixel rolling ball radius.

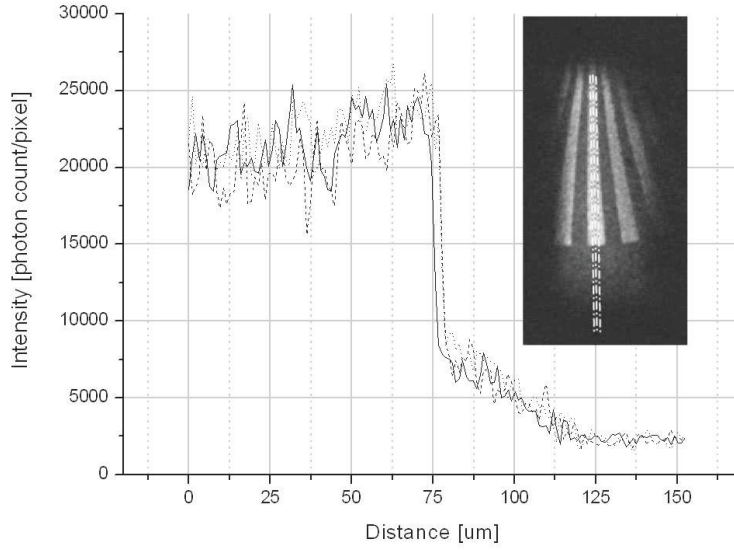


Fig. 4.18: Illumination profiles at the Siemens star's bottom edge, showing the bright-to-dark contrast.

4.2.2 XUV Imaging Experiments

The sample was located between the spherical mirror pair in the object plane, with its position adjusted using a XYZ translation stage (Fig. 4.15). EUV images were taken of a Siemens star to assess the performance in terms of resolution, contrast and astigmatism (Fig. 4.17). The importance of using a coherent source for high quality inspection/imaging is experimentally demonstrated in Fig. 4.19. The image was a single coherent (LHS) - incoherent (RHS) snapshot (no stitching). One notes the difference between the region illuminated by the coherent beam (LHS) and the region illuminated by the incoherent light (RHS). The latter provides poorer sharpness, contrast and illumination, which can be assessed observing the outer edges of the Siemens star's spokes (see discussion above). Thus despite an increased source energy ($4.4\mu\text{J}$) the lack of collimation in the extended RHS region of Fig. 4.19 has a detrimental effect on the overall image quality.

The bright-to-dark contrast was measured for three traces at the spoke edge (Fig. 4.18). Contrast is defined using Eq. 2.3.3.1 and its mean value was found to be $\gamma = 61 \pm 6\%$, with practically a vertical edge, and limited by radiation flare around the transmissive spoke. We can argue that the recalculated results, corrected for stray radiation, are showing enhanced contrast. In fact, it is evident that the zone beyond the bright spoke is not fully blocking the probe radiation. A 4:1 intensity contrast was measured, whereas the Siemens star should provide bright and completely dark zones juxtaposed. To explain the observed 4:1 values it is likely that in-band stray light from the spontaneous component has reached the exposure chamber. If this is the case, any additive flare term ϕ that superimposes to the max and min intensity values, does not change the contrast max-to-min, yet the computed γ is degraded as follows:

$$\frac{d\gamma}{d\phi} = \frac{(I_{max} + \phi) - (I_{min} + \phi)}{(I_{max} + \phi) + (I_{min} + \phi)} = -\frac{2(I_{max} - I_{min})}{(I_{max} - I_{min} + 2\phi)^2} \quad (4.2.2.1)$$

This relation indicates that in our case, based on measured background values, the theoretical contrast is as high as 74%, in agreement with the obtained modulation transfer function, as discussed below.

Fig. 4.20 shows three contrast profiles of the exposed Siemens star along circular traces obtained at $R = 20, 60$, and 100 pixels from the Siemens star center. The illumination profile is influenced by the minimal astigmatism introduced by horizontal tilting of the condenser and objective, as discussed above. The number of photons was estimated from the counts and the CCD quantum efficiency which is 45% at 103.7 eV (12-nm Sn laser line). The average areal

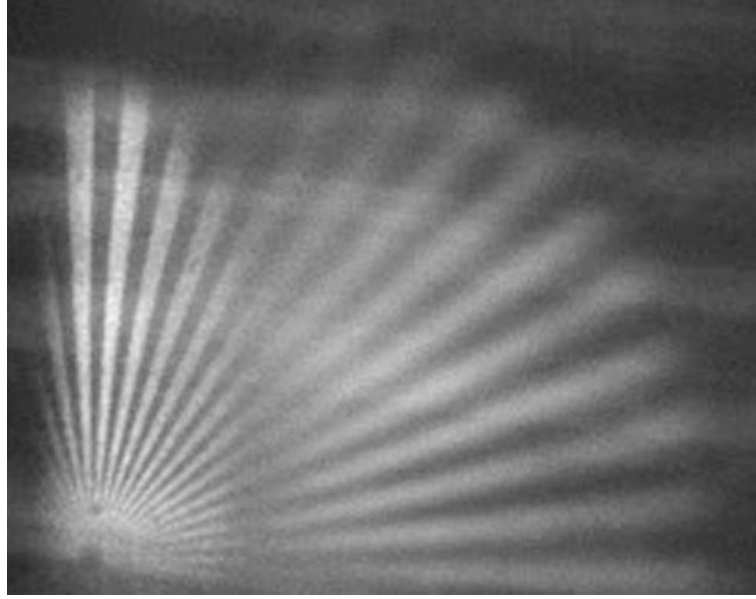


Fig. 4.19: Comparison of coherent (LHS) versus incoherent (RHS) EUV illumination for imaging.

illumination was characterized by a relative 1σ deviation (RSD) of 9% over the entire illuminated field. Knowing the collected image counts and considering the reflectivity of the Mo/Y mirror array, and the transmissivity of Si_3N_4 membrane (sample) and Zr foil (filter) as given in the experimental section, we could determine the source photons generated to be as high as 10^{11} photons that correspond to $1.8 \mu J$, in agreement with previous calibration experiments. The improvement of contrast at lower spatial frequency, i.e. at the Siemens star periphery, is evident. This can be quantified by means of the modulation transfer function (MTF).

We have computed the MTF for the unprocessed images, and also for images where an additional image processing was applied. The latter aimed at improving the background correction. The background correction was done considering a rolling ball radius of 10, 30, or 50 pixels around every pixel of the image. The obtained images after post-processing are shown in Fig. 4.17. In Fig. 4.21, the MTF is given for the four cases, where the case with 10 pixels rolling ball radius is not shown for clarity since it was identical to the unprocessed image. One notes that the image processing procedure did improve the resolution limit ($MTF = 0.09$) of a factor 3, from $1.1 \mu m$ to $330 nm$, and then a further factor of 4 from $330 nm$ to $83 nm$. The present resolution is limited by the available optics NA. Further improvement is underway since we are testing the Schwarzschild microscope, which will eliminate aberrations up to the third order. The consequence is an improvement in resolution as explained in Fig. 4.2.

4.2.3 Summary on Plasma Laser XUV Imaging

The two-mirror design discussed here, i.e. condenser and imager, is made-up of two juxtaposed concave spherical multilayer reflectors. Considering that the EUV light must be transported within and beyond the mirror pair gap, i.e. where the Siemens star was mounted, a certain tilt angle (here 3 degrees) has to be tolerated. The tilt induces astigmatism and coma aberrations in proportion to the cosine of the tilt angle. In order to address these drawbacks, we investigated Schwarzschild objective designs in the previous section. Schwarzschild objectives have been demonstrated to provide an aberration-free imaging with exactly two mirrors, and also of being capable of high resolution as required in EUV lithography. Fig. 4.22 shows the dramatic improvement in imaging quality and resolution in the vertical and horizontal dimensions when Schwarzschild optics (Fig. 4.22.B) is compared to the tilted two-concave-mirror design (Fig. 4.22.A), thanks to the collinear light transport. In spite of the dramatic improvement in resolution (values given in Fig 4.22), it remains however that the here investigated system acts as condenser/imager pair with two reflections only, whereas Schwarzschild optics uses already two reflections for just imaging, and potentially another two, if one needs to have a condenser.

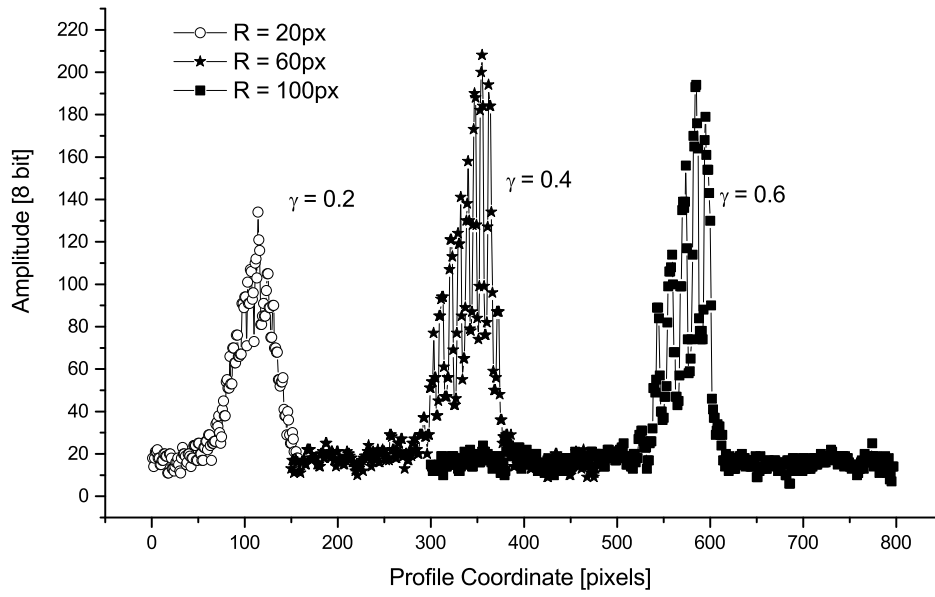


Fig. 4.20: Contrast profiles at three different radial distances (radii in pixels) from the Siemens star center. The corresponding contrast values (γ) are given.

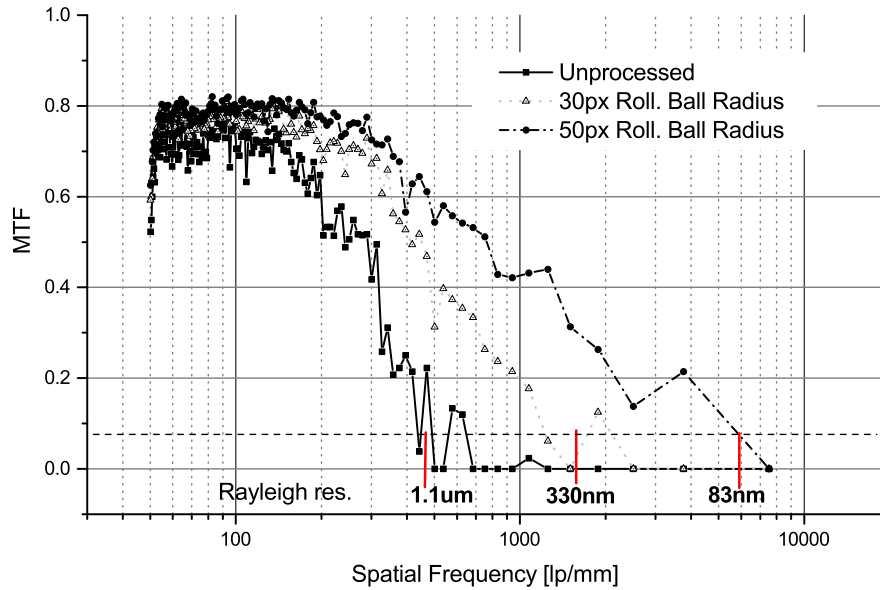


Fig. 4.21: Modulation transfer function as a function of spatial frequency, expressed as line pairs per mm (lp/mm). Different curves refer to the various discussed background subtraction procedures. Resolution are given as Rayleigh cutoffs.

Thus, considering a single multi-layer reflectivity of 45% at 12 nm, the two concave-mirror-design studied here allows an overall light throughput of 20% whereas the dual Schwarzschild design would allow as low as 4.1% overall throughput.

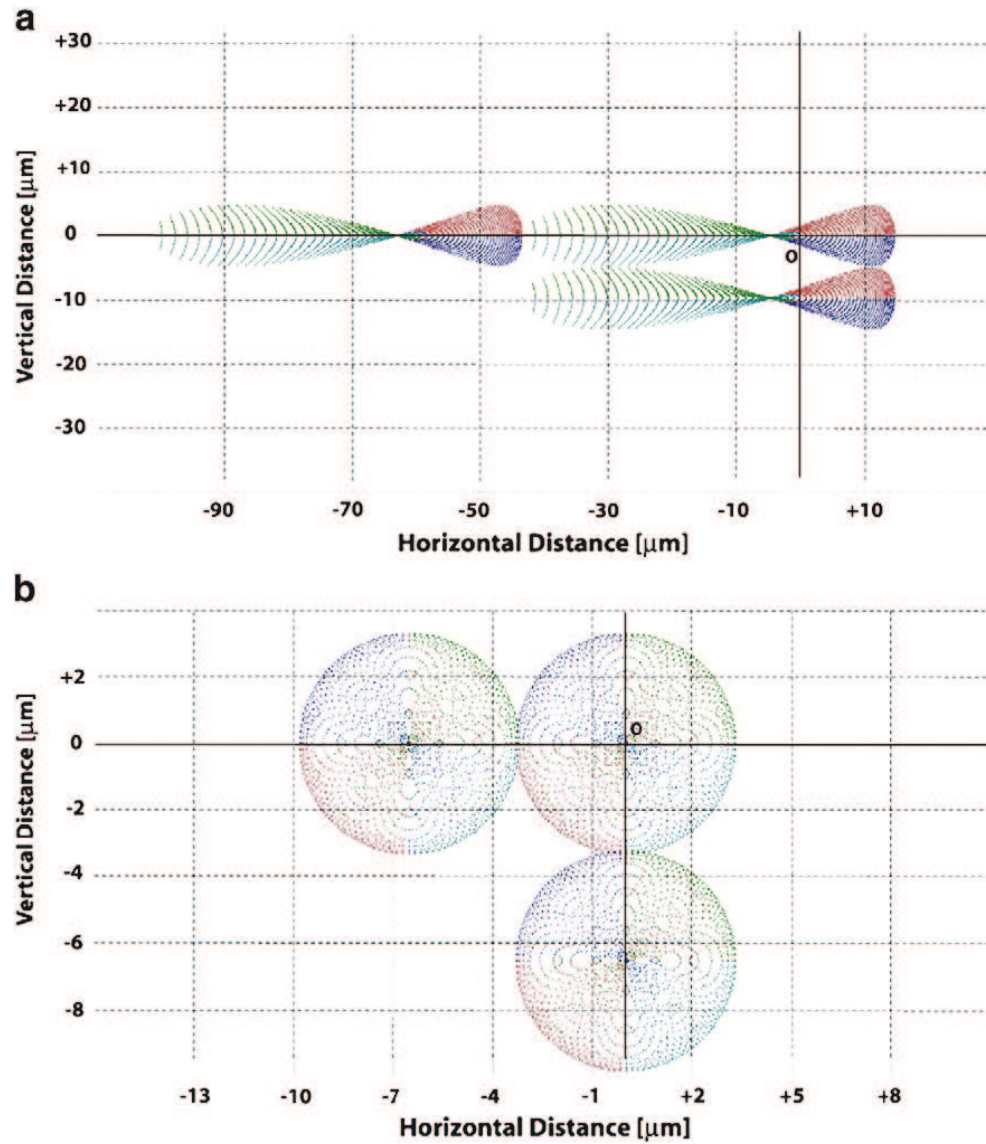


Fig. 4.22: Imaging spot diagrams obtained by ray tracing of (A) 3 degrees tilted concave mirror with a radius of curvature of 241.3 mm; (B) Schwarzschild objective with 50-fold magnification. The four quadrants have different colors as follows: green (NW), red (NE), blue (SE), cyan (SW). The imaging is shown for three points to visualize the vertical and horizontal resolution limit (spots edge-contact). For the case in (A) the resolution is $3\ \mu\text{m}$ horizontal and $0.5\ \mu\text{m}$ vertical. For the case in (B) the resolution is $0.13\ \mu\text{m}$ horizontal and $0.13\ \mu\text{m}$ vertical.

4.3 Two-color XUV Laser for Nano-spectroscopy

Published in Masoudnia et al. Phys. of Plasmas, in press 2016. Main themes here:

- *Advantage of Two-Color Laser : Monopole & Dipole Plasma-Laser*
- *Spectroscopy & Computational Analysis*
- *Tunability of the Plasma Laser*

X-ray pulses with bimodal spectra ("two-color") are very insightful pump-probes to investigate the structure of matter, the dynamics of physical processes, and chemical reactions [123, 191]. Theoretically, the timescales of rotation, vibration, dissociation of molecules, atomic excitation, atomic ionization, etc. are known [17, 69]. Ideally, one would measure experimentally such timescales by time-resolved means using dual X-ray pulses with specific time delays and spectral separation. Furthermore, near-edge X-ray absorption spectroscopy to simultaneously probe the structure and surface chemistry is another application for two-color probes [329]. Besides, the soft X-ray high energy resolution off-resonance spectroscopy (HEROS) technique by means of two-color can be a powerful method to study the local electronic and geometric structures of matter [43, 312, 313].

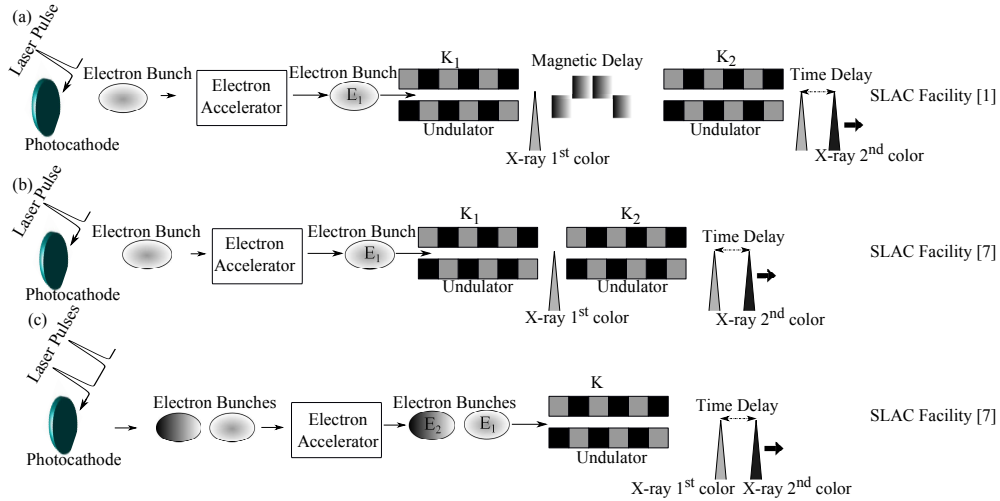


Fig. 4.23: Layout of the two-color options at accelerator facilities [191, 199]: (a) double split undulator mode, (b) gain-modulated undulator mode, (c) double-bunch undulator mode.

In 2013, SLAC researchers demonstrated for the first time pairs of X-ray laser pulses [191, 200] through self-amplified spontaneous emission (SASE) by means of X-ray Free-Electron Lasers, with wavelengths at ≈ 0.81 nm ($E \approx 1530.7$ eV) and ≈ 0.83 nm ($E \approx 1493.8$ eV), i.e. a spectral separation as small as 0.2 angstroms. The SACLA facility can currently produce pairs of X-ray laser pulses at ≈ 0.09 nm ($E \approx 13'776$ eV) and ≈ 0.12 nm ($E \approx 10'332$ eV) [123]. The two radiation pulses were delayed from coincidence to a maximum delay as long as 40 fs [191].

Two pulses with different photon energies ("two-color pulses") have been generated in an accelerator [123, 191, 199, 200], using three different schemes: (i) double split undulator mode (Fig. 4.23a), (ii) gain-modulated undulator mode (Fig. 4.23b), and (iii) double-bunch undulator mode (Fig. 4.23c).

The "*double split undulator mode*" (see Fig. 4.23a) is divided into two parts, with a magnetic delay (magnetic chicane) placed in the middle [123, 191]. In this scheme, the wavelengths of the two X-ray pulses are given by the expression: $\lambda_{1,2} = \lambda_w \frac{1+K_{1,2}^2}{2\gamma^2}$, where λ_w , K , and γ are respectively the undulator wavelength, undulator parameter, and electron Lorentz factor. The "magnetic delay" between the two undulators allows a temporal compression of the electron bunch, i.e., the rotation of electron bunch in the energy-time plane. Since both X-ray pulses are emitted by the same electron bunch, the first of the two pulses cannot be amplified to saturation. Indeed, the energy-spread induced by the XFEL process would prevent lasing on the second color.

The "*gain-modulated undulator mode*" (see Fig. 4.23b) is composed of the sections of alternating magnetic field strength [199]. Here, the wavelengths of two radiated X-rays are equal to $\lambda_{1,2} = \lambda_w \frac{1+K_{1,2}^2}{2\gamma^2}$. Since the two colors are emitted by the same electron bunch, the same limitation as above applies. In addition, the spectrum of a gain-modulated XFEL can exhibit more than two peaks, due to complex spectral features arising from the interference of the radiation emitted in two consecutive resonant undulators [191, 199].

The "*double-bunch undulator mode*" (see Fig. 4.23c) is performed by using two electron bunches with different energies and overlapped in time, so that two wavelengths appear at the exit of the undulator with a separation in the wavelength [200, 201, 346]. In this scheme, the wavelengths of two radiated X-rays are equal to $\lambda_{1,2} = \lambda_w \frac{1+K^2}{2\gamma_{1,2}^2}$. All these are possible at large scale facilities, with however the limitation in spectral separation of the two colors.

Short-wavelength free-electron lasers (XFEL) facilities are currently available in a few sites, due to the remarkable cost of construction and operation [36]. In this respect the laboratory-scale two-color XUV plasma-based laser can be a more widely-accessible platform [31].

It has been demonstrated at the LLNL that laser-produced plasmas are able to produce two XUV coherent pulses by focusing an intense laser pump on a target [149]. Two XUV lasers produced by a target have wavelengths separated by as much as 5.1 nm ($\Delta E = 10.5$ eV). In the laser-produced plasma, lasing lines come from a given radiator (e. g. Mo) through two different pumping processes: (i) collisional-pumping (monopole: $\Delta J = 0$, $J = 0 \rightarrow 0$) or (ii) photo-pumping (dipole: $\Delta J = 1$, $J = 0 \rightarrow 1$) processes. The collisional laser line is pumped through electron collisions and is the result of the transition $3d^9 4d^1(J=0) \rightarrow 3d^9 4p^1(J=1)$ for Ni-like ions. On the other hand the photo-pumped laser line is pumped by a strong radiation (e.g., $\Delta E \simeq 353$ eV $\equiv 3.51$ nm for Ni-like Mo) producing a laser line (XUV), which is the result of the transition $3d^9 4f^1(J=1) \rightarrow 3d^9 4d^1(J=1)$ for Ni-like ions.

Fig. 4.24a summarizes two-color XUV wavelengths generated by electron collisional-pumping and photo-pumping in Ni-like ions with different plasma lasing schemes. In Nilsen et al. [149], a 1 J pulse with pulse duration of 600 ps illuminates the Nb target (Nb^{+13}) followed 700 ps later by a 5 J and 1 ps pulse. In Li et al. [344], lasing in Zr^{+12} is produced by the combination of a long pulse (800 ps) and a short pulse (1 ps) with the delay between the two pulses set at 1.6 ns, and the maximum energy in the long and short pulses each being 5 J. In Nilsen et al. [148], the scheme for lasing is irradiating the Mo target (Mo^{+14}) with a 4 J, 1.5 ns pulse followed with a 3 J, 1 ps pulse.

The photo-pumped four-level system (dipole transition) and collisionally excited three-level system (monopole transition) for Ni-like ions are shown in Fig. 4.24b. Indeed, Ni-like ions with electron configuration of $[Ar] 3d^{10}$ are excited through monopole or dipole transition (see Fig. 4.24b).

Here, the aim is to demonstrate the key characteristics of two-color XUV lasers generated in the own lab within a micro-plasma active medium of Ni-like Mo (Mo^{+14}) and Ni-like Pd (Pd^{+18}). Thus, characteristics of two-color XUV lasers, such as divergence and pointing stability, are obtained experimentally. Then, computational results to investigate plasma hydro-characteristics at the lasing region for the two XUV laser lines are presented. The time difference that maximizes the gain for two-color emission in the plasma medium is obtained. Here, it is mainly interesting to investigate the hydrodynamics and atomic physics descriptions and difference between

characteristics of plasmas producing collisionally-pumped and photo-pumped lines.

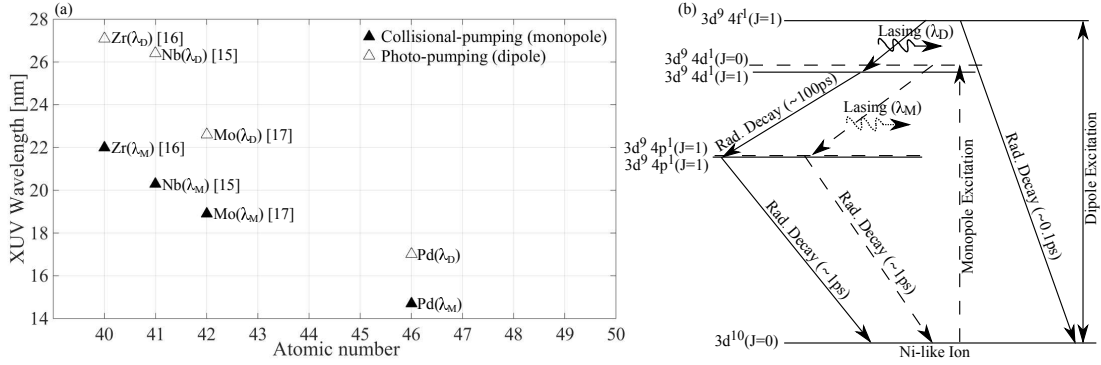


Fig. 4.24: (a) Plasma laser wavelength versus atomic number that exhibit dual wavelength emission due to either photo-pumping (λ_D) and electron collisional-pumping (λ_M) in Ni-like ions [148, 149, 344]. It shows for the Ni-like ion: $\lambda_M < \lambda_D$. (b) The four-level system (solid-line) due to the dipole and three-level system (dashed-line) due to the monopole transition for Ni-like atom. Time scales of radiative decays (Rad-decay) are order of magnitude.

4.3.1 Two-color Laser Theory & Model

4.3.2 Two-color Atomic model of the Gain Medium

For the calculation of the XUV gain produced by *collisional-pumping* a three-level system is examined as shown in Fig. 4.25a. For the calculation of the XUV gain produced by *photo-pumping* a four-level system is examined as shown in Fig. 4.25b.

4.3.2.1 Gain with Electron Collisional Pumping (Monopole Mode)

Fig. 4.25a shows a three-level system composed of the upper $|2\rangle$, lower $|1\rangle$, and the ground $|0\rangle$ state pumped by a transient collisional-pumping (collisional excitation) scheme. Due to the selection rule the transition from the lower level ($J=0$) to the upper level ($J=0$) is only achieved by the monopole collisional excitation, and the photo-pumping (dipole excitation) is here not allowed (see Fig. 4.25a).

Considering the steady state in a three-level model, rate equations are solved taking into account all the populating, depopulating, and radiative processes:

$$\frac{dn_i}{dt} = n_e \left(\sum_{i < j} n_i C_{ij}^e + \sum_{i > j} n_i C_{ij}^d \right) + \sum_{i > j} n_i A_{ij}. \quad (4.3.2.1)$$

Calculation of n_i , the population of the corresponding level $|i\rangle$, and calculation of gain due to collisional-pumping (monopole) have been extensively explained in the previous publications.

4.3.2.2 Gain with Photo-pumping (Dipole Mode)

Fig. 4.25b shows the lasing due to photo-pumping for a four-level system. It shows energy levels schematically are composed of the upper $|3\rangle$ and lower $|2\rangle$ lasing states and intermediate level $|1\rangle$ and the ground $|0\rangle$ state. The transition from lower level ($J=0$) to upper level ($J=1$) is achieved via both the monopole collisional excitation (C_{03}) and dipole excitation (R_{03}^P), as shown in Fig. 4.25b.

The upper level $|3\rangle$ is populated by both electron collisional-pumping and photo-pumping. The level populations of Ni-like ions are computed by solving the steady-state rate equations of a four-level laser model:

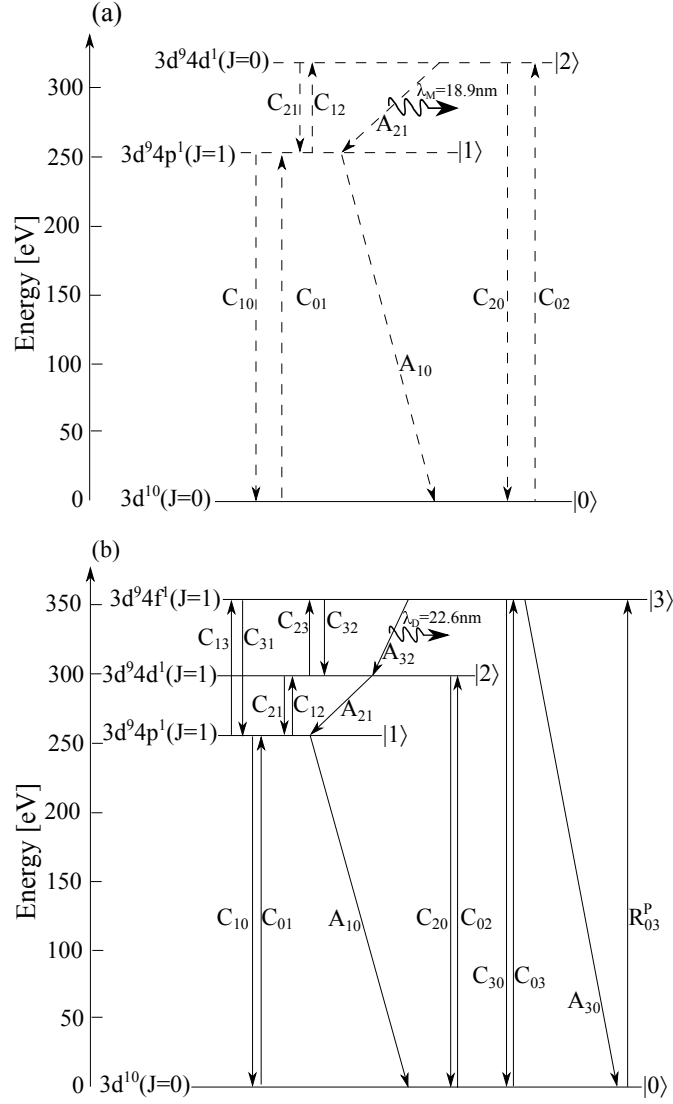


Fig. 4.25: (a) Grotrian scheme for monopole lasing (λ_M) of the Ni-like Mo. (c) Grotrian scheme for dipole lasing (λ_D) of the Ni-like Mo.

$$\frac{dn_i}{dt} = n_e \left(\sum_{i < j} n_i C_{ij}^e + \sum_{i > j} n_i C_{ij}^d \right) + \sum_{i > j} n_i A_{ij} + \sum_{i < j} n_i R_{ij}^P. \quad (4.3.2.2)$$

Here C_{ij}^e and C_{ij}^d are respectively collisional excitation and de-excitation rates in cm^3/s . A_{ij} and R_{ij}^P are the spontaneous emission and photo-pumping rate, respectively. In a four level systems, it is found:

$$\begin{aligned} n_1 &= \Omega \\ n_2 &= \Omega \Theta + \phi \\ n_3 &= \frac{\Omega(\gamma + \Theta \beta) + \phi \beta + \Psi}{\alpha} \end{aligned} \quad (4.3.2.3)$$

where n_i is the population of the corresponding level $|i\rangle$, and: $\Psi = n_0 (n_e C_{03} + R_{03}^P)$, $\eta = n_0 n_e C_{02}$, $\alpha = A_{32} + A_{30} + n_e (C_{32} + C_{30} + C_{31})$, $\gamma = n_e C_{13}$, $\Lambda = C_{32} n_e + A_{32}$, $\zeta = n_e (C_{21} + C_{23} + C_{20}) + A_{21}$, $\Xi = C_{12} n_e$, $\chi = n_e C_{21} + A_{21}$, $\Upsilon = A_{10} + n_e (C_{10} + C_{12} + C_{13})$, $\Delta = n_0 n_e C_{01}$, $\beta = C_{23} n_e$, $\varrho = C_{31} n_e$, $\Theta = \frac{\gamma \Lambda + \Xi \alpha}{\zeta \alpha - \beta \Lambda}$, $\phi = \frac{\Psi \Lambda + \eta \alpha}{\zeta \alpha - \beta \Lambda}$, $\Omega = \frac{\phi(\beta \varrho + \chi \alpha) + \Psi \varrho + \Delta \alpha}{\Upsilon \alpha - \gamma \varrho - \Theta(\beta \varrho + \chi \alpha)}$.

The photo-pumping rate (R_{03}^P) is determined as follows [150]:

$$R_{03}^P [s^{-1}] = \frac{n_{ph}}{1 + n_{ph} \gamma_0} A_{30} \quad (4.3.2.4)$$

where γ_i, γ_j are the degeneracies of the i -th, j -th levels, and the degeneracy of each level is $2J+1$ (statistical weight). n_{ph} is the number of photons per mode, which is given as follows [121]:

$$n_{ph} = \frac{1}{e^{h\nu/kT_{rad}} - 1} \quad (4.3.2.5)$$

where kT_{rad} is the radiation temperature of the pump-line. The gain given as the small signal gain coefficient describes the amplification in the system without considering its origin [90]. The small signal gain is given by the expression below:

$$g_0 = n_3\sigma_{stim} - n_2\sigma_{ab} \approx n_3\sigma_{stim}F \quad (4.3.2.6)$$

where $\sigma_{stim}, \sigma_{ab}$ are the cross section for stimulated emission and absorption, where the cross section for the stimulated emission is [90]:

$$\sigma_{stim} = 1.3 \cdot 10^{-36} A_{32} \frac{\lambda^3}{\Delta\lambda/\lambda} \quad (4.3.2.7)$$

where λ is in Ångström units and $\Delta\lambda/\lambda$ is relative spectral bandwidth. It is obtained through convolution of Doppler broadening (λ_D) and collisional broadening (λ_L) [228]. In a plasma, Doppler broadening due to the thermal motion of ions produces a Gaussian-shaped line function, where $\Delta\lambda_D = \frac{\sqrt{2kT_{ion}/M}}{c} \lambda$. Here kT_{ion} is the ion temperature and M is the ion mass. Our hydro calculation shows that at the lasing region the ion temperature is approximately 3.5 times less than the electron temperature. The electron impact broadening produces a Lorentzian-shaped line function, where $\Delta\lambda_L \propto n_e$ [115]. The inversion factor (F) is the population inversion factor, defined as follows:

$$F = 1 - \left(\frac{\gamma_3}{\gamma_2} \right) \frac{n_2}{n_3} \quad (4.3.2.8)$$

where γ_i and γ_j are the degeneracies of the i -th and j -th levels. The degeneracy of each level is $2J+1$ (statistical weight).

4.3.3 Two-color Lasing Process & Saturation

Assuming a line profile with a width of $\Delta\lambda$, the saturation intensity is [184, 274]:

$$I_{sat} = \frac{8\pi hc^2}{\lambda^4} \frac{\Delta\lambda}{\lambda}. \quad (4.3.3.1)$$

The upper limit for total X-ray intensity can be approximated by following equation [222]:

$$I_{tot} = I_{sat} g_0 L \quad (4.3.3.2)$$

where $g_0 L$ is small signal gain-length product obtained by considering:

$$g_0 L = \int_0^L g_0(z) dz \quad (4.3.3.3)$$

where dz is along the target surface.

4.3.4 Two-color Light Propagation across the Gain Medium

4.3.4.1 XUV Ray-tracing

An important effect limiting the gain is refraction, which bends the pump away from the high gain zone. In this sub-section, the ray trajectory is analyzed for 2D propagation. Considering Maxwell's equations, and the eikonal equation [321] namely,

$$\frac{d}{ds} \left(n(\mathbf{r}, \omega) \frac{d\mathbf{r}}{ds} \right) = \nabla n(\mathbf{r}, \omega) \quad (4.3.4.1)$$

where ds is the element of distance along the ray, \mathbf{r} is the position vector for a ray point, and n is the refractive index of the medium:

$$n = \sqrt{1 - \frac{n_e}{n_c}} \quad (4.3.4.2)$$

where n_c is the critical electron density at the frequency of the propagating ray:

$$n_c[cm^{-3}] = \frac{1.1 \cdot 10^{21}}{\lambda^2} \quad (4.3.4.3)$$

where λ is the wavelength in μm .

The XUV refraction angle turns out to be given by the following expression [80, 157]:

$$\phi_r = \sqrt{\frac{n_{e0}}{n_c}} \quad (4.3.4.4)$$

where n_c is the critical density, n_{e0} is the maximum electron density within the gain region, and ϕ_r is refraction angle from horizontal axis at which a ray exits the side of the plasma.

4.3.4.2 Divergence and Pointing-stability

Pointing stability and divergence are properties used to characterize laser or laser-like radiation source such as a plasma based XRL or an XFEL. For diagnosing the pointing stability and the divergence of the X-ray pulses a flat-field spectrometer is used, as shown in Fig. 2.6. The vertical axis on the CCD image is wavelength. The horizontal axis provides spatial resolution which can be converted into pulse divergence for any single shot. A series of shots may be used to obtain information on pointing stability as follows. The pointing stability is given by spatial fluctuation of the maximum peak of intensity (Gaussian-function) of the images obtained and calculated as the standard deviation (1σ precision) of the peak coordinates. A variation in the range of mrad is expected for table-top systems [192]. Distance to the target and density of the plasma are related to the refraction angle of XUV lasers. The latter determines the coordinates of the maximum peak of intensity. The data are given in mrad in terms of the mean, the uncertainty, and the standard deviation of the experimental measurements. The divergence is introduced as the full width at $1/e^2$ of peak intensity.

4.3.5 Experimental Two-color Laser Characterization

4.3.5.1 Molybdenum Two-color Laser

Two-color XUV lasing at $\lambda_M = 18.9$ nm ($E_M = 65.6$ eV) and $\lambda_D = 22.6$ nm ($E_D = 54.9$ eV) generated by electron collisional-pumping and photo-pumping in Ni-like Mo were observed. The measured spectrum showed that the two wavelengths from Mo exhibit different pulse characteristics, such as pointing stability and divergence. These are affected by plasma inhomogeneity, e.g. temperature or density gradients.

Fig. 4.26a shows the mean intensity for lasing lines observed in the experiment from the Mo laser. It shows that the peak intensity of XUV lasing at $\lambda_M = 18.9$ nm is a factor of ≈ 18 higher than the peak intensity at $\lambda_D = 22.6$ nm. Fig. 4.26b shows the experimentally measured spectrum. Since there is free propagation of the XUV in the horizontal direction giving information about the XUV divergence, Fig. 4.26c. and Fig. 4.26c show that 10.2 ± 1.0 mrad and 8.3 ± 1.4 mrad are divergences determined for the full width of the profile at $1/e^2$ of the peak intensity for $\lambda_M = 18.9$ nm and $\lambda_D = 22.6$ nm, respectively. Fig. 4.26c shows also that the mean peak intensity of each of the two wavelengths appear on the CCD-detector shifted by some 3.2 mrad. Table. 4.4 summarizes the mean of pointing stability, divergence, and intensity of two-color

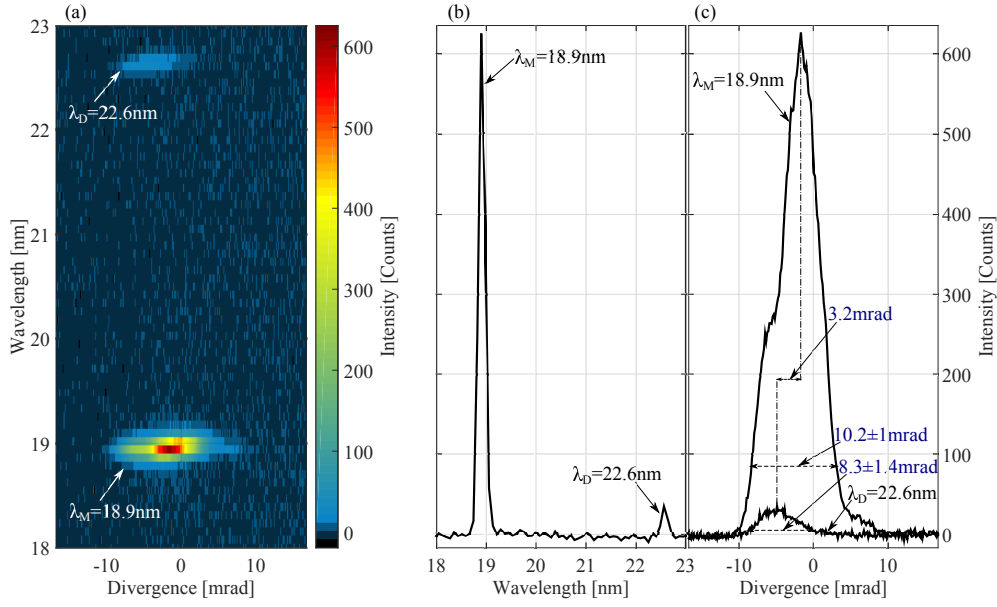


Fig. 4.26: (a) The experimentally measured mean intensity for lasing lines observed for Ni-like Mo at wavelengths $\lambda_M = 18.9$ nm and $\lambda_D = 22.6$ nm. (b) Wavelength profile (vertical axis in (a)). (c) Divergence profile (horizontal axis in (a)). In subplot (a) and (c), the number 0 at the x-axis is the center of the image on the CCD-detector.

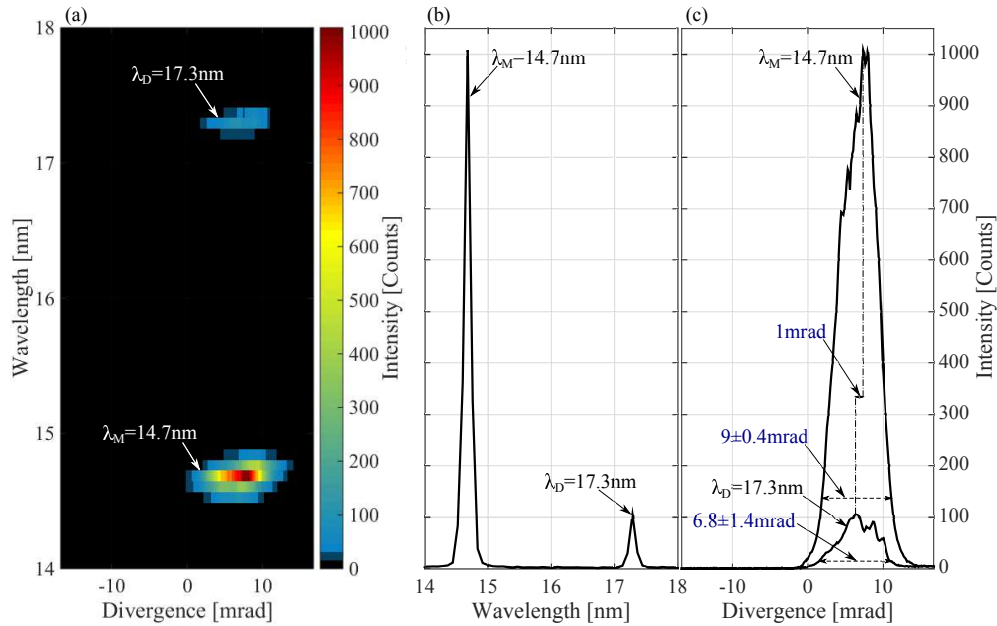


Fig. 4.27: (a) The experimentally measured mean intensity for lasing lines observed for Ni-like Pd at wavelengths $\lambda_M = 14.7$ nm and $\lambda_D = 17.3$ nm. (b) Wavelength profile (vertical axis in (a)). (c) Divergence profile (horizontal axis in (a)). In subplot (a) and (c), the number 0 at the x-axis is the center of the image on the CCD-detector.

produced irradiating Mo target. The measured divergence at $\lambda_M = 18.9$ nm is ≈ 1.2 times larger than the experimental divergence at $\lambda_D = 22.6$ nm. The relative bandwidth ($\Delta\lambda/\lambda$) of 18.9 is 50% larger than the relative bandwidth of 22.6nm.

Tab. 4.4: Experimentally measured dual pulse characteristics (mean) of XUV laser lines observed in the experiment for Mo.

Wavelength [nm]	Experimental divergence (mean) [mrad]	Experimental pointing stability [mrad]	Relative bandwidth ($\Delta\lambda/\lambda$)
$\lambda_M=18.9$	10.2 ± 1.0	1.4	$9 \cdot 10^{-3}$
$\lambda_D=22.6$	8.3 ± 1.4	1.4	$6 \cdot 10^{-3}$

4.3.5.2 Palladium Two-color Laser

Two-color XUV wavelengths at $\lambda_M = 14.7$ nm ($E_M = 84.3$ eV) and $\lambda_D = 17.3$ nm ($E_D = 71.7$ eV) generated by electron collisional-pumping and photo-pumping in Ni-like Pd were observed. The measured spectrum showed that two laser emission wavelengths from Pd exhibit different pulse characteristics.

Fig. 4.27a shows the mean intensity for lasing lines observed in the experiment with Pd. It shows that the peak intensity of the XUV laser at $\lambda_M = 14.7$ nm is ≈ 10 times higher than the peak intensity of the XUV laser at $\lambda_D = 17.3$ nm. Fig. 4.27b shows the experimentally measured spectrum. In Fig. 4.27c, 9.0 ± 0.4 and 6.8 ± 1.4 are divergences determined for the full width of the profile at $1/e^2$ of the peak intensities at wavelengths $\lambda_M = 14.7$ nm and $\lambda_D = 17.3$ nm, respectively. Fig. 4.27c shows that the mean peak intensities of each of the two wavelengths appear on the CCD-detector shifted by some 1 mrad.

Table 4.5 summarizes the divergence of the XUV laser lines observed in the experiment with Pd for an optimized-total pulse energy 2.6 ± 0.1 J (see Fig. 4.27). It shows that experimentally measured divergence at wavelength $\lambda_M = 14.7$ nm is ≈ 1.3 times larger than the experimental divergence at $\lambda_D = 17.3$ nm. The relative bandwidth ($\Delta\lambda/\lambda$) of 14.7 is 30% larger than the relative bandwidth of 17.3nm.

Tab. 4.5: Experimentally measured dual pulse characteristics (mean) of the XUV laser lines observed in the experiment for Pd.

Wavelength [nm]	Experimental divergence [mrad]	Experimental pointing stability [mrad]	Relative bandwidth ($\Delta\lambda/\lambda$)
$\lambda_M=14.7$	9.0 ± 0.4	1.0	$8 \cdot 10^{-3}$
$\lambda_D=17.3$	6.8 ± 1.4	2.5	$6 \cdot 10^{-3}$

4.3.6 Computational Modeling

4.3.6.1 Calculation of the Two-color XUV Lasing Process

Fig. 4.28 shows the lifetime of each level due to radiative decay, where dashed lines represent a three-level system (collisional-pumping) and solid lines represent a four-level system (photo-pumping). For the Ni-like ions, a small population in the 4f state is expected because its fluorescences is fast ($\tau = 0.1ps$). The 3d \rightarrow 4f transition would be expected to be optically thick and so it creates a radiation field in the plasma that photon pumps electrons from the 3d ground state ($|0\rangle$) to the 4f excited state ($|3\rangle$). This process ensures a sufficient population in the 4f state so that it can lase to the 4d state. This in turn requires a high enough density so that collisions depopulate the 4d lower laser level. The lifetime of ground level is estimated from the required ionization time of ground level (Mo⁺¹⁴), where $t[s] = 10^{11}/n_e [\text{cm}^{-3}]$ [234].

Fig. 4.29a and Fig. 4.29b show the collisional excitation and de-excitation coefficients between levels of a three-level laser model (monopole). Fig. 4.29a shows that for $T_e \gtrsim 200$ eV the

dominant pumping is collisional from the coefficient C_{02} (from the ground level to the upper level). It is noteworthy to mention that the hydro calculation shows that at lasing region population in the ground level is approximately 3.4 times higher than population in the upper level. However, there is gain because the population of the upper level is greater than the population of the lower level.

Fig. 4.29a shows that monopole collisional excitation (C_{02}) after 600 eV start to slightly decrease. Furthermore, it shows that C_{02} has a saturation behavior with increasing temperature, i.e., C_{02} increases ≈ 100 times by increasing temperature from 50 eV to 350 eV meanwhile C_{02} increases just 20% by increasing temperature from 350 eV to 600 eV.

Fig. 4.29c and Fig. 4.29d summarize calculated collisional coefficients for population and depopulation of the four-level laser model (dipole), as a function of the electron temperature. They show that with increasing temperature the collisional de-excitation decreases meanwhile the collisional pumping increases, especially in the first hundreds of eV. Fig. 4.29c shows that for $T_e \gtrsim 400$ eV the dominant collisional-pumping is through the coefficient C_{03} (from the ground level to the upper level).

Fig. 4.29c shows that dipole collisional excitation (C_{03}) constantly increases by increasing temperature (up to 2000 eV). It shows that C_{03} also has a saturation behavior with increasing temperature, i.e., C_{03} increases ≈ 400 times by increasing temperature from 50 eV to 600 eV meanwhile C_{03} increases just 30% by increasing temperature from 600 eV to 1500 eV.

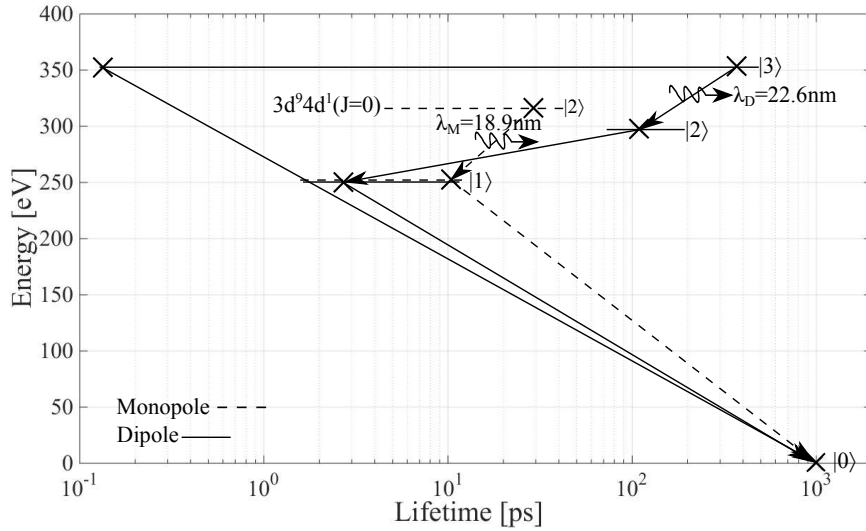


Fig. 4.28: Chrono-energy diagram for Ni-like Mo. The lifetime of each level due to radiative decay is shown by a marker: \times . The three-level is for lasing due to monopole pumping (dashed lines). The four-level is for the lasing due to dipole pumping (solid lines).

4.3.6.2 Calculation of Time and Space Distribution of Two-color Gain

Fig. 4.30a shows the gain as a function of time. The starting time corresponds to 1 ps after arrival of the main-pulse (Fig. 4.30a). At the time of 2.4 ps the peak of the main-pulse is deposited to the pre-plasma. The peaks of the gains produced by the two lines of 18.9 nm ($E_M = 65.6$ eV) and 22.6 nm ($E_D = 54.9$ eV) happen at 2.7 ps and 2.9 ps. Thus, the instant at which maximum gain occurs have a time separation of ≈ 0.2 ps, i.e., the peak of the monopole XUV laser is $\approx 20\%$ of pulse duration (pump pulse).

Fig. 4.30 shows that the gain at $\lambda_M = 18.9$ nm ($E_M = 65.6$ eV) is ≈ 4 times higher than the gain at $\lambda_D = 22.6$ nm ($E_D = 54.9$ eV). It shows a peak gain of 230 cm^{-1} at $\lambda_M = 18.9$ nm for the $4d^1(J=0) \rightarrow 4p^1(J=1)$ transition. It shows a peak gain of 55 cm^{-1} at $\lambda_D = 22.6$ nm with inclusion of the photo-pumping rate (Eq. 4.3.2.4) for the $4f^1(J=1) \rightarrow 4d^1(J=1)$ transition. Meanwhile, the computation shows that ignoring photo-pumping (Eq. 4.3.2.4), no gain is obtained on the $4f^1(J=1) \rightarrow 4d^1(J=1)$ transition. Thus, the computational study shows that considering photo-pumping excitation improves the gain for the $4f^1(J=1) \rightarrow 4d^1(J=1)$ transition.

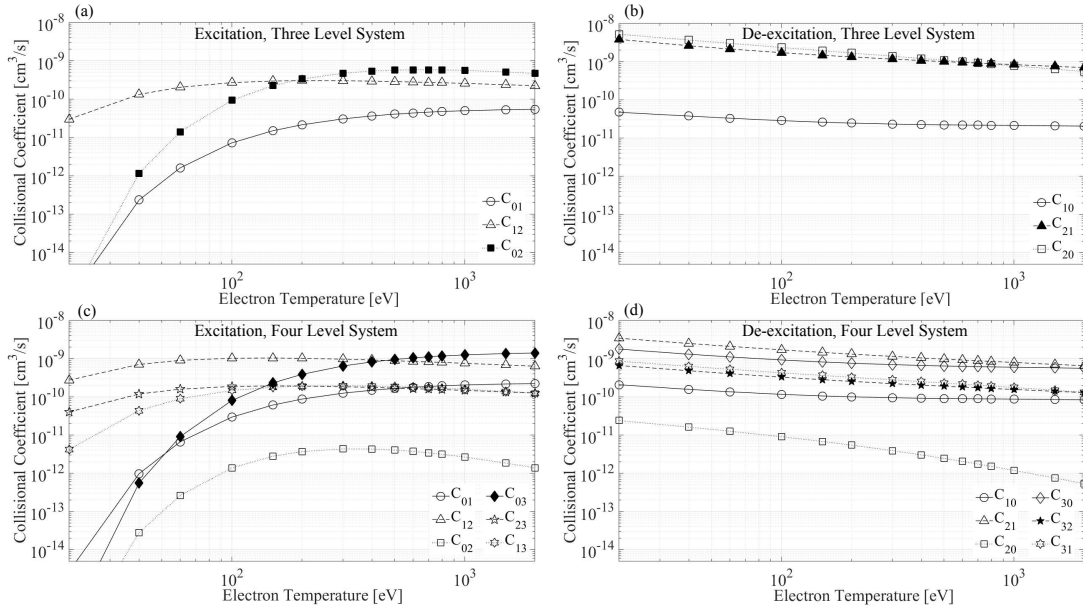


Fig. 4.29: Calculated collisional (a) excitation and (b) de-excitation coefficients for three-level system as a function of the electron temperature for monopole lasing in Ni-like Mo. Calculated collisional (c) excitation and (d) de-excitation coefficients for four-level system as a function of the electron temperature for dipole lasing in Ni-like ions.

transition.

Fig. 4.30b shows the gain as a function of space, i.e., height above the target. The peaks of the gain produced by two lines of $\lambda_M = 18.9$ nm ($E_M = 65.6$ eV) and $\lambda_D = 22.6$ nm ($E_D = 54.9$ eV) are at heights 75.6 μm and 70.4 μm , respectively. The active-medium thickness and gain lifetime are considered as the full width at half maximum of the gain, as shown in Fig. 4.30a and Fig. 4.30b. Fig. 4.30a shows that the gain lifetime at $\lambda_M = 18.9$ nm ($E_M = 65.6$ eV) is a factor of ≈ 5 larger than the gain lifetime at $\lambda_D = 22.6$ nm. Fig. 4.30b shows that the gain thickness at $\lambda_M = 18.9$ nm ($E_M = 65.6$ eV) is a factor of ≈ 1.8 larger than the gain thickness at $\lambda_D = 22.6$ nm.

Fig. 4.30a shows that gain build-up time (required time to arrive maximum) due to collisional- and photo-pumping are 0.7 ps and 0.9 ps, respectively. Fig. 4.30b shows that the build-up length-scale of the gain (required length to arrive maximum) due to collisional- and photo-pumping are 11.5 μm and 6.3 μm , respectively.

In Fig. 4.31 the electron density, electron temperature, and photo-pumping rate versus height above the target at the times that maximize the gains due to the collisional- and photo-pumping are shown, respectively.

Fig. 4.30b (see x-axis) confirms that the gain-area at wavelength λ_D overlaps quite well the

Tab. 4.6: Calculated characteristics for the $4d^1(J=0) \rightarrow 4p^1(J=1)$ (monopole) and $4f^1(J=1) \rightarrow 4d^1(J=1)$ (dipole) two-color XUV laser for the Ni-like Mo system.

Specification	Monopole Laser	Dipole Laser
Wavelength	18.9nm	22.6nm
Peak gain	230cm^{-1}	55^{-1}
Gain lifetime	5.7ps	1.1ps
Gain thickness	32.8 μm	18.2 μm
Optimum Density	$1.2 \cdot 10^{20}\text{cm}^{-3}$	$2.1 \cdot 10^{20}\text{cm}^{-3}$
Optimum Temperature	295eV	350eV
Propagation Divergence	6.2mrad	9.8mrad
Phase Velocity	$(1 + 1.9 \cdot 10^{-5})c$	$(1 + 5.2 \cdot 10^{-5})c$

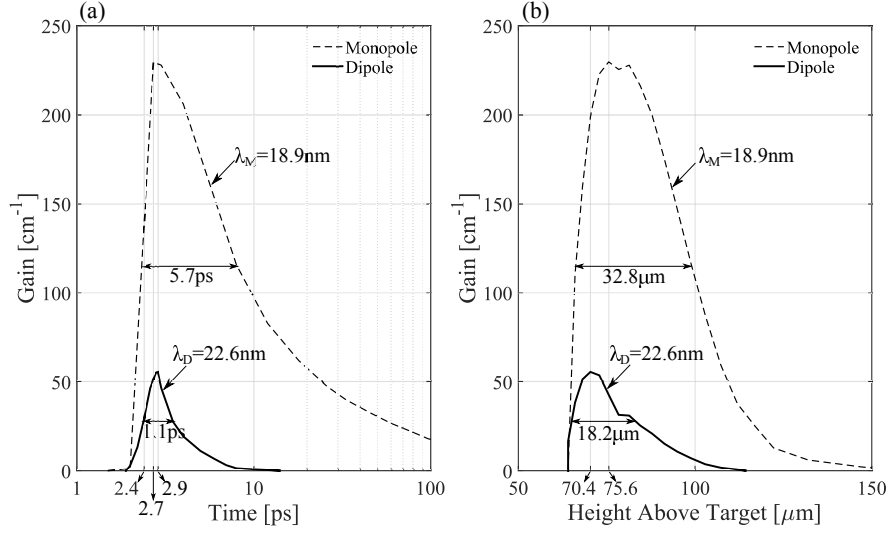


Fig. 4.30: (a) Temporally resolved and (b) spatially resolved calculated gain for the transitions $4d^1(J=0) \rightarrow 4p^1(J=1)$, $\lambda_M = 18.9$ nm, and $4f^1(J=1) \rightarrow 4d^1(J=1)$, $\lambda_D = 22.6$ nm. (a) The starting time in x-axis is from 1 ps, which corresponds to 1 ps after arrival of main-pulse. (a) Time 2.4 ps corresponds to the arrival time of the peak of the main-pulse.

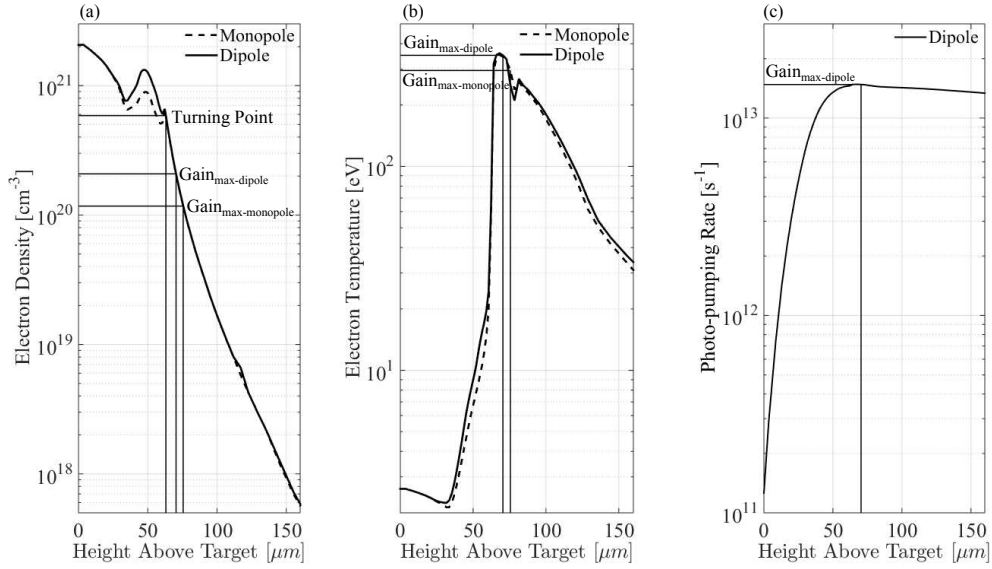


Fig. 4.31: (a) Electron density and (b) electron temperature of lasing Mo at the time corresponding to maximum gain for the monopole ($\lambda_M = 18.9$ nm) and dipole ($\lambda_D = 22.6$ nm) transition are shown, which are calculated with the hydrodynamics code. (c) By calculating radiation temperature with the hydrodynamics code, photo-pumping rate (Eq. 4.3.2.4) at the time corresponding to maximum gain for the dipole transition is obtained. The height above the target is in the direction normal to the surface of target. The peaks of the gain ($Gain_{max}$) produced by two transitions are at heights 70.4 μm (dipole) and 75.6 μm (monopole) above the target.

gain-area at wavelength λ_M . It shows that the maximum electron density within the gain region for both wavelength is the same. Then, considering the refraction angle in Eq. 4.3.4.4 yields:

$$\frac{\phi_{r-18.9nm}}{\phi_{r-22.6nm}} = \sqrt{\frac{n_{c-22.6nm}}{n_{c-18.9nm}}} = 1.2 \quad (4.3.6.1)$$

which shows that the refraction angle at λ_M is 20% times larger than the refraction angle at λ_D . This is in agreement with experimental results (see Sec.4.3.5.1). In Sec.4.3.5.1, it is shown that

the experimentally measured divergence of $\lambda_M = 18.9$ nm is ≈ 1.2 times larger than the one of $\lambda_D = 22.6$ nm.

Fig. 4.31a shows that lasing of both XUV lines (monopole and dipole) occurs directly and very efficiently in the region beyond the turning point to heat up a plasma in order to achieve the optimum temperature required to produce strong pumping to the upper laser level, allowing the lasing process to begin. Considering $\theta = 40^\circ$ (see Fig.2.6), the electron density at the turning point of the pump pulse is:

$$n_{te} = n_c \cos^2 \theta \approx 5.9 \cdot 10^{20} \text{ cm}^{-3} \quad (4.3.6.2)$$

where, the critical density for the pump pulse is $n_c \approx 10^{21} \text{ cm}^{-3}$.

Fig. 4.31c shows that at the point maximum gain the photo-pumping rate is also at its maximum value, which is $R_{03}^p \approx 1.5 \cdot 10^{13} \text{ s}^{-1}$ ($\tau_{03}^p = 1/R_{03}^p = 67$ fs).

Table. 4.6 summarizes the gain lifetime, gain thickness, the electron density, and the electron temperature maximizing the gain, and the phase velocity (v_p) for double-color in Ni-like Mo plasma.

As it is shown in Table. 4.6, the electron density and electron temperature corresponding to the maximum gain at wavelength λ_D are 1.7 and 1.2 times higher than the electron density and electron temperature which maximize the gain at wavelength λ_M .

By considering electron densities in Table. 4.6 and using Eq. 4.3.4.4, divergences at the points of maximum gain for dipole and monopole transitions are obtained respectively as 9.8 mrad and 6.2 mrad, a difference of 3.6 mrad. It is in agreement with the experimental result. As it is shown in Fig. 4.26c, the mean peak intensity of two-color occurs with 3.2 mrad difference.

Table. 4.6 shows the phase velocity at these two points. The phase velocity of XUV laser in the plasma is calculated by $v_p = c/n$, where n is refractive index of plasma. The critical densities (n_c) at wavelengths $\lambda_D = 22.6$ nm and $\lambda_M = 18.9$ nm are $2.2 \cdot 10^{24} \text{ cm}^{-3}$ and $3.1 \cdot 10^{24} \text{ cm}^{-3}$, respectively. It shows that the phase velocity at the point of maximum gain for dual color lasing has a difference of $\approx 3.3 \cdot 10^{-5}c$.

Taking into account the electron density profile that maximizes gain (see Fig. 4.31a), the monopole and dipole XUV laser trajectories along the plasma gain medium can be calculated and it is shown in Fig. 4.32a. Fig. 4.32a shows that the monopole XUV trajectory is longer, which will maximize amplification length.

The gain-length product along the target can be obtained by combination of a ray tracing calculation (see Fig. 4.32a) and gain calculation (see Fig. 4.30).

Fig. 4.32b shows the small signal gain-length product for monopole- and dipole-pumping, respectively. In fact, by knowing the gain above the target and using the ray trajectory equation, the gain-length product is calculated along the target. In Fig. 4.32b, the gain-length product is shown.

Fig. 4.32 shows $(g_0L)_{\text{monopole}}/(g_0L)_{\text{dipole}} \approx 8$ (Eq. 4.3.3.3). The saturated intensity (Eq. 4.3.3.1) of the monopole laser line is 3 times larger than saturated intensity of dipole one. Thus, considering Eq. 4.3.3.2 shows that the total intensity of monopole pulse is ≈ 24 times larger than total intensity of dipole pulse. In Fig. 4.26, the integration of the experimentally measured intensity profile of monopole and dipole lines shows that the total intensity of the monopole pumping is ≈ 25 times larger than dipole one. Then, a good agreement between computational and experimental results is proved, where $(I_{tot_M}/I_{tot_D})_{\text{computation}} \approx 24$ and $(I_{tot_M}/I_{tot_D})_{\text{experiment}} \approx 25$.

4.3.7 Discrete Tunability of Two-color XUV Laser

Two XUV lines for Ni-like Mo and Pd were here measured experimentally. Complete computational analysis of Mo target has been presented. Here, it is shown that by changing the target material the two-color XUV laser can be made tunable over the entire soft X-ray domain.

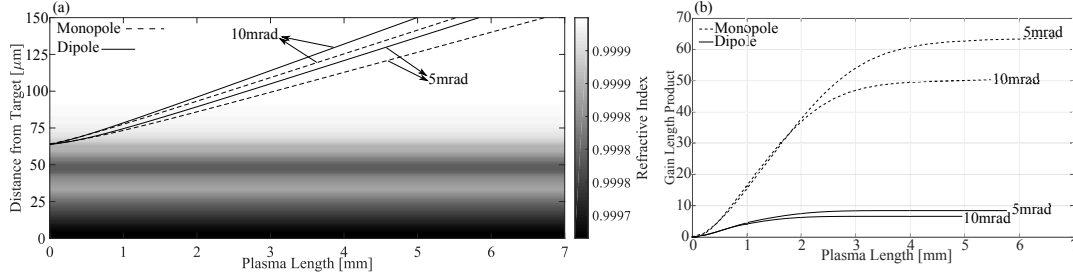


Fig. 4.32: (a) Short-wavelength laser trajectory along the plasma gain medium. The monopole X-ray pulse remains within the plasma gain region for longer. (b) Gain-length product of monopole and dipole lines (Eq. 4.3.3.3).

Tab. 4.7: Calculated wavelengths due to photo-pumping in Ni-like ions. The experimentally measured wavelengths by other literatures [149, 344] are presented. The experimentally measured wavelengths for Mo and Pd in this work are presented. λ_{D-FAC} gives a value calculated by FAC code. λ_D is a value estimated by considering a correction factor, which is obtained by comparison of experimentally and computationally calculated wavelengths.

Ni-like ion	λ_{D-FAC} [nm]	λ_D [nm] (Correction factor)	λ_D [nm] (Experiment)
Y^{+11} ($Z = 39$)	28.8	30.4	—
Zr^{+12} ($Z = 40$)	26.0	27.1	27.1 [344]
Nb^{+13} ($Z = 41$)	23.7	24.6	24.6 [149]
Mo^{+14} ($Z = 42$)	21.8	22.6	22.6 (this work)
Pd^{+18} ($Z = 46$)	16.4	17.3	17.3 (this work)
Ag^{+19} ($Z = 47$)	15.5	16.3	—
Cd^{+20} ($Z = 48$)	14.7	15.5	—
In^{+21} ($Z = 49$)	13.9	14.7	—
Sn^{+22} ($Z = 50$)	13.2	14.0	—
Te^{+24} ($Z = 52$)	12.1	12.7	—
Sm^{+34} ($Z = 62$)	8.4	8.8	—

Table. 4.7 shows the photo-pumping wavelengths for some other Ni-like atoms calculated by atomic calculations (FAC) and experiment. Since calculations are approximations, the correction factor is considered on the computationally calculated wavelengths (Table. 4.7). Photo-pumping wavelengths with the correction factor can be predicted based on comparison between wavelengths calculated by FAC and wavelengths obtained experimentally. Table. 4.7 shows that with increasing the atomic number the estimated wavelengths are closer to those calculated by atomic calculations (FAC) due to fact that FAC is a code based on j-j coupling which better described for high- Z atoms or heavily ionized atoms.

4.3.8 Summary on Plasma Laser Spectroscopy

Plasma-driven XUV lasers offer the possibility of multiple transitions in a target material to generate a two-color XUV laser in a table-top setup. Indeed, such a mode of operation is not simple at all in accelerator facilities for X-ray laser sources, such as Free electron lasers. In this work, experimental and computational results on two-color XUV lasing using a Ni-like plasma as a gain medium were shown. We highlighted the atomic physics of the collisionally pumped laser (monopole pumping) versus the photo-pumped laser (dipole pumping).

Both computational and experimental results showed that the divergence of the monopole excited XUV pulse is 20% larger than the divergence for the pulse corresponding to the dipole transition. The mean peak intensity of the two colors (monopole and dipole) are separated on the far field by 3.2 mrad. Computational results show that the refraction angle at the points corresponding to maximum gain for dipole and monopole transitions are respectively as 9.8 mrad and 6.2 mrad, i.e., a significant difference in light propagation across the inhomogeneous plasma gain-medium. The plasma that maximizes the dipole transition rate is hotter and denser than the plasma that optimizes the monopole transition rate. The electron density and electron temperature maximizing the gain at λ_D are a factor of 1.7 and 1.2 higher than

the electron density and electron temperature maximizing the gain at λ_M . It is demonstrated computationally that the peaks of the gain for both λ_M and λ_D form after the turning point at heights of 75.6 μm and 70.4 μm above the target.

This computational study showed that the peak of the gain of two colors (monopole and dipole) occurs at the time difference of $\Delta t \approx 0.2$ ps. The gain of monopole is a factor of 4 higher than the gain for the dipole. The gain lifetime at λ_M is a factor of ≈ 5 larger than the gain lifetime at λ_D . The gain thickness at λ_M is a factor of ≈ 1.8 larger than the gain thickness at λ_D . It is shown that the gain build-up time due to collisional- and photo-pumping are 0.7 ps and 0.9 ps, respectively. It is shown that the build-up length-scale of the gain due to collisional- and photo-pumping are 11.5 μm and 6.3 μm , respectively. It is shown that ignoring photo-pumping, no gain is obtained on the $3d^9 4f^1(J=1) \rightarrow 3d^9 4d^1(J=1)$ transition. We have extrapolated our study to a larger set of target material, in order to highlight the potential for tunability.

5. GENERAL DISCUSSION & CONCLUSIONS

My research program funded under the SNSF Professorship scheme (2001-2015) was confronted with a challenging task, that of demonstrating feasibility of advanced analytical technologies on a table-top X-ray laser system. The task was indeed challenging, because performed exactly in the same years of initial operation of a number of world-wide X-ray free-electron lasers (fourth generation synchrotrons). The inherent disbelief of the community for a miniaturization of the tool has been addressed here with a systematic study on the potentials of plasma-lasing, and comparing the specs with the requirements. Fig. 5.1 was prepared comparing the specification of a number of short-wavelength sources (see Sect. 1.1) with the requirements for a number of science cases. One observes that the X-ray laser (XRL) produced by plasma amplification does match the needs for these advanced science cases in materials and technology.

Indeed, the present work has highlighted a number of strengths, and has contributed to reduce the gap concerning the weaknesses. In Chapter "*Methods*" and in the theoretical sections of the various results parts, I have discussed the suitability of certain algorithms for the simulation of the lasing process across a plasma column, e.g. LTE versus non-LTE models. I have also contributed in the development of procedures, and in the obtainment of scaling-laws, that predict the performance in agreement with experimental observations. For instance optimum plasma conditions for efficient lasing, such as required temperature and required electron density, can be now estimated after my treatment. Similarly, a simple equation predicts the maximum (saturated) laser output for a given plasma column. These computational procedures were largely used in the specific chapters on fundamental and applied results.

In Chapter "*Optimization of Plasma X-Ray Lasing*" I investigated **fundamental aspects** on the generation of soft X-ray plasma lasing. Line focusing with the aid of a tilted spherical mirror proved effective. The intensity should not exceed a minimum "lasing threshold". In case the pump energy is redundant, it is advisable to stretch the focus length and achieve longer amplification length. Tilting the target induces intensity-inhomogeneous line-focus. Computational data were benchmarked with direct measurement of the energy deposition at the light focus and travelling wave excitation. The latter has been parameter-wise investigated.

Furthermore, it emerged that for *scaling-down the wavelength*, large angles of target-incidence are essential to penetrate the pump deep into the plasma. On the other hand, to maximize the interaction length between the pump and the plasma medium, and *have better efficiency*, a small target-incidence irradiation is preferred. The fundamental conclusion was a trade-off between

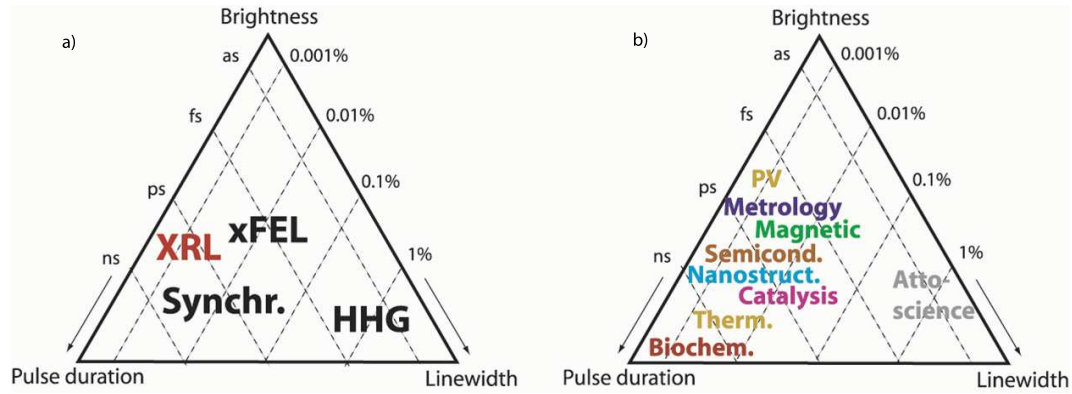


Fig. 5.1: Comparison of a) source specifications and b) science case requirements, in terms of brightness, spectral resolution, and time resolution. One notes that the plasma laser (XRL) fits well into the domain of science case requirements.

wavelength scalability vs. efficiency of the plasma laser. However, by adopting a "traveling-wave excitation" scheme such trade-off was overcome in this work. However, the latter requires a focusing system with drastic magnification (e.g. $M > 10x$) in order to achieve full speed-of-light compensation.

Pump-pulse characteristics, such as shape, duration and delay from pre-pulses, have been also investigated. In order to obtain population inversion, it is speculated that the pump pulse must not be *just short* but fast, i.e. faster pumping than spontaneous relaxation. If the laser energy is coupled quickly to the free electron ensemble, and then collisional transferred to bound states, population inversion can be achieved. Technically speaking, "fast laser pulses" are found in system with "short laser pulses". This means that *rise time* and *duration* of a laser pulse are strictly linked at the current stand of the technology. Ideally, for population inversion and homogeneous plasma heating, one would implement fast-rising ($\Delta\tau_{10-90} < 10\text{ps}$) long-duration ($\Delta\tau_{FWHM} > 10\text{ps}$) pulses.

Given the technology constraints between *rise time* and *duration*, I have thought to clip the leading-edge of a long-duration pulse, in order to steepen its rise time. How technologically to achieve this is proprietary and is not disclosed here. Computational results have shown that if this is achieved with more than 50% waste of the pulse energy, the gain is not improved. *The rapid pumping with little energy is not productive*, whereas rapid pumping preserving the pulse energy improves the gain as high as factor of 2 (Fig. 3.10). Similarly, the shape of the pulse from Gaussian to a flat-top is advantageous, if this does not sacrifice the pulse energy (Fig. 3.11). *Sufficient energy deposition is important to obtain a homogeneously heated plasma column across the entire volume.*

The optimum plasma conditions for lasing have been investigated showing that temperatures of hundreds eV ($1\text{ eV} \approx 11'604\text{K}$) are needed, along with sub-critical densities (the critical density was defined in Eq. 1.2.1.4). Above 80-100eV the total pumping time of the upper laser level is faster than that of the lower. On the other hand, while depopulation of the lower laser level was found temperature-insensitive, the upper laser level was increasingly long-lived (*metastable*) at several hundreds eV. The optimum is found close to 500eV (Fig. 3.17). Clearly, the optimum is a function of the element used as radiator, i.e. the target composition. The maximum saturated output was predicted with a self-derived equation (Eq. 3.5.1.10), and shown to depend on the plasma column dimensions. A novel pumping technique, based on travelling-wave excitation (TWE) was investigated and its potential for high-efficiency plasma lasing discussed.

It was a major achievement to demonstrate a theoretical limit for the scalability of X-ray plasma lasing up to the rare earths (REE). Typically, increasing the atomic number Z would imply a reduction of laser wavelength (Fig. 1.20). I have shown that using a $1\text{-}\mu\text{m}$ pump radiation (1ω or fundamental harmonic) the highest saturated radiator is at $Z = 59$ (Pr, a member of the REE), as shown in Fig. 3.29, which corresponds to a X-ray laser wavelength of approx. $\lambda = 5\text{nm}$. Further reduction of the wavelength is excluded. Only working with 2ω pump radiation, to penetrate deeper in the plasma medium, the water-window range may be approached. The *water window* consists of the soft x-rays between the K-absorption edge of oxygen at a wavelength of 2.34 nm and the K-absorption edge of carbon at 4.4 nm (x-ray energies of 530 and 280 eV, respectively). Water is transparent to these x-rays while nitrogen and other elements found in biological specimens are absorbing. These wavelengths could be used in an x-ray microscope for viewing in-vivo bio-specimens.

Besides such extensive discussion on fundamental aspects, In Chapter "Advanced Analytics" I demonstrated **applied results** on imaging as well as related self-developed instrumentation for lasing and diagnostics. Further, I investigated spectroscopic capabilities of the soft X-ray plasma laser as well as the generation of "two-color" pulses. The resolution of $< 100\text{nm}$ was obtained with single-shot illumination, and shown to be limited by the characteristics of the X-ray optics. The X-ray optics unfortunately also experiences aging and damage shot after shot, especially at high intensity and photon energy, as I have shown elsewhere [35]. Thus, ongoing research efforts are to enable *lensless imaging*, which is based on coherent diffractive imaging and phase retrieval through mathematical processing.

Nevertheless, I have presented a demonstrator of a Schwarzschild objective with all performance details. The system is currently being used in the nano-scale resolved elemental analysis of advanced samples for energy, catalysis, health, etc. The possibility to combine morphological and chemical imaging from a single probing process is extremely interesting, and has the enabling

chanter discussed in the opening on this thesis. The discussion of such ongoing research is beyond the scope of the present monograph, but it remains the preparatory relevance on the results summarized in this work. Finally, it is noteworthy that plasma chemistry clearly relies on a highly metastable states and far-from-equilibrium: *The ability to gain control on the plasma kinetics and intermediate species is a critical aspect in the future of table-top plasma-driven X-ray laser research.*

Acknowledgements

The present work was funded by the Swiss National Science Foundation under the grant number PP00P2-133564/1. The Gebert Rüf Stiftung, The Gulotti & Partner Stiftung and the Holcim Stiftung funded parts of it, related to the realisation of the demonstrators.

The author is grateful to R. Alberto for promoting the work for the Venia Legendi at the UZH. The author is indebted to Y. Arbelo, I. Artyoukov, F. Barbato, D. Batani, V. Bakshi, J.E. Balmer, A. Bieler, G. Bona, A. Borgschulte, B. Buchmann, J. Costello, Y. Ekinici, Th. Feurer, M. Frenz, Ch. Imesch, K. Lacher, L. Masoudnia, A. Michette, L. Roso, M. Ruiz-Lopez, S. Sebban, F. Staub, L. Volpe, P. Wurz, Ph. Zeitoun for professional contributions.

The author is also warmly grateful to S. Wyss, L. Caponetti, M. Bleiner, P. Bleiner, M. Brugmann, in first place and the also to F. Brawand, B. Buchmann, M. Hirt, A. Kammerer, B. Mischo, B. Moretti, M. Nann, Ch. Precht, A. Stefanov, D. Stutz-Lazo-Flores, M. Trebiatewska, M. Tyagi, A. Vananti for the advises and human support, especially during the difficult phases of this research.

REFERENCES

- [1] W. S. Abdelaziz, H. M. Hamed Ibrahim, Optics and Photonics Journal., 1, 110, (2011).
- [2] W. S. Abdelaziz, Eur. Phys. J. D, 55, 17, (2009).
- [3] K.M. Aggarwal, F. P. Keenan, At. Data Nucl. Data Tables, 99, 156, (2013).
- [4] R. Akre, A. Brachmann, F.-J. Decker, Y. Ding, D. Dowell, P. Emma, J. Frisch, S. Gilevich, G.
- [5] S Akturk, X Gu, E Zeek, R Trebino 2004 *Opt. Express* **12** 4399
- [6] D Alessi, BM Luther, Y Wang, MA Larotonda, M Berrill, JJ Rocca, *Opt. Expr.* **13** 2093, 2005
- [7] D. Alessi, D. H. Martz, Y. Wang, M. Berrill, B. M. Luther, and J. J. Rocca, Opt. Lett., 35(3), 414, (2010).
- [8] I.G. Artioukov, K.M. Krymski, Opt. Eng. 39, 2163 (2000).
- [9] K. Cassou, S. Kazamias, A. Klisnick, D. Ros, Ph. Zeitoun, E. Oliva, P. Velarde, C. Garcia, and F. Ogando, X-Ray Lasers 2006, Springer Proceedings in Physics, 115, 275, (2007).
- [10] D. Attwood, Soft X-rays, New York: Cambridge Uni Press, (1999).
- [11] Y. B. S. R. Prasad, S. Nigam, K. Aneesh, S. Barnwal, P. K. Tripathi, P. A. Naik, C. P. Navathe, and P. D. Gupta, Sadhana Indian Acad. Sci., 36, 349, (2011).
- [12] V. Bakshi Ed., EUV Sources for Lithography, SPIE Press Monograph vol PM 149, 2006
- [13] J. E. Balmer, R. Weber, P.F. Cunningham, and P. Ldrach, Laser Part. Beams, 8, 327, (1990).
- [14] J.E. Balmer, D. Bleiner, F. Staub 2012, *J. Micro/Nanolith. MEMS MOEMS* **11** 021119
- [15] Dictionary of Material Science and High Energy Physics, Ed.: Dipak K. Basu, A volume in the comprehensive dictionary of physics, CRC Press, (2001).
- [16] M. Benedict, Quantum theory of atoms, molecules and their interaction with light, University of Szeged, TÁMOP-4.1.2 A1 and TÁMOP-4.1.2 A2, (2014).
- [17] S. Benkovic, and S. Hammes-Schiffer, Science, 301(5637), 1196, (2003).
- [18] B. R. Benware, A. Ozols, J. J. Rocca, I. A. Artioukov, V. V. Kondratenko, and A. V. Vinogradov 1999, *Opt. Lett.* **24** 1714
- [19] B. R. Benware, C. D. Macchietto, C. H. Moreno, and J. J. Rocca, Phys. Rev. Lett., 81, 5804, (1998). "
- [20] F. A. Berezin and M. A. Shubin, The Schrödinger equation, Springer Science, Kluwer academic publisher, (1991)."
- [21] M. Bitter, M. F. Gu, L. A. Vainshtein, P. Beiersdorfer, G. Bertschinger, O. Marchuk, R. Bell, B. LeBlanc, K. W. Hill, D. Johnson, et al., Phys. Rev. Lett., 91, 265001, (2003).
- [22] B. J. MacGowan, S. Maxon, P. L. Hagelstein, C. J. Keane, R. A. London, D. L. Matthews, M. D. Rosen, J. H. Scofield, and D. A. Whelan, Phys. Rev. Lett., 59(19), (1987).
- [23] D. Bleiner, J. E. Balmer, and F. Staub, Appl. Opt., 50, 6689, (2011).
- [24] D. Bleiner, T. Feurer, Appl. Opt., 51(36), (2012).
- [25] D. Bleiner, Y. Arbelo-Pena, L. Masoudnia, and M. Ruiz-Lopez, Phys. Scr., T162, 014050, (2014).
- [26] D. Bleiner, Appl. Phys. Lett., 101, 081105, (2012).
- [27] D. Bleiner, J. Balmer, Appl. Phys. Lett., vol.98, 181501, (2011)
- [28] D. Bleiner, F. Staub, V. Guzenko, Y. Ekinici, J. Balmer, Opt. Commun., 284, 19, 4577-4583, (2011)
- [29] D. Bleiner, F. Staub, J.E. Balmer, 2012, Handbook on Short-wavelength Laboratory-scale Sources, Ed. A. Michette, RSC, in press

- [30] D. Bleiner, Th. Feurer 2012, Proc. ICXRL 2012.
- [31] D. Bleiner, Coherent short-wavelength plasma radiation for lab-scale nano-inspection tools, Proc. ICXRL 2012, 147, Chap. 7, 39, (2012).
- [32] D. Bleiner, J.E. Balmer, F. Staub, Appl. Opt., 50, 6689, (2011).
- [33] D. Bleiner, Y. Arbelo-Pena, L. Masoudnia, and M. Ruiz-Lopez, Phys. Scr. T162, 014050, (2014).
- [34] D. Bleiner, F. Staub, J. Balmer, Proceeding of SPIE 8140, (2011)
- [35] D. Bleiner, S. Yulin, J. Martynczuk, M. Ruiz-Lopez, Y. Arbelo, J.E. Balmer, D. Gauthier, Actinic Damage Of Y/Mo Multilayer Optics In A Table-Top Plasma-Driven X-Ray Laser (2014) Applied Optics, (22), pp. 4894-4902
- [36] D. Bleiner, Short-Wavelength Imaging and Spectroscopy Sources, Proc. SPIE, 8678, 867806, (2012).
- [37] S. Bollanti et al, Appl. Phys. B85, 603 (2006)
- [38] L. Bonnet, S. Jacquemot, and J. L. Miquel, Proc. SPIE, Soft X-Ray Lasers and Applications II, 3156, 98, (1997).
- [39] K. Miyamoto, Fundamentals of Plasma Physics and Controlled Fusion, Tokyo: Iwanami Book Service Centre, (2000).
- [40] J. A. Bittencourt, Fundamentals of Plasma Physics, Great Britain: A. Wheaton and Co. Ltd., (1986).
- [41] R. Fitzpatrick, The Physics of Plasmas, eBook, Publisher: Lulu, (2011).
- [42] V. V. Zheleznyakov, Radiation in Astrophysical Plasmas, U. S. A.: Kluwer Academic Publishers, (1996).
- [43] X-Ray Data Booklet, Lawrence Berkeley National Laboratory, Berkeley, (2009).
- [44] M. Born and E. Wolf, Principles of optics: electromagnetic theory of propagation, interference and diffraction of light, 7th edition, New York: Cambridge University Press, (1959).
- [45] M. Braud. Doctoral Dissertation. IAP University of Bern, Switzerland, (2003)
- [46] M. Brio, A. R. Zakharian, and G. M. Webb, J. Comput. Phys., 167, 177, (2001).
- [47] F. Brizuela, C. Brewer, S. Fernandez, D. Martz, M. Marconi, W. Chao, E. Anderson, A. Vinogradov, I. Artyukov, A. G Ponomareko, V. Kondratenko, D. Attwood, K. Bertness, N. Sanford, J. Rocca and C. Menoni, J. Phys. 186, (2009)
- [48] W. Brunner and R. W. John, Laser Part. Beams, 13, 403, (1995).
- [49] N. H. Burnett and P. B. Corkum, J. Opt. Soc. Am. B, 6, 1195, (1989).
- [50] F. Capotondi, E. Pedersoli, M. Kiskinova, A.V. Martin, M. Barthelmess, H. N. Chapman, Opt. Express, 20, 22, (2012)
- [51] T. A. Carlson, C. W. Nestor, JR., N. Wasserman, and J. D. McDowell, Atomic Data, 2, 63, (1970). "
- [52] K. Cassou, P. Zeitoun, P. Velarde, F. Roy, F. Ogando, M. Fajardo, G. Faivre, and D. Ros, Phys. Rev. A, 74, 045802, (2006).
- [53] K Cassou, S Kazamias, D Ros, F Ple, G Jamelot, A Klisnick, O Lundh, F Lindau, A Persson, CG Wahlstroem, S de Rossi, D Joyeux, B Zielbauer, D Ursescu, T Kuehl, *Opt. Lett.* **32** 139, 2007
- [54] J.C. Chanteloup, E. Salmon, C. Sauteret, A. Migus, P. Zeitoun, A. Klisnick, A. Carillon, S. Hubert, D. Ros, P. Nickles, M. Kalachnikov, Pulse-front control of 15 TW pulses with a tilted compressor, and application to the subpicosecond travelling-wave pumping of soft-x-ray laser, J. Opt. Soc. Am. B 17/1, (2000), 151
- [55] L. Masoudnia and D. Bleiner, Photonics, 2, 164, (2015).
- [56] F. F. Chen, Introduction to plasma physics and controlled fusion, Vol. 1: Plasma Physics, Springer: Los Angeles, (1983).
- [57] H. K. Chung, M. H. Chen, W. L. Morgan, Y. Ralchenko, R. W. Lee, High Energy Density Physics, 1(1), 3, (2005).
- [58] H. K. Chung, R. W. Lee, High Energy Density Physics, 5, 1, (2009).
- [59] R. Coffee, F. J. Decker, Y. Ding, D. Dowel, S. Edstrom, A. Fisher, J. Frisch, S. Gilevich, "

- [60] I. A. Vartanyants, A. Singer, A. Mancuso, O. Yefanov, A. Sakdinawat, Y. Liu, E. Bang, G. J. Williams, G. Cadenazzi, B. Abbey, H. Sinn, D. Attwood, K. A. Nugent, E. Weckert, T. Wang, D. Zhu, B. Wu, C. Graves, A. Scherz, J. J. Turner, W. F. Schlotter, M. Messerschmidt, J. Luning, Y. Acremann, P. Heimann, D. C. Mancini, V. Joshi, J. Krzywinski, R. Soufli, M. Fernandez-Perea, S. Hau-Riege, A. G. Peele, Y. Feng, O. Krupin, S. Moeller, and W. Wurth, *Phys. Rev. Lett.* **107**, 144801, (2011) ” ”
- [61] R. D. Cowan, *The Theory of Atomic Structure and Spectra*, Berkeley: University of California Press, (1981).
- [62] M. Csele, *Fundamentals of light sources and lasers*, A Wiley-Interscience publication, (2004).
- [63] H. Daido, I. Choi, C. Nam, R. Kodama, K. Murai, G. Yuan, M. Takagi, and Y. Kato, *Opt. Lett.*, **20**, 61, (1995).
- [64] H. Daido, Y. Kato, K. Murai, S. Ninomiya, R. Kodama, G. Yuan, Y. Oshikane, M. Takagi, and H. Takabe, *Phys. Rev. Lett.*, **75**, 1074, (1995).
- [65] H. Daido, K. Murai, R. Kodama, and G. Yuan, *J. Appl. Phys. B*, **62**, 129, (1996).
- [66] H. Daido, S. Ninomiya, T. Imani, Y. Okaichi, M. Takagi, R. Kodama, H. Takabe, and Y. Kato, *Int. J. Mod Phys B*, **11**(8), 945, (1997).
- [67] H. Daido, *Rep. Prog. Phys.*, **65**, 1513, (2002).
- [68] D. Alessi, D. H. Martz, Y. Wang, M. Berrill, B. M. Luther, and J. J. Rocca, *Opt. Lett.*, **35**(3), 414, (2010).
- [69] M. Dantus, R. M. Bowman, and A. H. Zewail, *Nature*, **343**, 737, (1990).
- [70] LB Da Silva, BJ MacGowan, S Mrowka, JA Koch, RA London, DL Matthews, JH Underwood, *Opt. Lett.* **18** 1174, 1993
- [71] D. Bleiner, J. Costello, F. de Dortan, G. O’Sullivan, L. Pina, and A. Michette, *Short Wavelength Laboratory Sources: Principles and Practices*, The Royal Society of Chemistry, (2015).
- [72] M. Davidkova, L. Juha, M. Bittner, S. Koptyaev, V. Hajkova, J. Krasa, M. Pfeifer, V. Stisova, A. Bartnik, H. Fiedorowicz, J. Mikolajczyk, L. Ryc, L. Pina, M. Horvath, D. Babankova, J. Cihelka, and S. Civis, *Radiat. Res.*, **168**, 382, (2007).
- [73] Diels JC, Rudolph W 2006 *Ultrashort Laser Pulse Phenomena*, Elsevier
- [74] QL Dong, SJ Wang, ZH Wang, J Zhao, ZY Wei, J Zhang, *Chn. Phys. Lett.* **26** 064214, 2009
- [75] G. W. F. Drake, *Springer Handbook of Atomic, Molecular, and Optical Physics*, Germany: Springer Science, (2006).
- [76] MA Dungay, PM Rentzepis, *Appl. Phys. Lett.* **10** 350, 1967 ”
- [77] J. Dunn, R. F. Smith, J. Nilsen, H. Fiedorowicz, A. Bartnik, and V. N. Shlyaptsev, *J. Opt. Soc. Am. B*, **20**, 203, (2003).
- [78] J. Dunn, R. Keenan, and V. N. Shlyaptsev, *SPIE International Society for Optical Engineering conference on Soft X-ray Lasers and Applications VI*, 5919, (2005)
- [79] J. Dunn, Y. Li, A. L. Osterheld, J. Nilsen, J. R. Hunter, and V. N. Shlyaptsev, *Phys. Rev. Lett.*, **84**(21), 4834, (2000).
- [80] J. Dunn, R. Keenan, P. K. Patel, D. F. Price, R. F. Smith, and V. N. Shlyaptsev, *proceeding on X-Ray Lasers*, ed J Zhang, London: Taylor and Francis, (2004).
- [81] J. Dunn, V. N. Shlyaptsev, J. Nilsen, R. F. Smith, R. Keenan, S. J. Soon, J. Filevich, J. Rocca, A. J. Nelson, J. R. Hunter, M. C. Marconi, Y. L. Li, A. L. Osterheld, R. Shepherd, H. Fiedorowicz, A. Bartnik, A. Ya, Faenov, T. A. Pikuz, P. Zeitoun, S. Hubert, S. Jacquemot, and M. Fajardo, *X-Ray Lasers Proceedings*, **3156**, 1, (2006).
- [82] J Dunn, AI Osterheld, L Yuelin, J Nilsen, VN Shlyaptsev, *Sel. Top. Quant. El. IEEE* **5** 1441, 1999
- [83] J. Dunn, R. F. Smith, J. Nilsen, H. Fiedorowicz, A. Bartnik, V. N. Shlyaptsev, *J. Opt. Soc. Am. B*, **20**, 203, (2003).
- [84] D. C. Eder, P. Amendt, P. R. Bolton, L. B. Da Silva, L. A. Hackel, R. A. London, B. J. MacGowan, D. L. Matthews, M. D. Rosen, R. E. Stewart, and S. C. Wilks, *SPIE, Ultrashort Wavelength Lasers II*, 2072, 165, (1993).
- [85] Euro xFEL website, <https://www.xfel.eu>
- [86] K. Eidmann, *Laser Part. Beams*, **12**(2), 223, (1994).
- [87] E. Kacar, and P. Demir, *Opt. Commun.*, **281**, 718, (2008).

- [88] S. Eliezer, The Interaction of High-Power Lasers with Plasmas, Eds.: S. Cowley, P. Stott, and H. Wilhelmsson, IOP Publishing Ltd, London: Institute of Physics, (2002).
- [89] U. Ellenberger, B. Soom, A. Glinz, and J. E. Balmer, *Opt. Commun.*, 104, 65, (1993).
- [90] R.C. Elton 1990, *X-ray Lasers* Academic Press
- [91] P. Emma, R. Akre, J. Arthur, R. Bionta, C. Bostedt, J. Bozek, A. Brachmann, P. Bucksbaum,
- [92] M. F. Gu, The Flexible Atomic Code (FAC), *Can. J. Phys.*, 86, 675, (2008).
- [93] D. Oepts, A.F.G. van der Meer, P. W. Amersfoort, *Infrared Phys. Technol.*, 36, 297, (1995).
- [94] J. Feldhaus, J. Arthur, J.B. Hastings 2005, *J. Phys. B:Atomic, Molecular and Optical Physics* **38** S799
- [95] F. Staub, C. Imesch, D. Bleiner, J.E. Balmer, *Opt. Commun.*, 285, 2118, (2012).
- [96] H. Merbold, A. Bitzer, T. Feurer, *Opt.Express* 19, 8, (2011)
- [97] H. Fiedorowicz, A. Bartnik, R. Jarocki, J. Kostecki, J. Mikolajczyk, R. Rakowski, M. Szczurek, *Laser plasma light source based on a gas puff target for EUV metrology applications*, *Microproc. & Nanotechn.* 7954075 (2003), 314.
- [98] H. Fiedorowicz, A. Bartnik, Y. Li, P. Lu, and E. Fill, *Phys. Rev. Lett.*, 76, 415, (1996). "
- [99] H. Fiedorowicz, A. Bartnik, J. Kostecki, M. Szczurek, E. Fill, Y. Li, P. Lu, G. Pretzler, and J. Nilsen, *Conf. on X-ray lasers 1996, Lund, Sweden*, in *Inst. Phys. Conf. Ser.*, No 151: Section 2, Page. 76, IOP Publishing Ltd: Bristol, UK, (1996).""
"
- [100] H. Fiedorowicz, A. Bartnik, Y. Li, P. Lu, and E. Fill, *Phys. Rev. Lett.*, 76, 415, (1996). "
- [101] H. Fiedorowicz and A. Bartnik, *Bull. Pol. Acad. Sci.: Tech. Sci.*, 53, 103, (2005).
- [102] H. Fiedorowicz, A. Bartnik, J. Dunn, R. F. Smith, J. Hunter, J. Nilsen, A. L. Osterheld, and V. N. Shlyaptsev, *Opt. Lett.*, 26, 1403, (2001).
- [103] D. J. Fields, R. S. Walling, G. M. Shimkaveg, B. J. MacGowan, L. B. Da Silva, J. H. Scofield, A. L. Osterheld, T. W. Phillips, M. D. Rosen, D. L. Matthews, W. H. Goldstein, and R. E. Stewart, *Phys. Rev. A*, 46(3), 1606, (1992).
- [104] E.E. Fill, *J. Opt. Soc. Am. B*, 14, 1505, (1997).
- [105] E.E. Fill, *Opt. Comm.* **67** 441, 1998
- [106] C Fiorini, C Sauteret, C Rouyer, N Blanchot, S Seznec, A Migus 1994 *IEEE J. Quant. Electr.* **30** 1662
- [107] FLASH website, <https://flash.desy.de>
- [108] H. K. Chung, M. H. Chen, W. L. Morgan, Y. Ralchenko, and R. W. Lee, *High Energy Density Phys.*, 1, 3, (2005).
- [109] J.A. Fulop, J Hebling, In: *Recent Optical and Photonic Technologies*, Ed. by K.Y. Kim 2010, Intech. Publ.
- [110] V.L. Ginzburg, *Propagation of Electromagnetic Waves in Plasma*, Addison-Wesley, Reading, (1964).
- [111] J. Ph. Goddet, S. Sebban, J. Gautier, Ph. Zeitoun, C. Valentin, F. Tissandier, T. Marchenko, G. Lambert, M. Ribières, D. Douillet, T. Lefrou, G. Iaquaniello, F. Burgy, G. Maynard, B. Cros, B. Robillard, T. Mocek, J. Nejd, M. Kozlova, and K. Jakubczak, *Opt. Lett.*, 34 (16), 2438, (2009).
- [112] K.A. Goldberg and I. Mochi, *J.Vac.Sci.Technol.*, B 28(6), C6E1-10, (2010)
- [113] W. H. Goldstein, J. Oreg, A. Zigler, A. Bar-Shalom, and M. Klapisch, *Phys. Rev. A*, 38(4), (1998).
- [114] JW Goodman, 2004 *Introduction to Fourier Optics*, Roberts & Co. Publ.
- [115] H. R. Griem, *Principle of Plasma Spectroscopy*, New York: Cambridge University Press, (1997).
- [116] J. S. D. Groot, K. G. Estabrook, W. L. Kruer, R.P. Drake, K. Mizuno, and S. M. Cameron, *Phys. Fluids.*, 4, 701, (1992).
- [117] M. Grünig, C. Imesch, F. Staub, J.E. Balmer, *Optics Communication*, 282, 267-271, (2009)"
- [118] G. P. Gupta and B. K. Sinha, *J. Appl. Phys.*, 77, 2287, (1995).
- [119] G. P. Gupta and B. K. Sinha., *J. Appl. Phys.*, 79, 619, (1996).
- [120] G. P. Gupta and B. K. Sinha, *Phys. Rev. E*, 56(2), (1997).

-
- [121] P. L. Hagelstein, *Plasma Phys.*, 25, 1345, (1983).
 - [122] L.I. Jones, *Handbook of Optics*, Ch.18, V.II, Ed. M. Bass, E. W. Van Stryland, D. R. Williams, W. Wolfe, 2nd Edition, (1995)
 - [123] T. Hara, Y. Inubushi, T. Katayama, T. Sato, H. Tanaka, T. Tanaka, T. Togashi, K. Togawa, K. Tono, M. Yabashi, and T. Ishikawa, *Nat Commun.*, 4, 2919, (2013).
 - [124] N. Hasegawa, R. Tai, M. Kishimoto, M. Kado, K. Nagashima, H. Daido, Y. Kato, and H. Fiedorowicz, Photon energy conversion from IR femtosecond laser pulses to X-ray pulses with electrolyte aqueous solutions in air, *AIP Conference Proc.*, 634, 260, (2002).
 - [125] J. Hastings, G. Hays, Ph. Hering, Z. Huang, R. Iverson, H. Loos, M. Messerschmidt,
 - [126] Hays, Ph. Hering, Z. Huang, R. Iverson, C. Limborg-Deprey, H. Loos, S. Molloy, A. Miahnahri,
 - [127] E. Hecht, *Optics*, 3th Ed, Addison Wesley, (1998)
 - [128] S. Heinbuch, M. Grisham, D. Martz, F. Dong, E. R. Bernstein, and J. J. Rocca, *Soft X-Ray Lasers and Applications VI*, Ed.: Ernst E. Fill, *Proc. of SPIE Vol. 5919*, San Diego, California, USA, 591907, (2005).
 - [129] HELIOS Radiation-Hydrodynamics Code, Prism Computational Sciences Inc., USA, (1998). "
 - [130] C. M. Heyl, J. Güddel, A. L'Huillier, and U. H^ofer, *J. Phys. B: At. Mol. Opt. Phys.*, 45, 074020, (2012)."
 - [131] A. K. Hicks, C. R. Canizares, *Astrophys. J.*, 556, 468, (2001).
 - [132] T. Kita, T. Harada, N. Nakano, and H. Kuroda, *Appl. Opt.*, 22, 512, (1983).
 - [133] H. Hogan, *Extreme Ultraviolet: A New Frontier for Lasers*, *Photonics Spectra*, 11, 54, (2011).
 - [134] PB Holden, B Rus, GJ Pert, *Phys. Rev. A* **74** 2164, 1995
 - [135] T. Holstein, *Phys. Rev.*, 72, 1212, (1947).
 - [136] C. Honoré, P. Hennequin, A. Truc, and A. Quéméneur, 7th International Reflectometry Workshop, (2005).
 - [137] J. D. Huba, *NRL Plasma Formulary*, Washington: Naval research laboratory, (1994).
 - [138] R. H. Huddleston, S. L. Leonard, *Plasma Diagnostic Techniques*, New York: Academic Press, (1965).
 - [139] T. P. Hughes, *Plasmas and Laser Light*, Bristol: Adam Hilger Ltd., (1975).
 - [140] M. Klapisch, *Comput. Phys. Comm.*, 2, 239, (1971).
 - [141] J. T. Larsen, HYADES- A Plasma Hydrodynamics Code for Dense Plasma Studies, Cascade Applied Sciences Inc., (1990).
 - [142] I. Artyoukov, K. Krymski, *Opt. Eng.* 39(8) 2163, 2170, (2000)
 - [143] N. Ishii, K. Kaneshima, K. Kitano, T. Kanai, S. Watanabe, and J. Itatani, *Nat. Commun.*, 5, (2014).
 - [144] P. Jaeglé, *Coherent Sources of XUV Radiation Soft X-Ray Lasers and High-Order Harmonic Generation*, Springer Series in Optical Sciences, (2006).
 - [145] G. Jamelot, P. Jaegle, A. Carillon 1984 *Ann. Phys. Fr.* **9**, 657
 - [146] K. A. Janulewicz, L. A. G. Priebe, W. Sandner, and P. V. Nickles, *Phys. Rev. A*, 68, 051802(R), (2003).
 - [147] K. A. Janulewicz, and C. M. Kim, *Phys. Rev. E*, 82, 056405, (2010).
 - [148] J. Nilsen, *J. Opt. Soc. Am. B*, 14(6), 1511, (1997).
 - [149] J. Nilsen, J. Dunn, A. L. Osterheld, and Y. Li, *Phys. Rev. A*, 4, R2677, (1999).
 - [150] J. Nilsen, *Phys. Rev. A*, 53(6), 4539, (1996).
 - [151] J. Zhang, A. G. MacPhee, J. Lin, E. Wolfrum, R. Smith, C. Danson, M. H. Key, C. L. S. Lewis, D. Neely, J. Nilsen, G. J. Pert, G. J. Tallents, and J. S. Wark, *Science*, 276, 1097, (1997).
 - [152] E. Kacar, and P. Demir, *Opt. Commun.*, 281, 718, (2008).
 - [153] Y. Kato, S. Wang, H. Daido, Z. Lin, G. Zhang, Y. Gu, G. Huang, H. Tang, T. Imani, S. Sezaki, S. Hirose, K. Murai, G. Y. Yoon, T. Jitsuno, M. Takagi, H. Takenaka, K. Mima and X. Deng: *SPIE* 3156, 2, (1997).
 - [154] S Kazamias, K Cassou, D Ros, F Ple, G Jamelot, A Klisnick, O Lundh, F Lindau, A Persson, CG Wahlstroem, S de Rossi, D Joyeux, B Zielbauer, D Ursescu, T Kuehl, *Phys. Rev. A* **77** 33812, 2008

- [155] R. Keenan, J. Dunn, V.N. Shlyaptsev, R.F. Smith, P.K. Patel, D.F. Price, Efficient pumping schemes for high average brightness collisional X-ray lasers, *Proc. SPIE 5197 Soft X-ray Lasers and Applications*, 213 (2003)
- [156] R. Keenan, J. Dunn, PK Patel, DF Price, RF Smith, VN Shlyaptsev, *Phys. Rev. Lett.* **94** 103901, 2005
- [157] R. Keenan, J. Dunn, V. N. Shlyaptsev, R. F. Smith, P. K. Patel, and D. F. Price, *Proc. SPIE*, 5197, 213, (2003).
- [158] Key, C. L. S. Lewis, D. Neely, J. Nilsen, G. J. Pert, G. J. Tallents, and J. S.
- [159] K Kim, IW Choi, N Hafz, JH Sung, TJ Yu, KH Hong, TM Jeong, YC Noh, DK Ko, KA Janulewicz, J Tuemmler, PV Nickles, W Sandner, J Lee, *Phys. Rev. A Lett.* **77** 23802, 2008
- [160] R. E. King, G. J. Pert, S. P. McCabe, P. A. Simms, A. G. MacPhee, C. L. S. Lewis, R. Keenan, R. M. N. O'Rourke, G. J. Tallents, S. J. Pestehe, F. Strati, D. Neely, and R. Allott, *Physical Rev. A*, 64, 053810, (2001).
- [161] A Klisnick, A Sureau, H Guennou, C Moeller, J Virmont, *Ann. Phys. Fr.* **15** 529, 1990
- [162] A. Klisnick, P. Zeitoun, D. Ros, A. Carillon, P. Fourcade, S. Hubert, G. Jamelot, C. Lewis, A. MacPhee, R. O'Rourke, R. Keenan, P. Nickles, K. Janulewicz, M. Kalashnikov, J. Warwick, J. Chanteloup, A. Migus, E. Salmon, C. Sauteret, J.P. Zou, *Journal of the Optical Society of America B*, 7(6):1093, (2000)
- [163] JA Koch, BJ MacGowan, LB Da Silva, DL Matthews, JH Underwood, PJ Bateson, S Mrowka, *Phys. Rev. Lett.* **68** 3291, 1992
- [164] A. C. Kolb and R. W. P. McWhirter, *Phys. Fluid*, 7, 519, (1964).
- [165] V. Krishan, *Astrophysical plasmas and fluids*, Netherlands: Kluwer Academic Publishers, (1999).
- [166] W. Kruer, *The Physics Of Laser Plasma Interactions* , Westview Press (2003)
- [167] J. Kuba, A. Klisnick, D. Ros, P. Fourcade, G. Jamelot, J. L. Miquel, N. Blanchot, and J. F. Wyart, *Phys. Rev. A*, 62, 043808, (2000).
- [168] H. J. Kunze, *Introduction to Plasma Spectroscopy*, New York: Springer Heidelberg Dordrecht, (2009).
- [169] M. L. Kutner, *Astronomy: A Physical Perspective*, United Kingdom at the university Press: Cambridge, (2003).
- [170] K. Cassou, S. Kazamias, D. Ros, F. Ple, G. Jamelot, A. Klisnick, O. Lundh, F. Lindau, A. Persson, C.-G. Wahlstroem, S. de Rossi, D. Joyeux, B. Zielbauer, D. Ursescu, and T. Kuehl 2007 *Opt. Lett.* **32**, 139
- [171] G. B. Zimmerman and W. L. Kruer, *Comm. Plasma Phys. Controlled Fusion*, 2, 51, (1975).
- [172] J. Nilsen, *J. Opt. Soc. Am. B*, 14, 1511, (1997).
- [173] X-Ray Data Booklet, Berkeley: Lawrence Berkeley National Laboratory, (2009).
- [174] LCLS website, <https://lcls.slac.stanford.edu>
- [175] T. N. Lee, E. A. McLean, and R. C. Elton, *Phys. Rev. Lett.*, 59, 1185, (1987).
- [176] L. Masoudnia, D. Bleiner, *Laser Physics*, 23, 056003, (2013)
- [177] C. L. S. Lewis, "D. Neely, D. M. O'Neill, J. O. Uhomobhi, M. H. Key, Y. Al Hadithi, G. J. Tallents, and S. A. Ramsden, *Opt. Commun.*, 91, 1-2, 71, (1992).
- [178] Y. Li, P. Lu, G. Pretzler, and E. E. Fill, *Opt. Commun.*, 133, 196, (1997).
- [179] Y. Li, J. Nilsen, J. Dunn, A. L. Osterheld, A. Ryabtsev, and S. Churilov, *Phys. Rev. A*, 58, R2668, (1998).
- [180] Y. Li and J. Nilsen, *Phys. Scr.*, 57, 237, (1998).
- [181] J. Y. Lin, G. J. Tallents, J. Zhang, A. G. MacPhee, C. L. S. Lewis, D. Neely, J. Nilsen, G. J. Pert, R. M. N. O'Rourke, R. Smith, and E. Wolfrum, *Opt. Commun.*, 158, 55, (1998). "
- [182] G.J. Linford, E.R. Peresini, W. R. Sooy, and M. L. Spaeth, *Appl. Opt.*, 13, 379, (1974).""
- [183] Y. Liu, M. Seminario. F. G. Tomasel, C. Chang, J. J. Rocca, and D. T. Attwood, *Phys. Rev. A*, 63, 033802, (2001).
- [184] R. A. London, *Phys. Fluids*, 31, 184, (1988). "
- [185] E. Lorek, E. W. Larsen, C. M. Heyl, S. Carlström, D. Paleček, D. Zigmantas, and J. Mauritsson, *Review of Scientific Instruments*, 85, 123106, (2014)."

-
- [186] P. Lu, T. Kawachi, M. Kishimoto, K. Sukegawa, M. Tanaka, N. Hasegawa, M. Suzuki, R. Tai, M. Kado, K. Nagashima, H. Daido, and Y. Kato, *Opt. Lett.*, 27, 1911, (2002).
 - [187] P. Lu, T. Kawachi, M. Suzuki, K. Sukegawa, S. Namba, M. Tanaka, N. Hasegawa, R. Tai, M. Kishimoto, M. Kado, K. Nagashima, H. Daido, Y. Kato, and H. Fiedorowicz, Photon energy conversion from IR femtosecond laser pulses to X-ray pulses with electrolyte aqueous solutions in air, *AIP Conference Proc.*, 634, 260, (2002).
 - [188] P. Lu, T. Kawachi, M. Suzuki, K. Sukegawa, S. Namba, M. Tanaka,
 - [189] J. G. Lunney, *Appl. Phys. Lett.*, 48, 891, (1986)
 - [190] B. M. Luther, Y. Wang, M. A. Larotonda, D. Alessi, M. Berrill, J. J. Rocca, J. Dunn, R. Keenan, and
 - [191] A. A. Lutman, R. Coffee, Y. Ding, Z. Huang, J. Krzywinski, T. Maxwell, M. Messerschmidt, and H. D. Nuhn, *Phys. Rev. Lett.*, 110, 13480, (2013).
 - [192] M. Ruiz-Lopez, D. Bleiner, *Appl. Phys. B*, 115(3), 311, (2014).
 - [193] C. D. Macchietto, B. R. Benware, and J. J. Rocca, *Opt. Lett.*, 24, 1115, (1999).
 - [194] B. J. MacGowan, S. Maxon, P. L. Hagelstein, C. J. Keane, R. A. London, D. L. Matthews, M. D. Rosen, J. H. Scofield, and D. A. Whelan, *Phys. Rev. Lett.*, 59(19), (1987).
 - [195] B. J. MacGowan, S. Maxon, C. J. Keane, R. A. London, D. L. Matthews, and D. A. Whelan, *J. Opt. Soc. Am. B*, 5(9), (1988).
 - [196] B. J. MacGowan, S. Maxon, L. B. Da Silva, D. J. Fields, C. J. Keane, D. L. Matthews, A. L. Osterheld, J. H. Scofield, G. Shimkaveg, and G. F. Stone, *Phys. Rev. Lett.*, 65(4), 420, (1990).
 - [197] B. J. MacGowan, L. B. Da Silva, D. J. Fields, C. J. Keane, J. A. Koch, R. A. London, D. L. Matthews, S. Maxon, S. Mrowka, A. L. Osterheld, J. H. Scofield, G. Shimkaveg, J. E. Trebes, and R. S. Walling, *Phys. Fluids B*, 4, 2326, (1992).
”
 - [198] W. B. Wetherell, *Proc. SPIE 0028, Instrumentation in Astronomy I*, 45 (1972);”
 - [199] A. Marinelli, A. A. Lutman, J. Wu, Y. Ding, J. Krzywinski, H.D. Nuhn, Y. Feng, R. N. Coffee, and C. Pellegrini, *Phys. Rev. Lett.*, 111, 134801, (2013).
 - [200] A. Marinelli, M. Park, *Proceedings of IPAC, THPPA01, Dresden, Germany*, (2014).
 - [201] A. Marinelli, D. Ratner, A.A. Lutman, J. Turner, J. Welch, F. J. Decker, H. Loos, C. Behrens, S. Gilevich, A. A. Miahnahri, S. Vetter, T.J. Maxwell, Y. Ding, R. Coffee, S. Wakatsuki, and Z. Huang, *Nat Commun.*, 6:6369, (2015). ”
 - [202] M. Masnavi, M. Nakajima, and K. Horioka, *Appl. Phys.*, 95, 434, (2004).
 - [203] L. Masoudnia and D. Bleiner, *Nucl. Inst. Methods Phys. Res. B*, 323, 59, (2014).
 - [204] L. Masoudnia, B. Maraghechi, and T. Mohsenpour, *Phys. Plasmas*, 16, 072108, (2009).
 - [205] L. Masoudnia and D. Bleiner, *Laser Phys.*, 23, 056003, (2013).
 - [206] L. Masoudnia and D. Bleiner, *Photonics*, 2, 164, (2015).
 - [207] D. L. Matthews, P. L. Hagelstein, M. D. Rosen, M. J. Eckart, N. M. Ceglio, A. U. Hazi, H. Medeck, B. J. MacGowan, J. E. Trebes, B. L. Whitten, E. M. Campbell, C. W. Hatcher, A. M. Hawryluk, R. L. Kauffman, L. D. Pleasance, G. Rambach, J. H. Scofield, G. Stone, and T. A. Weaver, *Phys. Rev. Lett.*, 54, 110, (1985).
 - [208] S. Maxon, P. Hagelstein, B. MacGowan, R. London, M. Rosen, J. Scofield, S. Dalhed, and M. Chen, *Phys. Rev. A*, 37(6), 2227, (1988).
 - [209] S. Maxon, S. Dalhed, P. L. Hagelstein, R. A. London, B. J. MacGowan, M. D. Rosen, G. Charatis, and G. Busch, *Phys. Rev. Lett.*, 63(3), 236, (1989).
 - [210] S. Maxon, K. G. Estabrook, M. K. Prasad, A. L. Osterheld, R. A. London, and D. C. Eder, *Phys. Rev. Lett.*, 70(15), 22
 - [211] M.J. May, P. Beiersdorfer, N. Jordan, J.H. Scofield, K.J. Reed, S.B. Hansen, K.B. Fournier, M.F. Gu, G.V. Brown, F. S.Porter, et al., *Nucl. Inst. Methods Phys. Res. B*, 235, 231, (2005).
”
 - [212] M. J. May, P. Beiersdorfer, N. Jordan, J. H. Scofield, K. J. Reed, S. B. Hansen, K. B. Fournier, M. F. Gu, G. V. Brown, F. S. Porter, R. Kelley, C.A. Kilbourne, and K. R. Boyce, *Nucl. Inst. Methods Phys. Res. B*, 235, 231, (2005).”””

- [213] S. McCabe, G. J. Pert, P. A. Simms, X-Ray Lasers 1998 Proceedings, 379, IOP PUBLISHING LTD, (1999).
- [214] S. McCabe and G. J. Pert, Phys. Rev. A, 61, 033804, (2000).
- [215] S. McCabe, G. J. Pert, and P. A. Simms, X-Ray Lasers 1998 Proceedings, 379, IOP Publishing LTD, (1999).
- [216] E. A. McLean, T. N. Lee, J. A. Stamper, C. K. Manka, and H. R. Griem, J. Opt. Soc. Am. B, 9, 350, (1992). "
- [217] R. McWhirter, Plasma Diagnostic Techniques, Eds.: R. Huddleston and S. Leonard, Academic Press: New York, NY, USA, Chapter 5, 201, (1965).""
- [218] J.P. Christiansen, D.E.T.F. Ashby, and K.V. Roberts, Comput. Phys. Commun., 7, 271, (1974).
- [219] L. M. Meng, D. Alessi, O. Guilbaud, Y. Wang, M. Berrill, B.M. Luther, S. R. Domingue, D. H. Martz, D. Joyeux, S. De Rossi, J. J. Rocca, and A. Klisnick, Opt. express, Optical Society of America, 19 (13), 12087, (2011).
- [220] A. Miahnahri, S. Moeller, H.-D. Nuhn, G. Pile, D. Ratner, J. Rzepiela, D. Schultz, T. Smith,
- [221] J. Miao, P. Charalambous, J. Kirz and D. Sayre, Nature 400, 342-344, (1999)
- [222] P. W. Milonni, J. H. Eberly, Laser Physics, John Wiley and Sons, Inc., New Jersey, USA, (2010).
- [223] K. Hamamoto, Y. Tanaka, T. Yoshizumi, Y. Fukushima, H. Shiotani, N. Sakaya, M. Hosoya, T. Shoki, T. Watanabe and H. Kinoshita, Proc. SPIE 6151, 615119, (2006)
- [224] M. Mohan, New Trends in Atomic and Molecular Physics: Advanced Technological Applications, Springer-Verlag Berlin Heidelberg, 76, (2013).
- [225] JC Moreno, J Nilsen, LB Da Silva, *Opt. Comm.* **110** 585, 1994
- [226] D. Strickland and G. Morou, Opt.Comm. 56,229-221,(1985).
- [227] E. Oliva, P. Zeitoun, P. Velarde, M. Fajardo, K. Cassou, D. Ros, S. Sebban, D. Portillo, and S. le Pape, Phys. Rev. E, 82, 056408, (2010).
- [228] J. J. Olivero, R. L. Longbothum, J. Quant. Spectrosc. Radiat. Transf., 17, 233, (1977).
- [229] OSLO, Lambda Research Corporation, (2001).
- [230] G O'Sullivan, A Cummings, C Z Dong, P Dunne, P Hayden, O Morris, E Sokell, F O'Reilly, M G Su and J White (2009) 'Emission and absorption in laser produced plasmas: processes and applications'. J. Phys. Conf. Series, 163 (012003).
- [231] L.J. Palumbo, R.C. Elton 1977, *J. Opt. Soc. Am.* **67** 480
- [232] B. D. Patterson, R. Abela, H-H. Braun, U. Flechsig, R. Ganter, Y. Kim, E. Kirk, A. Oppelt, M. Pedrozzi, S. Reiche, L. Rivkin, Th. Schmidt, B. Schmitt, V. N. Strocov, S. Tsujino, and A. F. Wrulich, New. J. Phys., 12, 035012, (2010).
- [233] A. L. Peratt, Astrophys. Space Sci., 242, Issue 1-2, 93, (1996).
- [234] G.J. Pert, Phys. Rev. A 73, 033809 (2006)
- [235] P. H. Lin, M. C. Chou, C. A. Lin, H. H. Chu, J. Y. Lin, J. Wang, and S. Y. Chen, Phys. Rev. A, 76, 053817, (2007).
- [236] P. Jaegle, G. Jamelot, A. Carillon, A. Klisnick, A. Sureau, and H. Guennou, J. Opt. Soc. Am., 4: 563, (1987).
- [237] A.R. Präg, T.Mocek, M.Kozlová , B.Rus, K.Rohlena, Eur. Phys.J.D, 26 59.65, (2003)
- [238] G Pretzler, A Kasper, KJ Witte 2000 *Appl. Phys. B* **70** 1
- [239] A. Ritucci, G. Tomasselti, A. Reale, F. Flora, L. Mezi, Phys. Rev. A, 70, 023313, (2004)
- [240] K.S. Raines, S. Salha, R.L.Sandberg, H. Jiang, J.A. Rodriguez, B.P. Fahimian, H.C.Kapteyn, J. Du, J. Miao, Nature, 463, 214-217, (2010)
- [241] R. Rakowski, J. Mikocajczyk, A. Bartnik, H. Fiedorowicz, F. de Gaufridy de Dortan, R. Jarocki, J. Kostecki, M. Szczurek and P. Wachulak, Laser-produced plasma EUV source based on tin-rich, thin-layer targets, Appl. Phys. B: Lasers & Optics, DOI: 10.1007/s00340-010-4193-5

-
- [242] A. Ravasio¹, D. Gauthier, F. R. N. C. Maia, M. Billon, J-P. Caumes, D. Garzella, M. Geleoc, O. Gobert, J-F. Hergott, A-M. Pena, H. Perez, B. Carre, E. Bourhis, J. Gierak, A. Madouri, D. Mailly, B. Schiedt, M. Fajardo, J. Gautier, P. Zeitoun, P. H. Bucksbaum, J. Hajdu, and H. Merdji, *Phys. Rev. Lett.*, 103, 028104, (2009)
 - [243] H. V. Regemorter, *J. Astrophys.*, 136, 906, (1962).
 - [244] R. F. Smith, J. Dunn, J. Filevich, S. Moon, J. Nilsen, R. Keenan, V. N. Shlyaptsev, J. J. Rocca, J. R. Hunter, and M. C. Marconi, *Phys. Rev. E*, 72, 036404, (2005).
 - [245] M. Richardson, D. Torres, Ch. DePriest, F. Jin and G. Shimkaveg, Mass-limited, debris-free laser-plasma EUV source, *Opt. Comm.*, 145 (1998), 109-112
 - [246] B. Ehlers, Y. Platonov, B. Verman, J. Rodriguez, personal comment.
 - [247] A. Ritucci, G. Tomasselti, A. Reale, F. Flora, L. Mezi, *Phys. Rev. A*, 70, 023313, (2004) "
 - [248] J. J. Rocca, V. Shlyaptsev, F. G. Tomasel, O. D. Cortazar, D. Hartshorn, and J. L. A. Chilla, *Phys. Rev. Lett.*, 73, 2192, (1994).""
 - [249] Y. Liu, M. Seminario, G. Tomasel, C. Chang, J. J. Rocca and D. T. Attwood, *Phys. Rev. A*, 63, 033802, (2001)
 - [250] J. J. Rocca, Y. Wang, M. A. Larotonda, B. M. Luther, M. Berrill, and D. Alessi, *Optics Letters* 30, 2581-2583, (2005).
 - [251] J. Filevich, J. J. Rocca, M. C. Marconi, R. F. Smith, J. Dunn, R. Keenan, J. R. Hunter, S. J. Moon, J. Nilsen, A. Ng, and V. Shlyaptsev, *App. Optics*, 43, 19, (2004)
 - [252] F. Brizuela, Y. Wang, C. A. Brewer, F. Pedaci, W. Chao, E. H. Anderson, Y. Liu, K. A. Goldberg, P. Naulleau, P. Wachulak, M. C. Marconi, D. T. Attwood, J. J. Rocca and C. S. Menoni, *Opt. Lett.*, 34, 3, 271-273, (2009)
 - [253] JJ Rocca, Y Wang, MA Larotonda, BM Luther, M Berrill, D Alessi, *Opt. Lett.* 30, 2581, 2005
 - [254] Brendan A. Reagan, Keith A. Wernsing, Alden H. Curtis, Federico J. Furch, Bradley M. Luther, Dinesh Patel, Carmen S. Menoni, and Jorge J. Rocca, *Optics Letters*, 37, 17, 3624-3626, (2012)
 - [255] J. J. Rocca, Y. Wang, M. A. Larotonda, B. M. Luther, M. Berrill, and D. Alessi, *Opt. Lett.*, 30(19), 2581, (2005).
 - [256] JJ Rocca, V Shlyaptsev, FG Tomasel, OD Cortazar, D Hartshorn, JLA Chilla, *Phys. Rev. Lett.* 73, 2192, 1994
 - [257] J.J. Rocca, F.G. Tomasel, M.C. Marconi, V.N. Shlyaptsev, J.L.A. Chilla, B.T. Szapiro, G. Giudice 1995, *Phys. Plasmas* **2** 2547
 - [258] J.J. Rocca 1999 *Rev. Scient. Instrum.* **70** 3799
 - [259] J. J. Rocca, V. Shlyaptsev, F. G. Tomasel, O. D. Cortazar, D. Hartshorn, and J. L. A. Chilla, *Phys. Rev. Lett.*, 73, 2192, (1994).
 - [260] J. J. Rocca, Y. Wang, M. A. Larotonda, B. M. Luther, M. Berrill, and D. Alessi, *Opt. Lett.*, 30(19), 2581, (2005).
 - [261] Y. Wang, E. Granados, F. Pedaci, D. Alessi, B. Luther, M. Berrill, and J. J. Rocca, *Nature Photonics*, 2, 94 , (2008).
 - [262] N. Rohringer, D. Ryan, R.A. London, M. Purvis, F. Albert, J. Dunn, J.D. Bozek, C. Bostedt, A. Graf, R. Hill, S.P. Hau-Riege, J.J. Rocca, 2012 *Nature* **481** 488
 - [263] N Rohringer, D Ryan, RA London, M Purvis, F Albert, J Dunn, JD Bozek, Ch Bostedt, A Graf, R Hill, SP Hau-Riege, JJ Rocca, *Nature* **481** 488, 2012
 - [264] I.N. Ross, E.M. Hodgson, Some optical designs for the generation of high quality line foci, *J. Phys. E.: Sci. Instrum.* 18, 169 (1985)
 - [265] I.N. Ross, J. Boon, R. Corbett, A. Damerell, P. Gottfeldt, C. Hooker, M.H. Key, G. Kiehn, C. Lewis, O. Willi, Design and performance of a new line focus geometry for x-ray laser experiments, *Appl. Opt.* 26, 1584 (1987)
 - [266] M. Ruiz-Lopez, F. Staub, D. Bleiner 2012, *Proc. ICXRL 2012*
 - [267] M. Ruiz-Lopez, D. Bleiner, *Appl. Phys. B*, 115(3), 311, (2014).
 - [268] B Rus, T Mocek, M Kozlova, J Polan, P Homer, K Jukubczak, M Stupka, GJ Tallents, MH Edwards, N Booth, Z Zhai, J Dunn, AJ Nelson, ME Foord, RL Shepherd, M Fajardo, P Zeitoun, W Rozmus, HA Baldis, J Sobota, *Proc. SPIE* **6702** 67020G, 2007 "

- [269] B. Rus, T. Mocek, A. R. Präg, M. Kozlová, G. Jamelot, A. Carillon, D. Ros, D. Joyeux, and D. Phalippou, *Phys. Rev. A*, **66**, 063806, (2002)."
- [270] SACLA website, <https://xfel.riken.jp/eng>
- [271] B. E. A. Saleh and M. C. Teich, *Fundamentals of Photonics*, New York: John Wiley and Sons, Inc., (1991)."
- [272] D. Salzmann, *Atomic Physics in Hot Plasmas*, Oxford University Press: New York, NY, USA, (1998).
- [273] D. Salzmann and A. Krumbein, *J. Appl. Phys.*, **49**, 3229, (1978).
- [274] S. De . Silvestri, M. Nisoli, G. Sansone, S. Stagira, and C. Vozzi, *Strong Field Laser Physics*, Ed.: T. Brabec, Springer Series in Optical Sciences 134, Springer-Verlag New York, (2009).
- [275] A. Sasaki, A. Sunahara, K. Nishihara, T. Nishikawa, K. Fujima, T. Kagawa, K. Koike, H. Tanuma, *Atomic Modelling of the plasma EUV sources*, *High Energy Density Physics*, **3** (2007), 250-255
- [276] A. Sasaki, H. Yoneda, K. Ueda, and H. Takuma, *Laser Part. Beams* **11**, 25, (1993).
- [277] *Attosecond and XUV Spectroscopy: Ultrafast Dynamics and Spectroscopy*, Eds.: T. Schultz and M. Vrakking, Weinheim, Germany: Wiley-VCH, (2014).
- [278] K. Schwarzschild, *Abh. Wiss. Goett. Math. Phys. K1 NF4*, **1** (1905).
- [279] Y. Horikawa, S. Mochimaru, Y. Iketaki and Koumei Nagai, *SPIE* **1720**, 217, (1992)
- [280] Paul Scherrer Institute 2009, *Int. rep.* **09-10**
- [281] P Sebbah, C Vanneste, *Phys. Rev. B* **66** 144202, 2002
- [282] S. Sebban, D. Ros, A. G. MacPhee, F. Albert, A. Carillon, P. Jaeglé, G. Jamelot, A. Klisnick, C. L. S. Lewis, R. Smith, G. J. Tallents, a part of SPIE's 42nd Annual Meeting, San Diego CA, *Soft X-Ray Lasers and Applications II*, Eds.: J. J. Rocca and L. B. Da Silva, *Proceedings of the SPIE*, **3156**, 11, (1997).
- [283] S. Sebban, R. Haroutunian, Ph. Balcou, G. Grillon, A. Rousse, S. Kazamias, T. Marin, J. P. Rousseau, L. Notebaert, M. Pittman, J. P. Chambaret, A. Antonetti, D. Hulin, D. Ros, A. Klisnick, A. Carillon, P. Jaeglé, G. Jamelot, and J. F. Wyart, *Phys. Rev. Lett.*, **86**, 3004, (2001).
- [284] S. Sebban, T. Mocek, D. Ros, L. Upcraft, Ph. Balcou, R. Haroutunian, G. Grillon, B. Rus, A. Klisnick, A. Carillon, G. Jamelot, C. Valentin, A. Rousse, J. P. Rousseau, L. Notebaert, M. Pittman, and D. Hulin, *Phys. Rev. Lett.*, **89**, 253901, (2002).
- [285] H.A. Buchdahl, *Optical Aberration Coefficients*, Dover Publications, (1968)
- [286] V. P. Shevelko, *Atoms and Their Spectroscopic Properties*, Springer Series on Atomic, Optical, and Plasma Physics, Verlag Berlin Heidelberg New York, (1997).
- [287] V. N. Shlyaptsev, *IEEE J. Quant.*, **42**, 1, (2006).
- [288] V. N. Shlyaptsev, J. Dunn, S. Moon, R. Smith, R. Keenan, J. Nilsen, K. B. Fournier, J. Kuba, A. L. Osterheld, J. J. G. Rocca, B. M. Luther, Y. Wang, and M. C. Marconi, in *Soft X-Ray Lasers and Applications V*, Ed.: E. E. F. S. Suckewer, *SPIE*, **5197**, 221, (2003).
- [289] A. E. Siegman, *Lasers*, Sausalito: University Science Books, (1986).
- [290] W.T. Silfvast, *IEEE J.Quant*, **El. 358**, 700, (1999)
- [291] W.T. Silfvast, L. Sun, J. E. Harvey, University of Central of Florida Orlando, Technical report, AN: ADA318404, (1996)
- [292] L. Da Silva, B. MacGowan, S. Mrowka, J. Koch, R. London, D. Matthews, and J. Underwood, *Opt. Lett.*, **18**, 1174, (1993).
- [293] L. B. Da Silva, T. W. Barbee Jr, R. Cauble, P. Celliers, C. D. Decker, D. H. Kalantar, M. H. Key, R A. London, J. C. Moreno, J. E. Trebes, A. S. Wan, and F. Weber, *5th International Conference on X-ray Lasers*, Lund, Sweden, (1996).
- [294] J. Silverman, Is there a light 10 billion times brighter than the sun?, (2007) "
- [295] M. Skibowski, B. Feuerbacher, Dr. W. Steinmann, and R. P. Godwin, *Zeitschrift für Physik*, **211**, 342, (1968)."
- [296] C. H. Skinner, *Phys. Fluids B*, **3**, 2420, 0899, (1991).
- [297] S. Maxon, P. Hagelstein, B. MacGowan, R. London, M. Rosen, J. Scofield, S. Dalhed, and M. Chen, *Phys. Rev. A*, **37(6)**, 2227, (1988).

- [298] S. Maxon, S. Dalhed, P. L. Hagelstein, R. A. London, B. J. MacGowan, M. D. Rosen, G. Charatis, and G. Busch, *Phys. Rev. Lett.*, **63**(3), 236, (1989).
- [299] S. McCabe and G. J. Pert, *Phys. Rev. A*, **61**, 033804, (2000).
- [300] W. J. Smith, *Modern Optical Engineering*, SPIE Spress , Ch.15 ed. 4 (2007)
- [301] R. F. Smith, J. Dunn, J. Filevich, S. Moon, J. Nilsen, R. Keenan, V. N. Shlyaptsev, J. J. Rocca, J. R. Hunter, and M. C. Marconi, *Phys. Rev. E*, **72**, 036404, (2005).
- [302] J.W. Hardy, *Adaptive optics for astronomical telescopes*, Ed. Oxford University Press, p. 128, (1998)
- [303] B. Soom, U. Ellenberger, R. Weber, and J. E. Balmer, *Opt. Commun.*, **84**, 23, (1991).
- [304] F. Staub, M. Braud, J.E. Balmer, J. Nilsen, S.Bajt, *Applied Physics B*, **78**, 7-8, (2004)
- [305] D. G. Steel, P. D. Rockett, D. R. Bach, and P. L. Coldestock, *Rev. Sci. Instrum*, **49**(4), 456, (1978).
- [306] P. Stefan, H. Tompkins, J. Turner, J. Welch, W. White, J. Wu, G. Yocky, and J. Galayda, *Nat. Photonics*, **4**, (2010). ”
- [307] G. Korn, A. Thiss, H. Stiel, U. Vogt, M. Richardson, Th. Elsässer, M. Faubel, *Opt. Letters*, **27**, 866, (2009)”
- [308] C. Stockl and G. D. Tsakiris, *Laser Interaction with Matter*, Singapore: World Scientific, (1989).
- [309] S. Suckewer, P. Jaegle, X-ray Laser: past, present, and future, *Laser Phys. Lett.* **6** (2009), 411-436
- [310] SwissFEL website, <https://www.psi.ch/swissfel/> ”
- [311] A. Filipponi, M. Borowski, D. T. Bowron, S. Ansell, A. di Cicco, S. de Panfilis, and J. P. Itie, *Rev. Sci. Instrum.*, **71**, 2422, (2000).””
- [312] J. Szlachetko, C. J. Milne, J. Hoszowska, J.-Cl. Dousse, W. B. Iachucki, J. Sá, Y. Kayser, M. Messerschmidt, R. Abela, S. Boutet, C. David, G. Williams, M. Pajek, D. B. Patterson, G. Smolentsev, J. A. Van Bokhoven, and M. Nachtegaal, *Structural Dynamics*, **1**, 021101, (2014). ”
- [313] J. Szlachetko, M. Nachtegaal, J. Sá, J.-Cl. Dousse, J. Hoszowska, E. Kleymenov, M. Janousch, O. V. Safonova, C. Köhlig, and J. A. van Bokhoven, *Chem. Commun.*, **48**, 10898, (2012).”
- [314] E. J. Takahashi, T. Kanai, K. L. Ishikawa, Y. Nabekawa, and K. Midorikawa, *Phys. Rev. Lett.*, **101**, 253901, (2008).
- [315] J. Tallents, *J. Phys. D: Appl. Phys.*, **36**, R259, (2003).
- [316] F. Tavella, N. Stojanovic, G. Geloni, et al. 2011, *Nature Photonics* **5** 162
- [317] G. Tomassetti, A. Ritucci, A. Reale, L. Palladino, L. Reale, S. V. Kulkhlevsky, F. Flora, L. Mezi, A. Faenov, T. Pikuz, A. Gaudieri, *Opt. Comm.* **231** 403, 2003
- [318] R. Tommasini, E. Fill 2000 *Phys. Rev. A* **62**03 4701 ”
- [319] R. Tommasini, F. L’aoenthal, and J. E. Balmer, *Phys. Rev. A*, **59**, 1577, (1999).”
- [320] G. Tomassetti, A. Ritucci, L. Palladino, L. Reale, O. Consorte, S. V. Kulkhlevsky, I. Zs. Kozma, F. Flora, L. Mezi and J. Kaiser, 2002 *Czech. J. Phys* **52** 405
- [321] F. Trager, *Springer Handbook of Lasers and Optics*, Springer, (2007).
- [322] H. Stiel, J. Tuemmler, R. Jung, P.V. Nickles, W. Sandner 2009 *SPIE Proc. Soft X-ray Lasers and Appl.* **7451**, 109-1
- [323] J.L. Turner, R. Akre, A. Brachmann, F.-J. Decker, Y.T. Ding, P. Emma, Y. Feng, A.S. Fisher, J.C. Frisch, A. Gilevich, P. Hering, K. Horovitz, Z. Huang, R.H. Iverson, D. Kharakh, A. Krasnykh, J. Krzywinski, H. Loos, M. Messerschmidt, S.P. Moeller, H.-D. Nuhn, D.F. Ratner, T.J. Smith, J.J. Welch, J. Wu *Proceedings of Particle Accelerator Conference*, THP168, (2011)
- [324] D. Ursescu, Ph.D. Thesis, J. Gutenberg University, Mainz, Germany. (2006) ”
- [325] D. Ursescu, B. Zielbaver, Th. Köhler, P. Neumayer, G. Pert, *Phys. Rev. E* **75**, 045401, (2007)”
- [326] J. J. Olivero and R. L. Longbothum, *J. Quant. Spectrosc. Radiat. Transf.*, **17**, 233, (1977).
- [327] G. Vampa, C. R. McDonald, G. Orlando, D. D. Klug, P. B. Corkum, and T. Brabec, *Phys. Rev. Lett.*, **113**, 073901, (2014).
- [328] V. Vavryčuk, *Geophysics*, **77**, 4, T109, (2012).

- [329] R. M. van der Veen, J. J. Kas, C. J. Milne, V. T. Pham, A. El Nahhas, F. A. Lima, D. A. Vithanage, J. J. Rehr, R. Abela, M. Chergui, *Phys. Chem. Chem. Phys.*, 12(21), 5551, (2010).
- [330] G. S. Voronov, *At. Data Nucl. Data Tables*, 65, 1, (1997).
- [331] P. Wachulak, A. Bartnik, H. Fiedorowicz, *Proc. of the School on Short-wavelength Imag. Spectrosc. Sources*, D. Bleiner Ed., (Bern 10-11 Sept. 2012), SPIE Digital Library, (2012)
- [332] Y. Wang, M.A. Larotonda, B.M. Luther, D. Alessi, B. Berrill, V.N. Shlyaptsev, J.J. Rocca, Demonstration of high-repetition-rate tabletop soft-x-ray lasers with saturated output at wavelengths down to 13.9 nm and gain down to 10.9 nm. *Phys. Rev. A* 72, 053807 (2005)
- [333] Y. Wang, M. A. Larotonda, B. M. Luther, D. Alessi, M. Berrill, V. N. Shlyaptsev, and J. J. Rocca, *Phys. Rev. A*, 72, 053807, (2005).
- [334] X. L. Wang, C. Z. Dong, M. G. Su, *Nucl. Instr. Meth. Phys. Res. B*, 280, 93, (2012).
- [335] Wark, *Science*, 276, 1097, (1997).
- [336] M. J. Weber, *Handbook of Laser Wavelengths*, Boca Raton: CRC Press LLC, (1999).
- [337] S. Weinberg, *Phys. Rev.*, 126, 1899, (1962).
- [338] *Plasma Physics: Nonlinear Theory and Experiments*, Series: Nobel Foundation Symposia 36, Ed.: H. Wilhelmsson, (1977).
- [339] C. Winterfeldt, C. Spielmann, and G. Gerber, *Rev. Mod. Phys.*, 80, (2008).
- [340] W. S. Abdelaziz, *Eur. Phys. J. D*, 55, 17, (2009).
- [341] W. S. Abdelaziz and H. M. H. Ibrahim, *Opt. Photonics*, 1, 110, (2011).
- [342] X. Zeng, X. Mao, S. S. Mao, J. H. Yoo, R. Greif, and R. E. Russo, *Appl. Phys.*, 95, 816, (2004).
- [343] F. Yan, J. Zhang, X. Lu, J.Y. Zhong, *Appl. Phys. B*, 79, 229, (2004).
- [344] Y. Li, J. Nilsen, J. Dunn, A. L. Osterheld, A. Ryabtsev, and S. Churilov, *Phys. Rev. A*, 58(4), R2668, (1998).
- [345] R. E. Fischer, B. Tadic-Galeb, and P. R. Yoder, *Optical System Design*, New York: McGraw-Hill, (2008).
- [346] Z. Zhang, Y. Ding, A. Marinelli, and Z. Huang, *Phys. Rev. ST Accel. Beams*, 18, 030702, (2015).
- [347] XQ Zhang, YL Cheng, Q Wang, *Laser Phys.* **18** 958, 2008
- [348] J. Zhang, A. G. MacPhee, J. Lin, E. Wolfrum, R. Smith, C. Danson, M. H.
- [349] J. Zhang, A.G. MacPhee, J. Nilsen, J. Lin, T. W. Barbee Jr, C. Danson, M. H. Key, C. L. S. Lewis, D. Neely, R. M. N. O'Rourke, G. J. Pert, R. Smith, G. J. Tallents, J. S. Wark, and E. Wolfrum, *Phys. Rev. Lett.*, 78, 20, (1997).
- [350] J. Zhang, M. H. Key, P. A. Norreys, G. J. Tallents, A. Behjat, C. Danson, A. Demir, L. Dwivedi, M. Holden, P. B. Holden, C. L. S. Lewis, A. G. MacPhee, D. Neely, G. J. Pert, S. A. Ramsden, S. J. Rose, Y. F. Shao, O. Thomas, F. Walsh, and Y. L. You, *Phys. Rev. Lett.*, 74 (8), 1335, (1995).
- [351] D Zimmer, B Zielbauer, M Pittman, O Guilbaud, J Habib, S Kazamias, D Ros, V Bagnoud, Th Kuehl, *Opt. Lett.* **35** 450, 2010
- [352] D Zimmer, D Ros, J Habib, S Kazamias, D Zielbauer, V Bagnoud, B Ecker, DC Hochhaus, B Aurand, P Neumayer, T Kuehl, *Phys. Rev. A* **82** 13803, 2010
- [353] D. Zimmer, B. Zielbauer, V. Bagnoud, U. Eisenbarth, D. Javorkova, and T. Kuehl, *Opt. Lett.*, 16(14), 10399, (2008).